Sharma, Sidharath

Numerical characterisation of flow-induced noise in a small high-speed centrifugal compressor with casing treatment

Numerical characterisation of flow-induced noise in a small high-speed centrifugal compressor with casing treatment

Sidharath Sharma

Supervisor: Prof. J.M. Allport

School of Computing & Engineering
University of Huddersfield

This dissertation is submitted for the degree of
Doctor of Philosophy

Turbocharger Research Institute September 2019

Bharat Bhushan Sharma

Jacob Bhushan Sharma

Declaration

I hereby declare that except where specific reference is made to the work of others, the contents of this dissertation are original and have not been submitted in whole or in part for consideration for any other degree or qualification in this, or any other university. The work leading up to this thesis has been published or undergoing peer-review with following titles:

List of published & accepted work

[1] Sidharath Sharma, Alberto Broatch, Jorge García-Tíscar, AK Nickson, and JM Allport. Acoustic and pressure characteristics of a ported shroud turbocompressor operating at near surge conditions. *Applied Acoustics,* 148:434–447, 2019.

[2] Sidharath Sharma, Alberto Broatch, Jorge García-Tíscar, John M Allport, and Ambrose K Nickson. Acoustic characteristics of a ported shroud turbocompressor operating at design conditions. *International J of Engine Research,* 1:15, 2018.

[3] Sidharath Sharma, Jorge García-Tíscar, John M Allport, Martyn L Jupp, and Ambrose K Nickson. Impact of impeller casing treatment on the acoustics of a small high speed centrifugal compressor. In ASME *Turbo Expo 2018: Turbomachinery Technical Conference and Exposition,* pages V02BT43A010–V02BT43A010. American Society of Mechanical Engineers, 2018.

[4] Sidharath Sharma, Martyn Jupp, Simon Barrans, and Keith Nickson. The impact of housing features relative location on a turbocharger compressor flow. *International Journal of Mechanical Engineering and Robotics Research,* 6(6):451–457, 2017.

[5] Sidharath Sharma, Martyn L Jupp, Ambrose K Nickson, and John M Allport. Ported shroud flow processes and their effect on turbocharger compressor operation. In ASME *Turbo Expo 2017: Turbomachinery Technical Conference and Exposition,* pages V02CT44A017–V02CT44A017. American Society of Mechanical Engineers, 2017.

List of articles undergoing peer-review

[6] Sidharath Sharma, Alberto Broatch, Jorge García-Tíscar, John M Allport, and Ambrose K Nickson. Acoustic characterisation of a small high-speed centrifugal compressor with casing treatment: An experimental study. *Manuscript accepted by the journal of Aerospace Science and Technology,* 2019.

[7] Sidharath Sharma, Simon Barrans, Jorge García-Tíscar, John M Allport, and Ambrose K Nickson. Evaluation of modelling parameters for computing flow-induced noise in a small high-speed centrifugal compressor. *Manuscript submitted to the journal of Aerospace Science and Technology,* 2019.

[8] Sidharath Sharma, Simon Barrans, Jorge García-Tíscar, John M Allport, and Ambrose K Nickson. Effects of ported shroud casing treatment on the acoustic and flow behaviour of a centrifugal compressor. *Manuscript accepted by the International Journal of Engine Research,* 2019.

[9] Sidharath Sharma, Simon Barrans, Jorge García-Tíscar, John M Allport, and Ambrose K Nickson. Impact of operational speed on the acoustic characteristics of a high-speed centrifugal compressor with and without casing treatment. *Manuscript to be submitted to the International Journal of Engine Research,* 2019.

The work presented in this thesis was done in collaboration with other researchers. The respondent is the first and corresponding author of all papers on which this thesis is based. The respondent implemented the numerical methodologies and analysed the computed results. Discussions were performed in collaboration with supervisor Prof. Allport and the rest of the co-authors. Experimental measurements were performed with the help of the team at CMT – Motores Térmicos, and are thus gratefully acknowledged. This dissertation contains fewer than 70,000 words including appendices, bibliography, footnotes, tables and equations and has fewer than 80 figures.

Sidharath Sharma
September 2019

Abstract

Centrifugal turbomachines of smaller sizes operating at higher speeds have become pervasive due to the increased specific power and reliability achieved by improvements in manufacturing, materials and computational methods. The presence of these small turbomachines, specifically compressors, in helicopters, unmanned aerial vehicles (UAVs), auxiliary power units (APUs), turbochargers and micro gas turbines necessitates superior aerodynamic performance over a broad operational range which is widely achieved by ported shroud casing designs. In addition to aerodynamic performance, acoustic emissions have become a critical aspect of design for these small centrifugal compressors due to high operational speeds. Therefore, in this thesis, a high-speed turbocharger compressor with the ported shroud (PS) casing treatment is used as a subject to understand the flow-induced noise in high-speed centrifugal machines using high-fidelity numerical (CFD) methods. Furthermore, the impact of PS design and operating speed on the acoustic emission of the compressor is also established by comparing the operation of PS *open* and PS *blocked* compressor configurations at 99 krpm and 130 krpm speedlines.

The numerical model to predict the acoustic characteristics of the compressor is developed and validated by comparing the acoustic and performance results with the experimental values. The impact of various critical parameters on the performance and acoustic predictions is quantified by exploring a range of statistical and scale resolving methods of turbulence formulations along with their sensitivity to spatial and temporal resolution. The results demonstrate the need for higher spatial resolution for scale resolving models to yield credible acoustic predictions.

The results from the selected numerical configuration are analysed to establish the relationship between the flow field and the acoustic characteristics of the compressor. The acoustic spectra for the design point are seen to be dominated by a characteristic 'buzz-saw' or Rotating Order (RO) tonal noise. These 'buzz-saw' or RO tones are confirmed to be caused by the sonic conditions on the leading edges of the impeller blades. For the near surge operation, the low-frequency broadband features associated with near surge operation are alleviated by the PS casing treatment and are not observed in the corresponding spectra. Furthermore, the characteristic 'whoosh' noise is also not observed in the spectra of either design or near surge points.

The flow is further investigated by the modal decomposition of the dynamic pressure field using Proper Orthogonal Decomposition (POD) to compute the high-energy coherent structures and their corresponding spectral characteristics. For the design operation, the results showed the accumulation of higher energy content in the first two modes that are related to the RO and blade pass tones. The diffuser and the PS cavity are found to house the energetic sources of the oscillations. For the near surge point, the energy is seen to be distributed much more evenly among the modes. The diffuser and volute are observed to house the more energetic sources of broadband content without any significant contribution from the PS cavity.

The comparison of the open and blocked configurations operating at design conditions shows higher tonal content in the inlet duct spectrum of the open configuration. For the near surge operation, the broadband elevations in the lower and medium frequency regions are observed for the blocked configuration. Furthermore, characteristic ‘whoosh’ noise is also identified in the outlet duct spectrum of the blocked configuration. The increase in operational speed causes a general increase in the overall acoustic emission of the compressor for both configurations.

Keywords: Compressor, Aeroacoustics, LES, Modal decomposition, POD, DES, SBES, CFD

Acknowledgements

I would like to express my gratitude, first and foremost, to my supervisors Prof. John Allport, Dr Martyn Jupp, Dr Simon Barrans and Dr Keith Nickson for their guidance and support including the resources required in the pursuit of this research. I am especially grateful to Prof. Allport for agreeing to take over the role of my primary advisor in the final year of the project and seeing me through the finish line.

I would also like to thank Prof. Alberto Broatch, Dr Jorge García-Tíscar and Ferran Roig for welcoming me as a visiting researcher in the CMT – Motores Térmicos and for their support with the experimental campaign. I am indebted to *Jorge* for his invaluable help with various programming and visual tools along with the insights on numerical and experimental results. I would not be far from the truth in saying that without your help, I could not have developed this work to the same level of satisfaction.

I would also like to acknowledge the help and support of BorgWarner, specifically Dr Keith Nickson in providing the necessary compressor data and components. Also thanks to the HPC department in UoH, specifically *Josh* for his support with computing infrastructure.

This acknowledgement would be incomplete without the mention of my colleagues in *TRI*, especially *Sam*, *Shams*, *Mahir* and *Ahmed*; thank you for such a memorable time.

Finally, I would like to thank my family and friends for their constant support, especially my parents from whom I inherited the appreciation for mathematics and science. I was not able to visit you as much as you would have liked during the course of this program; I promise to make it up to you.

Huddersfield, 2018

सुखं त्विदानीं त्रिविधं श्रृणु मे भरतर्षभ ।
अभ्यासाद्रमते यत्र दुःखान्तं च निगच्छति
यत्तदग्रे विषमिव परिणामेऽमृतोपमम् ।
तत्सुखं सात्त्विकं प्रोक्तमात्मबुद्धिप्रसादजम्

भगवद् गीता १८.३६-३७

"The happiness which comes from long practice, which leads to the end of suffering, which at first is like poison, but at last like nectar - this kind of happiness arises from the serenity of one's own mind"

Bhagavad Gita, *18.36,37*

Table of contents

List of figures

List of tables

List of Symbols

Latin characters

A	Area	m^2
a	Speed of sound	$m\,s^{-1}$
$\mathbf{a}_j$	Expansion coefficients	
C	Courant number	[-]
C_{DES}	Model constant, 0.61	
D	Duct diameter	m
d_s	Sensor separation	m
F	Blending or shielding function	Hz
f_c	Cut-off frequency	Hz
I	Sound Intensity	$W\,m^{-2}$
k	Turbulent kinetic energy	$m^2\,s^{-2}$
L	Level (SPL, SIL or PVL)	dB
L_t	Turbulent length scale	m
$\dot{m}$	Mass flow rate	$kg\,s^{-1}$
M	Mach number	$-$
N	Compressor rotational speed	rpm
p	Pressure	Pa
Q	Volumetric flow rate	$kg\,m^{-3}$
$\mathbf{R}$	Covariance matrix	
r	Duct radius	m
T	Temperature	K
T_d	Sensor time interval	s
t	Time	s
U	Mean velocity	$m\,s^{-1}$
y	Distance of the first cell from the wall	m
y^+	Non-dimensional boundary layer distance	$-$

Greek

Δ	Local grid spacing	
$\Delta t, f, x$	Time or frequency or distance *step*	s or Hz or m
γ	Ratio of specific heats	–
ε	Relative deviation	%
η_s	Isentropic efficiency	%
θ	Direction of arrival	rad
λ	Eigenvalue	–
Π_{t-t}	Pressure ratio	–
ρ	Density	$\mathrm{kg\,m^{-3}}$
σ	Standard deviation	–
τ	Compressor torque	$\mathrm{kg\,m^{2}\,s^{-2}}$
ϕ	Generic variable	–
Φ	mode	–
ψ	Flow coefficient	–
ω	Specific turbulence dissipation rate	$\mathrm{s^{-1}}$

Sub- and superscripts

$+$	Forward-travelling variable
$-$	Backward-travelling variable
$*$	Corrected variable
0	Stagnation variable
$1, 2, 3$	Related to 1^{st}, 2^{nd} or 3^{rd} downstream sensor
a	(Freq.) related to an asymmetric acoustic mode
back	Backward travelling wave
CFD	Variable simulated through CFD
exp	Variable measured experimentally
i/in	Related to the inlet duct
forw	Forward-travelling wave
N	(Freq.) related to the spatial Nyquist criterion
o/out	Related to the outlet duct
r	(Freq.) related to a radial acoustic mode
s	Isentropic
ref	Reference value
T	(Sub.) Total or stagnation variable | (Sup.) Transposed
t-t	Total to total ratio
tip	Related to the blade tip

Acronyms

BPF	Blade Passing Frequency
BPF	Best Efficiency Point
CAA	Computational AeroAcoustics
CAD	Computer-Aided Design
CFD	Computational Fluid Dynamics
CFL	Courant-Friedrich-Levy (number)
DAQ	Data Acquisition
DES	Detached Eddy Simulation
DDES	Delayed Detached Eddy Simulation
DMD	Dynamic Mode Decomposition
DNS	Direct Numerical Simulation
LCMV	Linearly-Constrained Minimum Variance
LES	Large Eddy Simulation
MoC	Method of Characteristics
MRF	Multiple Reference Frame
NRBC	Non-Reflecting Boundary Condition
NS	Near Surge (point)
PIV	Particle Image Velocimetry
POD	Proper Orthogonal Decomposition
PS	Ported Shroud
PSD	Power Spectral Density
RANS	Reynolds-Averaged Navier-Stokes
RBM	Rigid Body Motion
RO	Rotating Order
RPM	Revolutions Per Minute
TCN	Tip Clearance Noise
SBES	Stress Blended Eddy Simulation
SIL	Sound Intensity Level
SPL	Sound Pressure Level
SST	Shear Stress Transport
SVD	Singular Value Decomposition
URANS	Unsteady Reynolds-Averaged Navier-Stokes

Chapter 1

Introduction

Contents

1.1 Motivation

Turbomachines have a surprisingly long association with technological growth seen in the human industrial society. Although the earliest use of turbomachines can be attributed to the water wheels used by the people in the Mediterranean region between the 3rd and 1st century BCE, the accounts in recent time are credited to Papin, who presented his work on centrifugal pumps and blowers in 1705 [10]. In the start of nineteenth century, the need to extract work from falling water drove the developments in hydraulic turbines while the necessities of industrial revolution era led to advancements in steam turbines for marine propulsions and electric power generation. While the turbines underwent accelerated developments during this time, the use of pumps and blowers were limited to ventilation. This was about to change due to two prominent developments of twentieth century: the gas turbine engine and the internal combustion engine turbocharger. Unlike steam cycle, the input work required to drive the compressor is a significant fraction of the total work output in gas turbine cycle. This necessitated higher efficiencies of both compressor and turbines to make gas turbine engine viable. Furthermore, the two fold demand of high efficiency and high specific work for turbojet and turbofan applications gave impetus to push the limits of technology. The aforementioned demands of twentieth century led to the developments in compressible flow turbomachines.

Research in gas turbine engines post Second World War, specifically for aircraft applications led to massive developments in axial turbomachinery, whilst supercharging and turbocharging of internal combustion engines provided a market for centrifugal machines to flourish. The operational requirements for turbocharging vary rather significantly from gas turbines as the former requires a wider stable flow range. It can be pointed out the for small size scales, axial machines are a less attractive option as compared to centrifugal equivalents due to a variety of reasons, including higher friction losses and blockage effects, severe tip leakage losses and manufacturing costs. Another aspect of turbomachines, usually undesirable, is the noise associated with their operation. For instance, the primary noise features associated with a gas turbine engine are compressor self-noise, direct combustion noise, turbine self-noise, nozzle self-noise and jet mixing noise. Furthermore, the change in aerodynamic output is proportional to the third order of change in rotor tip speed while the change in sound power is proportional to fifth or sixth order [11] of change in rotor tip speed. Therefore, the increase in the acoustic output is significantly higher than the aerodynamic output for a particular increase in the rotor tip speed.

With the advancements in manufacturing, materials and computational methods, turbomachinery designs got more efficient over time providing higher aerodynamic output and reliability with lower weight and cost. The specific power output increased owing to incorporation of innovative control technologies, specialised materials and sophisticated aerodynamic designs.

In other words, the rotational speed of turbomachines increased while the overall machine size decreased for the similar power output as demonstrated in Fig. 1.1. This led to the collapse of the barrier that limited the applications of turbomachinery to large industrial set-ups like power generation or aircraft engines and made it pervasive in our daily lives. As mentioned before, centrifugal machines, specifically compressors, are better suited for smaller sizes and hence, small high-speed turbomachines are dominated by centrifugal configurations. These small turbomachines, specifically compressors, are pervasive in home appliances like vacuum cleaners, hair dryers and fans to helicopters, unmanned aerial vehicles (UAVs), auxiliary power units (APUs), turbochargers and micro gas turbines and even artificial heart pumps. These applications necessitates superior aerodynamic performance over a broad operational range which is widely achieved by ported shroud casing designs. In addition to aerodynamic performance, acoustic emissions have become a critical aspect of design for these small centrifugal compressors due to high operational speeds.

The history of turbomachines is primarily that of their applications and the needs of human society for those very applications. The next big challenge put forward for turbomachines is that of environment preservation by efficient and sustainable use of energy. The candidate that has shown promise for this cause of reducing emissions and exploitation of renewable energy sources is micro gas turbine [12] as the means for distributed power generation. In a micro gas turbine, the compressor and turbine configuration is similar to an automotive turbocharger. Furthermore, similarities in design and volume flow rates along with decades of development experience makes turbochargers an excellent basis for the development of micro gas turbines. This cause is shaping the future of small centrifugal turbomachines in the same way aircraft applications shaped large axial machines. The work of Olivero [13], *"Evolution of a Centrifugal Compressor- From turbocharger to micro gas turbine application"* provides a detailed overview of the subject.

With the increase of appliances using small high-speed centrifugal compressors, the aforementioned issue of noise becomes critical; even more so when the appliance is operated in the house or a residential setting. These small high-speed machines should deliver good aerodynamic performance over a wide range of operation with lower acoustic emissions. In order to achieve this objective of lower acoustic emissions effectively, a systematic approach to characterise and understand the acoustic spectra of the emitter is necessary. Therefore, noise generated in a small and wide flow high-speed centrifugal compressor is investigated in this thesis. The most prominent of these small turbomachines with a wide experience in development is a ported shroud automotive turbocharger compressor, thereby, being the rightful candidate for current acoustic investigation.

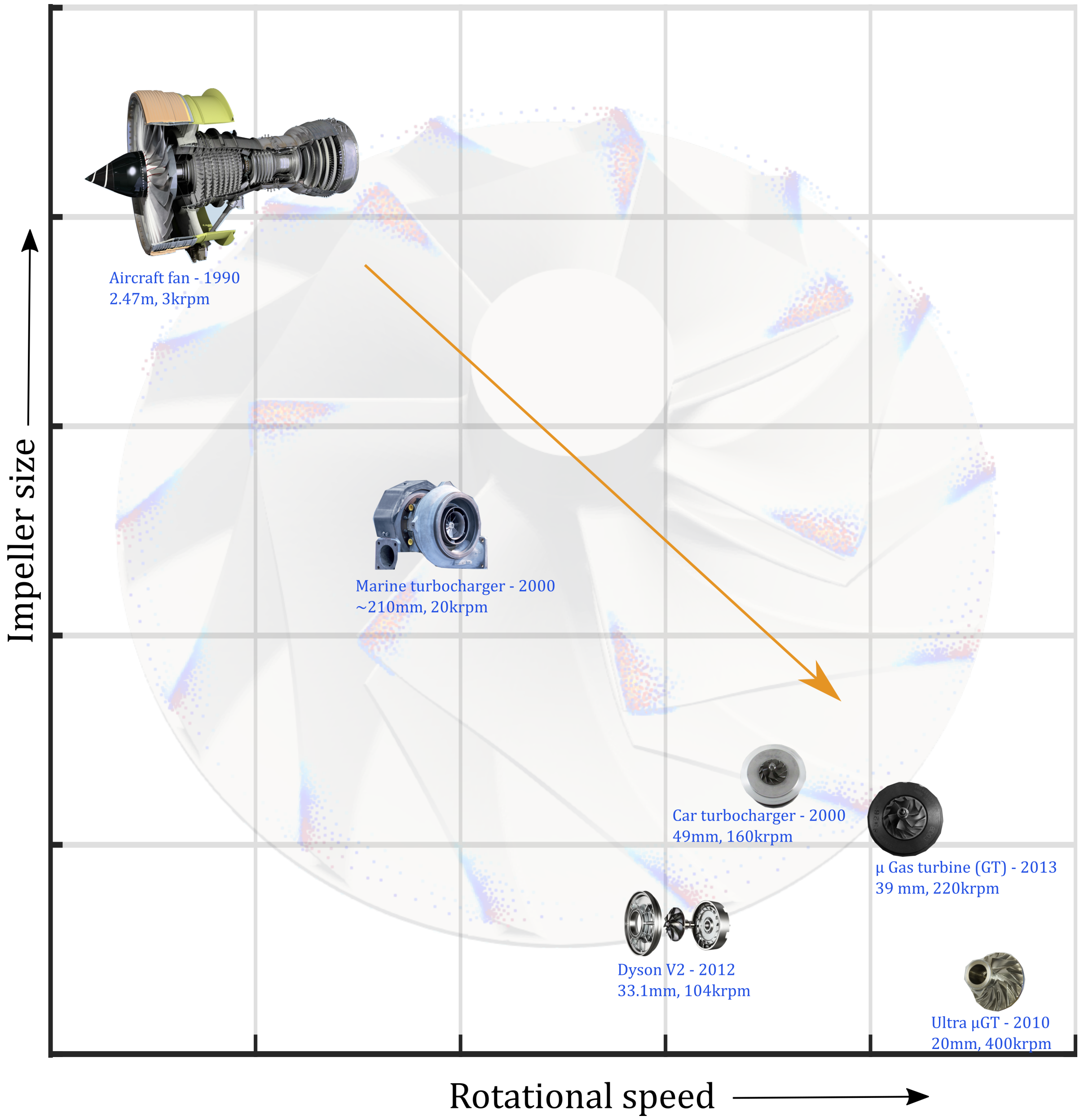

Fig. 1.1 Reference impeller size and operating speed for various turbomachines are presented. In recent times, the development of small high-speed centrifugal machines is on the rise. Please, note that size and operating speed are for references as the applications have multiple impellers and/or operate at various speeds. The references to the data are presented in Appendix A.

1.1.1 Turbochargers

Turbocharging in its contemporary form was introduced by Büchi in the year 1905 with an intent to increase the rated power of engines. At that time, the application of turbochargers was limited to reciprocating engines powering aircraft flying at altitude associated with decreased air density. Turbochargers were later paired with large displacement marine diesel engines. High density intake charge from turbochargers provided two fold benefit to diesel engines. The first one is the increase in specific power and the second one is the increase in efficiency due to better combustion characteristics of the high pressure and high temperature charge. Although the introduction of turbocharging in automotive engines started in the 1960s, it was not until the 1980s that reliable and mature designs were successfully implemented. The intent was again to increase the rated power and decrease brake specific fuel consumption of engines. However, the problem of so called turbocharger lag inhibited the wide scale application of turbochargers. It was in the 1990s, when stringent pollution norms challenged the automotive engine manufacturers making turbocharging necessary to better control air flow and enable the use of emission control methods like exhaust gas recirculation. Waste gate and variable geometry configurations were then developed to further alleviate the issue of lag and enhance the control of air flow.

In this era, turbocharging is used for more than just increasing power or better fuel economy and emissions. The high-density intake charge that increases the power output of the engine, also allows us to decrease the engine size and operating speed of the prime mover whilst maintaining similar power output; thereby generating fewer losses, improved emissions and efficiency. This is termed as downsizing and down speeding of engines. The downsized engine should ideally yield a uniform torque curve over the majority of an engine operating cycle along with high torque at low engine speeds to maintain the driving experience of the vehicle similar to the one with an equivalent high displacement engine. This new operating environment presents a whole new level of challenges for the turbomachinery. In the turbocharger compressor side, the requirement of high torque at low engine speeds corresponds to delay in the onset of stall [14] and efficient operation in the near surge region.

A delay in the onset of surge and enhancement of the stable flow region of the compressor operation is achieved by either using active flow control devices [15, 16] or passive flow control devices [17–19]. Active flow control strategies include inlet/diffuser guide vanes, diffuser bleed valves, air injection or a movable plenum wall. Passive flow control strategies that include casing treatment, a bleed system and internal recirculation or ported shroud are based on the principle of recirculating the low momentum fluid that blocks the blade passage back to the compressor inlet. Active flow control devices are space and cost intensive and require regular maintenance due to their complicated design. This limits the use of active flow devices in automotive turbochargers, which demand compact and reliable designs, making passive control the preferred strategy to enhance the stable flow region.

An additional aspect of downsized engines is their relatively quieter operation than their naturally aspirated counterparts, specifically in the low-speed range [20]. Furthermore, the developments in powertrain refinement over the last two decades have made the turbocharger noise prominent to the customer. In particular, a broadband noise detected during full load, tip-in and tip-out manoeuvres discussed in the upcoming section is of particular interest to automotive manufacturers. Therefore, the acoustic characteristics of a ported shroud turbocharger compressor are investigated in this thesis.

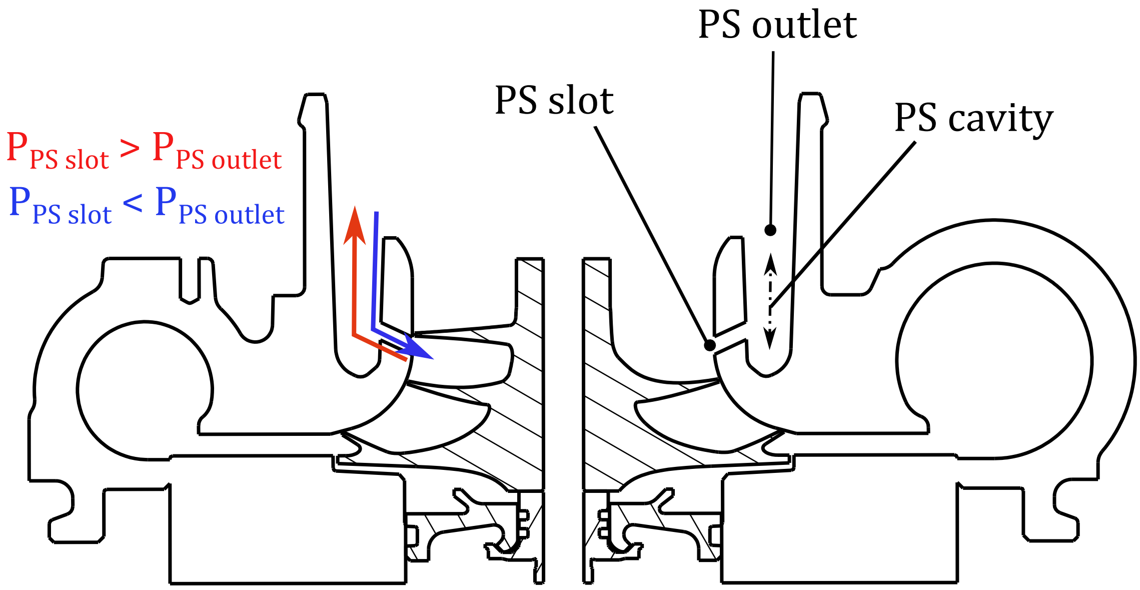

Fig. 1.2 Cross section of a PS compressor is marked with various parts of PS design. Furthermore, the pressure differential and corresponding fluid flow in the PS for the near surge (Red) and near choke (Blue) are also demonstrated.

Ported shroud compressor

Ported Shroud (PS) is essentially a self-recirculating casing treatment that provides a secondary pathway for fluid flow to partially bypass the impeller. It consists of two slots as shown in Figure 1.2, one of which is positioned upstream of the impeller leading edge (PS Outlet) and another one is located downstream of the inducer throat (PS Slot). These two openings are connected by the PS cavity hosted inside the impeller shroud, which provides a secondary pathway for a fraction of inlet flow to circulate between the inducer and impeller. The positions of the end slots of PS are chosen in such a way that it provides a pressure deferential facilitating the flow to move from PS outlet to PS slot bypassing the inducer throat for near choke conditions and recirculate the flow from PS slot into the PS outlet for near surge conditions. In other words, $P_{PS\ Slot} > P_{PS\ Outlet}$ for near surge operation of the compressor while $P_{PS\ Slot} < P_{PS\ Outlet}$ during near choke operation.

1.2 Background

In an effort to put the necessity and development of this work in perspective, a broad review of the literature pertinent to the acoustic characterisation of centrifugal compressors has been carried out. Although results from the related subject of the turbomachines and fluid mechanics were considered, the review has been focused on small high-speed centrifugal compressors, specifically automotive turbocompressors.

The research on the acoustic behaviour of axial compressors can be dated back well over half a century [21, 22] but literature on centrifugal machines is relatively scarce. The initial research interest in noise generated by centrifugal turbomachinery picked up during nineties [23–26] and was focused primarily on large scale centrifugal fans or pumps while the examination of small high-speed centrifugal machines is a relatively recent phenomena.

The researchers in Pennsylvania State University were among the first to explore the acoustic characteristics of the centrifugal machines. An excerpt of the extensive research carried out by these researchers can be seen in the publications by Mongeau et al. [25, 26] and Choi et al. [23, 24] wherein they used an anechoic flow bench to experimentally investigate the operation of a centrifugal pump without any diffuser. In-duct noise, radiated noise and pressure distribution across the blade surface were measured in these studies. Furthermore, these studies identified the Blade Passing Frequency (BPF) effect in the acoustic spectra and also implied the association of stall with increased noise. However, the application of inferences drawn in these investigations on to small high-speed centrifugal machines like present day automotive turbocharger compressors is difficult due to the significant differences in scale, geometry and operational speed. For instance, the pump investigated in the work of Mongeau et al. [25, 26] had an exducer diameter of 32 cm operating between 1000-3600 rotations per minute (rpm) while the compressor considered in this thesis has an exducer diameter of 77 mm operating between 100-130 krpm. In order to focus on the specific issues pertaining to the small high-speed centrifugal compressors, selected works on turbocharger compressors are discussed in the following paragraphs.

Although not numerous, several examples of research into the acoustical behaviour of turbocharger compressors can be found in literature. The exploration of the aforementioned topic started in the early 2000s [27–30] and since then, this is an area of active research. Starting from the investigations of Trochon [29], Evans and Ward [28], Raitor and Neise [27] to the recent studies done in the CMT-Motores Térmicos [31–34] and the Swedish Royal Institute of Technology (KTH) [35–38], researchers have explored various aspects of the turbocharger compressor acoustics using varied approaches. While the early studies on the acoustics of the compressor were of experimental nature, the investigations of Mendonça et al. [39] and Karim et al. [40] established the potential of numerical methods to model flow-induced noise.

Recent studies by Broatch et al. [34, 41], Sundström and Mihaescu [37] and Torregrosa et al. [42, 43] employ sophisticated numerical and experimental techniques to study various aspects of compressor flow and acoustics. In order to provide better context, the literature can be broadly classified on the basis of methodology as experimental and numerical research. The following experimental subsection encompasses the studies that used experimental means as the principal method of investigation while the campaigns that explored primarily using numerical approaches are covered in the numerical subsection.

1.2.1 Experimental literature

Initial studies on the acoustic characteristics of the compressor like Trochon [29], Evans and Ward [28], Calvo et al. [44], Sevginer et al. [45], Gaudé et al. [46] and Teng and Homco [47] were focused on the issue of broadband radiated noise identified by the auto manufacturers. The primary objectives of these 'industrial' studies were to quantify the problematic frequencies and present passive means to alleviate the problems instead of investigating the mechanisms responsible for the generation of broadband noise. The radiated noise was measured from the turbocharger mounted on an engine or from engine itself to locate the broadband region. This broadband noise was identified by onomatopoeic descriptions like 'whoosh' [28, 45, 47], 'blow' [29] or 'hiss' [44, 46] noise.

Trochon [29] and Evans and Ward [28] identified 1.5-3 kHz as the critical regions of broadband noise while Teng and Homco [47] pointed out 5-7 kHz as the critical broadband region. Examination of the data presented by Teng and Homco [47] certainly points to the existence of broadband content in the region between 1-2 kHz, which is in line with the findings of Trochon [29] and Evans and Ward [28]. A correlation between the increase in inlet temperature and noise in 5-7 kHz range is presented by authors [47], indicating the relationship between the broadband content and reverse flow due to blade stall. The authors demonstrated the use of resonators in compressor outlet hoses [28, 45, 47] as an effective means to reduce the radiated tonal noise. The conditions leading to the generation of this broadband noise were identified primarily as high load and low engine speed tip in/out manoeuvres with the compressor operating near surge [28, 47] while Trochon [29] mentioned high mass-flow rate implying the operation at design conditions. Furthermore, turbulence 'inside the compressor' was postulated as the flow phenomena responsible for broadband noise without providing any assertive evidence in these studies [28, 29, 44–47].

Calvo et al. [44] and Gaudé et al. [46] compiled a comprehensive list of acoustic phenomena involved in a turbocharger which included several tonal noises and the aforementioned 'hiss' broadband noise. In addition to the broadband 'hiss' noise, Calvo et al. [44] also mentioned tonal noises namely 'whistling', 'howling' and 'whine'. The source of broadband noise was also postulated as turbulence in the compressor while the sources of tonal noises were linked to rotor-dynamics such as imbalance, lack of symmetry, irregularities and aerodynamics such as blade pass.

Research campaigns exploring standalone compressors can provide a better picture of the compressor behaviour as the effects of reciprocating engine operation and pulsating flows are not present. Raitor and Neise [27] were among the first to characterise the acoustics of a turbocharger compressor, followed by Tiikoja et at. [48] and Figurella et al. [49, 50] to the recent work of Torregrosa at al. [31, 42] and Galindo et al. [43].

Raitor and Neise [27] experimentally characterised the acoustic behaviour of a large turbocharger compressor operating at design conditions and attempted to describe the possible flow mechanisms of the observed acoustic features. The lower operating speeds corresponding to subsonic flow conditions were seen to be dominated by the so called Tip Clearance Noise (TCN) while higher rotational speeds corresponding to supersonic flow conditions in the impeller blade passages were dominated by 'buzz-saw' and blade tone noise. The authors specified tip clearance noise as a narrow band component which was observed at about half the BPF and hypothesised to be caused by the propagation of 'rotating instability' associated with secondary tip leakage flow. For instance, at the operating speed with the BPF of 8.4 kHz, TCN was observed in the range of 3-5 kHz, although, no indication of broadband similar to the aforementioned whoosh noise was seen in the paper, but content between 1.2-2 kHz and 2-2.8 kHz can be seen in the inlet spectrum. Tonal blade pass noise and 'buzz-saw' tones are postulated to be caused by shock waves in the rotor-alone pressure field present at sonic conditions when the compressor is operating at higher speeds.

The noise generation mechanisms of TCN and 'buzz-saw' tones postulated by Raitor and Neise [27] were drawn from the existing data of axial compressor characteristics [51] instead of rigorous experimental validation. Furthermore, no comments were made about the dependence of TCN on rotational speed. Later on, the work of Galindo et al. [33] numerically demonstrated the insignificance of the tip clearance gap by itself on the acoustic characteristics of a compressor. It is worth mentioning that the compressor investigated by Raitor and Neise [27] was large with an exducer diameter of about 224 mm, without any casing treatment and operating at the maximum speed of 50 krpm. In this thesis however, acoustic impact of casing treatment is among the primary objectives along with the identification of major flow mechanisms.

Rämmal et al. [52, 53] investigated passive effects of turbocharger acoustics to understand the propagation of low frequency engine pulsation into intake and exhaust system. The scattering and transmission coefficients for the turbocharger compressors were computed using a linear two port method. This work was then later extended by Tiikoja et al. [48], in which, along with passive transmission properties, active acoustic effects (i.e. noise generation in the turbocharger compressor) were also explored. Tonal and broadband noise features similar to the findings of Raitor and Neise [27] were identified in the pressure spectra of design, surge and choke operating conditions. The authors identified TCN in the regions 3–8 kHz and 5–11 kHz for the inlet and outlet side respectively, although few other smaller broadband ranges like 2.2–4 kHz in the inlet spectra of design and choke point and 0.6-2 kHz in the inlet and outlet spectra of surge point were not marked or discussed by the authors. These broadband ranges, specifically the one seen for surge point are somewhat consistent with the aforementioned reports of 'whoosh' noise.

Similar results reporting tonal and broadband noise features in the measured spectra of a turbocharger compressor were also presented by Lee at al. [54]. Rotating order tones, identified as 'pulsation noise' by Lee at al. [54] were postulated to be caused by the asymmetry and unbalance of shaft and impeller blades as opposed to the leading edge shock wave mechanism postulated by Raitor and Neise [27]. The authors also identified 'tonal noise with higher bandwidth' before the BPF for various operating speeds, which did not correspond to any harmonic of the rotor speed and attributed it to the 'flow fluctuation in the housing'. Furthermore, noise 'humps' in the range of 3-4.5 kHz were also seen, that could be whoosh noise but were disregarded by authors as experimental setup issues.

Figurella et al. [49, 50] also identified discrete tonal and broadband noise. The broadband noise in the range of 4-12 kHz was identified as 'whoosh' noise by the authors. The inlet spectra of choke and mid-low mass flow points presented in the article [49] show a dominant broadband noise in the ranges of 5-6.5 kHz, which are better in line with the TCN range in literature as opposed to the 'whoosh' noise. The smaller broadband effects in the ranges 0.8-2 kHz seen in the inlet spectra of 'Point 2' [49] are aligned to whoosh noise as noted by García-Tíscar [55] too.

Recent experimental studies performed by Torregrosa et al. [31, 42, 56] and Galindo et al. [43] explored experimental means to measure local flow variables [42, 55] and studied the impact of inlet geometry [43] on a turbocharger compressor system. A beamforming based method to characterise the acoustics of compressor was implemented by Torregrosa et al. [56] and demonstrated higher accuracy of this method over conventional two microphone and single microphone sound pressure methods in the plane wave region by comparing the results with those of a reference intensity probe. This beamforming based, in-duct noise approach was then carried forward to explore the impact of various inlet geometries [43] in which a 'convergent nozzle' inlet configuration yielded least acoustic emission for the investigated near surge operation. Local flow parameters of pressure, temperature and velocity for various operating conditions along an isospeed line were explored in the thesis [55] and in the article of

Torregrosa et al. [42]. A longitudinal and circumferential array of thermocouples were used at the compressor inlet to investigate the 'back flow' seen during near surge operation. Miniature pressure probes were installed in the inducer and diffuser as well as the inlet and outlet ducts to measure dynamic pressure fluctuations and in-turn, in-duct noise. Longitudinal and circumferential velocity features at the inlet were captured using Particle Image Velocimetry (PIV). The authors showcased the significance of the back flow on the inducer spectra. Interestingly, 'whoosh' noise was identified across the operating points including the conditions in which no back flow was identified, implying that the reverse or back flow is not the cause of 'whoosh' noise.

The experimental literature discussed so far is based on the compressor without any casing treatment. The data on the acoustic impact of casing treatment is scarce and the general perception is that the casing treatment deteriorates the acoustic characteristics by increasing the overall noise emission of the compressor. Chen and Lin [57] pointed out the 'noise issue' of the ported shroud compressor as the reason for its limited use in passenger cars. Furthermore, Chen and Lei [58] again pointed out the noise, specifically BPF as the reason restricting the use of ported shroud compressors. In both these studies, no evidence for the claims on the 'noise issue' were provided.

Guillou et al. [59–61] and Gancedo et al. [62–66] investigated the dynamic flow behaviour of a ported shrouded turbocharger compressor with an intent to further understand flow features associated with the ported shroud compressor and experimentally validate the predicted numerical features. The authors used PIV to capture the flow field at various impeller upstream positions and inside the ported shroud cavity [64] along with multiple pressure sensors placed in the inducer, diffuser and volute of the compressor [62]. The authors did not directly investigate acoustics in their work but the pressure spectra for various locations and operating conditions presented in the studies can be used to interpret the acoustic features. For instance, broadband in the 'whoosh' characteristic frequency range of 2–3.5 kHz can be identified in the outlet pressure spectra of all three investigated flow regimes presented by Gancedo et al. [62, 67]. Furthermore, these studies explored the flow features at the 'mixing' plane that are formed by the interaction of incoming flow with the flow coming out of the PS cavity during surge and identified the role of structural struts in the formation of exiting jets.

To summarise, two types of acoustic features namely tonal and broadband are consistently identified throughout the experimental literature on the noise spectra of turbocharger compressors. The tonal features include BPF and rotating orders or 'buzz-saw' tones while the broadband noise consists of 'whoosh' noise identified within plane wave range and TCN present outside plane wave range. Some authors seems to conflate these two broadband features into a single inclusive broadband but they appear to be two different phenomena. The lower frequency 'whoosh' noise can be identified within 1-4 kHz range while TCN is usually seen at higher frequencies before the BPF of the compressor.

The mechanism of BPF is well established in literature in contrast to the 'buzz-saw' tones, which are postulated to be caused by shock waves attached to the leading edges of the blades at sonic conditions by some authors, whilst others attribute them to the unbalance or asymmetry of the impeller blades. Similarly, there is no consensus on the mechanisms responsible for the generation of broadband 'whoosh' noise and TCN. As seen above, authors vaguely attribute these broadband features to turbulence inside the compressor, interaction of the back flow, or rotating instabilities caused by secondary tip leakage flow. Furthermore, the impact of ported shroud casing treatment on the acoustic characteristics of a turbocharger compressor is scarcely studied.

1.2.2 Numerical literature

Accurate characterisation of the three-dimensional flow developed inside in the compressor is necessary to understand the mechanisms of noise generation. Computational methods are better suited for this task as the constraints imposed by confined and complex geometry along with harsh operational conditions makes it difficult for contemporary measurement approaches to characterise the flow inside a turbocharger compressor. Therefore, studies exploring the problem at hand using Computational Fluid Dynamics (CFD) are discussed in the following paragraphs.

Sun et al. [68, 69] attempted to numerically predict the tonal noise of a large centrifugal compressor. The authors modelled the flow through the impeller and then used the computed pressures at impeller inlet and outlet to model noise sources using an acoustic analogy [70]. The propagation of noise to far field was handled using a boundary element method approach. The impeller flow was resolved using an Euler solver [68] and a Navier-Stokes solver [69] employing a Reynolds averaged $k-\omega$ turbulence model assuming that for the design condition, flow would be attached and steady. The authors did not present predicted noise spectra but only compared BPF and its two successive harmonics with the measured inlet spectrum. The tonal content seems to be in reasonable agreement in terms of frequency and amplitude although BPF is not convincingly captured. This may be because of omitting impeller upstream and downstream components in the numerical model. Furthermore, the results say nothing about performance parameters, trends of the noise spectrum or the broadband content predicted by the numerical model.

The aforementioned work of Lee at al. [54] also includes a numerical perspective. The approach used by authors is similar to Sun et al. [69] which uses the output of CFD as an input for an acoustic analogy approach although the method used for turbulence modelling is unclear.

The agreement between predicted and measure noise spectra was seen to be poor and this can be partly attributed to the use of the acoustic analogy approach for confined geometry and the use of data from only one impeller revolution to model noise sources.

The investigations of Mendonça et al. [39] and Karim et al. [40] established the potential of CFD to model acoustic behaviour of the compressor. Mendonça et al. [39] used Detached Eddy Simulation (DES) to model the in-duct noise of a turbocharger compressor operating near surge. The pressure fluctuations were recorded at the multiple inlet and outlet positions. These pressure fluctuations were then processed to yield the acoustic spectral information. BPF tonal noise and a narrow band broadband noise in the region of 2.5 kHz which is in line with ‘whoosh’ noise characteristic frequency, can be recognised in the estimated spectra. The rotating order or ‘buzz-saw’ tones and TCN are not clearly identifiable in the inlet or outlet spectra. This can be attributed to the masking of tonal noise by broadband noise generated during near surge operation. Mendonça et al. [39] did not present any experimental evidence to either validate the credibility of the numerical results or for the claim of rotating stall as the source of narrow band noise. Karim et al. [40] followed the similar approach and used Large Eddy Simulation (LES) to compute the pressure fluctuations at the compressor inlet and outlet. The noise spectra estimated using in-duct pressures were then used to evaluate various designs. The design that diminished the ‘whoosh’ noise was then successfully validated using experimental measurements. However, the comparisons of predicted and experimental noise spectra were not presented in the study. Similarly, Fontenasi et al. [71] used DES to investigate a specific noise seen in the experimental measurements but again, no comparisons between estimated and measured sound spectra were provided in the work. It is worth noting that the agreement of predicted global performance parameters with measured values does not guarantee the credible estimation of acoustic spectra. Therefore, some kind of experimental validation of flow field or pressure trace is necessary before making inferences on noise generation.

A numerical setup based on the work of Mendonça et al. [39] was further used by Broatch et al. [34, 41] and Galindo et al. [33] to numerically explore the flow-induced noise, specifically whoosh noise in a turbocharger compressor. Broatch et al. [34] used DES to model both design and near surge operation of a compressor. Beamforming based wave decomposition method and Method of Characteristics (MoC) [72] were employed to enhance the content coming from compressor. The predicted noise spectra showed good agreement with the beamformed experimental spectra up to the plane wave limit and ‘whoosh’ noise was identified. At higher frequencies, the outlet duct spectra showed reasonable correlation with experimental measurements except for 13-16 kHz broadband corresponding to tip clearance noise, while the correlation of inlet duct spectra showed significant problems. Nevertheless, this model was then used to investigate the generation of ‘whoosh’ noise [41], which reported higher sensitivity of design conditions to 'whoosh' noise relative to near surge operation. The authors [41] reported the presence of inducer stall cells at near surge conditions while diffuser stall cells of similar intensity were seen at both design and near surge conditions. Therefore, the authors believe that the diffuser stall is the main flow phenomenon responsible for 'whoosh' noise. This seems to be in contradiction with other studies reporting 'whoosh' noise as a near surge feature. Further evidence is required to credibly identify the mechanisms responsible for whoosh noise.

The model developed by Broatch et al. [34] was further used to study the impact of tip clearance on the acoustic emission of the compressor operating near surge by Galindo et al. [33]. Three different tip clearance ratios based on the turbo shaft movement were modelled and authors reported no significant changes in the noise spectra. The study was performed on near surge operation where the secondary flows are already significant. The impact of tip clearance for design operation might be different as postulated by Raitor and Neise [27]. Also, the study only accounts for passive tip clearance, while dynamic changes in blade tip clearance during the compressor operation due to shaft motion or aeroelastic and mechanical torsion in the blades could impact the acoustic signature of the compressor.

The numerical literature discussed so far is based on the compressor without any casing treatment. Similar to what seen in the experimental literature, numerical studies on the acoustic impact of casing treatment are scarce.

Researchers at KTH [35–38, 61] used LES to numerically model the ported shroud compressor used as subject in the experimental visualisation studies of Guillou et al. [59, 60] and Gancedo et al. [65, 66] over at the University of Cincinnati. A qualitative agreement between the predicted and measured inlet flow structures for design and near surge conditions was demonstrated by the authors [38, 61]. This model is then used to explore the operation of the compressor at various conditions. The focus of the authors is not specifically acoustic in nature, but the flow phenomena leading to compressor stall and/or surge. The dynamic pressure data along with decomposition of the velocity field presented in the work can potentially provide some clues on the relationship between the flow field and compressor surge.

Semlitsch et al. [38] compared the flow field of a ported shroud compressor with an equivalent compressor without ported shroud and identified high-speed jet like structures exiting ported shroud cavity at near surge conditions. Sundström and Mihăescu [37] computed the spectra of a point in diffuser for multiple design and near surge conditions. The authors identified narrow width broadband during near surge operation at the frequencies corresponding to half of impeller rotation per second (RPS) and twice of impeller rotation frequency (viz. 0.53 kHz and 2.13 kHz for 64000 rpm) respectively. Similar results were seen in the experimental characterisation of the compressor by Gancedo et al. [65]. The flow mechanisms responsible for identified features in the spectrum are then explored by Dynamic Mode Decomposition (DMD) of the velocity field inside the impeller. The authors suggests that the 0.53 kHz broadband is caused by the interaction of the shear flow around the ported shroud cavity with large vortical structures at the impeller inlet while the second broadband is attributed to the low pressure nodes rotating on the impeller surface. Similar 0.5 kHz features can be identified for the design condition too and ported shroud is known not to recirculate heavily at design conditions. This dictates the need for further investigation. Sundström et al. [35] and Semlitsch and Mihăescu [36] further investigated the mechanisms related to rotating stall and surge in compressors. The authors employed modal decomposition of the field variables and inferred that the swirl introduced by back-flow deteriorates the incidence, thereby, leading to an emptying and filling cycle.

To summarise, the numerical literature on acoustic modelling of a compressor is limited but the state-of-the-art modelling methods have demonstrated their capability in reasonably replicating the acoustic characteristics, specifically low frequency broadband and tonal features, of a turbocharger compressor. The ability of numerical methods to consistently capture high frequency broadband features needs further research. While wave decomposition and modal decomposition methods are good aids in investigating the flow phenomenon, mechanisms of broadband noise features are not yet understood. Furthermore, the understanding of the impact of ported shroud casing treatment on the acoustic characteristics of a turbocharger compressor is limited and scarcely studied.

1.2.3 Summary of the literature

After reviewing several experimental and numerical investigations on the acoustics characteristics of turbocharger compressor, some arguments on the state of the art can be synthesised:

- While the research on the acoustic behaviour of axial compressors can be dated back half a century, noise generation in small centrifugal compressors is a new area of research. Furthermore, the acoustic impact of casing treatment is scarcely studied.

- Two main features in the spectra of centrifugal compressor are consistently identified in literature. The first one is tonal noise that includes BPF and 'buzz-saw' tones while second one is broadband that includes a characteristic feature in the plane wave region ('whoosh' noise) and a high frequency feature (TCN) near BPF. The mechanism of BPF is well established while the mechanisms responsible for 'buzz-saw' tones and broadband noise need further research.

- Computational methods (CFD) are demonstrated to successfully predict the evolution of flow features in compressors operating at design and near surge. However, accurate estimation of flow-induced noise, specifically at higher frequencies still needs further research.

- Modal decomposition methods can be used to extract insights on the relationship between the flow field and corresponding acoustic features.

It can be easily seen from the state-of-the-art conditions that further research is necessary to understand the impact of ported shroud casing treatment on acoustic characteristics of compressor.

1.3 Objectives

The aim of this research is to enhance the understanding of the impact of ported shroud casing treatment on the flow induced acoustic characteristics of a small high-speed turbocharger compressor. This broader research goal is dissected into specific individual objectives which are enumerated as:

- Evaluation of the acoustic and aerodynamic performance characteristics of the compressor with ported shroud casing treatment operating at design and surge conditions.
- Investigate the relationship between the flow field mechanisms and the acoustic emission of the compressor.
- Understand the differences in the acoustic features due to the implementation of the casing treatment.
- Analyse the changes in the flow behaviour and acoustic characteristics with an increase in the operating speed by investigating the operation of the compressor at a higher iso-speedline.

1.4 Methodologies to compute the flow-induced noise

The generation and propagation of the flow induced noise are aerodynamic phenomena. Although the fluid flow dynamics and the resultant acoustics are both governed by mass and momentum conservation equations, former is of convective and/or diffusive nature while the latter is propagative showing insignificant attenuation due to viscosity except for small viscothermal losses. Experimental methods can be used to characterise the acoustic behaviour of a compressor system, but identification of the flow field and mechanisms responsible for noise generation in complex turbomachinery systems is not within reach of contemporary measurement methodologies. Developments in computing infrastructure and methods over the last decade have enhanced the potential of numerical methods to reasonably predict the aerodynamic noise. Numerical studies presented in Section 1.2 further reinforce this argument. Therefore, numerical modelling of the compressor flow is preferred to explore the objectives listed for this thesis.

In spite of developments in computing, aeroacoustic modelling especially of systems with intricate geometries and complex flow is challenging because of difficulties in the accurate tractable representation of turbulent viscous flows. There are various approaches to compute the aerodynamic noise depending on the application. In this section, a succinct description of the Direct and Hybrid approaches to perform Computational AeroAcoustics (CAA) is presented.

1.4.1 Direct approach

In this approach, both generation and propagation of aerodynamic noise is computed 'directly' by solving the unsteady compressible Navier-Stokes equations, hence the name 'Direct'. Essentially this approach involves altering the aerodynamic model to capture the acoustic parameters of the system. The modifications in a typical aerodynamic or CFD model for encapsulating the objectives of an aero-acoustic problem are largely based on the following characteristics [73]:

- *Spectral bandwidth*: The spectrum of the noise generated by the flow, specifically broadband noise generated by turbulence ranges from low to very high frequencies. This results in the requirements of a high spatial resolution in the computational grid as dictated by the highest frequency of interest. Furthermore, three-dimensional modelling is necessary due to the inherent three-dimensional nature of turbulence.

- *Energy disparity*: A large disparity between the energy distribution among the acoustic and aerodynamic/flow field can be seen in most cases with former accounting for a much smaller fraction than the latter. This mandates the use of higher-order accurate schemes for ensuring numerical error values to be significantly lower than the magnitude of acoustic waves to yield accurate predictions.

- *Distinct length scales*: While in aerodynamic problems, the length scales vary from Kolmogorov scale to the largest eddy of interest, acoustic fluctuations are characterised by the acoustical wavelength which is much larger than the aerodynamically limiting Kolmogorov scale. For accurately capturing the noise generated by flow mechanisms, grid size of the order corresponding to Kolmogorov scale is required while, the grid size for the propagation of noise is dictated by the acoustical wavelength leading to the use of limiting grid size for both near and far-field situations. The use of lower grid size further imposes the use of lower computational time-step value to maintain numerical stability in finite difference schemes.

- *Propagation properties*: As mentioned before, aerodynamic fluctuations readily dissipates while acoustic wave exhibit no significant dissipation leading to the differences in numerical and physical waves properties. These differences are incurred as dispersion and dissipation error in the numerical schemes. In order to maintain a uniform numerical accuracy in the computational domain, low dispersion and dissipation schemes need to deployed.

- *Boundary conditions*: Spurious numerical reflections generated by the boundary conditions sufficient for aerodynamic modelling can be of the same order of magnitude as the acoustic fluctuations. Therefore, treatment at the boundaries is required for ensuring the minimum reflection of flow and acoustic fluctuations while exiting the domain.

- *Nonlinearities*: While aerodynamic fluctuations are non-linear, acoustic problems for most situations can be considered as linear due to the small magnitude of acoustic fluctuations. Therefore, non-linear treatment is required to capture noise generated by the flow while it is not really necessary for modelling the propagation of the noise.

In other words, the model should capture local non propagative aerodynamic disturbance field components and propagative fluid compressibility components for near field as well as gradual noise propagation in the far field. This necessitates the use of a high fidelity turbulence model for accurately computing the noise generation and higher order, low-dissipation and low-dispersion numerical schemes for acoustic propagation. These requirements can be translated on to a numerical set-up as the use of scale resolving turbulence models, with high-order discretisation in both space and time on very fine computational grids, extending till far field to achieve the Courant number in the range of ~ 1. The excessive computational cost along with the complexity in implementation limits the use of this approach.

Ideally, the complete resolution of the aerodynamic scales by the means of direct numerical simulation should be used for aero-acoustic applications but it is not computationally feasible. Alternatively, part of the turbulent spectrum resolved by the means of scale-resolving simulations can be used for aero-acoustic computations by hypothesising the efficient radiation of the noise by larger scales relative to smaller scales [74]. For example, the work of Wang et al. [75], Mankbadi et al. [76] and Hamed at al. [77] shows the successful use of scale-resolving models in the prediction of flow-induced noise. The works of Broatch et al. [34] and Mendonça et al. [39] demonstrated the specific use of the direct approach to compute the in-duct acoustic characteristics of a turbocharger compressor.

1.4.2 Hybrid approach

Hybrid approaches address the computational limitations associated with the solution of far field characteristics. The first method is a coupled approach in which the direct method is used for instabilities causing significant noise generation and then employing a wave equation system for the far field propagation. It is worth nothing that this method requires a good resolution of turbulent scales to capture the noise generation and an accurate transition treatment between near and far field at the boundary conditions. Another hybrid approach involves a complete decoupling of aerodynamic and acoustic computations by applying acoustic analogies. The acoustic sources are computed from the flow solution quantities that includes pressure fluctuations, velocity fluctuations, stress tensor and force terms. The propagation of the derived acoustic sources is handled using wave equations or linearized Euler equations as seen in the Lighthill analogy [78, 79], Curle analogy [80] and the Ffowcs Williams–Hawkings analogy (FW&H) [70].

It is important to note that the worthiness of the acoustic predictions made by using Hybrid approaches primarily depends on the accurate noise source modelling. This necessitates employing high fidelity scale resolving turbulence models, as the statistical Reynolds averaged formulation does not provide much information on instantaneous turbulent flow structures. The use of general aeroacoustic analogy is limited to the noise propagated in free and far field. The effects of reflections, diffractions and scattering are not accounted in these analogies, thereby limiting their suitability to predict the internal flow noise.

Khelladi et al. [81] presented the inability of FW&H formulation to predict the noise generated by a centrifugal fan due to the presence of a casing.

1.4.3 Broadband noise source models

Acoustic spectra of certain systems especially involving turbulent flows, do not have any distinct tonal characteristics. The broadband noise level or sound energy is distributed across a range of frequencies. For such cases, the use of computationally intensive direct and hybrid approaches that resolve noise sources, directivity and propagation are unnecessary. Therefore, a method based on statistical turbulence variables in conjunction with semi-empirical correlations can be used to predict the source of broadband noise. The statistical turbulence quantities are readily computable from the steady Reynolds averaged Navier-Stokes formulation (RANS), making broadband noise source models computationally best among the methods to predict the source of aerodynamic noise. However, broadband noise models provide information to estimate the noise sources but do not say anything about noise propagation. In other words, flow responsible for the generation of broadband noise can be identified by broadband source models without predicting the propagation of that noise from source to receiver. A few commonly used models available in commercial codes include Proudman's formula [82] for the estimation of quadruple power, boundary layer source model [83] for the estimation of dipole power and source terms in the linearised Euler equations [83].

It is worth pointing out that the acoustic spectra of turbomachinery include both tonal and broadband features. Broadband models can only be used to detect the broadband noise sources.

1.4.4 Selected approach

The direct method for computing near field characteristics described in Section 1.4.1 is used in this thesis to pursue the objectives stated in Section 1.3. Flow inside a complete three dimensional model of a turbocharger compressor is numerically simulated using a commercial CFD coupled solver, ANSYS CFX [84]. This code is based on a finite-volume approach, with hybrid second order discretisation in time and space along with double precision. The relationship between the flow field mechanisms and the acoustic emission of the compressor is explored by decomposing pressure field computed from the numerical model with the aid of modal decomposition techniques. During the framework of the thesis, ANSYS CFX [84] versions from 15.0 to 17.1 have been used.

1.5 Methodical objectives

There are some caveats associated with the use of aeroacoustic modelling to achieve the objectives defined in Section 1.3.

As mentioned in the Section 1.4, aeroacoustic modelling of turbocharger compressors is still in its early stages and not as mature as aerodynamic modelling in many aspects. Therefore, the credibility of numerical model must be validated by comparing the predictions with the equivalent experimental measurements. The foremost issue is about the method for comparing experimental and numerical results. The modelling of the complete measurement test rig which includes long ducts for the development of flow, is not computationally tractable. The meaningful comparison of the experimental and numerical duct spectra that are not obtained at the same location is necessary for making any conclusions about the credibility of the numerical model. One way around this problem is to use a location on the compressor to compare the experimental and numerical results. From this perspective, the author would use a position in the compressor inducer and one in the diffuser to compare the spectra. The comparison of duct spectra would be made using the aforementioned methodology used by Broatch et al. [34].

Other than this, the thesis should meet following methodological objectives:

- Investigate the impact of various numerical parameters like turbulence formulations, timestep size and grid size on the acoustic predictions. The quantification of this sensitivity study can serve as references for future work and help with the never-ending enigma of time and accuracy.

- Develop or find suitable methodology to perform modal decomposition of flow variables.

1.6 Thesis outline

After this introduction, the rest of the thesis is organised in the following fashion.

Chapter 2 presents the experimental campaign to measure the acoustic characteristics of the investigated compressor. This chapter will introduce the different measurement methodologies along with the compressor configurations and operating conditions used to characterise the internal sound field. The measured spectra will serve a two fold purpose of being used as means to validate the numerical model as well as drawing inferences on the acoustic impact of ported shroud casing treatment.

Chapter 3 is devoted to the development of the numerical model. The impact of various vital set-up parameters on the performance and acoustic predictions will be thoroughly analysed. A range of statistical and scale resolving methods of turbulence modelling will be explored and their sensitivity to spatial and temporal resolution from the standpoint of noise generation will be quantified.

In Chapter 4, the relationship between the flow field and the acoustic emission of the compressor is explored by decomposing the transient solution values obtained from the numerical models finalised in Chapter 3. This chapter will introduce the theoretical background of pertinent methods and developments in the modal decomposition of the flow field. The pressure field of the compressor operating at design and near-surge conditions will be decomposed using Proper Orthogonal Decomposition (POD) to identify the energetically dominant features of the flow and their corresponding acoustic characteristics.

Chapter 5 focuses on the impact of ported shroud (PS) casing treatment on the performance and acoustic characteristics of the compressor. This chapter introduces the computational *blocked* configuration of the compressor model in which the circumferential slot in the ported shroud cavity is sealed numerically. The acoustic as well as time-averaged flow characteristics of the ported shroud *open* and *blocked* configuration of the compressor will be compared for the design and near surge operation.

Chapter 6 builds upon the configurations introduced in Chapter 5 to investigate the effect of rotational speed on the characteristics of the compressor. The operating speed of the ported shroud *open* and *blocked* compressor configurations will be increased to explore the changes in the time-averaged flow field and the acoustic behaviour for both design and near surge conditions.

Finally, Chapter 7 incorporates the summary of various findings throughout this thesis as conclusions. Also, various interesting effects and issues that came across during the pursual of the thesis objectives but were not in the scope of current work, will be compiled as the recommendation for future work.

Chapter 2

Experimental measurements*

Contents

*Content presented in this chapter has been submitted for publication in the following paper:

- Acoustic characterisation of a small high-speed centrifugal compressor with casing treatment: An experimental study [6]

2.1 Introduction

As stated in Chapter 1, this thesis uses the numerical approach as the primary method to investigate the acoustic and flow behaviour associated with a turbocharger compressor. Since computational methodologies to predict the acoustic characteristics of high-speed compressors are not yet mature, experimental measurements are necessary to assess the credibility of numerical results and understand the limitations of the numerical model.

The objective of this chapter is to present the experimental campaign for acoustic characterisation of the compressor with an intent to gather data for assessing the ability of the numerical model to predict flow-induced noise. The campaign is further extended to establish the impact of ported shroud casing treatment on the acoustic emission of the compressor. Section 2.2 presents an overview of the various experimental approaches used in literature to measure compressor noise, followed by the approach used in this thesis which is similar to the one presented by Broatch et al. [34]. The procedure and set-up used for the measurement are described in Section 2.3 and Section 2.4, while the measured acoustic spectra are discussed in Section 2.5. Finally, the major findings of this chapter are synthesised as conclusions in Section 2.6.

2.2 Experimental methodology

In this section, approaches available to experimentally characterise the acoustics of a turbocharger compressor are evaluated in order to select the appropriate experimental method for this thesis. Literature is explored for various approaches used to measure compressor noise, followed by the method selected for current work.

2.2.1 Literature review

The literature on the acoustic characterisation of the compressors can be primarily divided into *internal* or *in-duct* noise measurements and *external* or *radiated* noise measurements. The internal noise is measured by the sensors in direct contact with the internal flow by placing them inside the compressor and/or ducts while external noise measurements capture the noise radiated by the compressor using the sensors positioned in the far field and/or near field or duct orifice. Dynamic, fast responding pressure sensors or transducers are frequently used for internal noise measurements while microphones are preferred for determining external noise. Another differentiation can be made on the parameter used to quantify the noise emitted by the system viz. *Sound Pressure Level* (SPL) and *Sound Intensity Level* (SIL). While the former is a scalar term representing the sum total of noise at a particular location, latter is a vector quantity whose directivity properties can be used to capture the noise emitted from a particular direction. Sound pressure levels can be computed with a single sensor and, are susceptible to the issues caused by the reflections and mode shapes of the geometry. The calculation of sound intensity levels necessitates two or more sensors and remains consistent along the geometry due to strong directivity properties.

External noise measurements were performed by Evans and Ward [28], Sun et al. [68, 69], Teng and Homco [47], Lee et al. [54], and Pai et al. [85, 86] using free field microphones to measure either the far field noise radiated by a turbocharger compressor or duct orifice noise. While Evans and Ward [28] and Teng and Homco [47] performed noise measurements on a powertrain dynamometer in a semi-anechoic chamber using external microphones to compute average SPL, orifice noise was measured using a microphone positioned near the inlet/outlet duct by Sun et al. [68, 69], Lee et al. [54] and Pai et al. [85, 86].

Internal or in-duct noise measurements were seen in the works of Gaudé et al. [46], Tiikoja et al. [48], Raitor and Neise [27], Broatch et al. [34] and Torregrosa et al. [56]. Trochon [29] and Evans and Ward [28] also presented in-duct noise plots, implying a coherence between internal and external noise measurements. Tiikoja et al. [48] used an acoustic two port method to compute the SPL of the noise generated by the compressor while Raitor and Neise [27], Trochon [29] and Evans and Ward [28] calculated SPLs from a single sensor. Gaudé et al. [46] used an array of pressure sensors each for inlet and outlet ducts in order to decompose the in-duct pressure wave for computing SIL. A similar approach was then used by Broatch et al. [34] to decompose the pressure wave using the beamforming based method in order to compare the experimental and numerical spectra of the compressor that are measured at different locations. Torregrosa et al. [56, 31] further demonstrated the robustness of a beamforming based pressure decomposition approach over conventional two port and single sensor methods. The authors also demonstrated a good correlation between internal and external noise measurement results.

Researchers like Ha et al. [87], Figurella et al. [49, 50], Fontanesi et al. [71] and Guillou et al. [59] used elements of both external and internal noise measurement in their work. The thesis of García-Tíscar [55] presents a comprehensive work on the experimental determination of the acoustic characteristics of various turbocharger compressors that include both internal and external noise measurement methodologies. Investigations performed by Zheng and Liu [88, 89] and Gancedo et al. [62] used dynamic pressure probes in the inducer, diffuser and volute of the compressor to explore stall and/or surge. These works are not entirely acoustical in nature, but the measured pressure fluctuations can be processed to generate in-duct noise spectra.

Although the external noise measurements are relatively straightforward to set up due to their non-intrusive nature, they do require anechoic conditions to yield accurate results.

On the contrary, internal noise measurements are relatively challenging to set up due to its intrusive nature, but they are free from the necessity of anechoic conditions. Additionally, the external radiated noise is not solely dependent on the noise generated by the flow but is also influenced by the geometry and the radiative properties of the material. The understanding of the flow mechanisms responsible for noise is a key objective of this thesis, making internal noise measurement the preferred choice in both numerical and experimental campaigns. Furthermore, numerical determination of internal noise is computationally efficient as compared to reliable external noise predictions. Therefore, internal or in-duct noise measurements are used in this thesis to assess the numerical model as well as to understand the acoustic impact of ported shroud casing treatment.

2.2.2 Selected method

Internal or in-duct noise measurement method similar to the one presented by Broatch et al. [34] is employed to characterise the acoustic behaviour of the compressor. Both single sensor and multi-sensor methods are considered in this work for exploring noise generation and noise propagation respectively. The noise generated in the compressor is measured at the impeller upstream and downstream positions by miniature pressure probes. The noise propagated at the compressor ducts is quantified by the pressure spectra obtained from the sensor arrays consisting of three piezoelectric sensors each for inlet and outlet duct. The pressures measured by these linear arrays of three piezoelectric sensors each are further processed to decompose pressure waves into its corresponding components by the beamforming based approach. Further details on in-duct noise measurement are discussed in the next section.

2.3 In-duct noise measurement

In-duct noise can be measured in terms of Sound pressure level (SPL) or Sound intensity level (SIL). Scalar SPL can be computed using a single sensor, while computation of vectorial SIL needs two or more sensors. As discussed in the Literature section, SPL is influenced by reflections and geometry whilst the directive properties of SIL make it less susceptible to such secondary effects, thereby making it a better and more robust indicator of the noise generated by a system.

The sound intensity measurements are based on the assumption that the pressure signal $p(t)$ recorded at a point in a duct is a linear superposition of two opposite waves travelling across each other with a phase difference of 180°. By the virtue of linear superposition assumption, the intensity computation is limited to the plane wave region. These wave components $p^{+}(t)$ and $p^{-}(t)$ are commonly referred to as forward and backward wave components respectively.

$$p(t) = p^{+}(t) + p^{-}(t) \tag{2.1}$$

The sound intensity at that point in the duct can then be calculated with the help of the expression proposed by Morfey [90]:

$$I = \frac{1}{\rho a}\left[\left|P^{+}\right|^{2}\left(1+M^{2}\right) - \left|P^{-}\right|^{2}\left(1-M^{2}\right)\right] \tag{2.2}$$

where P^{+} and P^{-} are the respective complex frequency spectra of $p^{+}(t)$ and $p^{-}(t)$ wave components, ρ is the mean density, a is the mean speed of the sound and M is the mean Mach number of the flow in the ducts.

In order to compute the sound intensity, the measured pressure wave needs to be decomposed into its forward and backward travelling components. This can be achieved with the understanding of the wave propagation through the duct in each direction, gained by comparing the pressure data for two or more subsequent spatial positions. One such wave decomposition method is beamforming, which is explained in the following section.

2.3.1 Beamforming wave decomposition

The beamforming based wave decomposition provides a mathematical method to 'steer' the content of a pressure signal into the forward and backward component. This decomposition method is based on the idea that the direction in which a particular wave originates impacts the time when it would be recorded by each sensor of a linear array. This is demonstrated in Figure 2.1, where a reference array encountering a plane wavefront originated in the direction closer to sensor 1 is shown to travel an extra distance to be measured by sensor 2 and sensor 3. This extra distance would lead to time and phase delay. Therefore, by comparing the simultaneous waves recorded by these sensors, the origin of the wavefront can be computed. Among the available beamformers, the Delay-Sum and Linearly Constrained Minimum Variance (LCMV) methods were explored, and the narrowband LCMV beamformer was selected for this work. The implementation of LCMV beamformer is based on the work of Broatch et al. [34] and Torregrosa et al. [31]. The details of the mathematical procedure are reproduced from Torregrosa et al. [31] and García-Tíscar [55] in Appendix B.

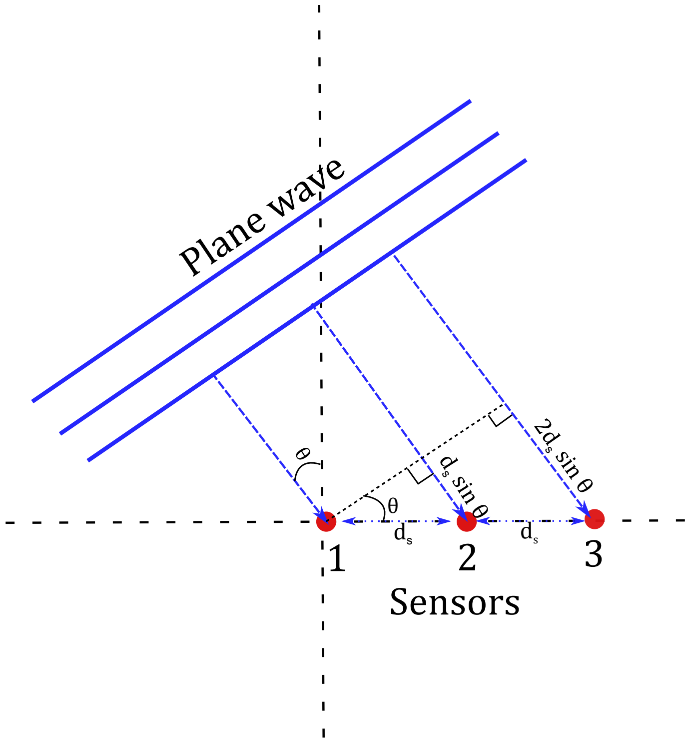

Fig. 2.1 Propagation of a planer wavefront moving with a velocity '*a*' towards an array of receivers. If d_s is the distance between two successive sensors, a delay corresponding to the distance of $d_s sin\theta$ would be introduced.

Experimental considerations

In this thesis, pressure spectra of the decomposed waves obtained from the beamforming of the pressure data measured by the inlet and outlet duct array are used to assess the quality of numerical results. The correct setup of the pressure sensor arrays is critical for obtaining credible measurements. For effective implementation of these beamforming arrays, a few practical concerns must be considered. Firstly, beamforming is based on the assumption that the decomposed wave is propagating within the plane wave region. Therefore, sufficient straight length should be provided before and after any sensor array to ensure plane wave flow at the arrays [91]. Torregrosa et al. [92] based on their experience of applying beamforming on multiple problems, recommended a minimum of 6 and 4 diameters straight length upstream and downstream of the array respectively. Another consideration regarding the position of array's sensor is to avoid the $1/5$ and $1/3$ nodes of the standing wave pattern in the duct [93].

One-dimensional plane wave propagation of the flow is limited by the onset of acoustic modes that introduces three-dimensional effects in the flow propagation. The limiting frequency for the beamforming and thereby, sound intensity can be predicted by computing the onset of these acoustic modes from the formulations provided by Eriksson [94]. According to author

[94], the wave propagation in a circular duct can be assumed of a planar or one dimensional nature below a particular cut-off frequency which marks the onset of first asymmetric mode defined as

$$f_{c,a} = 1.84\frac{a}{\pi D}\sqrt{1-M^2} \tag{2.3}$$

where D is the duct diameter, a is the speed of sound and M $(0 \leq M \leq 1)$ is the mean Mach number of the flow. The next acoustic mode is the radial mode, and its propagation is computed by

$$f_{c,r} = 3.83\frac{a}{\pi D}\sqrt{1-M^2} \tag{2.4}$$

These limiting frequencies $f_{c,a}$ and $f_{c,r}$ should be calculated with caution as they are not constants but rather a function of the operating conditions of the compressor due to their dependence on the temperature and mass flow. Other than the onset of the higher order modes discussed above, beamforming is also limited by a Nyquist like frequency criterion dictated by the spatial resolution of the sensor array. Spatial aliasing effects are seen above this Nyquist cut-off frequency, which is defined as less than half of the inherent frequency of the array [95]. As seen in Figure 2.1, the time delay between two subsequent sensors with spacing d_s is $d_s \sin\theta/a$. The inherent frequency for a perpendicular wave front can then be computed as a/d_s. Therefore, the cut-off for Nyquist like frequency criterion can be defined as

$$f_{c,\ N} < \frac{f_{array}}{2} = \frac{a}{2d_s} \tag{2.5}$$

Furthermore, the spacing d_s between sensors in the array is a compromise between high frequency and low frequency characteristics of the array. If d_s is decreased to improve the Nyquist limitations, the low frequency spatial resolution would be deteriorated as the wavelength at lower frequencies could exceed the distance between the sensors; defying the whole purpose of the array. Finally, the sensors should be flush mounted on the straight ducts and properly calibrated to give a coherent response. The calibration of the sensors used in this work is performed in an impulse test rig to obtain a clear reference pressure wave as detailed in Payri et al. [96]. The amplifier offset and gains are adjusted to find the best match in both time and frequency responses of all the sensors. The calibration of the individual sensors is validated by achieving similar spectra of the sensors mounted radially on the same section of the duct.

2.3.2 Method of characteristics

Method of Characteristics (MoC) [72] is an alternative to beamforming based approaches for the decomposition of pressure waves into their corresponding components. In this method, the information of the flow field is used to construct the pressure wave components using the following formulation:

$$
\begin{aligned}
p_{forw}(t) &= p_{ref}\left[\frac{1}{2}\left(1+\left(\frac{p}{p_{ref}}\right)^{\gamma-1/2\gamma}\left(1+\left(\frac{\gamma-1}{2}\right)\frac{u}{a}\right)\right)\right]^{\frac{2\gamma}{\gamma-1}} \\
p_{back}(t) &= p_{ref}\left[\frac{1}{2}\left(1+\left(\frac{p}{p_{ref}}\right)^{\gamma-1/2\gamma}\left(1-\left(\frac{\gamma-1}{2}\right)\frac{u}{a}\right)\right)\right]^{\frac{2\gamma}{\gamma-1}}
\end{aligned}
\tag{2.6}
$$

On the upside, the MoC can be computed using a single sensor and is not limited by the plane wave restrictions, but it requires additional measured variables that includes speed of sound and bulk velocity which are difficult to measure at a single point. The numerical computations allow easy access to these variables. Therefore, MoC would be used to reconstruct the decomposed pressure components from numerical results to compute the high-frequency spectra.

2.4 Measurement set-up

In this section, the set-up used for acoustic measurements is discussed, starting with the operational configurations of the compressor investigated in this thesis. Details of the measurement system and procedure followed to compute pressure spectra are then discussed in the subsequent subsections.

2.4.1 Compressor operational configurations

Discussion on the hardware and the operating conditions of the compressor explored in this experimental campaign are presented in the following paragraphs.

Compressor hardware

The series *B2G* turbocharger unit and digital geometry of the corresponding compressor are provided by industrial partner BorgWarner [97]. The compressor of this particular model incorporates Ported Shroud (PS) casing treatment with three symmetric structural struts supporting the cavity. The front and section views of the compressor geometry are shown in Figure 2.2.

The impeller features seven main and seven splitter blades that are designed as forward swept disseminating the flow into a vaneless diffuser.

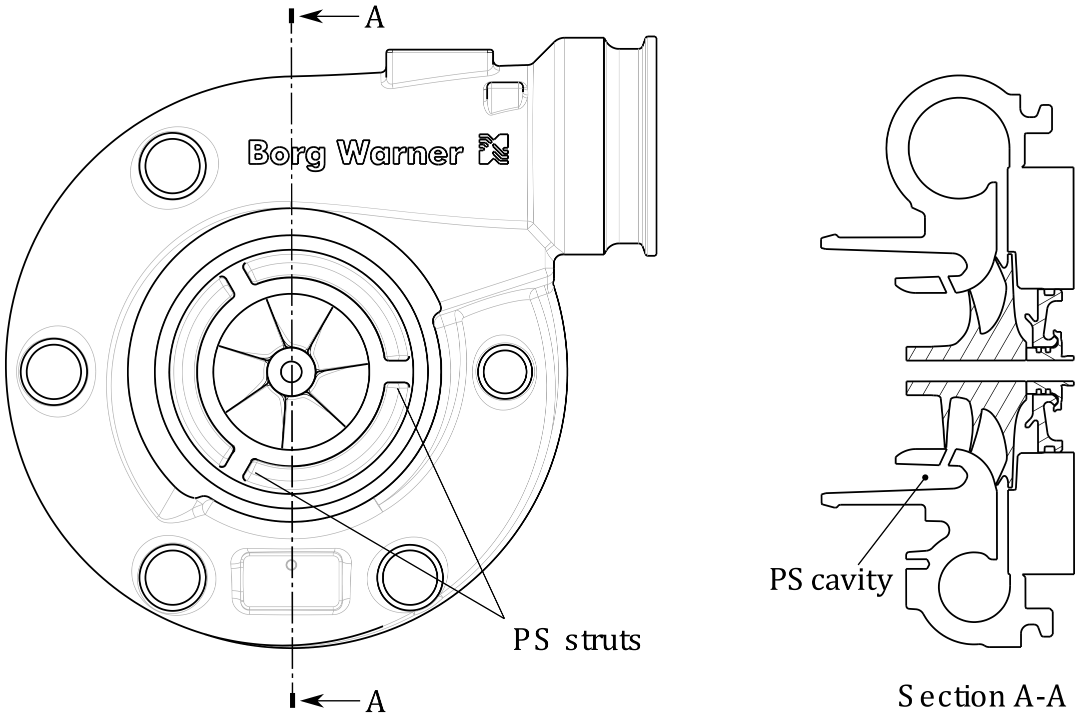

Fig. 2.2 Drawing of the investigated ported shroud compressor, showing the location of the supporting struts and the cavity geometry. Created from the CAD data provided by industrial partner [97].

As stated in the Introduction to this chapter, one of the objectives of this experimental campaign is to quantify the impact of the PS on the acoustic emission of the compressor. For this purpose, the inlet of the original or baseline compressor shown in Figure 2.2 is altered to *block* the PS slot. The state of the compressor with PS slot similar to the original configuration is referred as PS *open* configuration while the configuration with modified PS slot is called as PS *blocked* configuration in this thesis. These alternative configurations of the compressor shown in Figure 2.3 are realised by modifying the original compressor with a modular inlet design which uses two inlet inserts, one with the PS slot and one without PS slot for PS *open* and *blocked* configuration respectively. The modular design makes it feasible to retain compressor components other than the inlet insert for the two configurations; thereby, providing minimal variability in the experiments due to the manufacturing tolerances of these components.

Compressor performance maps

The performances of the aforementioned PS open and blocked compressor configurations are characterised by measuring the thermodynamic variables of the state attained by fixing

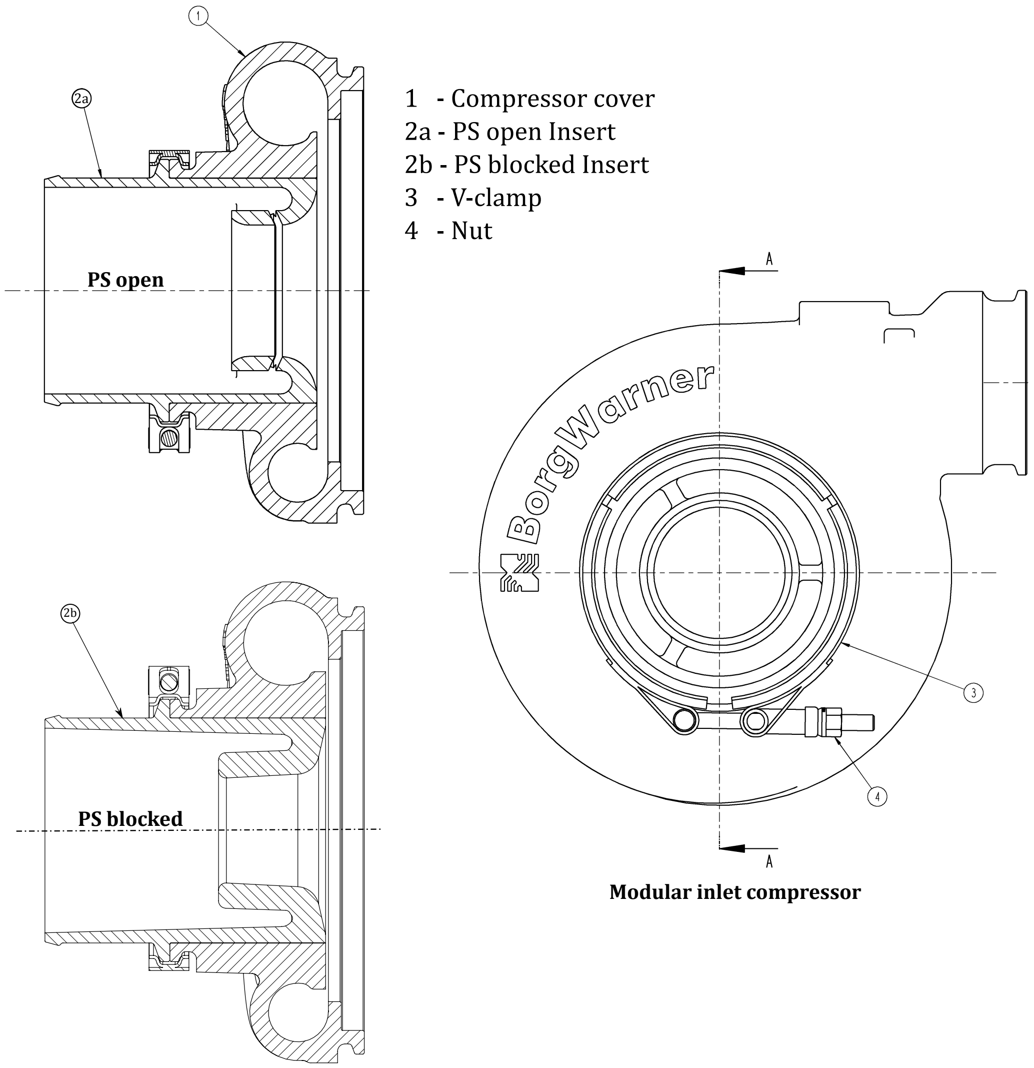

Fig. 2.3 Drawing of the compressor fitted with the modular inlet. The section views of the compressor with inlet inserts corresponding to PS open and blocked configurations are also shown. Created from the CAD data provided by industrial partner [97].

the air mass flow rate and the rotational speed of the impeller. The measurements were performed at the gas stand testing facility in BorgWarner Turbo Systems, Bradford [97]. Pressure and temperature values are recorded for multiple operating points that are achieved through incremental reduction of air flow whilst maintaining a fixed rotational speed. The air mass flow rate is regulated by the operation of a back pressure valve at the compressor outlet while the rotational speed of the compressor is regulated from the turbine end by controlling the conditions at the inlet of the turbine. Further details on the gas stand measurements are described in Sharma et al. [5]. Following this procedure, the thermodynamic state values are recorded for various rotating speeds ranging from 55 krpm to 130 krpm.

The measured air mass flow and compressor rotational speed values are corrected for Standard day conditions to account for the variations in ambient conditions on the day of measurements. The corrected mass flow rate and rotational speed values are computed using the following formulation:

$$\begin{aligned} \dot{m}^* &= \dot{m}\left[\frac{p_{ref}}{p_{in,0}}\right]\sqrt{\frac{T_{in,0}}{T_{ref}}} \\ N^* &= N\sqrt{\frac{T_{ref}}{T_{in,0}}} \end{aligned} \tag{2.7}$$

where N is compressor rotating speed, $\dot{m}$ is the air mass flow rate, $T_{in,0}$ is the total temperature at the compressor inlet, $p_{in,0}$ is total pressure at compressor inlet, T_{ref} is 288.15 K and p_{ref} is 1 atm.

The measured thermodynamic variables of each state are then used to compute compressor performance parameters viz. total-to-total pressure ratio Π_{t-t} and isentropic efficiency η_s.

$$\begin{aligned} \Pi_{t-t} &= \frac{p_{out,0}}{p_{in,0}} \\ \eta_s = \frac{\dot{W}_{is}}{\dot{W}} &= \frac{T_{in,0}}{T_{out,0} - T_{in,0}}\left(\Pi_{t-t}{}^{\gamma-1/\gamma} - 1\right) \end{aligned} \tag{2.8}$$

Total to total pressure ratio is plotted against the corrected air mass flow rate for the two measured compressor configurations in Figure 2.4, which is commonly known as the compressor map. It is worth mentioning that the surge limit identified in this map by the manufacturer is not that of deep surge but rather mild or soft surge [14] in order to safeguard the automotive engine. The extension of the surge limit can be clearly seen in the PS open configuration, especially at higher operating speeds.

The impact of PS on the acoustic emission of the compressor operating at design conditions can be established rather simply, by comparing the acoustic spectra of PS open and blocked configuration as the design points for two configurations are aerodynamically similar. On the contrary, surge limits and thereby, corresponding near surge points for two configurations are very different, and therefore, a direct comparison between the acoustic spectra of the two configurations operating near surge would not be an accurate means to quantify the impact of PS. The differences in the acoustic spectra of the near surge points for two configurations would not be limited to the deviations in the PS geometry but an amalgamation of the alterations caused by differences in geometries and aerodynamic phenomena due to different mass flow rates and corresponding thermodynamic variables. One way around this problem is the determination of two acoustically similar near surge states that can be meaningfully compared to establish the

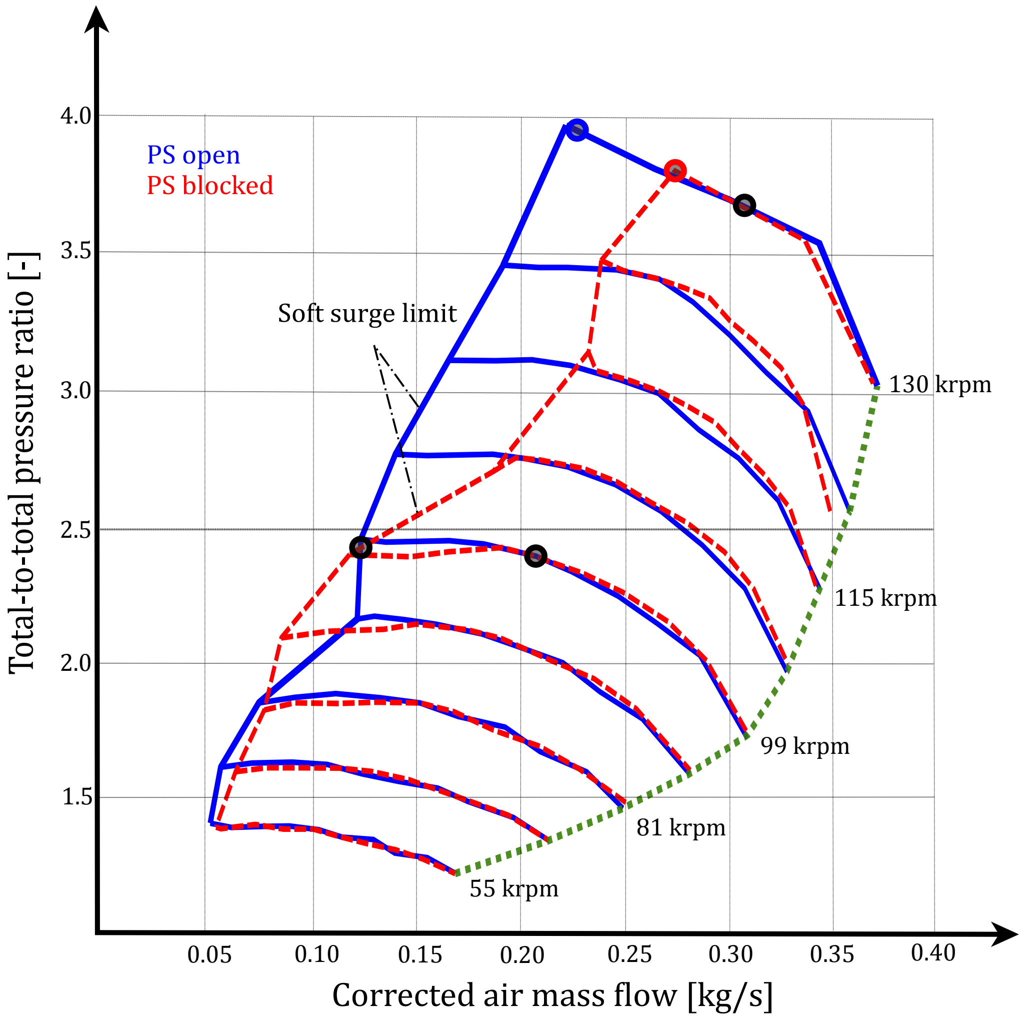

Fig. 2.4 Experimental compressor maps for the open and blocked configurations, highlighting the measured operating points which include design and near surge conditions of 99 krpm and 130 krpm speedlines in both configurations.

impact of the PS on the acoustic emission of near surge operation. The comparable near surge operating points can be determined by applying acoustic similarity laws [98–101]. Acoustic similarity laws are not used in this thesis as coincidently, near surge points of 99 krpm speed lines for two configurations are similar as seen in the compressor map.

Therefore, design and near surge operation for PS *open* and *blocked* configurations at 99 krpm are investigated to quantify the impact of the PS on the acoustic emission of the compressor. Furthermore, the compressor operation at 130 krpm is also studied to understand the evolution of acoustic spectra with an increase in rotational speed. The 99 krpm and 130 krpm iso-speedlines are also referred to as *low* and *high* speedline respectively in this thesis.

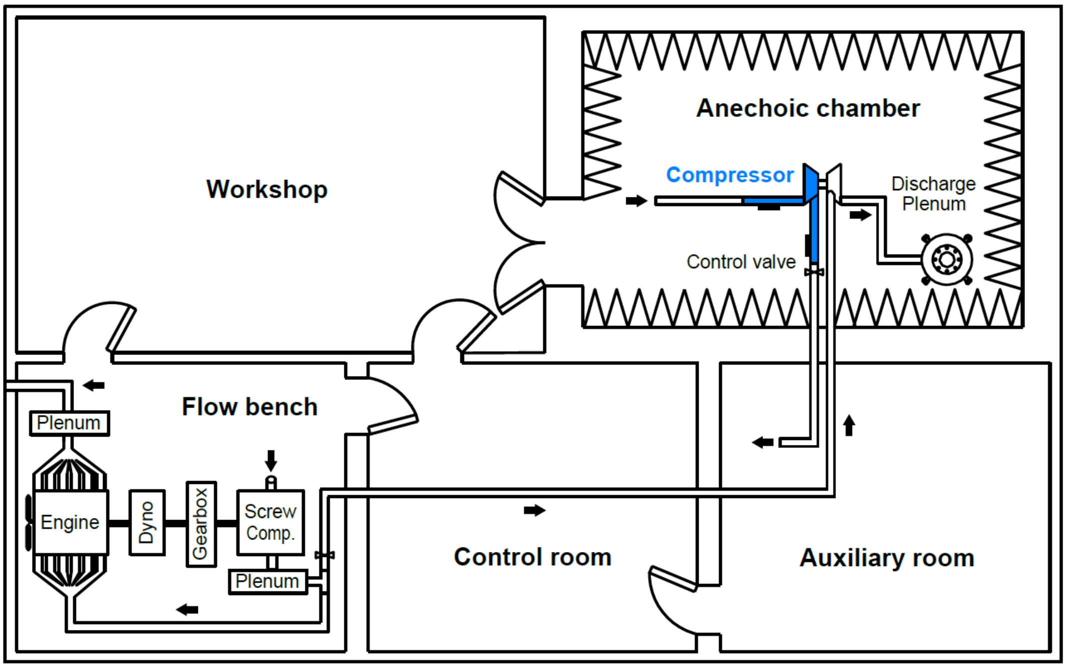

Fig. 2.5 Test rig layout showing the flow rig, turbocharger installation and the auxiliary systems. Reproduced from García-Tíscar [55].

2.4.2 Acoustic flow bench

The acoustic measurements for the selected operating points of PS open and blocked compressor configurations presented in this thesis were carried out in a flow bench facility hosted in CMT – Motores Térmicos [102]. The layout of the complete flow bench is presented in the Figure 2.5. The rig is powered by a heavy duty MIDR 06.20.45 Diesel engine which can generate up to 260 kW of power. This engine is connected to an asynchronous dynamometer and powers a 150 kW Atlas Copco ZA 110-3.5 volumetric screw compressor via a coupling gear. A detailed description of the gas stand used to power the turbocharger has been previously presented in the works of Galindo et al. [103, 104]. The compressed air is first passed through an charge air cooler and then collected in a reservoir to ensure a steady supply. The collected air in the reservoir is then routed to the engine and the turbine of the turbocharger. Therefore, the screw compressor acts as a supercharger for the Diesel engine as well as provides the air flow to the turbine of the installed turbocharger. The compressor draws the air from the ambient of the chamber and discharges to an adjacent room. The discharge of the turbine is carefully channelled to a reservoir equipped with a conical nozzle for minimising velocity and acoustic emissions. The combination of the mass flow rate at the turbine inlet and back pressure valve located at the compressor outlet is used to fix the operating point of the compressor unit of an installed turbocharger.

Alternatively, this test rig can also be used to measure the response of turbocharger for real engine conditions by directly feeding the exhaust gases of the engine to the turbine. This configuration would allow the pulsating content of the engine to be considered in the measurements. For the work presented in this thesis, pulsating flow was not used. The anechoic chamber shown in Figure 2.5 is certified with free field conditions up to a cut-off frequency of 100 Hz. The thesis of García-Tíscar [55] can be referred to for further details on this flow bench.

Instrumentation

For the measurements, the turbocharger with appropriate compressor configuration is installed on the flow bench. The inlet and outlet of the compressor are fitted with long straight pipes to ensure sufficient development of flow suitable for a plane wave to occur at the measurement sections. The diameters of the ducts are appropriate to preserve a cross-sectional area of the

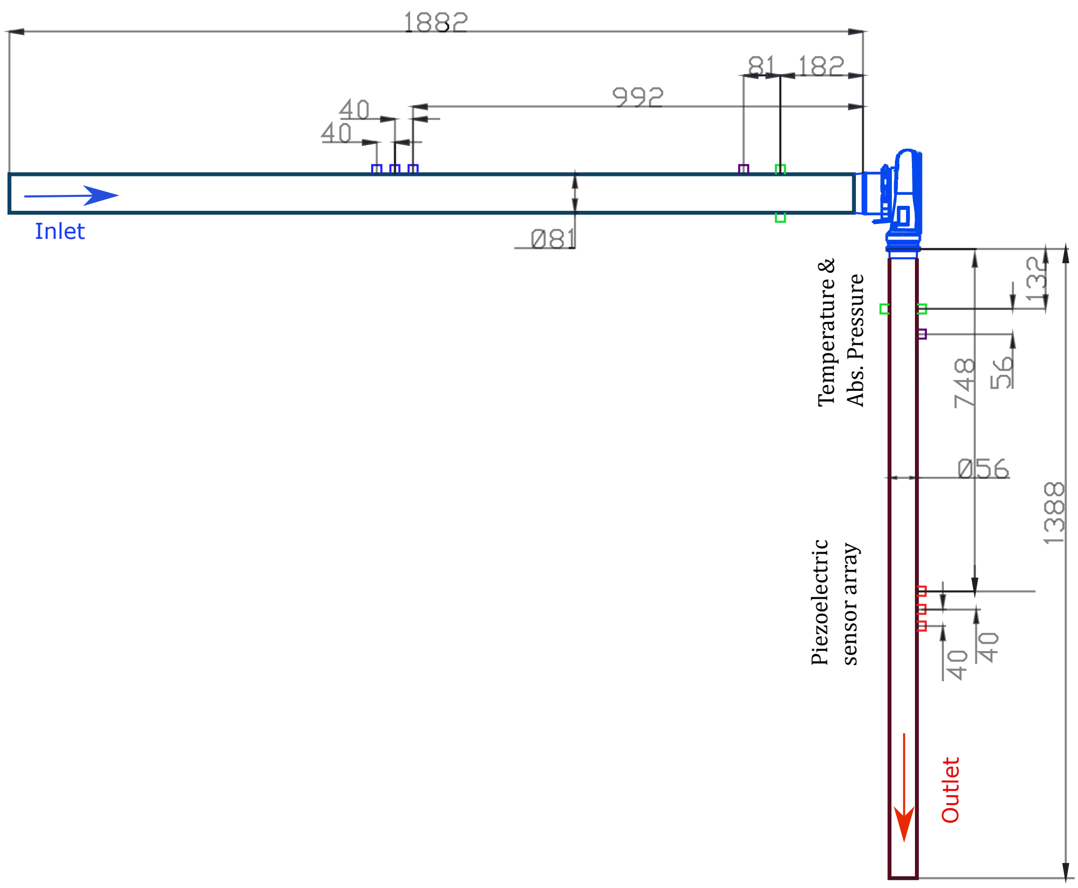

Fig. 2.6 Schematic of the test rig used for measuring the acoustic characteristics of the compressor is shown. The dimensions marked are in millimetres (mm). The location of various pressure and temperature instrumented on the rig are also shown.

adjacent compressor inlet/outlet section to avoid complex three-dimensional structures caused by singularities and impedance mismatch. Two piezoelectric sensor arrays consisting of three piezoelectric sensors each are positioned, one each at the inlet and outlet duct measurement section. The average pressure and temperature values are measured at the compressor inlet and outlet sections while the air mass flow rate is only measured at the compressor inlet. A schematic of the compressor measurement layout showing various sensors and their positions are shown in the Figure 2.6.

In addition to the sensors positioned in inlet and outlet ducts, the compressor is also instrumented to measure the rotational speed and to quantify the noise generated by the impeller. For the purpose of the noise generation, two miniaturised pressure probes are positioned in

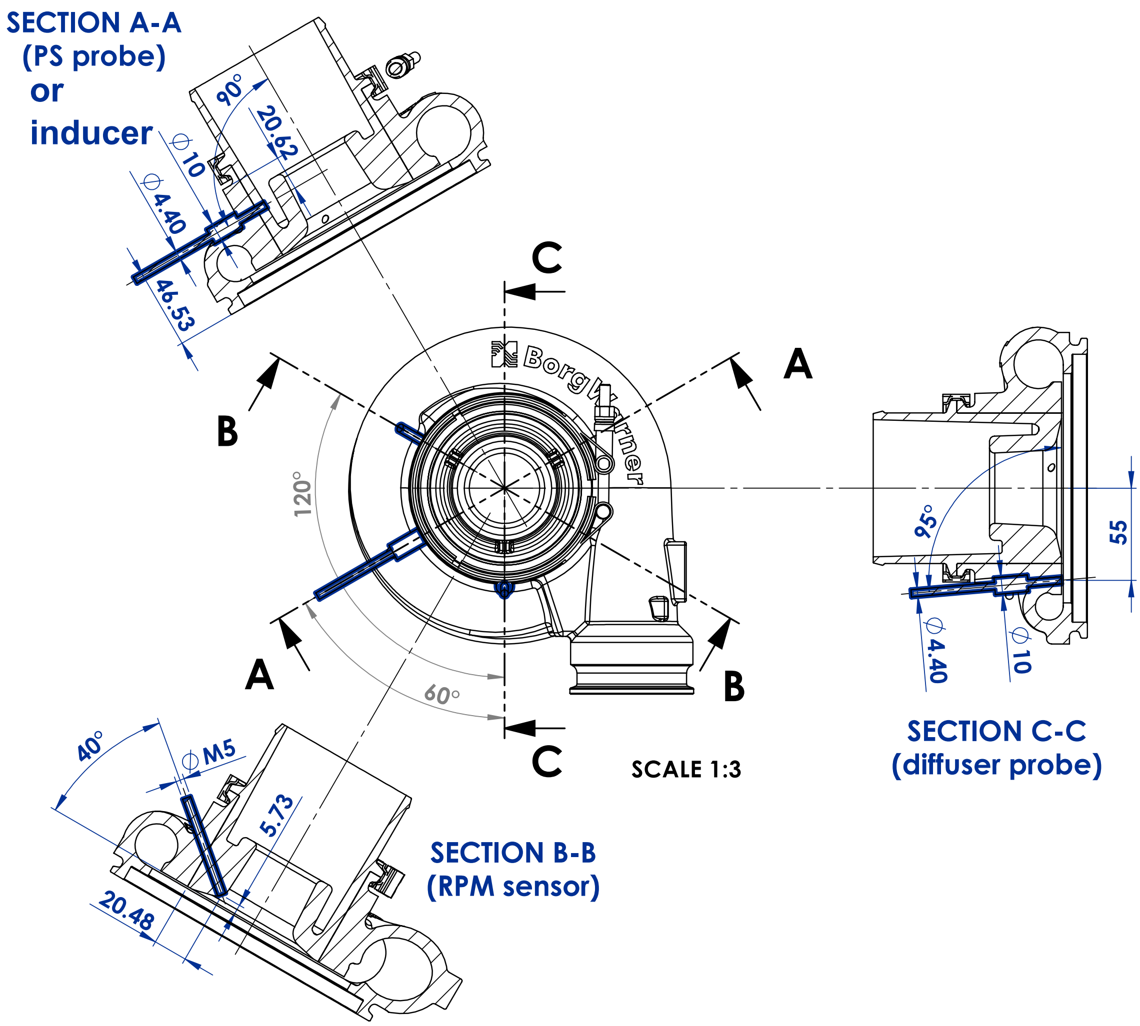

Fig. 2.7 Instrumentation on the turbocharger compressor, highlighting three sections corresponding to the position of inducer probe inside PS cavity, diffuser probe and RPM sensor. Created from the CAD data provided by industrial partner [97].

the inducer and diffuser of the compressor. The inducer probe is wall flushed in the PS cavity, and the diffuser probe is wall flushed at the middle along the length of the diffuser. The instrumented compressor along with the position of various probes are shown in Figure 2.7.

Table 2.1 Uncertainty details of the instrumentation used in the measurements

Sensor	Variable	Accuracy (%)
Piezoelectric sensor	In-duct dynamic pressure	± 0.70
Piezoresistive sensor	Absolute pressure	± 0.65
Thermocouples	Temperature	± 0.35
RPM sensor	Rotational speed	± 0.006
Air mass flow meter	Air mass	± 0.12

Dynamic pressure fluctuations obtained from the piezoelectric sensor arrays and miniaturised pressure probes are recorded for 1s with a sampling frequency of 200 kHz using a Yokogawa DL850V recorder [105]. The global variables of the experimental set-up are measured with an in-house custom-built data acquisition system that averages the sensor data over 5s. These parameters include air mass flow, turbo speed, static temperatures and absolute static pressures of the air flow with the last two variables being recorded for both inlet and outlet ducts. Temperature data is an average of thermocouples placed at different radial locations of the same cross-section. Table 2.1 presents the accuracy of the instrumentation [106] used in the experimental facilities as a reference for assessing the uncertainties of measurements.

2.4.3 Post-processing

Dynamic pressure fluctuations measured by sensor arrays and miniaturised pressure probes are processed to obtain the acoustic characteristics of the compressor. The acoustic results can be visualised in the form of pressure spectra and sound intensity spectrograms. The pressure spectra presented in terms of Power Spectral Density (PSD) are obtained using Welch's overlapped segmented averaging of the pressure data in accordance to Equation 2.9 [107]. The number of blocks is selected with an intent to achieve a frequency resolution of approximately 50 Hz. These blocks are then tapered using Hanning functions with 50% overlap. Spectra of the decomposed pressure wave components are computed similarly to calculate the PSD of the sound intensity.

$$S_x(f) = \frac{1}{K}\sum_{i=1}^{K} P_i(f) \tag{2.9}$$

where $S_x(f)$ is the Welch's estimate of the PSD for a data sequence x $(x(0)x(1)\ldots x(N-1))$ at some frequency f, the number of segments or blocks are denoted by K and $P_i(f)$ form the modified periodogram value obtained from a windowed discrete Fourier transform.

The sound intensity spectrograms are computed in accordance with the methodology recommended by Torregrosa et al. [31]. For a compressor operating at a point i, the overall

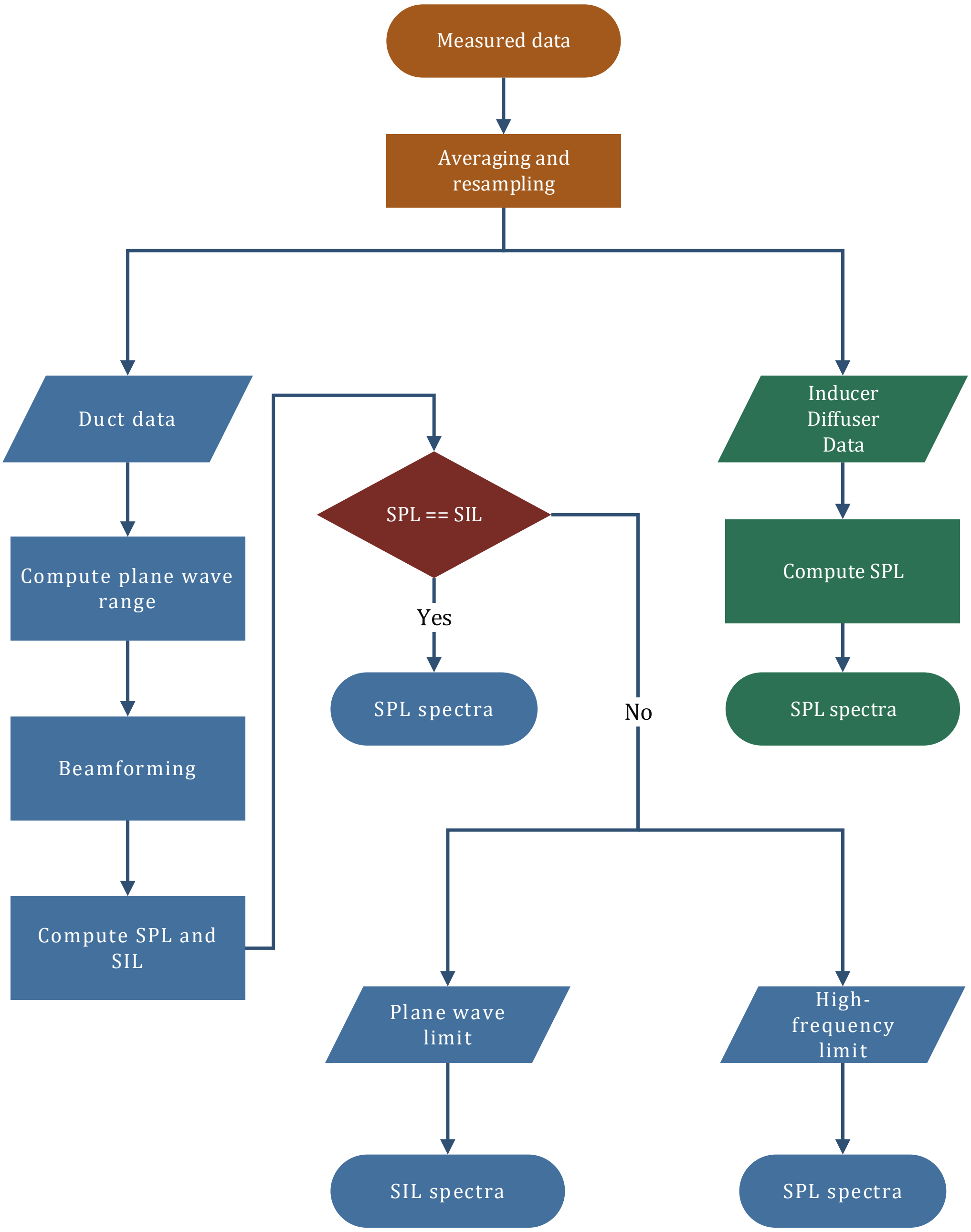

Fig. 2.8 Procedure followed to process the measured pressure data for obtaining acoustic spectra is illustrated.

level of the sound intensity L_i for a particular frequency range of $f_1 - f_2$ can be computed from the intensity spectra $I(f)$ as:

$$L_i = 10\log_{10}\left(10^{12}\sum_{f=f_1}^{f_2} I(f)\right) \tag{2.10}$$

Once L_i has been computed for multiple operating points across the compressor map, a cubic spline interpolation function can be used to obtain noise map and/or spectrogram based on the size of the frequency range. Since only a few operating points of the compressor map are acoustically characterised in this work, noise map of either compressor configuration is not presented.

The procedure followed to obtain the acoustic spectra at the various locations of the compressor is outlined by the flowchart shown in Figure 2.8. Wave decomposition can be used to compute the SIL and the spectra obtained from these decomposed components are primarily used to assess the quality of numerical results as covered in Chapter 3.

2.5 Measured pressure spectra

Pressure spectra for the operational configurations of the compressor specified in Section 2.4 are presented in this section. Acoustic characteristics of open and blocked PS configurations of the compressor operating at the design and near surge conditions for two aforementioned iso-speed lines viz. 99 krpm and 130 krpm are analysed in the following subsections.

2.5.1 99 krpm speedline

The acoustic characteristics of the PS open and blocked compressor configurations operating at the Design or Best Efficiency Point (BEP) and Near Surge (NS) conditions for 99 krpm iso-speedline are presented here. As discussed before, the operating points of this speedline are aerodynamically similar for both configurations and therefore, the results can be directly compared.

PS open configuration

Pressure spectra computed from piezoelectric arrays and miniature pressure probes for PS open compressor operating at the design and near surge conditions are presented in Figure 2.9 and Figure 2.10 respectively. The noise generated by the impeller is investigated from the spectra of inducer and diffuser probe while the propagation of the noise in to the compressor ducts is analysed from the spectra of duct arrays.

Design operation Upon analysing the pressure spectra of the probes located at the upstream of the impeller for the compressor operating at design condition (top of Figure 2.9), the following points can be made:

- The noise generated by the PS open configuration operating at the design condition as seen from the inducer spectrum is relatively flat with multiple tonal features that include the harmonics of Rotating Order (RO) [2] and Blade Pass Frequency (BPF) [3].
- In addition to expected RO tones, a low-frequency peak at approximately 0.4 RO is also seen in the inducer spectrum.
- The inlet spectra reasonably follow the inducer spectrum with an expected decrease in the levels. Broadband elevation in the characteristic 'whoosh' noise frequency range is not observed in either inducer or inlet duct spectra.
- The spectra of the individual sensors of the inlet piezoelectric array show good correlation, specifically between the spectra of the second and third probe. The spectrum of the first inlet probe deviates from the other two in terms of amplitude from 8.2 kHz. Broadband elevation in the range of 13.7-15.7 kHz (highlighted as 'I') spotted in the spectra of the second and third probe is also not identified in the spectrum of first inlet probe. Furthermore, this broadband is also not present in the spectrum of inducer probe and therefore, is expected to be a propagation effect related to either PS cavity and/or inlet duct.
- The onset of higher order duct modes, specifically the limiting first asymmetric mode at 2.5 kHz for the inlet duct is seen to cause a slight increase in the levels of inlet duct spectra.

Similarly, the following points can be made by analysing the spectra of probes positioned downstream of the impeller (bottom of Figure 2.9):

- The diffuser spectrum has fewer RO tones (1^{st} and 10^{th} RO and 1^{st} and 2^{nd} BPF) in contrast to the inducer spectrum. This is coherent with the hypothesised mechanism of RO tones as the shock waves corresponding to the sonic conditions at the leading edge of the impeller blades. Therefore, these tones are readily identified at the upstream locations, but not downstream.

[2] Also known as rotational frequency, RO = $n/60$ where n = rotational speed of the impeller in rotations per minute (rpm)

[3] BPF = RO $\times$ number of impeller main blades (7 in this case)

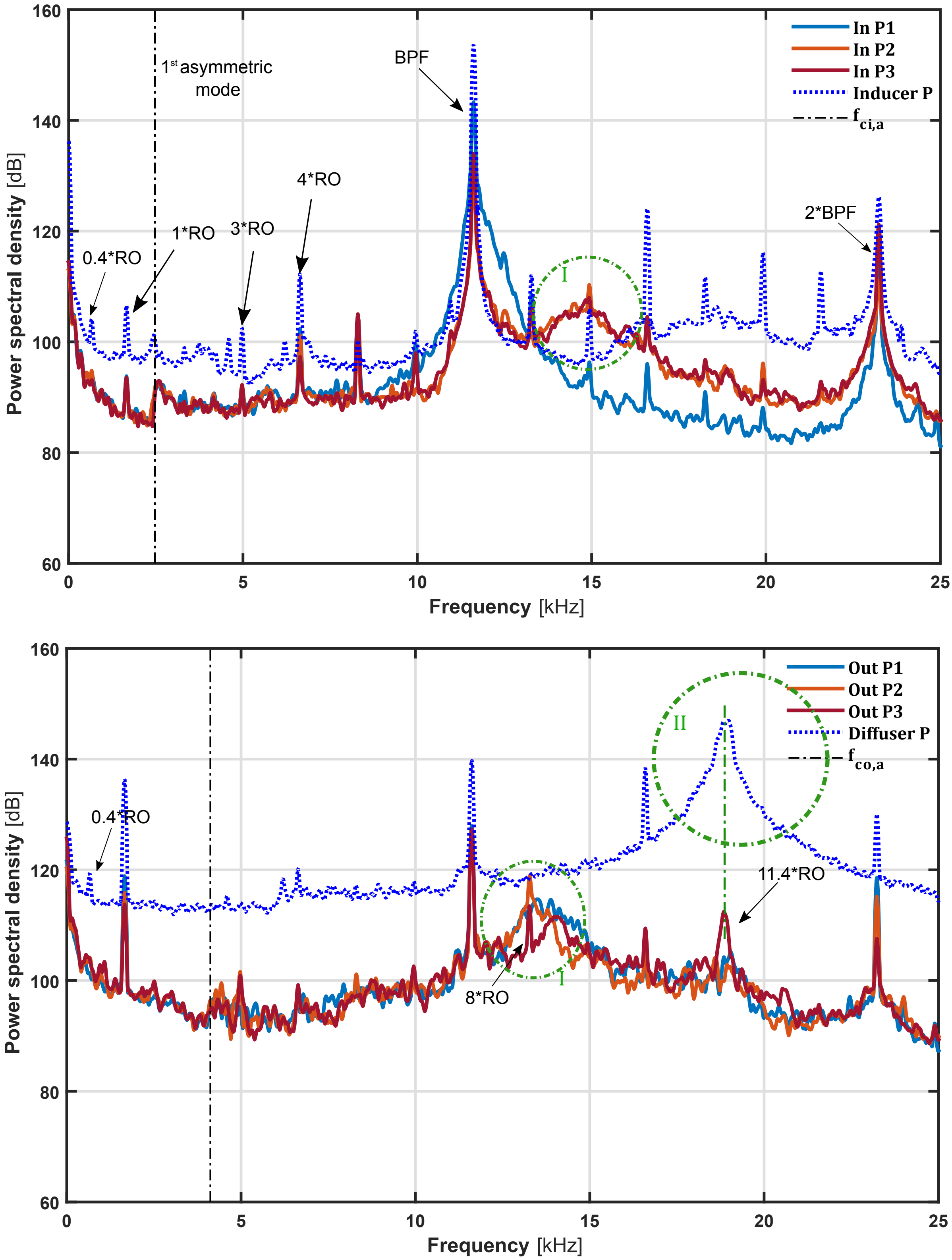

Fig. 2.9 Pressure spectra of the probes located upstream (top) and downstream (bottom) of the impeller for open compressor configuration operating at the design condition of 99 krpm speedline. Former corresponds to inducer and inlet duct array while latter includes diffuser and outlet duct array.

- The low-frequency peak at 0.4 RO is also present in the diffuser spectrum. Furthermore, narrow width broadband noise at 18.8 kHz (highlighted as 'II') corresponding to 11.4 RO is also identified in the diffuser spectrum.
- The spectra of the individual sensors forming the outlet piezoelectric sensor array are highly correlated and follow the diffuser spectra with an anticipated decrease in levels. Again, the broadband feature corresponding to 'whoosh' noise is not identified in the diffuser or outlet duct spectra.
- Small broadband noise levels in the region of 12.5-14.5 kHz (highlighted as 'I') are identified in the spectra of outlet duct probes but are non existent in the diffuser spectrum, implying a possible propagation feature. Additionally, broadband elevation 'II' seen in the diffuser spectrum does not seem to have propagated to outlet duct. Nevertheless, a peak corresponding to the diffuser broadband 'II' is observed in the spectrum of third outlet probe.
- Plane wave propagation in the outlet duct is also limited by the onset of the first asymmetric mode at 4.12 kHz. The impact of higher order modes is not as significant as seen for inlet duct spectra, although slight variations among otherwise highly coherent outlet spectra can be seen after the cut-off frequency.

An excellent correlation among the spectra of the individual sensors forming inlet and outlet duct arrays points out the precise calibration of individual transducers and complete development of the flow at the measurement sections. As for the design operation of the compressor, the flow at the inlet is expected to be steady and uniform while the swirl in the flow exiting the compressor is supposed to settle down by the time it reaches the measurement section. Therefore, the pressure spectrum does not change significantly with the axial position in the array. This being said, deviations are seen in the spectra of the first sensor of the inlet array relative to the other two. This is due to the three-dimensional effects introduced by higher order duct modes as the spectra of three sensors are similar within the plane wave region.

The RO and blade pass harmonics are hypothesised to be caused by the sonic condition at the leading edges, while the broadband elevations marked as 'I' in the spectra of inlet and outlet duct probes are expected to be propagation effects as these broadband noises are not identified in the inducer and diffuser spectra respectively. The broadband elevation marked as 'II' in the diffuser spectra is expected to signify the interaction of the volute tongue with the swirling flow coming out of diffuser. The source of the low-frequency peak at 0.4 RO seems rather interesting and, would need further investigation to locate the possible sources. The spectra of the compressor at other operating points throws some more light on these broadband features.

Near surge operation In a similar way, the spectra of the compressor operating near surge are analysed. The findings from the analysis of the pressure spectra of the probes located upstream to the impeller (top of Figure 2.10) are listed below:

- In contrast to the design operation, the RO tones are non existent in the inducer spectrum of the compressor operating near surge. Nonetheless, BPF and its harmonics can be clearly identified.
- Broadband elevation in the range of 17-21.5 kHz (marked as 'II') centred around 19 kHz can be seen in the inducer spectrum.
- Similar to the design operation, the spectra of the second and third sensor of the inlet duct array are highly correlated while deviation in the spectrum of the first probe can be observed from about 8.2 kHz. Furthermore, broadband elevation in the range of 13.5-16 kHz (marked as 'I') is identified in the spectra of the second and third sensor of inlet array while not existent in the spectrum of the first sensor. The presence of this broadband 'I' in the second and third sensor at both design and near surge operating points further reinforces the hypothesis of it being a propagation effect related to the geometry.
- Broadband 'II' identified in the inducer spectrum does not seem to have propagated in the inlet duct. It is interesting to point out the similarity of this broadband with the one seen in the spectrum of the diffuser for the compressor operating at design condition (see Figure 2.11 - bottom plot) for the same iso-speedline.
- The plane wave propagation in the inlet duct is again limited by the onset of the first asymmetric mode at 2.5 kHz causing a shift in the spectra of inlet duct array. Furthermore, broadband noise corresponding to the 'whoosh' frequency range is not identified in the spectra of the inlet duct for near surge operation either.

The analysis of the spectra of outlet duct array and diffuser probe spectra (bottom of Figure 2.10) are presented in the following points:

- In contrast to the spectrum of the inducer probe, some RO tones (1$^{\text{st}}$ and 10$^{\text{th}}$) are visible in the diffuser spectrum for near surge operation. In addition to that, a low-frequency tonal noise at approximately 0.37 RO is also identified similar to the 0.4RO tone in the diffuser spectrum of the design condition. Diffuser spectra for the design and near surge operation are reasonably similar as seen the Figure 2.11 (middle plot).

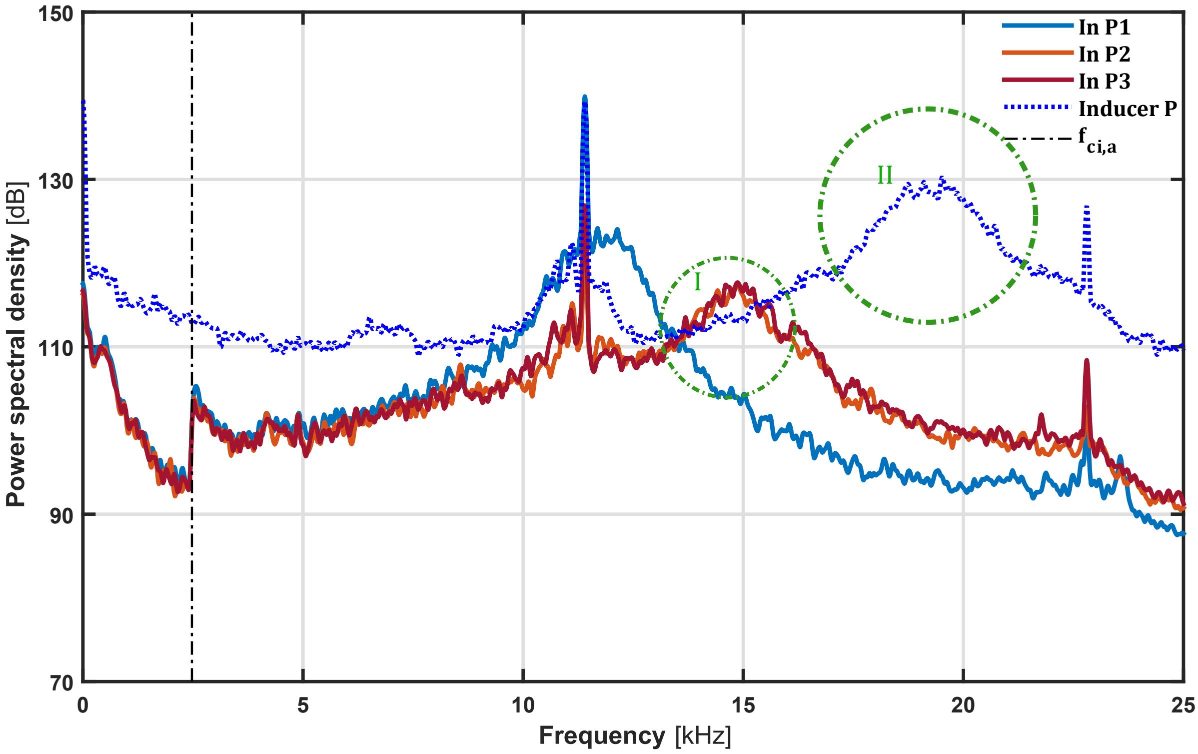

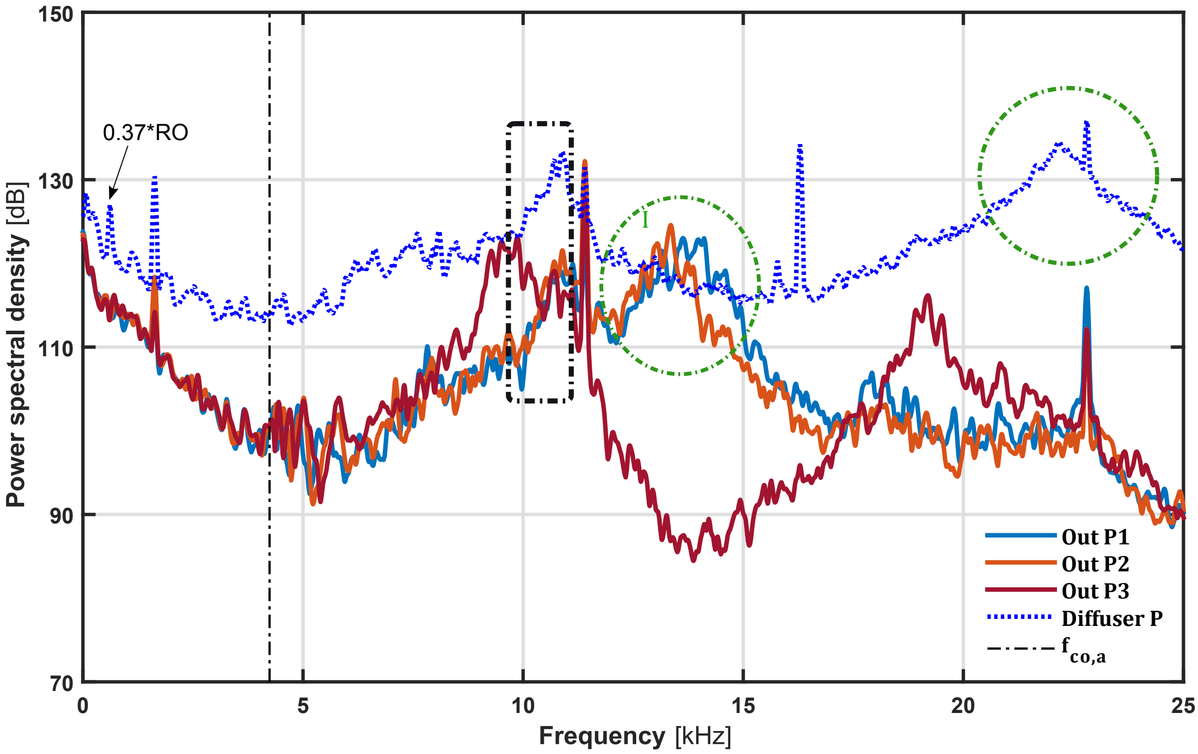

Fig. 2.10 Pressure spectra of the probes located upstream (top) and downstream (bottom) of the impeller for open compressor configuration operating at the near surge condition of 99 krpm speedline. Former corresponds to inducer and inlet duct array while latter includes diffuser and outlet duct array.

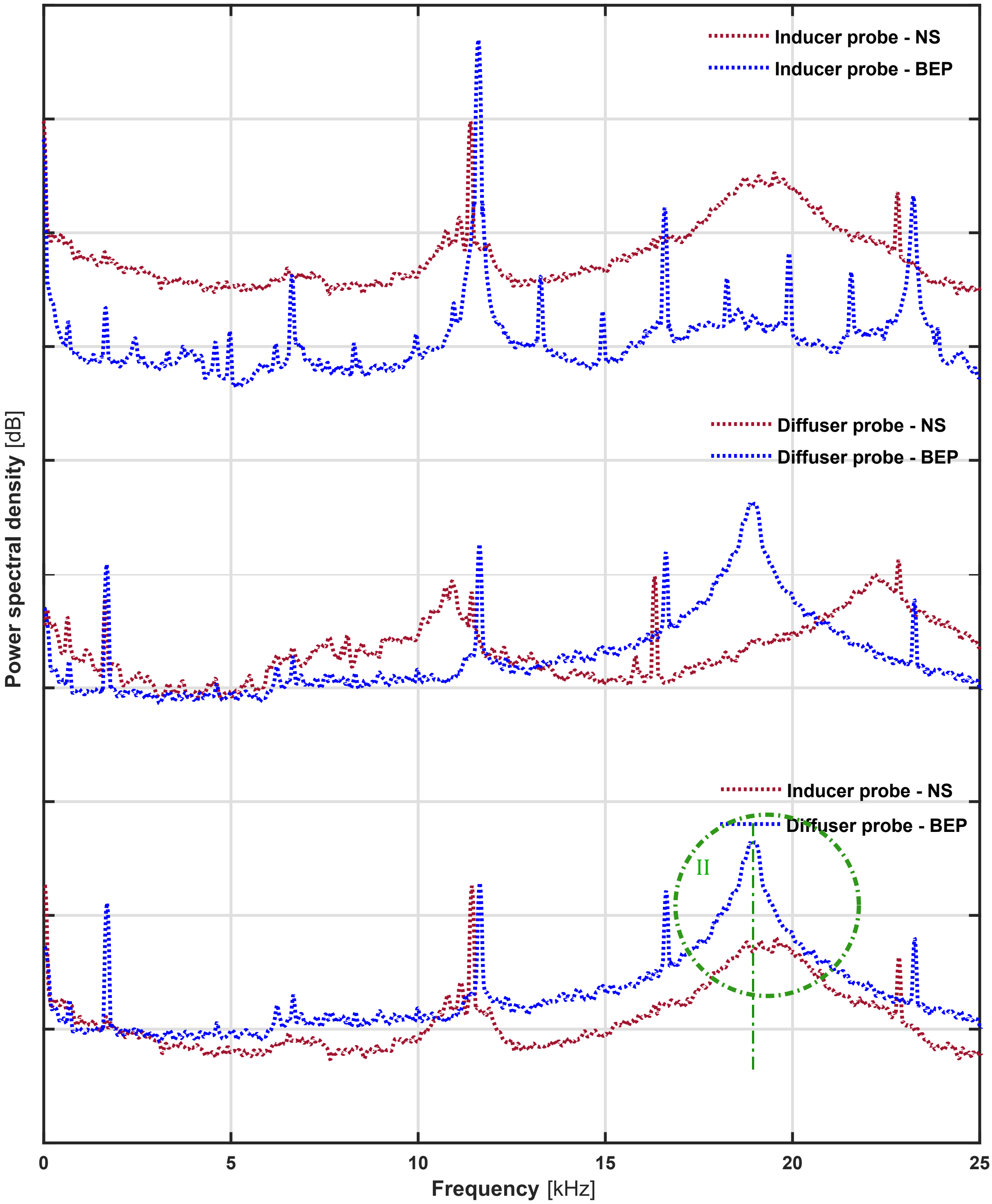

Fig. 2.11 Comparison of the design and near surge pressure spectra for the inducer (top) and diffuser (middle) probes of the open compressor configuration operating at 99 krpm. The similarity in the inducer spectrum of near surge operation and diffuser spectrum for design operation is also shown in the bottom plot. Y-axis differences are arbitrary, although the scale is kept at 20 dB per division.

- Broadband elevation in the ranges of 6-11 kHz and 20-22.5 kHz adjacent to the corresponding first and second harmonics of BPF is identified. The former broadband fits into the characteristic Tip Clearance Noise (TCN) frequency range while latter could be either a TCN like feature related to second harmonic of BPF or a broadband feature similar to the one identified in the diffuser spectrum at design conditions but shifted due to the downstream instabilities related to near surge operation. Furthermore, BPF is no longer a distinctive feature as the spectrum is dominated by broadband features.

- In contrast to the design condition, the spectra of the first and second sensors of the outlet array are correlated while significant deviation can be seen in the spectrum of the third sensor. Furthermore, broadband elevation in the range of 12.2-15 kHz (marked as 'I') is observed in the spectra of first and second outlet sensors. This is in coherence with the observations made in the outlet spectra at design conditions and reinforces the propagation nature of this broadband feature.

- The broadband feature similar to the TCN identified in the diffuser spectrum can also be observed in the spectra of the outlet sensors. The broadband adjacent to the second harmonic of BPF does not seem to have propagated to the outlet duct; thereby, making it similar to 'II' broadband instead of TCN. Furthermore, the broadband centred around 19 kHz observed in the diffuser and inducer spectra of design and near surge operation respectively, is also observed in the spectrum of the third sensor of the outlet array.

- Variations in the spectra of the outlet array's sensor can be seen after the onset of first asymmetric mode. Furthermore, the elevation corresponding to the 'whoosh' noise is not observed either.

The deviations in the spectra of the sensors forming duct arrays can be contributed to the three-dimensional effects caused by duct modes and the propagation of flow instability due to the operation of the compressor near surge. The deviation among the spectra of the inlet duct array is primarily due to duct modes as the flow instability is reported only to propagate few diameters upstream [5, 108]. Furthermore, a similar pattern is observed in the inlet spectra at design operation conditions thereby implying this to be a feature dependent on geometry rather than the flow conditions. The deviation in the spectra of the outlet duct array can primarily be attributed to the three-dimensional effects caused by swirl and flow instability present in the compressor outlet. Furthermore, the absence of these deviations in the outlet duct spectra at design conditions further reinforces this reasoning.

The broadband features marked as 'I' in the spectra of inlet and outlet ducts are expected to be caused by either PS geometry or the respective duct modes, as similar features are observed in the corresponding spectra of the design point. The broadband marked as ‘II’ in the inducer spectrum is hypothesised to be caused by the interaction of the swirling flow in the PS cavity with the structural struts, with three small peaks corresponding to three struts. The mechanism of this broadband is expected to be similar to the one seen in the diffuser spectrum at design conditions, hypothesised to be caused by the interaction of the swirling flow with volute tongue. The resemblance between the two spectra can be seen from the Figure 2.11 (bottom plot). The broadband relating to the flow interaction with the volute tongue is not explicitly observed in the same range as seen in the diffuser spectrum of near surge operation. The broadband could have been shifted due to the flow characteristics of near surge operation and would need further investigation. Additionally, broadband noise in the characteristic ‘whoosh’ frequency range is not observed, but a TCN like feature is identified in the diffuser and outlet spectra. Furthermore, the mechanism behind the strong presence of 0.4 RO, 1 RO and 10 RO in the diffuser spectrum also requires further flow analysis.

PS blocked configuration

The spectra of the PS blocked, and open compressor configurations are compared in this section. The impact of PS casing treatment on the acoustic emission of the compressor is established for both design and near surge operation of the selected iso-speedline.

Design operation The pressure spectra of the two compressor configurations operating at design conditions are compared in Figure 2.12 and Figure 2.13. The spectra of the probes located upstream of the impeller are presented in the former figure while latter displays the spectra of the probes positioned downstream of the impeller.

The following observations can be made by comparing the spectra of the inlet duct and inducer probes of two configurations (Figure 2.12):

- The inducer spectra for two configurations look similar with the overall levels for the blocked configuration approximately 3-5 dB lower than the open configuration beyond the first harmonic of BPF. In addition to that, a broadband elevation in the range of 6.8-8.8 kHz is identified in the spectrum of the blocked configuration. In contrast to the PS open configuration, the inducer probe is not in direct proximity to the impeller as the PS slot is closed. Therefore, the decreased levels and broadband feature could be the function of the noise propagation in the PS cavity instead of the noise generated by the impeller.

- Relative reduction in the tonal (RO and blade tones) content is observed in the inducer spectrum for the blocked configuration as the rotor-alone pressure does not directly

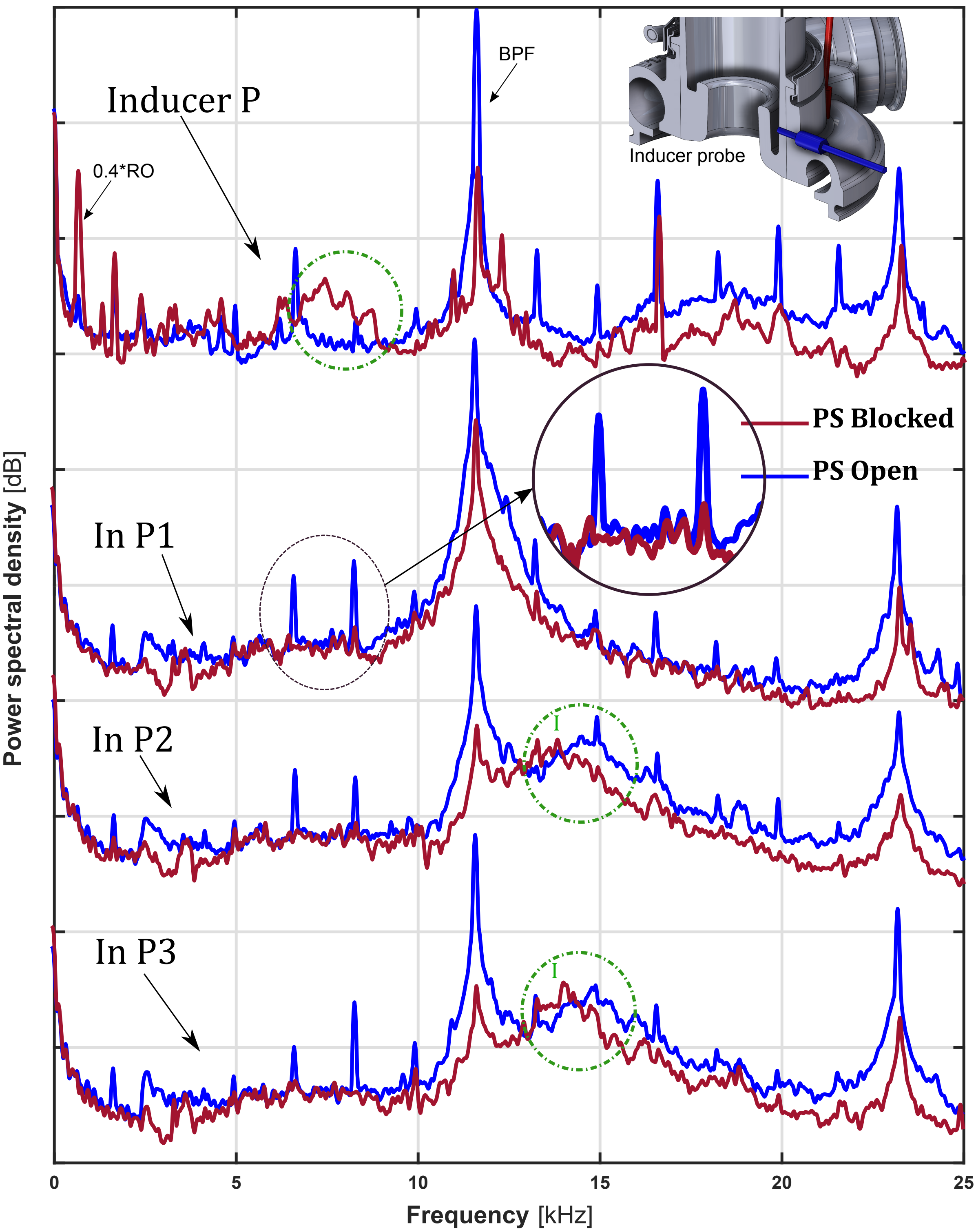

Fig. 2.12 Comparison of the pressure spectra computed from the probes located at the impeller upstream region for the open (blue) and blocked (red) compressors configuration operating at their respective design conditions of 99 krpm speedline. Y-axis differences are arbitrary, although the scale is kept at 20 dB per division.

impact the PS cavity. This being said, a low-frequency tone at 0.4 RO is accentuated in the spectrum of the blocked configuration.

- The spectra of the probes forming inlet duct array are similar for both configurations in terms of overall levels while the duct spectra of the blocked compressor show a significant reduction in the tonal content.

- Similar to the spectra of the open configuration, broadband elevation in the range of 13.7-15.7 kHz (highlighted as 'I') can also be observed in the spectra of the second and third inlet probes. This implies that the observed broadband is a propagation characteristic of the inlet duct.

- The impact of the onset of the first asymmetric mode on inlet duct spectra is again similar to the one observed for the PS open configuration. Furthermore, broadband noise in the 'whoosh' characteristic frequency is not observed either.

The comparison of diffuser and outlet duct probes for the two configurations (Figure 2.13) are detailed below:

- Although similar trends are shown by the diffuser spectra of the two configurations, the blocked configuration shows higher overall levels across the frequency range beyond the first rotating tone. Interestingly, the difference in levels is not propagated to the outlet duct as observed from the comparison of duct spectra.

- Similar to the inducer spectrum, a broadband elevation in the range of 6.2-7.2 kHz is observed in the diffuser spectrum of the PS blocked configuration. Additionally, broadband elevation centred at 18.8 kHz (highlighted as 'II') is identified in the diffuser spectra of both configurations.

- Tonal noise corresponding to 1 RO, BPF and 2 BPF is observed in the diffuser spectra of both configurations while 10 RO is only observed for the open configuration. This implies the possible involvement of PS geometry as the source of 10 RO tonal noise.

- The spectra of the outlet duct probes for two configurations are very similar except for the broadband elevation marked as 'I', identified in the spectra of open configuration is not existent in the spectra of blocked configuration. Therefore, this broadband 'I' is expected to be caused by the propagation within the PS cavity. Furthermore, broadband corresponding to the 'whoosh' noise is not observed in the spectra of the outlet duct.

The comparison of the duct spectra of two compressor configurations points that the PS casing treatment does not heavily alter the acoustic emission at the design conditions of the

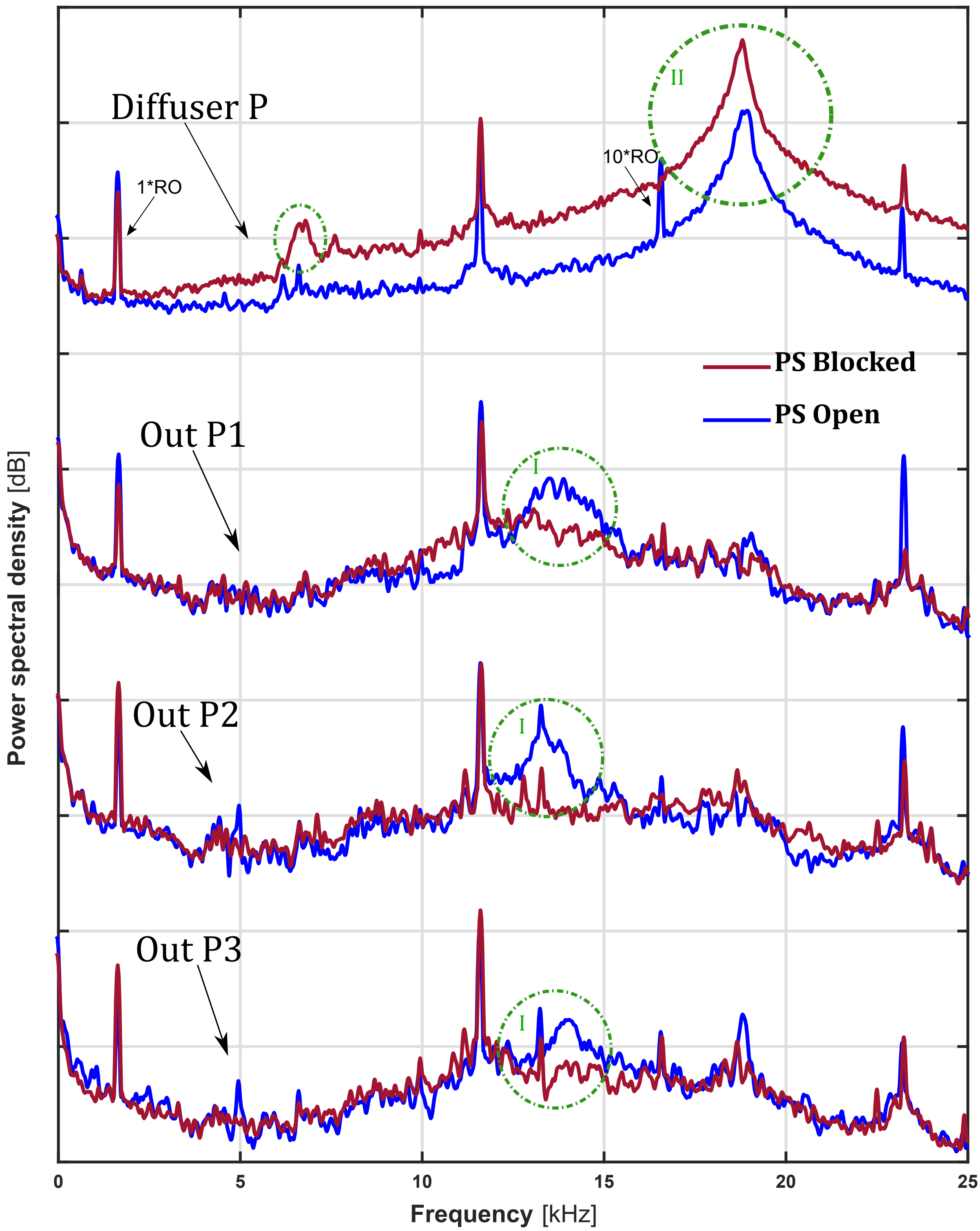

Fig. 2.13 Comparison of the pressure spectra computed from the probes located at the impeller downstream region for the open (blue) and blocked (red) compressors configuration operating at their respective design conditions of 99 krpm speedline. Y-axis differences are arbitrary, although the scale is kept at 20 dB per division.

studied iso-speedline. The results do point towards the role of the PS cavity in propagating tonal noise in the direction upstream to the impeller. The comparison of diffuser spectra shows a decrease in the noise generated by flow exiting the impeller by using a PS feature although a tonal noise at 10RO is seen to be caused by the PS. Furthermore, PS casing design is likely causing a broadband noise feature in the outlet duct spectra whilst suppressing a broadband feature in the inducer spectrum.

Near surge operation The pressure spectra of the probes located at the upstream and downstream of the impeller for two compressor configurations operating near surge are compared in Figure 2.14 and Figure 2.15 respectively.

The following observations can be made by comparing the spectra of the inlet duct and inducer probes of the two configurations (Figure 2.14):

- In contrast to the design condition, significant differences in the broadband features can be seen in the inducer spectra of the two configurations. Broadband elevations corresponding to 2.1-4.3 kHz and 5.5-8.0 kHz observed in the spectrum of the *blocked* configuration are not existent in the respective spectrum of the *open* configuration. Another broadband elevation (marked as 'II') centred around 19 kHz is only observed in the spectrum of the open configuration, reinforcing the earlier argument on the nature of this broadband being associated with the flow interaction inside the PS cavity. Furthermore, broadband noise corresponding to TCN is identified in the spectra of both configurations.

- In addition to the broadband features, peaks at 0.4 RO and 1.5 RO are also observed only in the inducer spectrum of the blocked configuration. Furthermore, significant differences in the overall levels are also observed in the spectra of the two configurations with the blocked compressor registering lower noise levels beyond 9 kHz and relatively higher levels in the frequencies below 9 kHz due to broadband content.

- The levels and trends of the inlet duct spectra for the two configurations are similar with the exception of broadband elevations in the range of 3.2-8.5 kHz observed for the *blocked* configuration. Multiple narrowband elevations in the 3.1-4.1 kHz, 5-6.2 kHz and 6.2-8.5 kHz ranges are conflated together as a broadband feature. The latter part of this broadband, i.e. 6.2-8.5 kHz is also observed in the inducer spectrum while the former narrowband, i.e. 3.1-4.1 kHz can be associated with the 'whoosh' noise. The presence of the 3.2-8.5 kHz broadband makes the blocked compressor noisier relative to the open configuration for near surge operation.

- Broadband highlighted as 'I' is again observed in the spectra of both open and blocked configurations implying this is a propagation characteristic of the inlet duct. Furthermore,

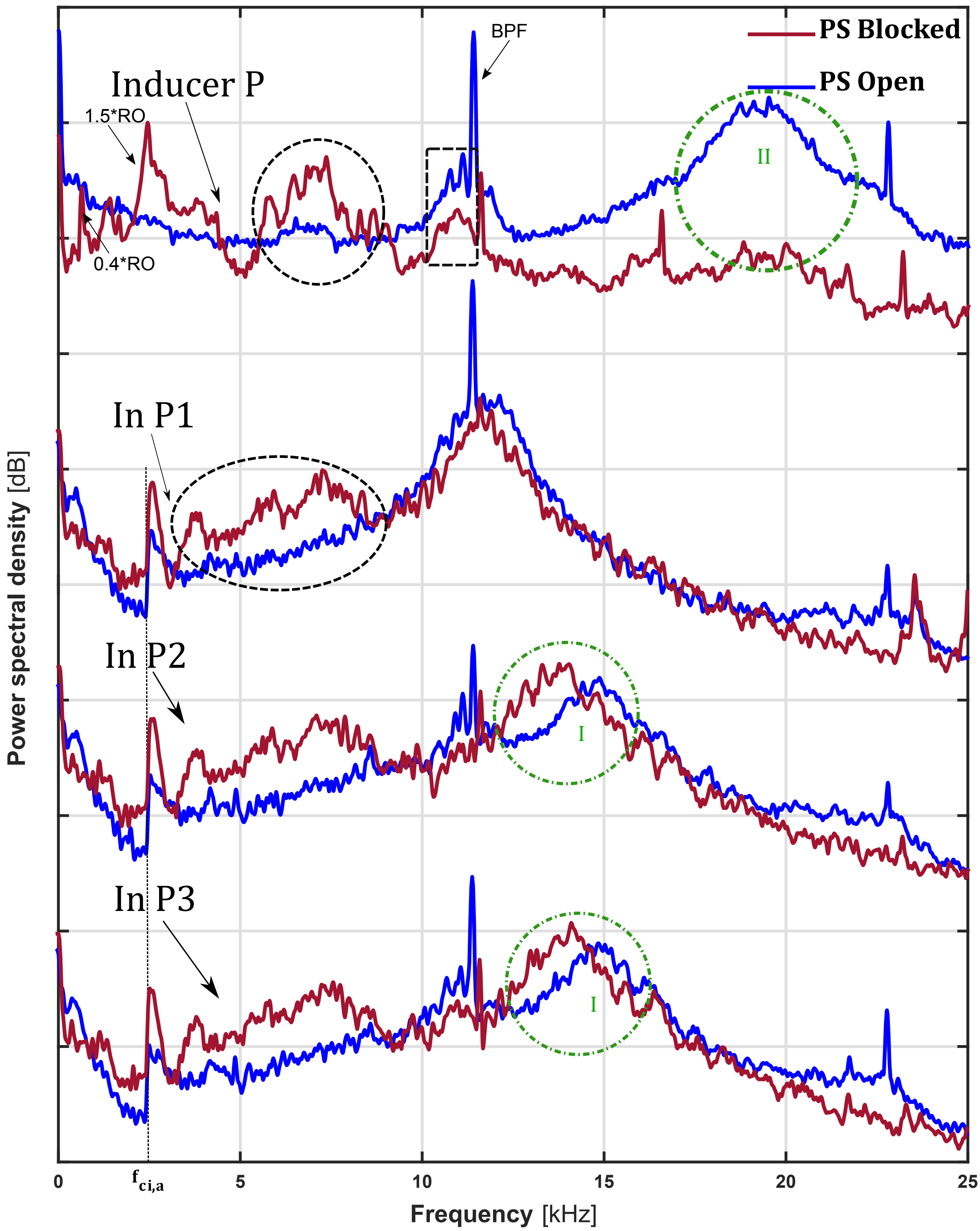

Fig. 2.14 Comparison of the pressure spectra computed from the probes located at the impeller upstream region for the open (blue) and blocked (red) compressors configuration operating at their respective near surge conditions of 99 krpm speedline. Y-axis differences are arbitrary, although the scale is kept at 20 dB per division.

the tonal noise at 1.5 RO observed in the inducer spectrum of the blocked configuration is also observed in the inlet duct spectra coincident with the onset of first asymmetric mode.

Discussion on the comparison of the diffuser and outlet duct spectra for two configurations (Figure 2.15) is presented below:

- Diffuser spectra of the two configurations share a similar trend with higher overall levels for the blocked configuration across the frequency range beyond the first rotating tone. Similar to the spectra of the upstream probes, a broadband elevation at 5.5-10 kHz range is observed in the spectra of the blocked case. Additionally, feeble narrowband elevations in the range of 1.8-3 kHz and 3.2-4.7 kHz are also observed in the blocked spectra with the former corresponding to the 'whoosh' characteristic frequency. Furthermore, BPF is masked by the broadband characteristics in both configurations while tonal noise at 10 RO is not observed in the blocked configuration.

- Although the spectra of outlet duct array for the blocked configuration is better correlated than the open configuration, multiple broadband and narrowband features in the ranges of 0.32-1.8 kHz, 2-3.5 kHz, 3.8-5 kHz and 6.5-9 kHz can be spotted in the outlet duct spectra of the blocked configuration. The first two broadband elevations are in the 'whoosh' noise frequency range, while the latter is consistently seen in the inducer and diffuser spectra. Furthermore, the presence of these broadband features makes the blocked configuration relatively noisier than the corresponding open configuration.

- Broadband corresponding to TCN which is observed in the spectra of the open configuration is not clearly identifiable in the spectra of the blocked configuration as it seems to be masked by the dominant broadband noise.

- Broadband elevation marked as 'I', identified in the spectra of the open configuration is relatively weaker in the spectra of the blocked configuration, implying its expected propagation within PS cavity.

The comparison of two compressor configurations operating near surge indicates that the PS casing treatment helps in improving the acoustic characteristics of the system. For the investigated iso-speedline, the compressor with the PS design demonstrated lower broadband noise features, including 'whoosh' noise, as well as relatively lower overall noise levels. The noise levels within the plane wave region are relatively similar for the inlet duct while significantly higher levels are seen in the outlet duct of the blocked configuration. The results point out that the alleviation of blockage in the blades passages by the PS design helps with the

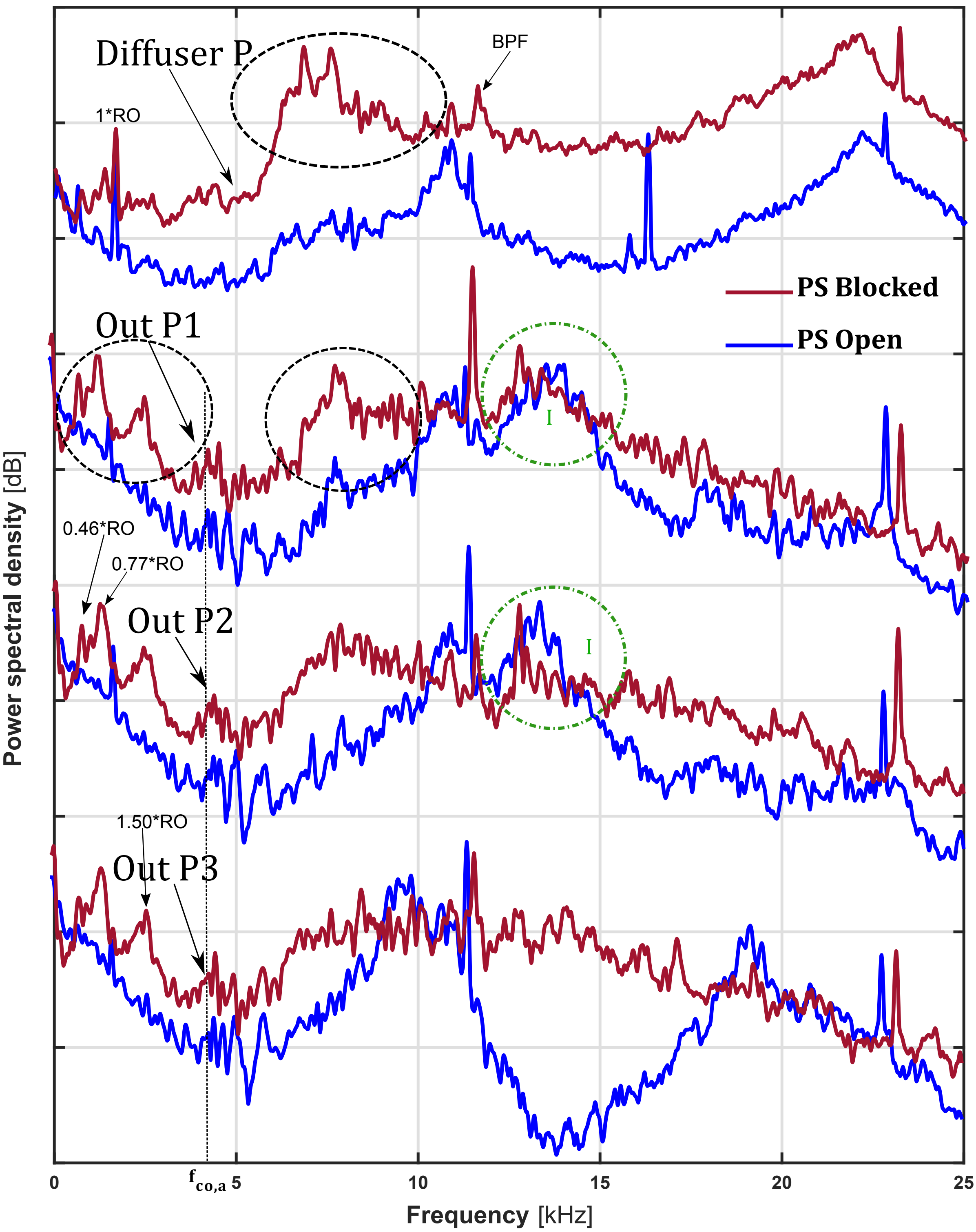

Fig. 2.15 Comparison of the pressure spectra computed from the probes located at the impeller downstream region for the open (blue) and blocked (red) compressors configuration operating at their respective near surge conditions of 99 krpm speedline. Y-axis differences are arbitrary, although the scale is kept at 20 dB per division.

Table 2.2 Differences in the overall sound pressure levels of PS open and blocked compressor configuration.

$\Delta_{f,l} = \mathrm{SPL}_{\mathrm{open}} - \mathrm{SPL}_{\mathrm{blocked}}$ [dB]					
Operating point	Frequency range [kHz]	Location			
		Δ Ind	Δ In	Δ Dif	Δ Out
99 krpm - Design	Plane wave region[4]	-10.7	0.5	1.6	-1.8
	BPF: 0.2 - 11.6	5.4	12.1	-4.2	-1.8
	0.2 - 25	22.7	12.4	-10.6	0.7
99 krpm - NS	Plane wave region	-0.8	1.2	-5.5	-5.3
	BPF: 0.2 - 11.6	3.6	2.8	-13.2	-3.3
	0.2 - 25	8.3	1.7	-13.8	-2.7
130 krpm - Design	Plane wave region[5]	2.8	0.2	0.4	0.7
	BPF: 0.2 - 15.33	3.9	9.6	2.9	11.6
	0.2 - 35	-0.3	10.5	-0.7	12.0
130 krpm - NS[6]	Plane wave region	1.4	6.3	0.4	2.6
	BPF: 0.2 - 15.33	8.8	9.7	-0.6	6.4
	0.2 - 35	2.6	4.6	-11.9	2.5

reduction of broadband noise sources. The flow mechanism of the broadband elevation in the range of 6-8 kHz in the spectra of blocked configuration needs further investigation. Also, the PS casing design is likely causing a broadband noise feature (marked as 'I') and tonal noise at 10 RO in the spectra of the outlet duct and diffuser respectively.

To quantify the differences in the investigated compressor configurations, the overall amplitude of sound pressure level spectra within specific frequency limits are computed from the root mean squared averaged of the pressure signal filtered using bandpass filter for the specified frequency range. Alternatively, the overall levels between frequency bounds f_1 and f_2 can also be computed directly from the spectra by

$$\mathrm{SPL}_{f_1-f_2} = 10\log_{10}\left(\sum_{i=f_1}^{f_2} 10^{\mathrm{SPL}_i/10}\right) \tag{2.11}$$

[4]Frequency bounds of the plane wave propagation for 99 krpm speedline are approximated to be 0.2-2.5 kHz and 0.2-4.0 kHz for inlet and outlet duct respectively.

[5]Frequency bounds of the plane wave propagation for 130 krpm speedline are approximated to be 0.2-2.5 kHz and 0.2-4.5 kHz for inlet and outlet duct respectively.

[6]These differences between the overall levels of open and blocked configurations for NS operation at 130 krpm speedline should be interpreted with caution as the points are not acoustically similar.

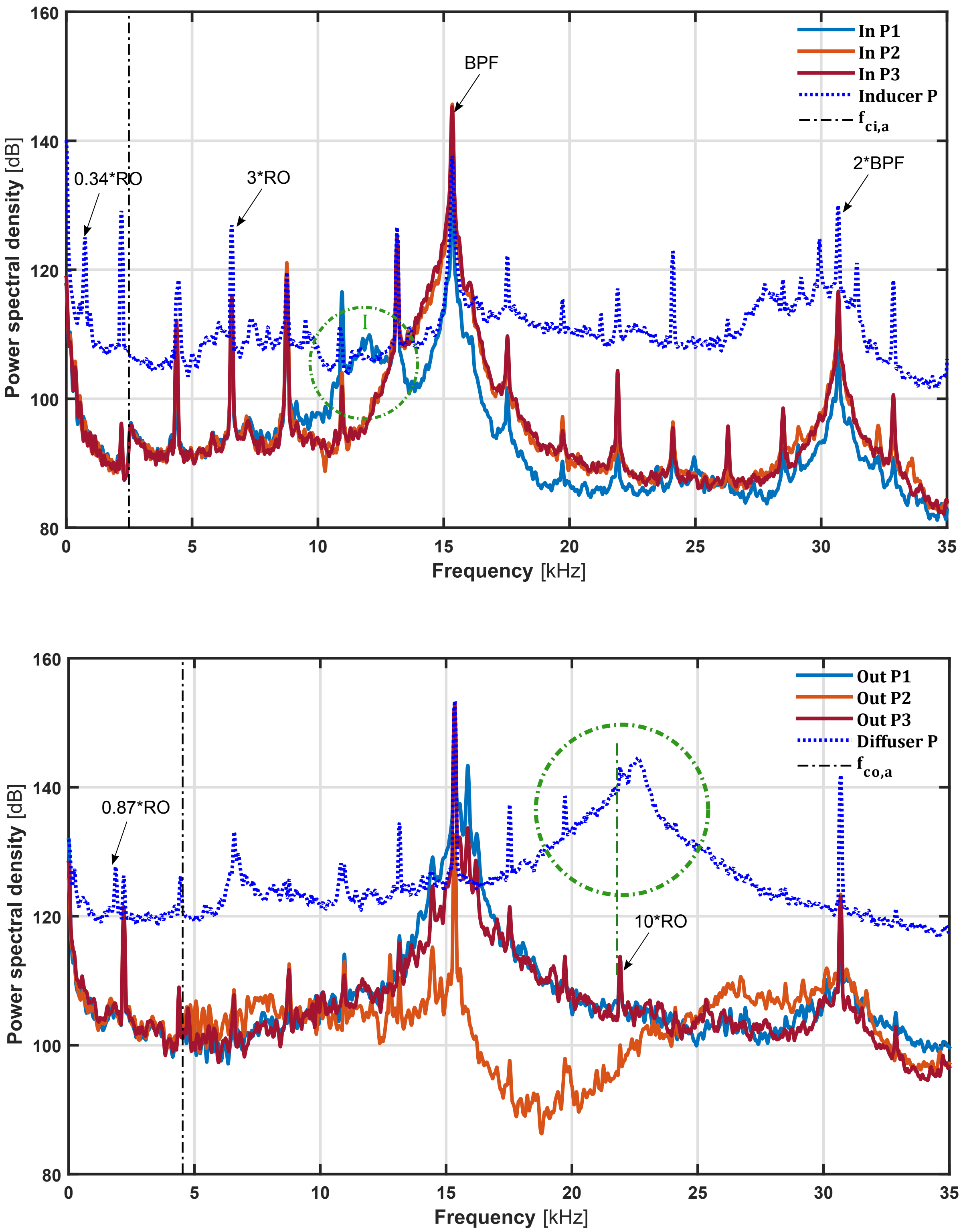

Fig. 2.16 Pressure spectra of the probes located upstream (top) and downstream (bottom) of the impeller for open compressor configuration operating at the design condition of 130 krpm speedline. Former corresponds to inducer and inlet duct array while latter includes diffuser and outlet duct array.

The difference in the overall levels between the PS open and the PS blocked compressor configurations within specified frequency limits (f) at particular location (l) i.e. $\Delta_{f,l} = \text{SPL}_{\text{open}} - \text{SPL}_{\text{blocked}}$ for various operating conditions are presented in Table 2.2. The frequency limits includes approximate plane wave regions, BPF and full spectrum while the locations included inducer probe, inlet duct probes, diffuser probe and outlet duct probes. The values for the inlet and outlet duct location are obtained by averaging the individual values of the sensor arrays.

2.5.2 130 krpm speedline

Acoustic characterisation of the open and blocked compressor configurations operating at the 130 krpm speedline is intended to serve two objectives. Firstly, comparing the acoustic spectra of the 130 krpm with the 99 krpm speed line would help in understanding the evolution of the acoustic behaviour with an increase in operational speed. Secondly, the impact of the PS design at higher speeds is explored by comparing the spectra of open and blocked compressor configurations operating at 130 krpm. It must be noted that the design states of two speedlines for both configurations are aerodynamically similar. Therefore, the inferences on the impact of operational speed and PS cavity can only be made by comparing the spectra of design points for 99 krpm with the 130 krpm speedline, and open and blocked configurations operating at 130 krpm respectively. The deviation in the near surge spectra of the two speedlines for both configurations are not only dependent on operating speed but on the different aerodynamic conditions too. Therefore, the direct comparison between the near surge states of the 99 krpm and 130 krpm speedlines is not correct. In this work, the near surge spectra are only used to draw a broader understanding instead of quantifying the impact of operation speed.

PS open configuration

The spectra of the various probes for the compressor operating at the design and near surge conditions of 130 krpm iso-speedline are presented in Figure 2.16 and Figure 2.17 respectively. The spectra of two iso-speedlines are similar in trend, with the higher speedline showing an increase of 5-10 dB in the overall levels. Furthermore, the noise features, both tonal and broadband are seen to have shifted with the change in operation speed.

The impact of operational speed on acoustic emission for design operation inferred from comparing the spectra of 99 krpm (Figure 2.9), and 130 krpm iso-speedlines (Figure 2.16) are listed below:

- The RO or ‘buzz-saw’ tones are accentuated in the inducer spectrum with an increase in rotational speed. Furthermore, the low-frequency tonal noise observed at 0.66 kHz

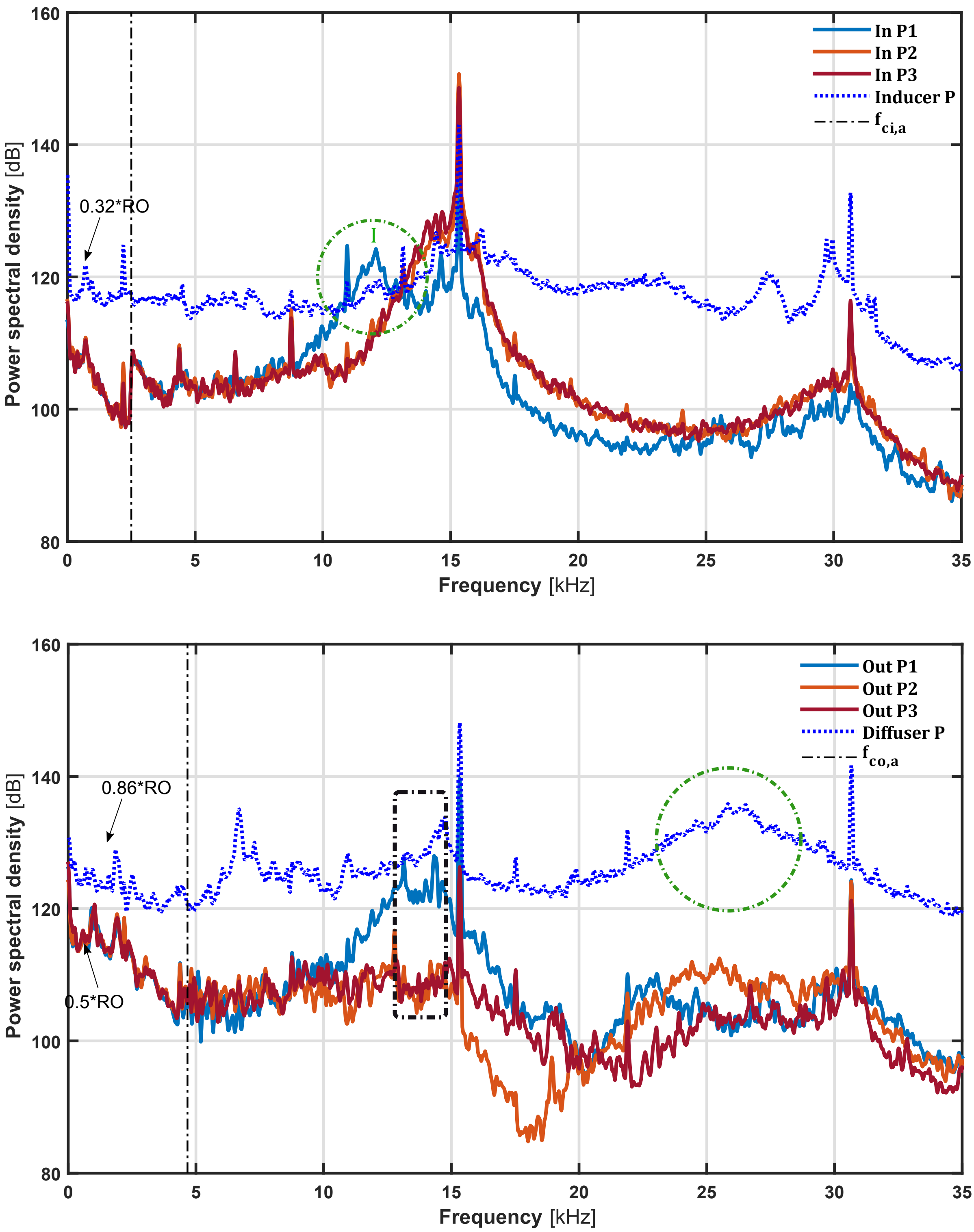

Fig. 2.17 Pressure spectra of the probes located upstream (top) and downstream (bottom) of the impeller for open compressor configuration operating at the near surge condition of 130 krpm speedline. Former corresponds to inducer and inlet duct array while latter includes diffuser and outlet duct array.

(0.4 RO) in the spectrum of 99 krpm speedline is seen to be shifted to 0.74 kHz (0.34 RO) in the spectrum 130 krpm speedline.

- The spectra of the piezoelectric sensor forming inlet duct array showcase similar trends as seen in the lower speedline, with the spectra of second and third sensors strongly correlated while some deviations can be observed in the spectra of the first sensor. Furthermore, a broadband elevation at 13.7-15.7 kHz (marked as 'I') observed in the spectra of the second and third inlet sensor of lower speedline seems to have shifted in the range of 10-14 kHz for 130 krpm speedline and is only observed in the spectra of first inlet sensor.

- The spectrum of the diffuser probe also shows higher tonal content with the increase in rotational speed. In addition to that, the lower frequency tonal peak has shifted from 0.66 kHz to 1.87 kHz with an increase in speed. Furthermore, a similar trend is seen with the shift in the broadband elevation centred on 18.8 kHz for the lower speedline to 22.6 kHz for the higher speedline.

- The spectra of the outlet duct array for the higher speed line show deviations in correlation as compared to the lower speed line. Also, broadband elevation seen in the range of 12.5-14.5 kHz in the outlet spectra of the lower speed line is not existent in the corresponding spectra of higher speedline. Analysis of the compressor configurations at the lower speedline pointed to the role of the PS cavity in the presence of this broadband. Therefore, further exploration of the causes of non-existence of this broadband is required.

As mentioned before, the direct comparison of the spectra of near surge points does not present an accurate impact of the rotational speed on the emission spectra for near surge operation. Nevertheless, the following points can be made by comparing the near surge spectra of 130 krpm (Figure 2.17) and 99 krpm (Figure 2.10) speedlines:

- Although an increase in the tonal content is observed in the inducer spectrum of higher speed line, the broadband (marked as 'II') in the inducer spectrum of the lower speedline is shifted and observed faintly for the higher speedline. As this broadband was expected to be associated with the interaction of the flow in PS cavity, the reasons for its fading needs further investigation.

- Similar to the design point, the broadband marked as 'I' in the inlet duct spectra of the 99 krpm speedline is shifted in the inlet duct spectra of the higher speed line.

- Similar to the design point, the shifts in the tonal and broadband noise features are seen with the increase in the rotational speed. Furthermore, broadband marked as 'I' in the outlet duct spectra of the lower speed line is also not observed in the corresponding spectra of the higher speed line.

The results clearly show an increase in overall noise levels and tonal content with an increase in the rotational speed for the operation of the compressor at design conditions. The increase in tonal noise is expected, as the higher tip speed would lead to severe transonic conditions and shock waves attached to the blade in the rotor alone pressure field. The shifts and decrease in the strength of the features associated with the recirculating flow in the PS cavity are expected due to the decreased flow recirculation in the PS cavity at higher operating speeds as shown by Sharma et al. [5]. This would be further explored with the aid of numerical results.

PS blocked configuration

The spectra of the PS blocked, and open compressor configurations operating at design conditions are compared in this section to understand the impact of PS casing treatment at higher operating speed. The spectra of the probes located upstream of the impeller are compared in the Figure 2.18 while Figure 2.19 shows the spectra of the probes positioned downstream of the impeller.

In contrast to the lower speedline (99 krpm), the differences in the noise generated by the compressors (inducer and diffuser spectra) for two configurations are insignificant. The expected reduction of the propagation of the tonal noise in the upstream impeller direction for the blocked configuration can be observed in the spectra of inducer and inlet duct probes. This reconfirms the role of the PS design in the upstream propagation of RO or 'buzz-saw' tones for the design operation of the compressor. The spectra of the probes positioned downstream of the impeller also shows similar results with insignificant impact on the overall levels, specifically within the plane wave region. Broadband elevation in the range of 6 - 8 kHz observed in the diffuser spectrum of the open configuration is not present in the corresponding blocked spectra. In addition to that, a low-frequency tone at 0.86RO is also observed only in the inducer spectrum of the open configuration. The outlet duct spectra indicate a quieter operation of the blocked configuration in the mid-frequency range of 10 – 20 kHz. While the impact of PS is limited to tonal propagation for the design condition, significant broadband impact is expected for near surge operating conditions. Again, the decreased impact of PS at higher operating speed can be attributed to the reduced flow recirculation via PS cavity but the flow mechanism underlying this reduced acoustic impact for higher speeds demands further exploration.

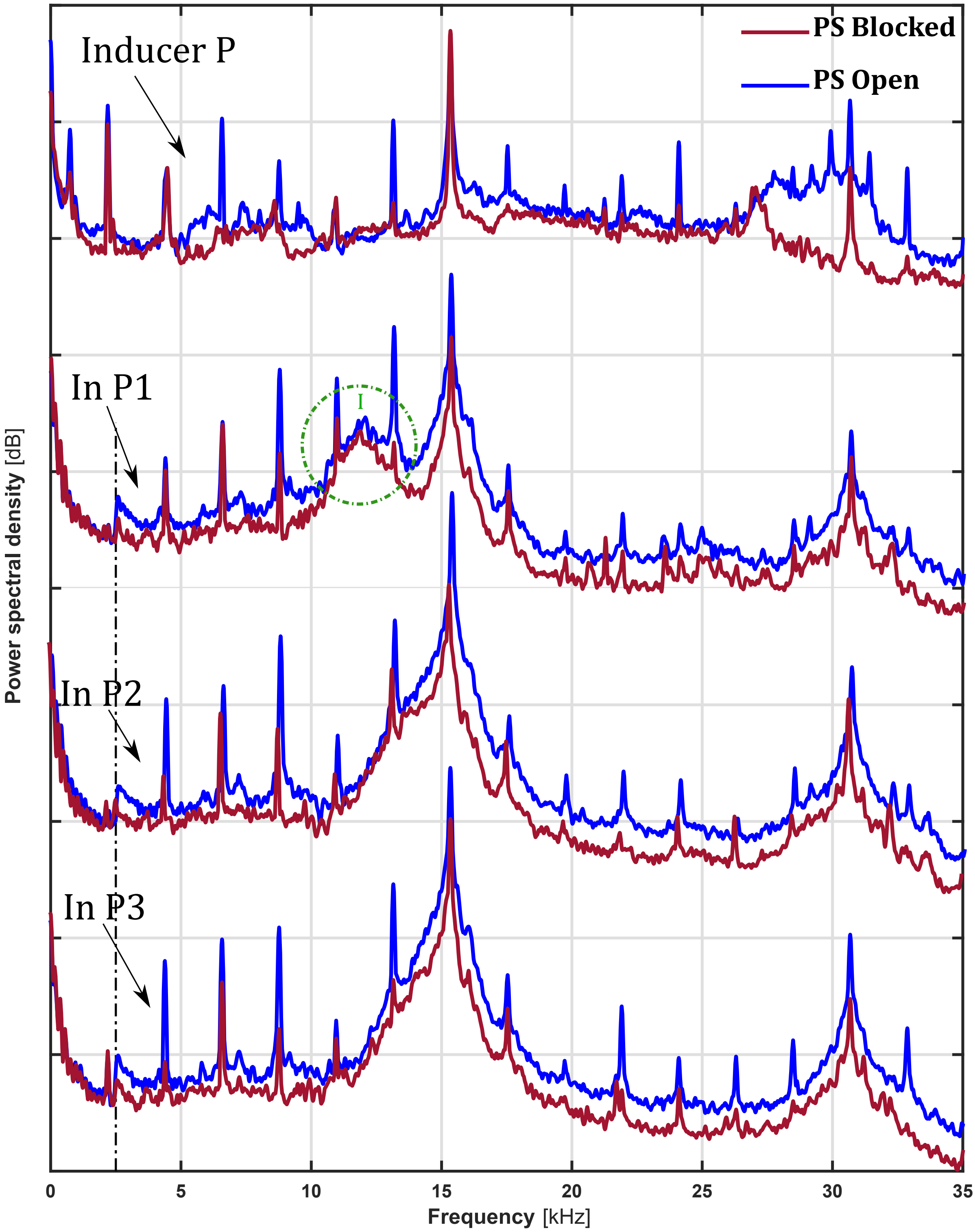

Fig. 2.18 Comparison of the pressure spectra computed from the probes located at the impeller upstream region for the open (blue) and blocked (red) compressors configuration operating at their respective design conditions of 130 krpm speedline. Y-axis differences are arbitrary, although the scale is kept at 20 dB per division.

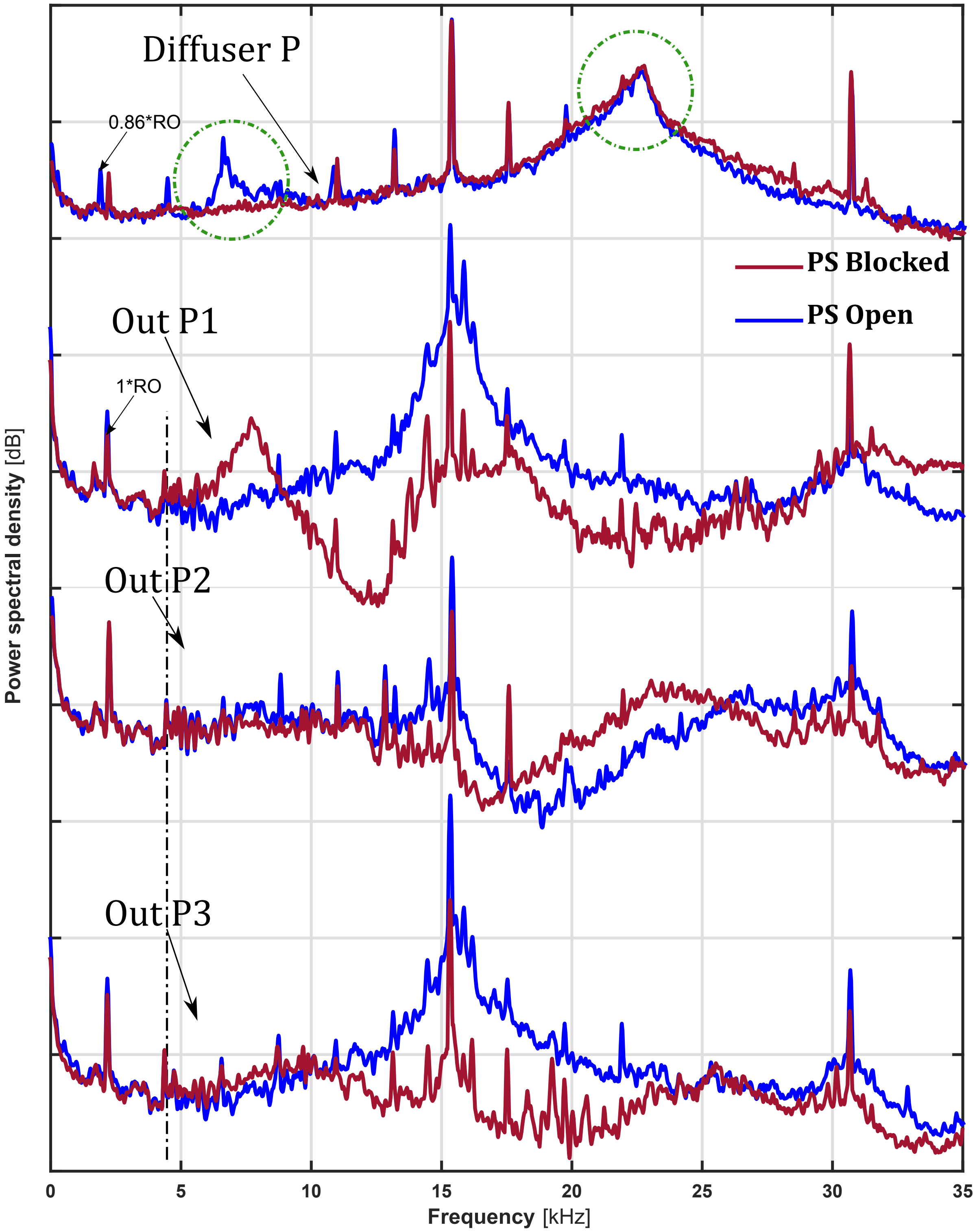

Fig. 2.19 Comparison of the pressure spectra computed from the probes located at the impeller downstream region for the open (blue) and blocked (red) compressors configuration operating at their respective design conditions of 130 krpm speedline. Y-axis differences are arbitrary, although the scale is kept at 20 dB per division.

2.6 Conclusions

The experimental campaign to characterise the acoustic behaviour of the compressor is presented in this chapter. The impact of PS casing treatment on the acoustics of the compressor is evaluated using open and blocked compressor configurations. Aerodynamically similar design and near surge operating points on the 99 krpm speedline for the two compressor configurations are selected for acoustic measurements. Additionally, the impact of operational speed on the acoustics is quantified by comparing aerodynamically similar operating points across 99 krpm and 130 krpm speedlines.

In-duct noise measurement method is used to characterise the acoustic emission of the compressor. The noise generated in the compressor is quantified by measuring pressure fluctuations near the inducer and diffuser while propagation of the generated noise is computed from an array of piezoelectric sensors in the inlet and outlet ducts. In addition to that, acoustical beamforming and MoC are introduced to decompose the pressure wave into corresponding forward and backward components in order to resolve sound intensity. Enhanced spectral content coming out of the compressor, computed from pressure wave decomposition, will be used to assess the credibility of numerical results in Chapter 3 of this thesis. Furthermore, the acoustic flow bench and the corresponding instrumentation used to characterise the compressor are described.

The inducer spectra for the design conditions are dominated by tonal noise which includes RO or 'buzz' saw tones and harmonic of BPF. The upstream propagation of tonal noise in the open compressor configuration can be identified in the spectra of the inlet duct while downstream propagation of these tones is limited, with only a few RO tones and BPF being observed in the diffuser spectrum. Although flat, an interesting broadband feature (marked as 'II') is identified in the diffuser spectrum. This is expected to be caused by the interaction of the swirling flow with the volute tongue. The spectra of the inlet and outlet duct arrays follow the general trends observed in the corresponding inducer and diffuser spectra with a few deviations caused by propagation effects. The broadband feature 'II' observed in the diffuser spectrum is not seen to be propagated to the outlet duct. Additionally, broadband features highlighted as 'I' are also observed in the inlet and outlet duct spectra. The broadband feature observed in the inlet duct is expected to be caused by three-dimensional effects introduced by higher order inlet duct modes, whilst the broadband noise observed in the outlet duct is expected to be caused by the propagation effects introduced by the PS cavity.

In contrast to the design conditions, a lack of RO tones is observed in the spectra of the inducer for near surge conditions. The spectra are dominated by broadband content with only BPF as an observed tonal feature. A broadband feature similar to the broadband 'II' seen in the diffuser spectra of the design point is observed in the spectrum of the inducer probe for the open compressor configuration operating near surge. This is expected to be caused by the interaction of swirling flow in the PS cavity with the structural struts. The first RO tone can be observed in the spectra of diffuser point, but the BPF tone is significantly feeble. Similar to the design spectra, broadband features ‘I’ are observed in the inlet and outlet duct spectra for near surge point too. Furthermore, broadband corresponding to TCN can also be observed in the diffuser and outlet duct spectra. Characteristic ‘whoosh’ noise broadband elevation is not observed for the open compressor configuration operating at 99 krpm.

For the design operation, whilst the PS cavity does not significantly alter the overall noise levels of the compressor, an increase of around 3 - 5 dB is seen in the frequency region beyond 10 kHz for the 99 krpm speedline. The casing treatment does seem to propagate tonal noise in the direction upstream of the impeller as seen from the comparison of inlet duct spectra, while the spectra of the outlet duct remain largely unchanged. On the other hand, acoustic characteristics of the compressor operating near surge are positively impacted by the PS casing treatment, causing a reduction of approximately 10 - 15 dB in the range up to blade pass frequency. Various broadband features in the frequency ranges of ‘whoosh’ and TCN that are observed in the inlet and outlet duct spectra of the blocked configuration are alleviated by the PS casing treatment. It is interesting to point out that the comparison of inducer and diffuser spectra of two configurations implies that the noise generated in the impeller upstream region increases while in the impeller downstream region decreases by the use of PS casing treatment. The higher levels of the noise at the inducer probe for open configuration could be due to the direct proximity to the rotating impeller which is not available for the blocked configuration.

Increase in operational speed shows an expected increase in the noise levels, specifically accentuated RO tonal features seen for the design operation. An expected shift in the frequency range of various spectral features due to change in the rotational speed can also be observed in the spectra of the higher speedline. It is interesting to point out that the broadband feature ‘I’ observed in the outlet duct for the operating points on 99 krpm line is not observed for corresponding points on 130 krpm speedline. Furthermore, broadband ‘II’ observed in the inducer spectrum of the near surge for 99 krpm is significantly frail in the corresponding spectrum of 130 krpm speedline. Both of these broadband features are associated with the PS cavity, and their strength decreased as the flow recirculated via PS cavity reduced at higher operating speed.

The impact of PS casing treatment on the compressor operating at design condition on the higher speedline is similar to the lower speedline but with reduced overall deviation. The noise generated for the two configurations at 130 krpm is similar, inferring reduced flow dynamics within PS cavity at higher speedlines.

Chapter 3

Development of numerical model*

Contents

*Content presented in this chapter has been submitted for publication in the following paper:

- Evaluation of modelling parameters for computing flow-induced noise in a small high-speed centrifugal compressor [7]

3.1 Introduction

As stated in Chapter 1, the objectives of this thesis are pursued by characterising near-field spectra of the compressor using three-dimensional CFD. The accurate prediction of the flow-induced noise and corresponding aerodynamic mechanisms are inherently dependent on the capability of the numerical model to accurately replicate flow dynamics of the system. Since the direct approach of modelling flow-induced noise in small high-speed compressors is still in its early stages, a comprehensive evaluation of various crucial parameters of the numerical set-up are undertaken in this chapter. Acoustic characteristics for the design and near surge point of the PS *open* configuration operating at the 99 krpm speedline shown in Figure 3.1 are the subject of this numerical pursuit. The critical decisions on the numerical set-up of the compressor are presented, evaluated and justified from the standpoint of predicting flow-induced noise with reasonable computational efficiency.

On the basis of available literature on the computation of flow-induced noise in turbocharger compressors, a preliminary numerical configuration is proposed and assessed in Section 3.2 and Section 3.3 respectively. The critical parameters of the numerical configuration that include spatial resolution, turbulence modelling and temporal resolution are scrutinised in Section 3.4. The sensitivity of the performance and acoustic predictions for the near surge and design points to these parameters are discussed in Section 3.5 and Section 3.6 respectively. Finally, the relevant findings of this chapter are concluded in Section 3.7.

3.2 Baseline numerical configuration

A preliminary configuration of the numerical model is realised based on the available literature. The various set-up parameters like grid density, timestep size, turbulence formulation and boundary conditions are carefully selected with an intent to achieve high computational efficiency, i.e. to obtain reasonable accuracy with available computational resources. The development of this baseline numerical model is discussed in the following subsections.

Table 3.1 Literature survey of the various numerical parameters crucial to model aerodynamics and noise generation in the compressors. Details of these parameters are covered in Section 3.4

Study	Tip diameter [mm]	Elements [million]	Prism layers [-]	Wheel rotation [-]	Turbulence method [-]	Boundary conditions		Timestep size	
						Inlet	Outlet	°/TS	TS/BP
Fardafshar and Koutsovasilis [109]	-	-	-	static	SAS-SST	-	-	-	-
Sundström and Mihăescu [37]	88	9	10	sliding	LES	pressure	mass flow	1	36
Fontenasi et al. [71]	-	9.6	11	sliding	DES	Mass flow	pressure	0.5	120
Broatch et al. [34]	48.6	9.6	-	sliding	DES	Mass flow	pressure	1	60
Mendonça et al. [39]	-	9	10	sliding	DES	pressure	pressure	1	60
Karim et al. [40]	-	-	-	sliding	LES	pressure	mass flow	-	-
Semlitsch et al. [38]	88	6		sliding	LES	mass flow	pressure	5	7.2
Jyothish Kumar et al. [110]	88	6		sliding	LES	mass flow	pressure	5	7.2
Tomita et al. [111]	50	3.2			URANS $(k-\varepsilon)$			3.6/7.2	20/ 12.5
Guo et al. [112]	182.8	2.5		sliding	URANS $(k-\varepsilon)$	pressure	mass flow	3	20

3.2.1 Literature review

The potential of numerically computing flow-induced noise in turbomachines, specifically for the turbocharger compressor was established by works of Mendonça et al. [39] and Karim et al. [40]. Mendonça et al. [39] computed in-duct noise using a DES approach for modelling turbulence with a timestep corresponding to 1° impeller rotation per iteration. Karim et al. [40] used LES formulation for turbulence in their work. The numerical configuration employed by Mendonça et al. [39] further stimulated the numerical studies of Broatch et al. [34] and Galindo et al. [33], in which a reasonable correlation between numerical and measured acoustic spectra is demonstrated. Fontenasi et al. [71] also used DES to investigate a specific noise seen in the experimental measurements although the comparison of estimated spectra with measured spectra was not presented in the work. Researchers at KTH, specifically Sundström and Mihăescu [37] computed the acoustic characteristics of a turbocharger compressor operating near surge using LES. Again, the direct comparison with the measured spectra was not shown although the credibility of the numerical model is validated using the PIV flow measurements at a plane upstream to the impeller. Fardafshar and Koutsovasilis [109] explored the impact of the ported shroud by modelling the near-field spectra of the compressors using the SST-SAS [113] turbulence model while Möhring's acoustic analogy [114] was used to model noise propagation on to far-field. The impact of the ported shroud was reasonably captured by the numerical model although the comparison between predicted and measured spectra was not presented in this case either.

Other than the aforementioned works, the investigations of Després et al. [108], Guo et al. [112], Tomita et al. [111], Semlitsch et al. [38] and JyothishKumar et al. [110] modelled the compressor using three-dimensional CFD to gain insight on the flow dynamics, specifically stall and/or surge. Although these works are not focused on the flow-induced noise, the numerical configurations can be used to model aerodynamic noise sources.

The various numerical parameters adopted in the aforementioned studies are presented in Table 3.1.

Baseline model

A numerical model of the compressor is built using the packages provided in ANSYS [115, 116] workbench. The digital geometry of the compressor provided by the industrial partner is cleaned up to extract the internal fluid volume. The tip clearance and the impeller backside cavity, i.e. the narrow gap between the impeller and the diffuser back-plate along with oil bearings are included in the model. The complete length of inlet and outlet ducts used in the measurement rig (see Figure 2.6) are not included in the model because of computational intractability,

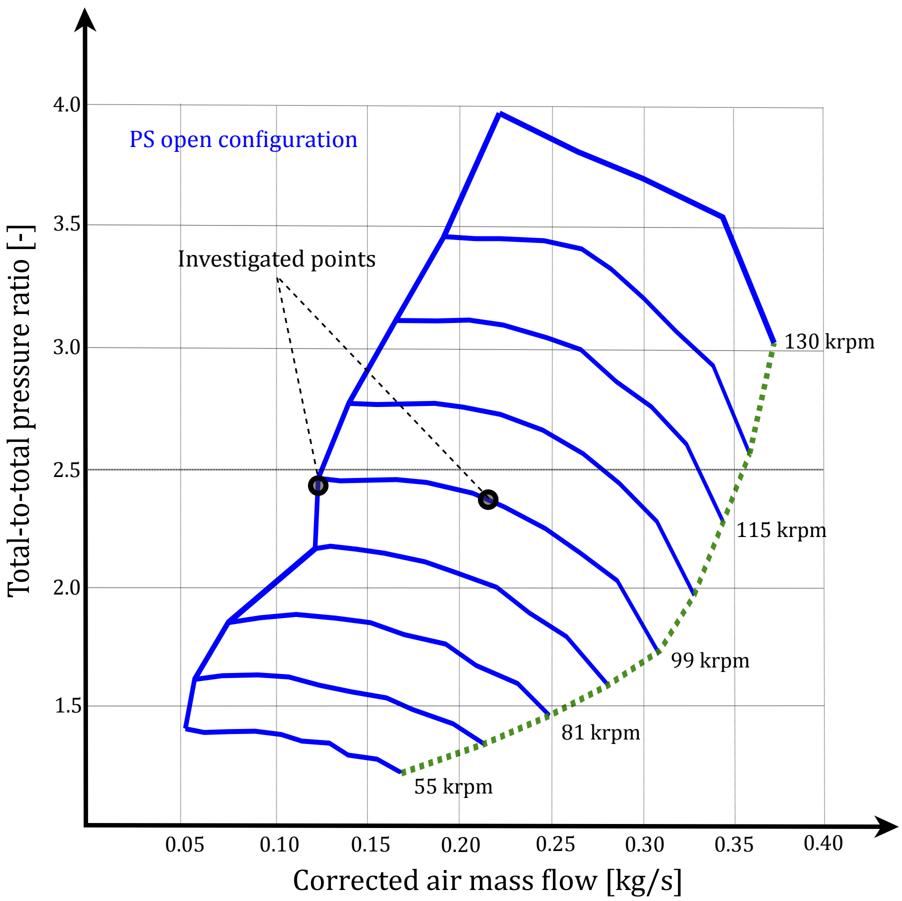

Fig. 3.1 Compressor map marking the design and near surge conditions on which the impact of various numerical parameters are investigated.

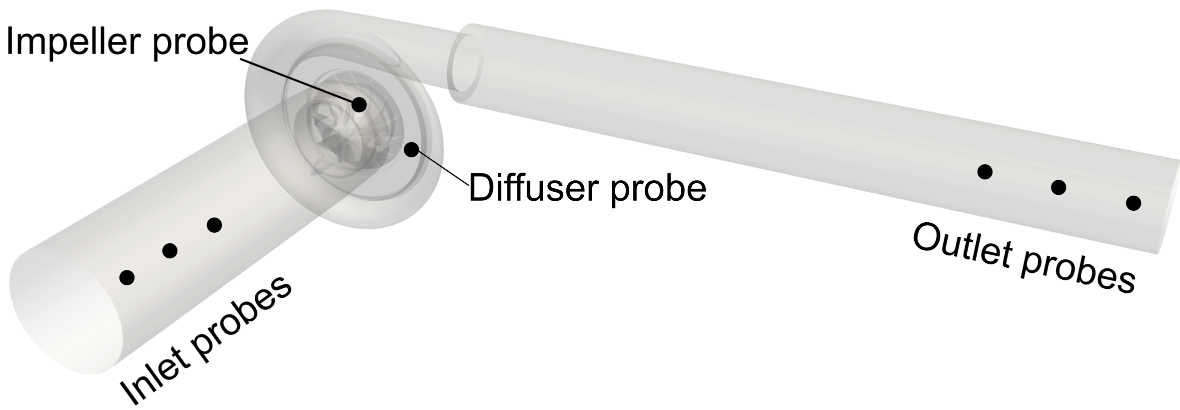

Fig. 3.2 Computational domain along with the location of various virtual pressure probes.

although parts of these ducts equivalent to 4 cross-sectional diameters long are modelled. The intent of including these duct sections is to decrease the impact of the boundary conditions on the mean flow as well as to capture the flow instability that might propagate upstream of the impeller. The modelled domain for the compressor is shown in Figure 3.2.

The computational domain is spatially discretised by an unstructured polyhedral control volume created from the tetrahedral cells generated in the ICEM CFD [115] by the vertex centred numerical approach in ANSYS CFX [116]. A domain size of approximately 10 million is selected on the basis of literature survey presented in Table 3.1. A polyhedral control volume is less diffusive and offers significant accuracy gains compared to an equivalent size unstructured grid of other cell types (i.e. tetrahedral) [117]. Although a structured grid would cause lower numerical diffusion and commensurately higher accuracy at the cost of significantly higher user effort, it can also lead to cells with unavoidably large aspect ratios or heavy skewness in regions of geometric complexity, resulting in unacceptable discretisation error. Furthermore, a polyhedral grid is expected to offer similar accuracy over the equivalent hexahedral grid in the cases where secondary flows are relevant [118], and therefore, off-design operating conditions can be accurately modelled using a polyhedral grid. The model along with a section view of the impeller grid is shown in Figure 3.3. The flow near the wall is resolved using 12 prism or inflation layers, and the height of the first cell was chosen to be $0.0005mm$ as to obtain y^+ values closer to unity for the impeller.

In spite of the prominence of scale resolving methods as the preferred choice for modelling turbulence, the statistical Reynolds averaging approach (U)RANS is selected for the baseline configuration. The limitations of Reynolds averaged approach in predicting broadband aeroacoustic sources for general unsteady flow are well established, but the limitations of the model specifically for predicting flow-induced noise in compressors are not available. Furthermore, the computational efficiency of the URNAS methods makes broader grid sensitivity studies tractable. The flow field is therefore computed by numerically solving the averaged form of unsteady Navier-Stokes equations for each control volume of the computational domain in their conservation form using the CFD coupled solver, ANSYS CFX [116]. The additional terms introduced by averaging, which are the product of fluctuating quantities, are modelled using a two-equation Shear Stress Transport ($k-\omega$ SST) closure model. The SST formulation is widely used in turbo machinery CFD problems due to its ability to accurately represent the boundary layer flow and therefore yields an accurate solution of detaching and swirling flows [119]. The turbulence is assumed to be isotropic with the curvature correction. The air used as working fluid in the compressor is assumed to be a perfect gas with the ideal gas law calculating the local density variation and Sutherland's law approximating the dynamic viscosity.

Table 3.2 Boundary conditions

Case	**Rotating speed** [rpm]	**Inlet** – $p_{in,0}$ [bar]	**Outlet** – $\dot{m}_{out}$ [kg/s]
Design	98529	1	0.211
Near surge		1	0.122

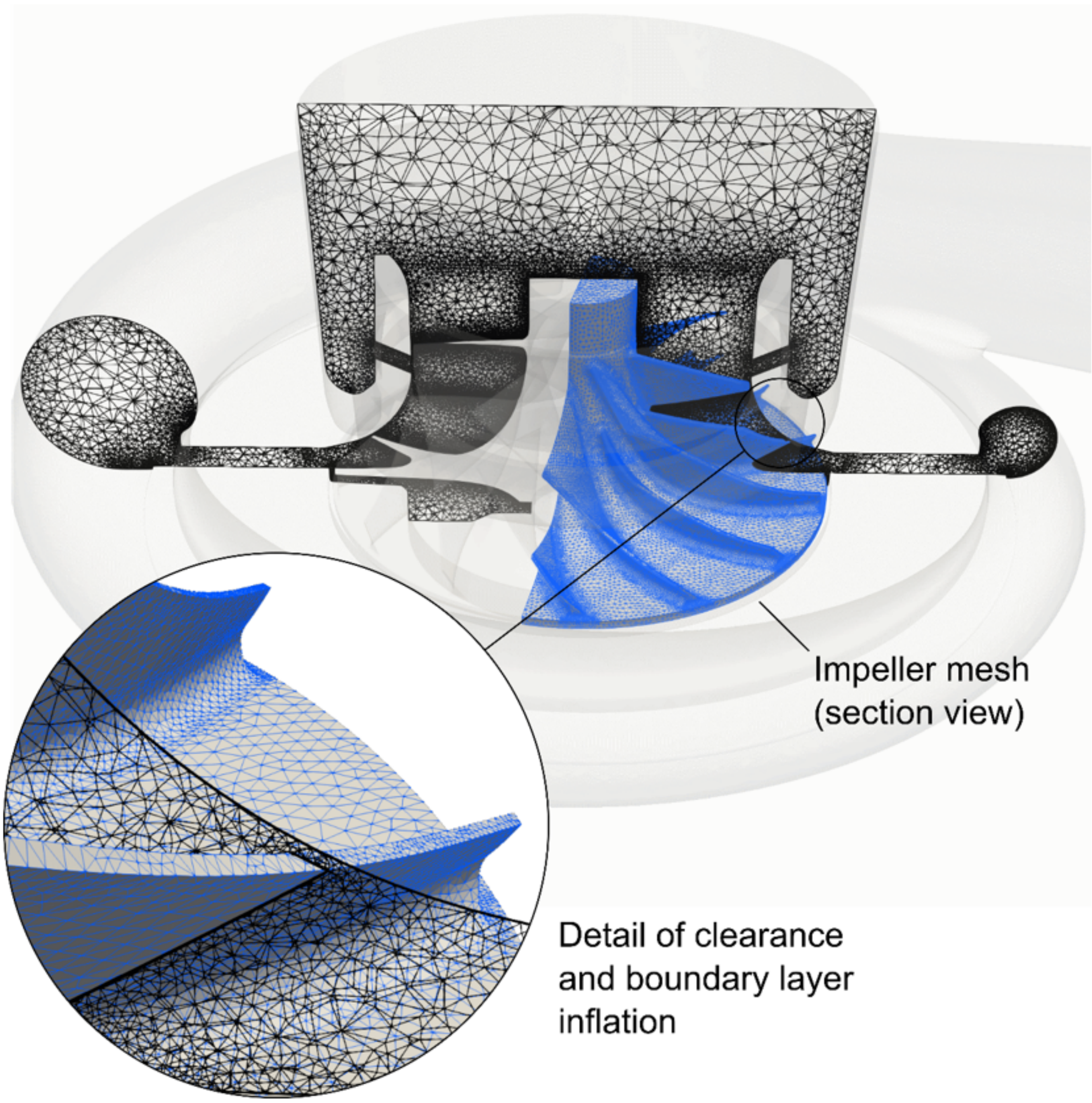

Fig. 3.3 View of the baseline computational grid, highlighting a slice of the fluid mesh and the rotor surface mesh. A detail view shows the clearance between the blades and the shroud along with the boundary layer inflation.

The convective terms are discretised using a blend of second order accurate central difference scheme and first-order upwind scheme to maintain the boundedness of the solution. The impeller motion is modelled using the Rigid Body Motion (RBM) approach, also known as sliding mesh in which the mesh actually rotates every timestep at the transient rotor-stator interface [84]. The time step for advancement is chosen in such a way that the impeller mesh turns by 4° per timestep. Transient terms are discretised using an implicit, second-order accurate scheme implemented in ANSYS CFX [116] as the second order backward Euler scheme. It is worth noting that the transient scheme for the turbulence equations is still first order, and a bounded second order scheme is used for the volume fraction equations. A steady boundary condition, as a combination of the total pressure at the inlet and mass flow rate at the outlet, is used. The values of mass flow rate and pressure used as boundary conditions in the numerical model are determined from the experimental campaign described in Chapter 2. The boundary conditions for the modelled design and near surge operating points marked in Figure 3.1 are presented in Table 3.2. The numerical set-up uses 1% turbulent intensity and a turbulent viscosity ratio of 10 at the inlet section. The effect of heat transfer and surface roughness is neglected by modelling wall as smooth with adiabatic and no-slip boundary conditions. Five inner coefficient loops are used for each iteration to achieve the convergence of residuals up to four orders (10^{-4}).

3.3 Assessment of the baseline numerical configuration

The ability of the numerical configuration described in Section 3.2 to yield meaningful aerodynamic and acoustic predictions is assessed by comparing numerical results with the corresponding experimental measurements. A two-step validation approach is followed in which both performance parameters and pressure spectra predicted by the numerical model are assessed against experimental data.

3.3.1 Performance parameters

Pressure ratio Π_{t-t} and isentropic efficiency η_s described in Equation 2.8 are used to assess the capability of the numerical model to predict the overall performance and behaviour of the compressor. It is worth pointing out that the variables used to compute these performance parameters are averaged over $1s$ in the experimental measurements and $0.08s$ in the numerical results.

The relative difference between experimental and numerical data is quantified using a relative deviation ε value, which for a generic variable ϕ, can be defined as

$$\varepsilon(\%) = \frac{|\phi_{\text{num}} - \phi_{\text{exp}}|}{\phi_{\text{exp}}} 100 \tag{3.1}$$

The comparison of the predicted and measured performance parameters is presented in Table 3.3. The numerical performance parameters are slightly under-predicted, which seems counter-intuitive as the walls are modelled smooth and adiabatic. Literature [120] shows that modelling the impeller backside cavity results in the lower values of the performance variables computed in the numerical model. Nevertheless, the computed results are in close agreement as the deviation from the measured values is within the range of $\pm 1.5\%$. The ability of the baseline model to predict flow-induced noise is assessed in the next section.

Table 3.3 Comparison of the performance parameters predicted by baseline numerical model with the experimental measurements for design and near surge points

Method	Case	Π_{t-t} [-]	η_s [%]	ε_π [%]	ε_η [%]
Experimental	Design	2.35	76.8	-	-
	Near surge	2.47	66.7	-	-
Numerical (Baseline)	Design	2.32	76	1.1	1.1
	Near surge	2.44	66	1.2	1.0

3.3.2 Pressure spectra

As explained in Section 2.4, probes located in the inducer and diffuser region are used to quantify the noise generated by the flow, whilst arrays of three piezoelectric sensors, positioned in each of the inlet and outlet ducts are utilised to measure the in-duct noise. The measured pressure spectra of the inducer and diffuser positions can be directly compared with the numerical spectra of the corresponding virtual probes. Since the whole flow rig could not be modelled due to computational overhead, the inlet and outlet duct spectra are evaluated using the approach presented by Broatch et al. [34] for comparing the characteristics that are measured at different locations. The basis of this approach is to decompose the pressure waves measured from the duct array into corresponding forward and backward components using the beamforming method that has been thoroughly discussed in Section 2.3. Two arrays of virtual probes (see Figure 3.2) created by following the recommendation of Piñero et al. [121] were positioned on the inlet and outlet duct of the model to emulate the arrays used in the measurements.

The pressure-time trace of a point obtained as the solution of the numerical model is used to compute Pressure Spectral Density (PSD) as described in Section 2.4. The pressure spectra of the near surge and design conditions are evaluated in the following subsections.

Pressure spectra of the near surge condition

The experimental pressure signals were measured for 1s while numerical data is computed only up till 0.1s of which 0.02s is treated as initial transient. Therefore, the both experimental and numerical pressure data were resampled and experimental data was interpolated in accordance with the time trace of the numerical data for computing PSD. The resampling of the data is achieved by detrending to compute the fluctuations (x_i') around the mean ($\bar{x}$) for the complete time series (x_i) using Equation 3.2. The spectra computed from the original experimental pressure up till 1s and the resampled pressure trace of 0.08s are similar as demonstrated in Figure 3.4.

$$x_i' = x_i - \bar{x} \tag{3.2}$$

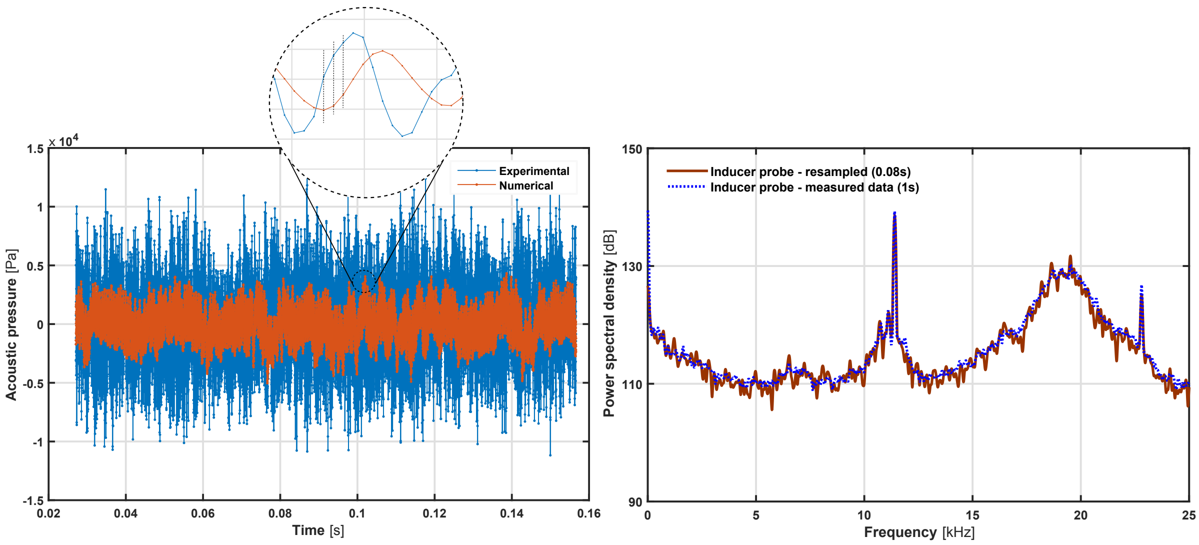

Fig. 3.4 Resampled and interpolated values of the experimentally measured pressure for inducer probe (left). The comparison of the inducer pressure spectra obtained from measured pressure data for 1s and resampled data up till 0.08s (right).

In Figure 3.5, the near surge pressure spectra for the inducer and diffuser probes obtained from baseline numerical configuration are compared with the experimental results. The overall amplitudes and the decay of the spectra are not well predicted by the baseline numerical model. In addition to that, the broadband elevation in the inducer spectrum which is hypothesised to be caused by the flow recirculating in the PS cavity is also not captured by the baseline

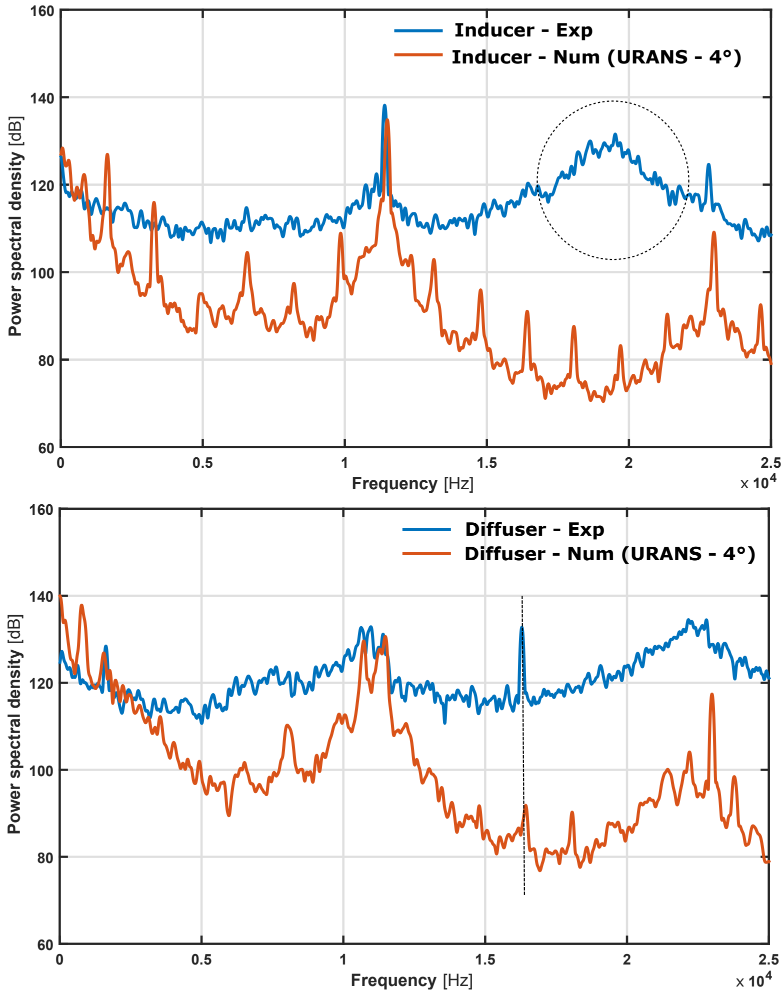

Fig. 3.5 Comparison of the inducer (top) and diffuser (bottom) PSD predicted by the baseline numerical model with the experimentally measured values for near surge operation. The broadband feature (highlighted) in the spectrum of the inducer probe is not captured by the numerical model.

numerical model. Overall trend and dominant features like BPF are reasonably reproduced in the numerical spectra of both positions.

As stated before, the comparison of duct spectra is made using the decomposed pressure wave obtained from the beamforming based method for plane wave region. An attempt to assess the duct spectra at higher frequencies is made by computing the numerical duct spectra from the pressure wave components obtained using MoC and comparing that with the experimental spectra from one of the sensors of the piezoelectric array. The duct spectra up till plane wave range for the near surge point obtained using beamforming and MoC are presented in Figure 3.6 (left). The spectra computed from experimental pressure signals and the corresponding beamformed experimental signal are also demonstrated to be well correlated for both ducts. The spectra of the inlet duct obtained by beamforming and MoC are observed to be well correlated to each other as well as in a reasonable agreement with the experimental spectrum, although fluctuations can be seen. On the contrary, the numerical spectra obtained by beamforming and MoC are not in agreement for the outlet duct. This is expected to be caused by the high swirl present at the outlet which leads to differences in the flow at individual sensors of the virtual beamforming array. Thus, the individual thermodynamic variables vary too significantly across the outlet array to give any credible beamforming results. Furthermore, the numerical spectrum obtained by MoC is in a good agreement with the experimental spectrum, specifically beyond 1000 Hz.

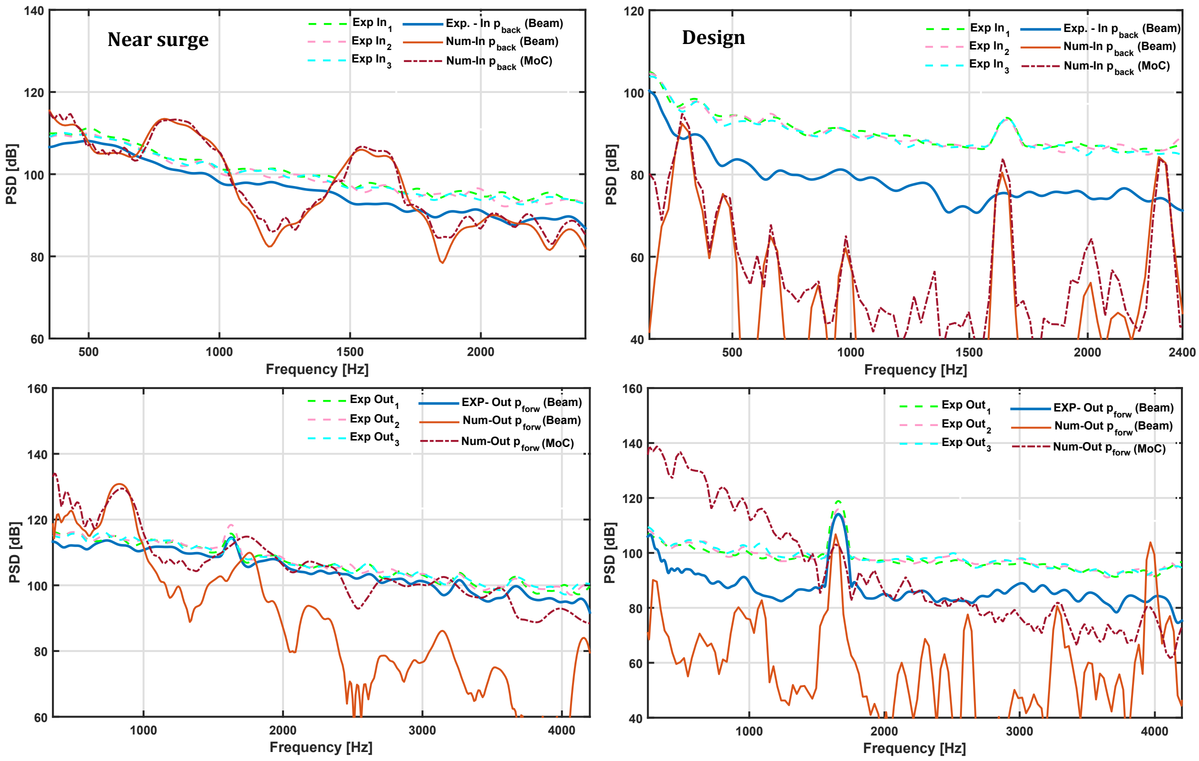

Fig. 3.6 Comparison of the inlet (top) and outlet (bottom) duct spectra up till plane wave limit, obtained from the beamforming of numerical and experimental data for both near surge (left) and design (right) conditions.

The beamforming based pressure decomposition method is demonstrated to be a useful method for enhancing the spectral content coming out of the compressor. Nonetheless, the beamforming method is limited by the plane wave constraints specified in Section 2.3, beyond which the numerical and experimental spectra cannot be compared using this method.

In Figure 3.7 (left), the spectra of the MoC pressure components are compared with the corresponding experimental spectra obtained from the individual probes. The spectra obtained from the MoC pressure components of each sensor of the virtual array were similar, and therefore, the first sensor of each array is used for the comparison. The results for both inlet

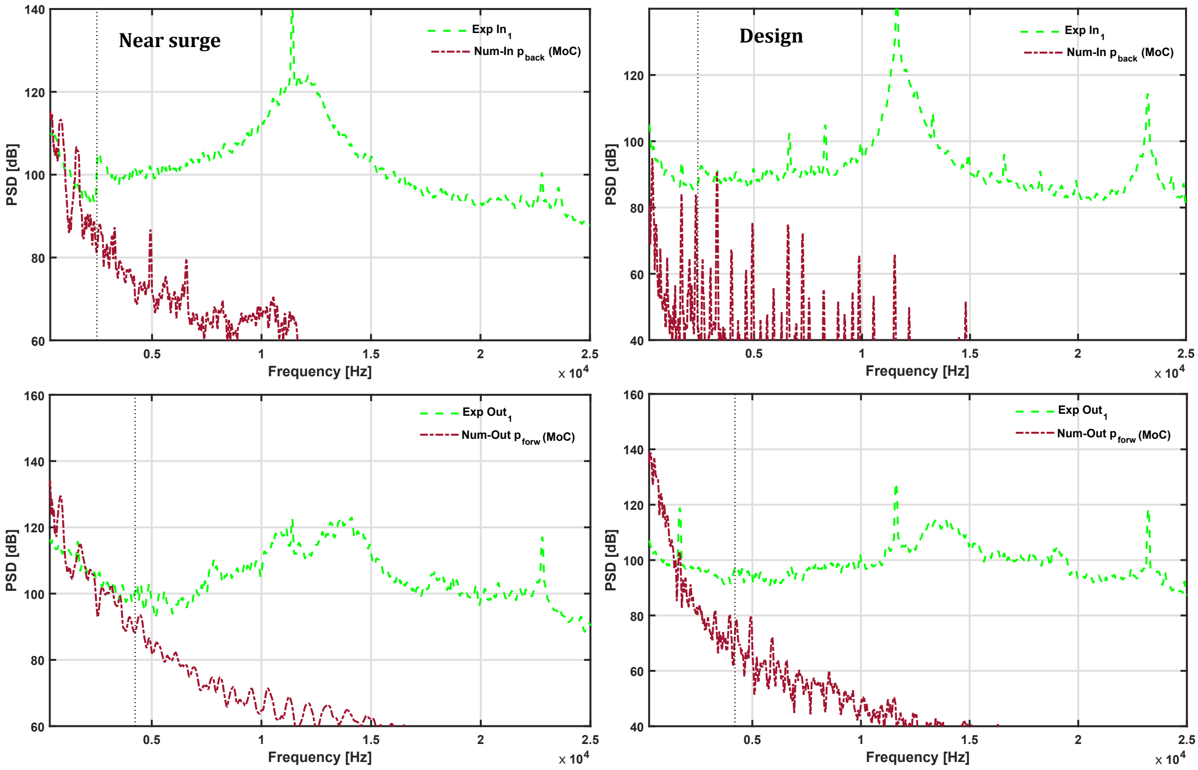

Fig. 3.7 Inlet (top) and outlet (bottom) duct spectra obtained by the MoC of numerical data and from the first sensor of the experimental duct array are compared for near surge (left) and design (right) conditions.

and outlet duct are not in agreement with the experimental data. The numerical spectra are seen to decay after the plane wave region and any features beyond that are not adequately captured by the baseline numerical configuration.

Pressure spectra of the design condition

The numerical and experimental spectra of inducer and diffuser probes for the design condition are compared in Figure 3.8. Similar to the near surge spectra, overall amplitudes are not well captured by the numerical model. Tonal features, including the ‘mid-tones’ that are seen in between the two RO tones, are heavily accentuated in the numerical spectra as compared to the measured spectra. Furthermore, broadband elevation in the diffuser spectra, which is hypothesised to be caused by the interaction of diffuser outlet flow with the volute tongue, is also not observed in the corresponding numerical spectra. Overall trend and dominant features like BPF and RO tones are reasonably captured in the numerical spectra of inducer and diffuser probes.

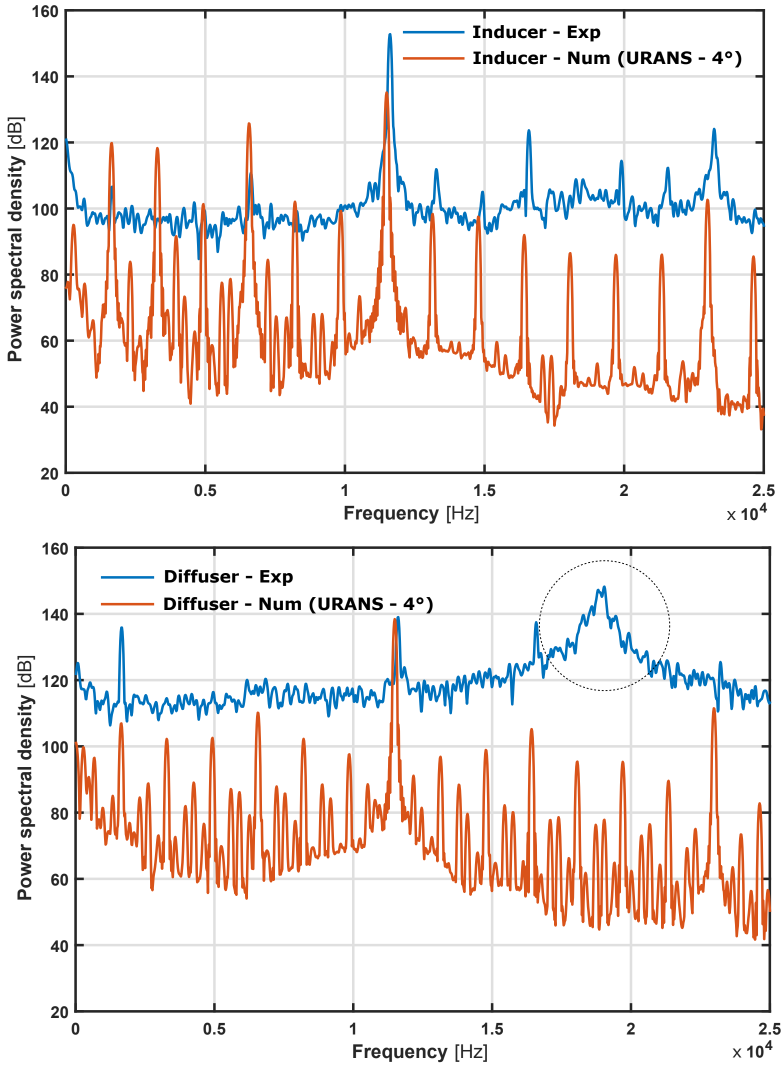

Fig. 3.8 Comparison of the inducer (top) and diffuser (bottom) PSD predicted by the baseline numerical model with the experimentally measured values for design operation. The broadband feature (highlighted) in the spectrum of the diffuser probe is not captured by the numerical model.

The low-frequency spectra up till the plane wave limit, and high-frequency spectra obtained using the method similar to the near surge case are presented in the Figure 3.6 (right) and Figure 3.7 (right) respectively. Contrary to the near surge condition, low-frequency spectra computed using both beamforming and MoC are in poor agreement with experimental spectra. The differences between the overall levels for both inlet and outlet duct spectra are significantly large as observed in Figure 3.6. Similar to the results of near surge state, the pressure spectra of the beamformed and MoC pressure components are correlated for the inlet duct while significant deviations are seen for the outlet duct. Furthermore, the agreement between measured and numerical spectra at higher frequencies is not good due to the abrupt decay of the numerical spectra beyond the plane wave limit.

To summarise, the overall trends and dominant features for inducer and diffuser probes can be reasonably replicated by the baseline numerical model, but significant deviations are seen in terms of overall levels. Broadband elevation in the inducer and diffuser spectra of respective near surge and design operation is not captured by the numerical model. Pressure decomposition methods are shown to be useful for comparing duct spectra within the plane wave limit, but correlation among numerical and measured duct spectra at higher frequencies is poor. Interestingly, characteristics of near surge operation are captured better than corresponding features of design operation.

3.4 Evaluation of numerical set-up

In an effort to improve the credibility of acoustic predictions, various parameters and decisions on the numerical configuration are scrutinized in this section.

3.4.1 Wheel rotation approach

The approach to model the impeller motion in turbomachinery CFD is one of particular importance. The primary methods to model wheel rotation are Multiple Reference Frame (MRF) and Rigid Body Motion (RBM). Multiple reference frame as the name suggests uses different coordinate systems to solve the flow equations for rotating and stationary zones. In this method, the impeller does not actually rotate and instead a coordinate system is used that rotates with the constant speed of wheel rotation. For the rotor region, the equations are solved in a rotational reference frame with Coriolis and centrifugal forces introduced as the source terms in the momentum part of Navier-Stokes equation. A steady-state solution obtained by neglecting time varying terms, along with the MRF approach can reduce computational effort by an order of magnitude as compared to transient simulation.

The domain interfaces, defined as a thin surface with mass and momentum set to conservative interface flux [116], are used to split the rotating (Impeller) and stationary zones (inlet and diffuser). The interface model then defines the way that the solver models the flow physics across the interface. The multiple reference frame approach can be employed as either the Frozen rotor [116] or Stage [116] frame change model in ANSYS CFX [84]. In the Frozen rotor model, the relative orientation of the components across the interface is fixed, and the two frames have a fixed relative position throughout the calculation. On the other hand, in the Stage model, instead of assuming a fixed relative position, a circumferential averaging of the fluxes on the interface is performed. The Frozen rotor approach is better suited for modelling the compressor [122] as the flow distortion caused by volute tongue and other asymmetric features like struts in the PS cavity can be preserved. While the works of Hillewaert and Van den Braembussche [123] and Liu and Hill [124] discussed the errors induced by the MRF approach, Zheng et al. [125] and Sharma et al. [5] demonstrated the capability of steady-state simulations using the MRF approach to model the performance of the compressor. Furthermore, an increase in deviation from experimental data was observed with an increase in the operational speed. Therefore, the authors [125, 5] acknowledged the limited capability of the Frozen rotor model to predict the impeller flow field and recommended the use of unsteady simulations to capture transient effects at higher speeds.

Another method to model the flow inside the compressor is by performing unsteady simulations in which the physical wheel rotation is modelled. This approach of modelling wheel rotation is called RBM, in which the impeller region is actually rotated at each time step and hence, the relative position of the grids on each side of the interface is updated at each time step. In ANSYS CFX [116], RBM is applied by using a transient rotor-stator interface [84]. Due to the increase in available computational resources, the RBM approach is being increasingly explored, and demonstrating an improvement in the agreement between numerical and experimental data [126], especially at higher operating speeds.

The focus of this thesis is on understanding the acoustic features and corresponding flow mechanism in the compressor. The impact of the unsteady flow phenomenon as the sources of noise cannot be neglected in this work; thereby necessitating the use of transient simulations. Although transient simulation limited to statistical turbulence models can be performed with the MRF approach, this would limit the numerical model in predicting features like BPF and RO tones. Therefore, transient simulations with RBM is the preferred configuration for this work.

3.4.2 Boundary conditions

Boundary conditions are the mandatory component of a mathematical model and need to be applied when solving the Navier-Stokes and continuity equations. Boundary conditions direct the motion of the fluid flow and specify various fluxes (mass, momentum, energy) into the computational domain. The standard mathematical boundary conditions are Neumann, Dirichlet and mixed boundary conditions [127]. In the Dirichlet boundary condition, the value of the variable at the boundary is specified, and in the Neumann boundary condition, the gradient of the variable normal to the boundary is specified. The mixed boundary condition is a function obtained by the combination of Dirichlet and Neumann boundary conditions. In this section, the discussion is focused on inlet and outlet boundary conditions as the impact of heat transfer to the surrounding and surface roughness can be neglected [128] for the current problem by modelling walls as smooth using adiabatic and no-slip conditions.

The boundary conditions used in modelling the turbocharger compressor are primarily steady in nature. The usual set of boundary conditions prescribed to model the centrifugal compressor as seen in the literature (see Table 3.1) are:

1. Total pressure and temperature imposed on inlet boundary and static pressure imposed on outlet boundary
2. Mass flow rate on the inlet and static pressure at the outlet
3. Total pressure and temperature on the inlet and mass flow rate at the outlet

The combination of total pressure at the inlet and static pressure at the outlet is sensitive to initial guess [116]. Hence, in this work, the total pressure and temperature are imposed at the inlet boundary, and the mass flow rate is prescribed at the outlet boundary. Furthermore, the ANSYS CFX modelling guide [116] lists the used set of boundary condition as robust.

3.4.3 Grid or spatial resolution

The grid of any computational model should accurately reproduce the geometry to yield credible numerical predictions. The key decisions involved in the spatial discretisation of the compressor model includes determination of the type of the cells for the mesh, number of the cells and extension of inlet and outlet ducts for maximum computational efficiency. In this section, the computational domain of the compressor is assessed to yield credible results by achieving flow solutions independent of mesh. The mesh independence investigation is performed on the baseline numerical model introduced in Section 3.2. The global compressor variables of isentropic efficiency and pressure ratio specified in Section 2.4 are used to assess the dependence of the solution on the mesh. The investigation is performed in two parts; firstly, the ability of the model to resolve the wall/boundary layer flow is evaluated for the design condition. The second step assesses the minimum number of cells required in the mesh to obtain an independent solution for both design and near surge condition.

Near-wall mesh resolution

The flow near the wall is primarily defined by two parameters viz. distance of the first cell's centroid to the wall and the thickness of the boundary layer. These parameters are evaluated in the following subsections.

Distance of the first cell from the wall The near wall region can be divided into the inner layer and the outer layer. The inner layer can be further subdivided into the viscous sublayer which is dominated by viscous shear, and the logarithmic layer which is dominated by turbulent effects. The region between viscous sublayer and the logarithmic layer is called the buffer layer, where both viscous effects and turbulent effects are significant. The near-wall region of a no-slip wall presents large gradients in the dependent variables, as well as the viscous effects on scalar transport processes like momentum transport, is large in these regions [129]. Therefore, it is necessary to accurately model the flow in the near-wall region to yield better numerical predictions of wall-bounded turbulent flows.

The flow in the near-wall region is commonly modelled using two approaches, namely the wall function method and the low Reynolds (Low-R_e) number method. The wall function approach uses empirical relations without resolving the boundary layer to calculate the fluid shear stress as a function of distance from the wall and the flow velocity. The Low-R_e method resolves the boundary layer by using small length scales which requires a high mesh resolution in the near-wall regions. The distance of the first node from the wall is central to the application of either near-wall treatment approaches. A dimensionless wall distance parameter y^+ is used to distinguish the different zones of the flow near the wall.
y^+ is defined as follows:

$$y^+ = \frac{yu_\tau}{\nu} \tag{3.3}$$

where y is the distance of the cell's centroid to the wall, ν is the kinematic viscosity and u_τ is the friction velocity or shear velocity.

Table 3.4 y^+ values for different values of y

y [mm]	**Global y^+ range**	**Impeller y^+ range**
0.001	$0 < y^+ < 4.5$	$0 < y^+ < 4.5$
0.0005 ($y_{baseline}$)	$0 < y^+ < 1.6$	$0 < y^+ < 1.6$
0.0001	$0 < y^+ < 0.6$	$0 < y^+ < 0.6$

The value of y^+ provided by a cell adjacent to the wall is used to decide the switch from logarithmic (log-law of the wall) layer to viscous (linear-law of the wall) sublayer. The region of $y^+ < 5$ is considered to be in the viscous sublayer and the flow in this region can be modelled provided the mesh resolution and turbulence model are appropriate. The cells with $y^+ > 30$ is said to be in the logarithmic layer and log-law is used to determine the flow velocity. The region with intermediate values of y^+ i.e. $5 < y^+ < 30$ is called a buffer layer and neither law is

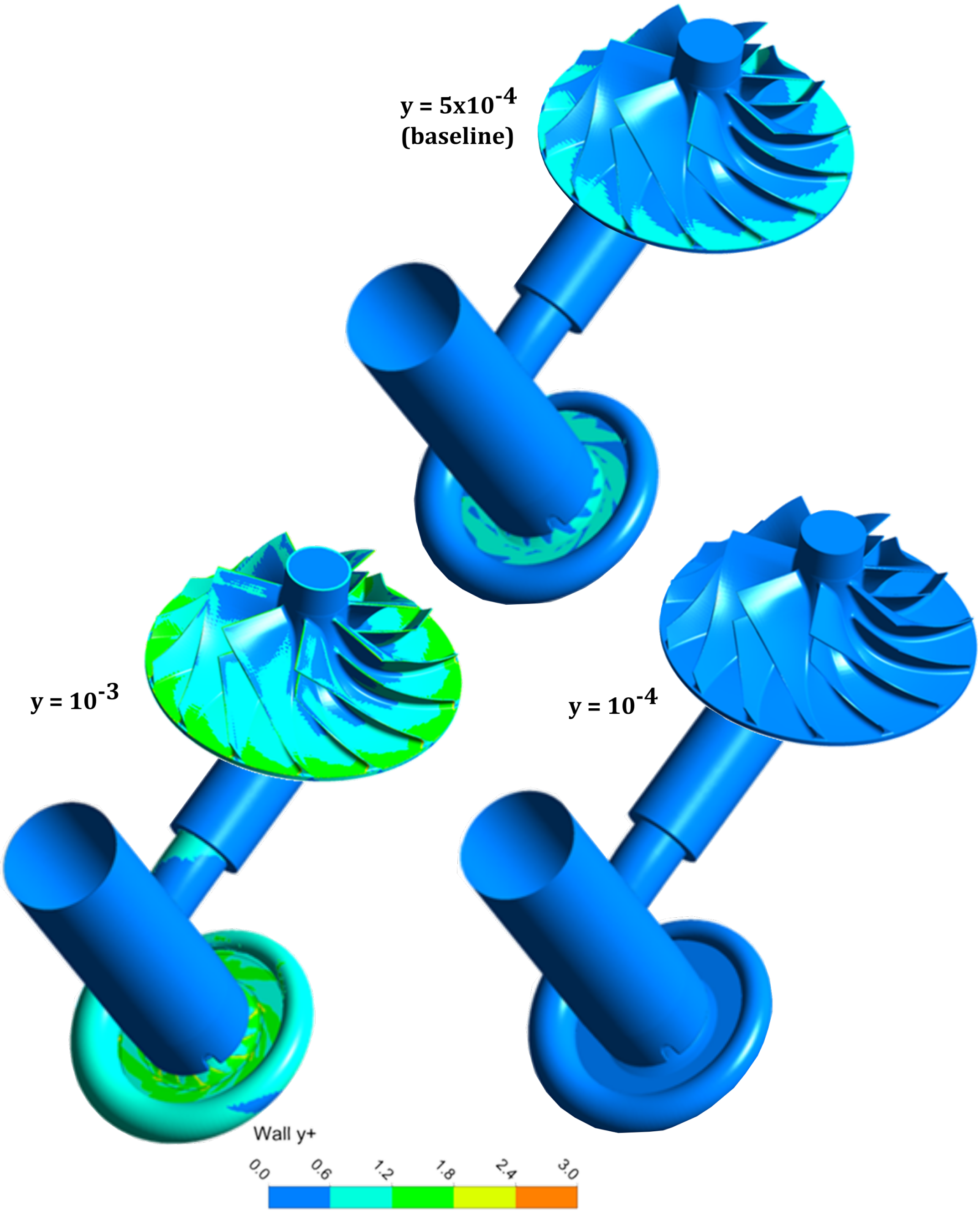

Fig. 3.9 Wall y^+ contours for different values of y specified in millimetres (mm).

applicable in this region. The linear law of the wall approximation provides a better depiction of the flow for $y^+ < 11$ and the log-law of the wall yields relatively accurate predictions for $y^+ > 11$ with the highest deviation observed at $y^+ = 11$ from either laws. Therefore, the velocity in the buffer layer is approximated by extrapolating and blending the velocity profile from other regions. The SST model can resolve the flow up to the viscous sublayer and is suitable for the Low-R_e method. Moreover, ANSYS CFX [84] uses automatic wall treatment that allows for a smooth shift from the wall function approach to Low-R_e formulation.

In this work, the values of y^+ are calculated using an internal routine adopted in the solver [84]. Alternatively, the values of kinematic viscosity ν and friction velocity u_τ can be exported from the flow solution and y^+ can be calculated using Equation 3.3. This approach is limited as it is difficult to ascertain the points among the whole grid on which the y^+ should be calculated to give an accurate view for the complete numerical domain.

As mentioned in Section 3.2, the distance of the first cell from the wall (y) is selected as $0.0005mm$. In this section, two additional values are investigated: one double that of the baseline model $(0.001mm)$ and other one as $0.0001mm$. The values of y^+ for corresponding values of y are presented in Table 3.4.

Figure 3.9 shows the global contours for the wall y^+ values including the distribution at the impeller for the studied values of the y specified in Table 3.4. The maximum value of y^+ in all the cases is less than 30 $(y^+ < 30)$ implying that wall functions are not used to model the flow in the near-wall region. Furthermore, the viscous sublayer can be resolved by all the models as y^+ values are less than 5 $(y^+ < 5)$. The near-wall mesh of baseline numerical configuration offers computationally and numerically optimal resolution to resolve the boundary layer as the maximum y^+ is observed to be 1.6 while in the other two cases, maximum values of y^+ were seen to be 0.6 and 4.5. Therefore, the baseline value of $y = 0.0005mm$ is kept as the distance of the first cell from the wall for further work in this thesis.

Boundary layer thickness In this section, the total thickness of the boundary layer is evaluated to ensure the independence of flow solution to the boundary layer thickness. Prism layers are used in this work to capture the shear or boundary layer physics. The inflation elements (prism, penta or hexa) are known to be more efficient in capturing the boundary layer physics as compared to the corresponding tetrahedral elements. The prism elements achieve better resolution of the solution normal to the surface by providing more elements perpendicular to the surface, without increasing the element density along the surface. The post inflation process is opted to create the prism elements between the boundary shell mesh and adjacent tetrahedral elements in ICEM CFD [115]. The thickness of the boundary layer is dependent on the number of prism layers, the value of initial height, growth law and height/growth ratio.

As mentioned in Section 3.2, 12 prism layers growing exponentially with the height ratio of 1.3 are used to model boundary layer flow in the baseline configuration. In this section, several other iterations for two specific height ratios of 1.2 and 1.3 are explored. The details of the iterations are listed in the Table 3.5. The models are simulated with each listed pair of height ratio and prism layers while the exponential growth law and initial height determined in the

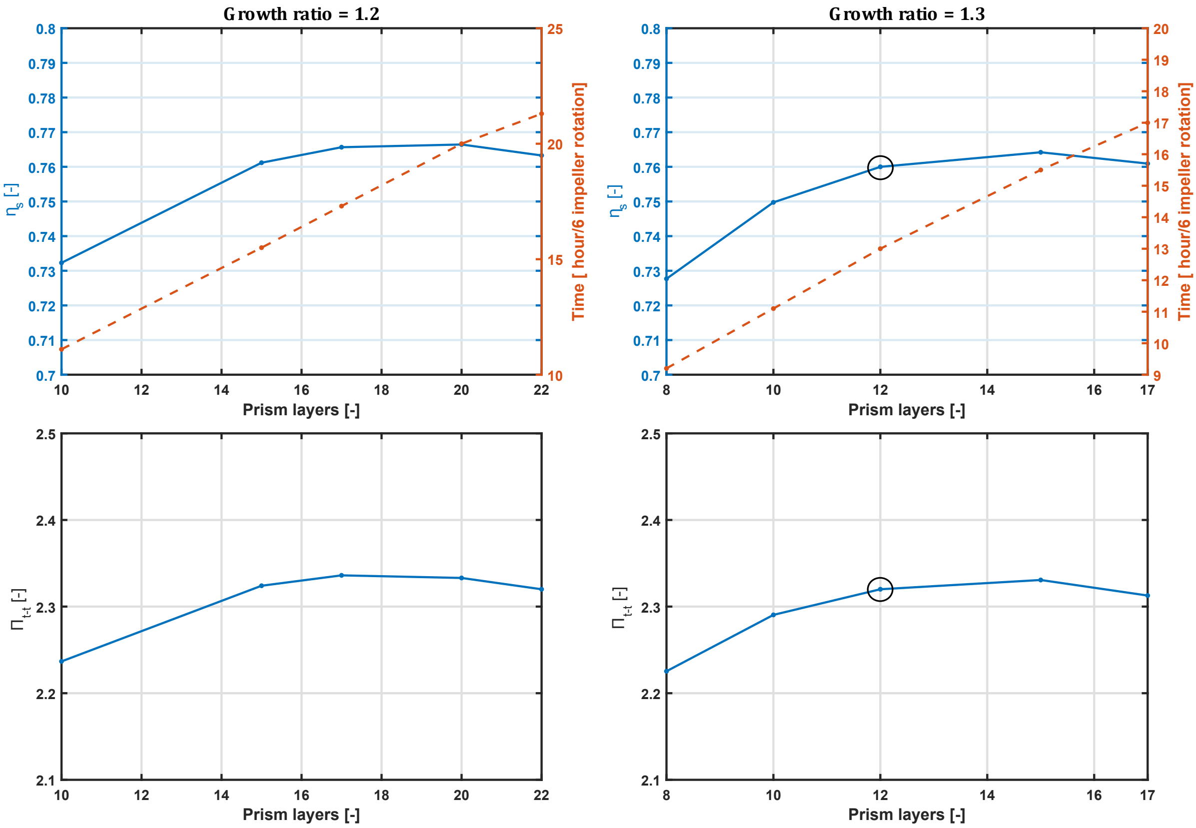

Fig. 3.10 Global performance variables for different boundary layer parameters. Baseline values (marked) are proven to be optimal.

subsection above are used throughout these iterations. The global performance results of the compressor for various cases are shown in Figure 3.10.

The global performance variables are seen to behave in an overdamped fashion, i.e. signal overshoots around an equilibrium point with a progressive reduction in amplitude although the amplitude of overshoot for any performance variable is observed to be minute. The baseline configuration of height ratio as 1.3 and number of prism layers as 12 is once again seen to be the computationally and numerically optimal combination for modelling boundary layer and therefore, is used in rest of the thesis.

Mesh resolution for free stream flow

The sensitivity of the compressor performance variables on the free stream grid resolution is explored in this section. The idea is to numerically model the compressor with a continuous increase in mesh density until the variation in the flow solution of two consecutive cases reaches a sufficiently small value that is computationally inefficient. The deviation parameter $(\varepsilon_{i,i+1})$ is used to quantify the difference between the values of a variable in two successive cases.

Table 3.5 Combination of height ratio and a number of prism layers analysed to deduce an appropriate thickness of the boundary layer.

Growth ratio	Number of prism layers
1.2	10
	15
	17
	20
	22
1.3	8
	10
	12 (baseline)
	15
	17

$$\varepsilon_{i,i+1}(\%) = \frac{\phi_{i+1} - \phi_i}{\phi_i} 100 \tag{3.4}$$

Additional meshes within the range of half of the elements in the baseline case (5 million) to over twice as fine (23 million) are explored with the configuration of the boundary layer determined in the section above. It is worth noting that in contrary to the study of the boundary layer, the free stream mesh study is performed for both design and near surge condition. The various mesh sizes are listed in the Table 3.6. The results of the simulations in terms of compressor performance variables are presented in Figure 3.11. The plots of the pressure ratio and isentropic efficiency for both design and near surge conditions follow a logarithmic curve shape till approximately 10 million cells, and small fluctuations of the underdamped fashion are observed beyond 10 million.

Table 3.6 Various mesh sizes used for free stream mesh independence study

Mesh	**Number of cells** [million]
$Mesh_1$	5
$Mesh_2$	6.5
$Mesh_{baseline}$	10
$Mesh_4$	16
$Mesh_5$	23

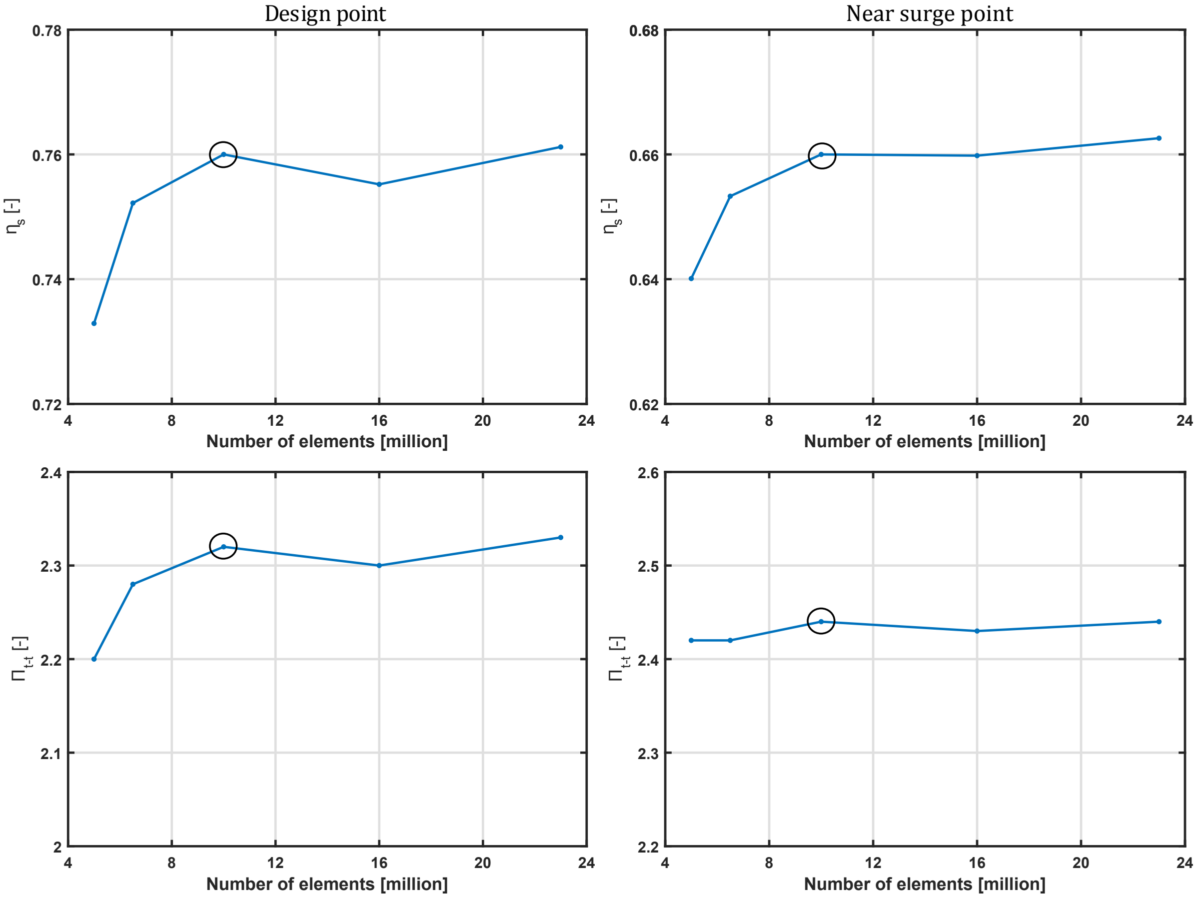

Fig. 3.11 The sensitivity of pressure ratio and isentropic efficiency to the density of free stream grid. The grid with 10 million cells is seen as the optimal configuration.

The deviation $(\varepsilon_{i,i+1}))$ between three cases (10, 16 and 23 million) is less than 2% for the performance parameters in both design and near surge condition. Therefore, the baseline grid made on the basis of literature review (see Table 3.1) with 10 million cells is the computationally appropriate mesh size to model the compressor operation with reasonable accuracy.

It is necessary to point out the limitation of this grid independence study in terms of the interpolation of the results derived on URANS onto the grids for scale resolving turbulence models. The grid requirements for the scale resolving methods presented in Section 3.4.4 are expected to be higher than the URANS model, and it is not ideal to use the same grid. Similar mesh independence studies for scale resolving models, specifically LES were not computationally tractable within the timeframe of the project. Therefore, the impact of grid density on performance and acoustic predictions for scale resolving turbulence model is briefly evaluated by using the finest mesh (23 million cells) as a standalone case.

3.4.4 Turbulence formulations

In an ideal world, one would use Direct Numerical Simulation (DNS) to resolve all the turbulent scales of interest by solving the unsteady Navier-Stokes equation with sufficient spatial and temporal resolution. The spatial resolution should be fine enough to resolve the Kolmogorov length scales meanwhile the temporal resolution should be small enough to resolve the period of fastest fluctuations in the flow [129]. The vortices smaller than that of Kolmogorov scale would dissipate their energy before a full turn. The computational infrastructure required for DNS is considerable, and even with the state-of-the-art computational resources, one can only handle DNS on very simple geometries at a relatively modest Reynolds number. An alternative to this problem is the use of turbulence models wherein the effects of turbulence are predicted by using an appropriate model without resolving all the scales of the turbulent fluctuations. Primary approaches to formulate turbulence are either statistical or scale resolving methods. Statistical models use the analytical procedures to modify the unsteady Navier-Stokes equation into an averaged form, for directly computing the mean flow solution. All the scales of turbulence field are modelled in such a statistical approach. The turbulence formulation based on the Reynolds averaging of the Navier-Stokes equation (U)RANS is the statistical model explored in this work, as seen in the baseline numerical configuration. On the other hand, scale resolving methods aim to resolve entirely or a portion of the turbulent spectrum. Large Eddy Simulation (LES) and Hybrid RANS-LES models like Detached Eddy Simulations (DES) are typical scale resolving turbulence models. The recent developments in hybrid RANS-LES models include Delayed Detached Eddy Simulation (DDES) [130] and Stress Blended Eddy Simulation (SBES) [131]. In this thesis, LES, DES and SBES scale resolving models are explored for modelling the acoustic characteristics of the compressor.

Statistical RANS is the first approach explored in this thesis to model turbulence. As stated before, RANS is based on Reynolds averaging of Navier-Stokes equations. The procedure assumes that the flow solution can be decomposed into a mean and a fluctuating component. The averaged equations are solved directly for the mean flow solution while the fluctuating component is modelled. This approach reduces the computation overhead by multiple orders of magnitude as the necessity of Kolmogorov microscale on the spatial resolution for modelling fluctuations is no longer applicable. In steady RANS, the mean component of flow solution is time independent while in Unsteady RANS (URANS) the mean component of flow solution is time-dependent. This unsteady mean value is computed by using ensemble averaging, which is a time-varying average of an instantaneous value of a variable/property over a number of identical experiments [34]. Ensemble averaging can be thought of as a time averaging over a turbulent time scale and is expected not to yield reliable results for the problems in which turbulent and mean flow time scales are of the same order [132].

The modification of the unsteady Navier-Stokes equation by Reynolds averaging introduces additional unknown terms. These unknown terms consist of the product of fluctuating quantities and act like additional stresses known as Reynolds stress tensors. The Reynolds stresses are modelled using an additional set of equations forming a closure model, also referred to as the RANS turbulence model. The major paradigms to model the Reynolds stress either uses an algebraic function as seen in eddy viscosity models or use additional differential equations such as the transport equation in Reynolds transport models. The introduction of additional differential equations will lead to similar problems of the additional unknown terms, and hence, algebraic functions have to be used at some point in the model [132]. As stated for the baseline configuration, in this thesis, ($k-\omega$ SST) [119] turbulence model is used to perform URANS simulations due to its ability to accurately represent the detaching and swirling flows with adverse pressure gradients.

The second approach explored in this thesis is the scale resolving LES method. The rationale of LES is to filter the time-dependent Navier-Stokes equation to a particular scale in the physical space. The turbulent eddies or vortices smaller than the filter scale (sub-grid scale) are modelled by appropriate means while the larger eddies and coherent structures in the flow are resolved. This stems from the fact that larger scales or structures are strongly dependent on the specific geometry and boundary conditions, therefore, difficult to accurately predict with a generic analytical model while the smaller scales of turbulence are local, homogeneous and isotropic in nature. These small scales are independent of macroscopic flow behaviour and are seen to be strongly dependent on the Reynolds number of the flow [35]. The role of these small turbulent scales is limited to the energy dissipation in the system and hence they are generally not of much interest. Various filter functions like local Gaussian distribution or top-hat with minimal differences [133] are employed in different formulations. The use of LES to model near-wall turbulence is particularly tricky because of the small turbulent length scales values and the reverse direction of energy cascade. For the flows with high Reynolds number, the computational difficulty in resolving near wall regions is further increased due to the decrease in the size of the viscous sublayer relative to the boundary layer. As most turbomachinery problems are wall-bounded flows at high Reynolds number, the LES approach would necessitate high spatial resolution. The author recommends Pope [129] and Tucker [134] to further explore the LES modelling, specifically for acoustic applications.

The larger scales resolved in LES aid in capturing the broadband noise sources and therefore LES is often used in computational aeroacoustics [134]. The application of LES to model the turbocharger compressor flow has been successfully demonstrated by Karim et al. [40] and the researchers from KTH [135, 136, 110, 37, 36, 137]. A good agreement between the numerical and measured flow structures [126, 38] further reinforces the faith in the capability of LES to accurately model flow-induced noise although direct comparison of the predicted and measured acoustic spectra is not seen in literature. In this work, the Wall-Adopted Local Eddy-viscosity (WALE) [138] formulation in CFX [84] is used with an intent to resolve the flow till the viscous sublayer assuming the wall resolution is sufficient. The WALE-LES uses an algebraic local eddy viscosity based subgrid model to dissipate eddies in viscous sublayer and near wall regions. This model improves upon the problem of the non-zero eddy viscosity in the laminar shear flow region observed in the Smagorinsky model [138].

Finally, the last approach explored in this thesis is the combination of the above two as Hybrid RANS-LES method. In this approach, LES is employed in free shear flows and massively separated regions where turbulent structures are of a dimensionally comparable order as the geometrical structures generating them while URANS is used for the attached region and mildly separated boundary layers. The application of one of such Hybrid RANS-LES model (DDES) to predict the acoustic characteristics of the turbocharger compressor is demonstrated by Broatch et al. [34, 32]. The Hybrid RANS-LES models considered in this thesis are SBES [131] and the extended DES model based on the SST formulation proposed by Menter and Kuntz [130].

Conventional DES models introduced by Spalart, Strelets and team [139] used a criterion based on the local grid size to switch between RANS and LES. The turbulent length scale (L_t) predicted by the RANS model is compared with the equivalent length scale of the LES model (L_t, LES) based on the local grid spacing Δ. The DES limiter is activated when the maximum edge length of the local computational cell is less than the turbulent length scale, implying that the turbulence length scale is larger than the local LES scale in those regions and the model switches from RANS to LES mode.

$$
\begin{aligned}
L_t &= \frac{\sqrt{k}}{\beta^* \omega} \\
L_{t,\text{LES}} &= C_{\text{DES}} \Delta \\
L_t < L_{t,\text{LES}} &\equiv L_t < C_{\text{DES}} \Delta \rightarrow \text{RANS} \\
L_t \geq L_{t,\text{LES}} &\equiv L_t \geq C_{\text{DES}} \Delta \rightarrow \text{LES} \\
\Delta &= \max(\Delta_x, \Delta_y, \Delta_z)
\end{aligned}
\tag{3.5}
$$

The actual formulation of the conventional DES based on the two-equation model [139] (Turbulent kinetic energy – Equation 3.6) implies the need for temporal and spatial resolution requirements as of the LES when grid spacing is used as the defining length scale, as all the relevant turbulence information needs to be resolved once the DES limiter is activated. Therefore, the conventional DES formulations are highly grid dependent and suffer from the issues of log-layer mismatch and grid-induced separation. The log layer in the RANS and LES zones does not line up, leading to an unphysical buffer layer seen near the RANS-LES interface. Also, refinement of the grid inside the attached boundary layer can lead to pre-activation of the DES limiter causing a reduction in the eddy viscosity of the RANS model, thereby leading to grid-induced separation.

$$\begin{gathered}\frac{\partial(\rho k)}{\partial t}+\frac{\partial(\rho\bar{U}_j k)}{\partial x_j}=P_k-\rho\frac{k^{3/2}}{\min(L_t,C_{\mathrm{DES}}\Delta_{max})}+\frac{\partial}{\partial x_j}\left(\left[\mu+\frac{\mu_t}{\sigma_k}\right]\frac{\partial k}{\partial x_j}\right)\\ L_t=\frac{k^{3/2}}{\varepsilon}=\frac{\sqrt{k}}{\beta^*\omega}\end{gathered}\tag{3.6}$$

The conventional formulation of DES is extended to Delayed DES (DDES) in order to ‘shield’ the boundary layer from the DES limiter. The reformulation of the dissipation term in the turbulent kinetic energy (k-equation) for the two-equation model is compared with the one of the DES model in Equation 3.7. The function F_{DDES} is designed to yield the value of 1 ($F_{\mathrm{DDES}}=1$) in the boundary layer region and the value of 0 ($F_{\mathrm{DDES}}=0$) for the region away from the wall [130]. The DES-SST formulation in CFX includes the shielding properties of DDES by formulating the blending functions of the SST model as the zonal DES limiter [130, 140]. The dissipation rate in the equation for the turbulent kinetic energy for the DES-SST formulation in CFX [130] is also replicated in Equation 3.7.

$$\begin{gathered}\varepsilon_{DES}=\rho\frac{k^{3/2}}{\min(L_t,C_{DES},\Delta)}=\rho\frac{k^{3/2}}{L_t\ \min\left(1,C_{DES}{}^{\Delta}/{}_{L_t}\right)}=\rho\frac{k^{3/2}}{L_t}\max\left(1,\frac{L_t}{C_{DES}\Delta}\right)\\ \varepsilon_{DDES}=\rho\frac{k^{3/2}}{L_t}\max\left[1,\frac{L_t}{C_{DES}\Delta}(1-F_{DDES})\right]\\ \varepsilon_{DES-CFX}=\rho\frac{k^{3/2}}{L_t}\max\left[1,\frac{L_t}{C_{DES}\Delta}(1-F_{SST})\right];with\ F_{SST}=0,\ F_1,F_2\end{gathered}\tag{3.7}$$

Stress Blended Eddy Simulation (SBES) is also an improvement over conventional Detached Eddy Simulation (DES), specifically in the shielding of the boundary layer and transition issues in separating shear layers [131]. The slow transition from RANS to LES is observed in the conventional DES model. This is caused by the large values of eddy viscosity computed in separating shear layers which leads to a slow break-up into resolved turbulence [131]. These problems are alleviated in SBES formulation by ‘blending’ the RANS and LES models using a shielding function. The stress and eddy viscosity blending formulations are shown in the Equation 3.8 [131]. The shielding function f_s provides improved asymptotic shielding of the RANS boundary layer against LES modification and produces significantly lower values of eddy viscosity in separating shear layers.

$$\begin{aligned}\tau_{ij} &= \tau_{ij}^{RANS} f_s + \tau_{ij}^{LES}(1 - f_s) \\ \mu_t &= \mu_t^{RANS} f_s + \mu_t^{LES}(1 - f_s)\end{aligned} \tag{3.8}$$

To summarise, URANS, DES, SBES and LES formulations are explored for their capability to model flow-induced noise in the compressor. The sensitivity of performance and acoustic predictions to these turbulence models for various timestep sizes are presented in Section 3.5 and Section 3.6.

3.4.5 Temporal resolution

Definition of the appropriate timestep size or temporal resolution is vital for any unsteady transient simulation, but it is of particular importance in this thesis as the objective is to predict the flow-induced noise. The adequate value of the timestep is dictated by several numerical and empirical conditions. The numerical criterions include the Nyquist condition and the Courant–Friedrichs–Lewy (CFL) condition. The former outlines the highest frequency (f_N) that can be resolved by a certain timestep size (Δt) while the latter provides the information on the flow of fluid across cells for each timestep. For the 20 kHz – 25 kHz range, the respective timestep size computed by Equation 3.9 for the Nyquist condition should be in the range of $2.5 \times 10^{-5}\,s - 2 \times 10^{-5}\,s$.

$$f_N = \frac{1}{2\,\Delta t} \tag{3.9}$$

The implication of the CFL condition is summed in terms of a dimensionless number commonly referred to as Courant number (C)

$$C = a\frac{\Delta t}{\Delta x} \tag{3.10}$$

where a is velocity magnitude and Δx is the distance between the adjacent mesh cells. For the explicit linear schemes, the value of Courant number should be equal or less than 1 to maintain numerical stability. The physical interpretation of this constraint is that the propagation of the flow information should be limited to the immediate neighbour of a cell. The unsteady term throughout this thesis is discretised using a second-order implicit temporal scheme for better accuracy. Although an implicit temporal scheme is not constrained by Courant number for numerical stability, Spalart [141] recommends a Courant number as 1 in LES for maintaining temporal accuracy.

The empirical suggestions in literature for selecting the appropriate timestep size for turbomachinery applications often follow a Strouhal number like approach in which the timestep size is usually expressed in degrees of impeller rotation per timestep (°/TS) or a number of timesteps per blade passing (TS/BP). The recommendation of Mendonça [39, 142] is to use 10 timesteps per acoustical wavelength leading to $5 \times 10^{-6} s$ while ANSYS CFX [116] recommends at least 20 timesteps per blade passing. As seen from Table 3.1, the range of $5° - 1°$ impeller rotation per timestep is pervasive in literature. Exceptions to the aforementioned range are seen in the works of Després et al. [108] and Hellstrom et al. [135] with the significantly lower values of the timestep size corresponding to 0.01° and 0.19° impeller rotation per timestep respectively. The use of such prohibitively small timestep sizes could be due to numerical stability issues associated with explicit temporal schemes. It is worth emphasising that the optimal size of timestep is critical as the computational overhead is doubled every time the timestep size is divided by two.

By considering the above-mentioned criteria, timestep sizes corresponding to 4°, 2° and 1° are explored for the various turbulence formulations in this thesis. The sensitivity of performance and acoustic predictions to these timestep sizes for various turbulence formulations are presented in Section 3.5 and Section 3.6.

3.5 Evaluation for near surge conditions

The impact of the turbulence formulation and the corresponding timestep size on performance and acoustic predictions for near surge operation are discussed in this section.

Impact on performance predictions

Table 3.7 presents the compressor performance parameters (Equation 2.8) viz. Pressure ratio Π_{t-t} and isentropic efficiency η_s along with the relative deviation from experimental values (Equation 3.1) obtained from various turbulence formulations and timestep sizes explored for modelling near surge operation. The performance parameters are predicted within 1.2% of the experimental values irrespective of the turbulence formulation and timestep size. Furthermore, the time-averaged velocity distribution values in the blade passages predicted by various numerical configurations (see Figure 3.12) are also similar. If the objective of the model was to predict the performance, the baseline configuration (URANS – 4°) would have been the computationally optimal choice. However, this thesis revolves around flow-induced noise, therefore, the impact of the turbulence formulation and timestep size on the acoustic predictions needs to be considered for finalising the optimal numerical configuration.

Table 3.7 Performance variables Π_{t-t} and η_s predicted by various numerical configurations for near surge operation are compared with the experimental results.

Method	Δt[°]	Grid [mil]	Π_{t-t} [-]	η_s [%]	ε_π [%]	ε_η [%]
Experimental	-	-	2.47	66.7	-	-
URANS	4°	10	2.44	66	1.2	1
	2°		2.44	65.9	1.2	1.2
DES	4°	10	2.46	66.1	0.4	0.9
	2°		2.44	66	1.2	1
SBES	4°	10	2.47	66.4	0.1	0.5
	2°		2.45	66.2	0.8	0.7
	1°		2.44	65.9	1.2	1.2
LES	2°	10	2.45	66.3	0.8	0.6
	1°		2.44	65.7	1.5	1.2
LES	2°	23	2.48	66.5	0.2	0.4

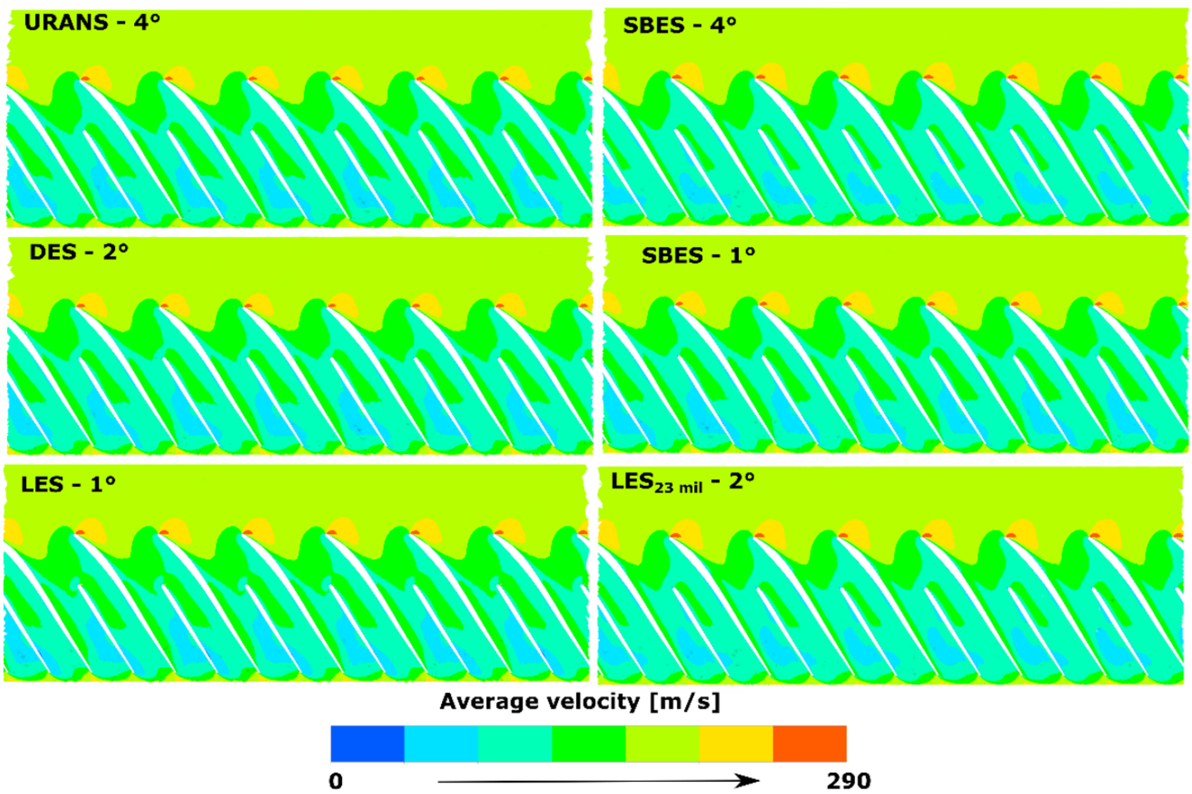

Fig. 3.12 Average velocity distribution for the near surge point predicted by various numerical configurations at the mid impeller span.

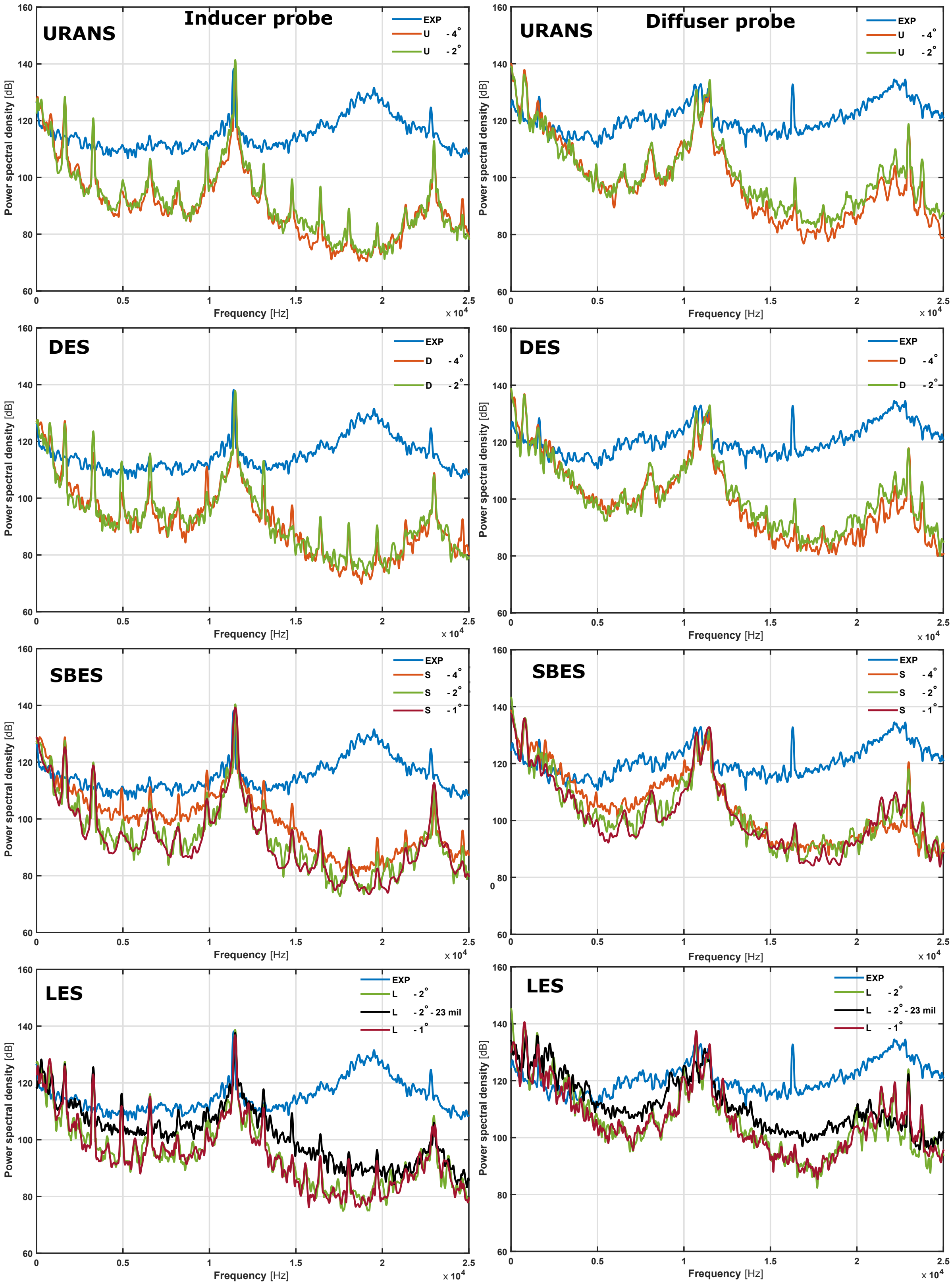

Fig. 3.13 Inducer (left) and diffuser (right) spectra computed from various turbulence models are compared with the experimentally measured values for near surge operation.

3.5.1 Impact on acoustic predictions

The impact of turbulence formulations and corresponding timestep size on the generation and propagation of noise are quantified with the help of inducer/diffuser probes and inlet/outlet duct probes respectively. In the spectra of inducer and diffuser probes (see Figure 3.13), the impact of timestep size seems insignificant irrespective of the turbulence formulation. In addition to that, the broadband elevation centred around 19 kHz observed in the measured inducer spectrum is not captured by any numerical configuration explored in this thesis. Overall trends of both inducer and diffuser spectra are reasonably captured regardless of the turbulence formulation. Tonal features are accentuated in the numerical spectra while overall levels are predicted significantly lower than corresponding experimental results. The correlation among overall levels is significantly improved by increasing the spatial resolution as observed from the results of the LES model with higher grid density (23 million).

The spectra predicted by URANS and DES formulations are similar although significant improvements in terms of amplitudes and the decay rates are observed for SBES and LES. This can be understood from the contours of the blending and shielding functions plotted in Figure 3.14, showing that the RANS model (blending function = 1) is used over a larger region for DES while LES region (shielding function = 0) is higher in the SBES model. Even though the same grid is employed for both URANS and DES formulations in this work, the use of the denser grid in the LES region of DES formulation is expected to improve the predictions. The LES formulation with respective temporal and spatial resolution corresponding to 2° impeller rotation per timestep and 23 million cells is seen to yield the best agreement with the measured results. This being said the baseline URANS formulation with 10 million cells and 4° timestep can reasonably capture the noise generated in the impeller operating near surge and thereby,

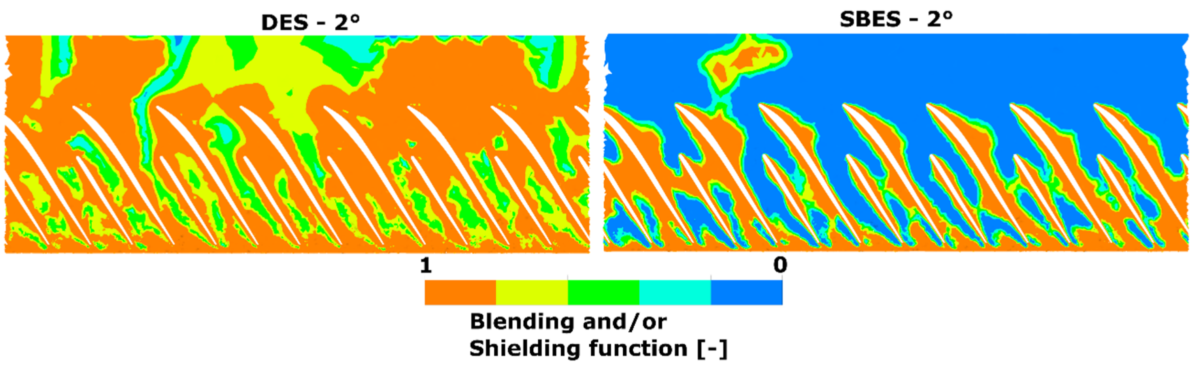

Fig. 3.14 Blending and shielding function for the DES and SBES model respectively for the compressor operating near surge are plotted at mid-blade span. Regions with the function value as 1 are modelled using RANS while the regions with 0 indicate the use of LES model.

makes a sensible choice for industrial work focused around the impact of a particular design change.

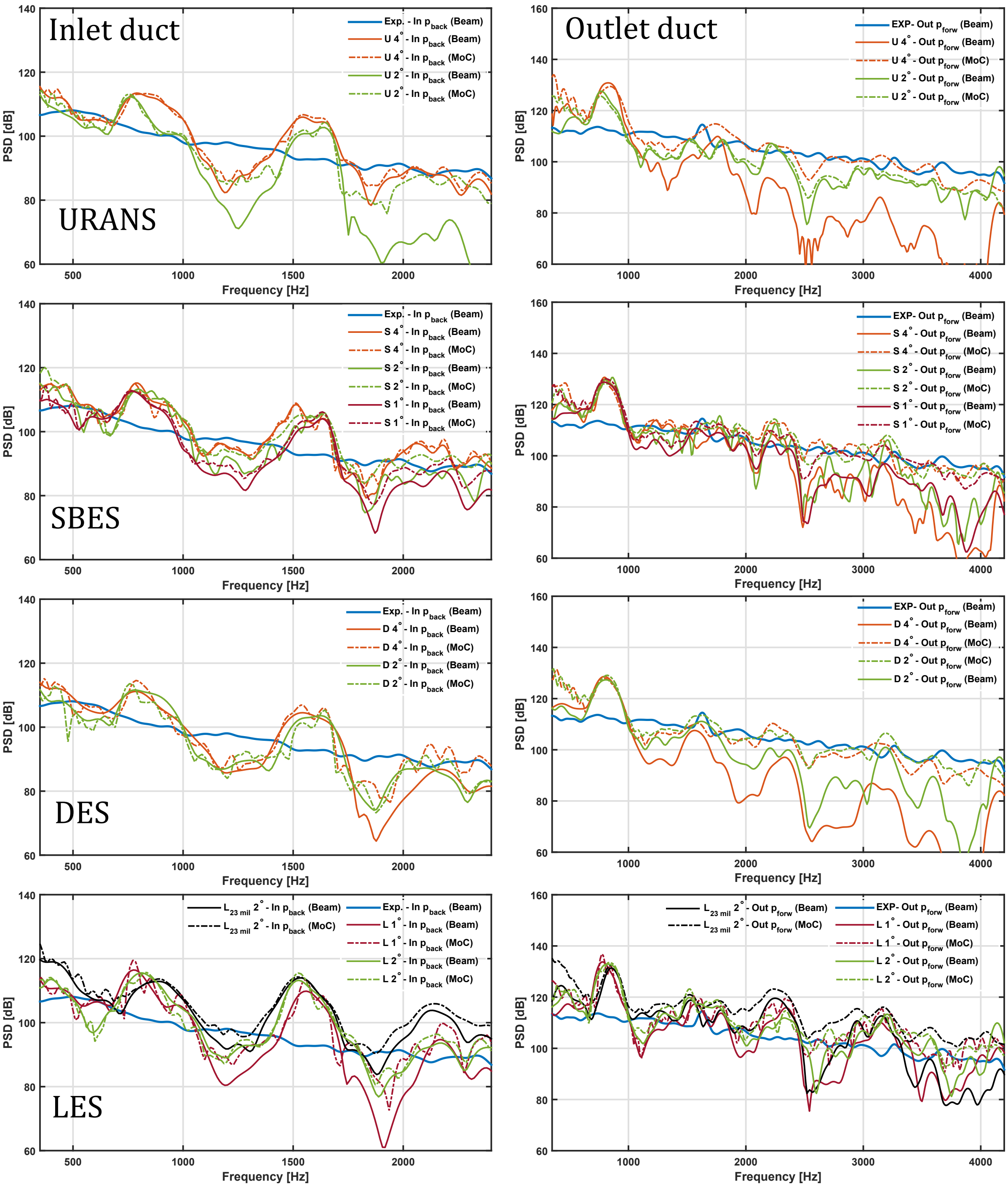

Fig. 3.15 Low-frequency inlet (left) and outlet (right) duct spectra computed by various turbulence models using beamforming (solid) and MoC (dashed) are compared with the beamformed experimental spectra for near surge operation.

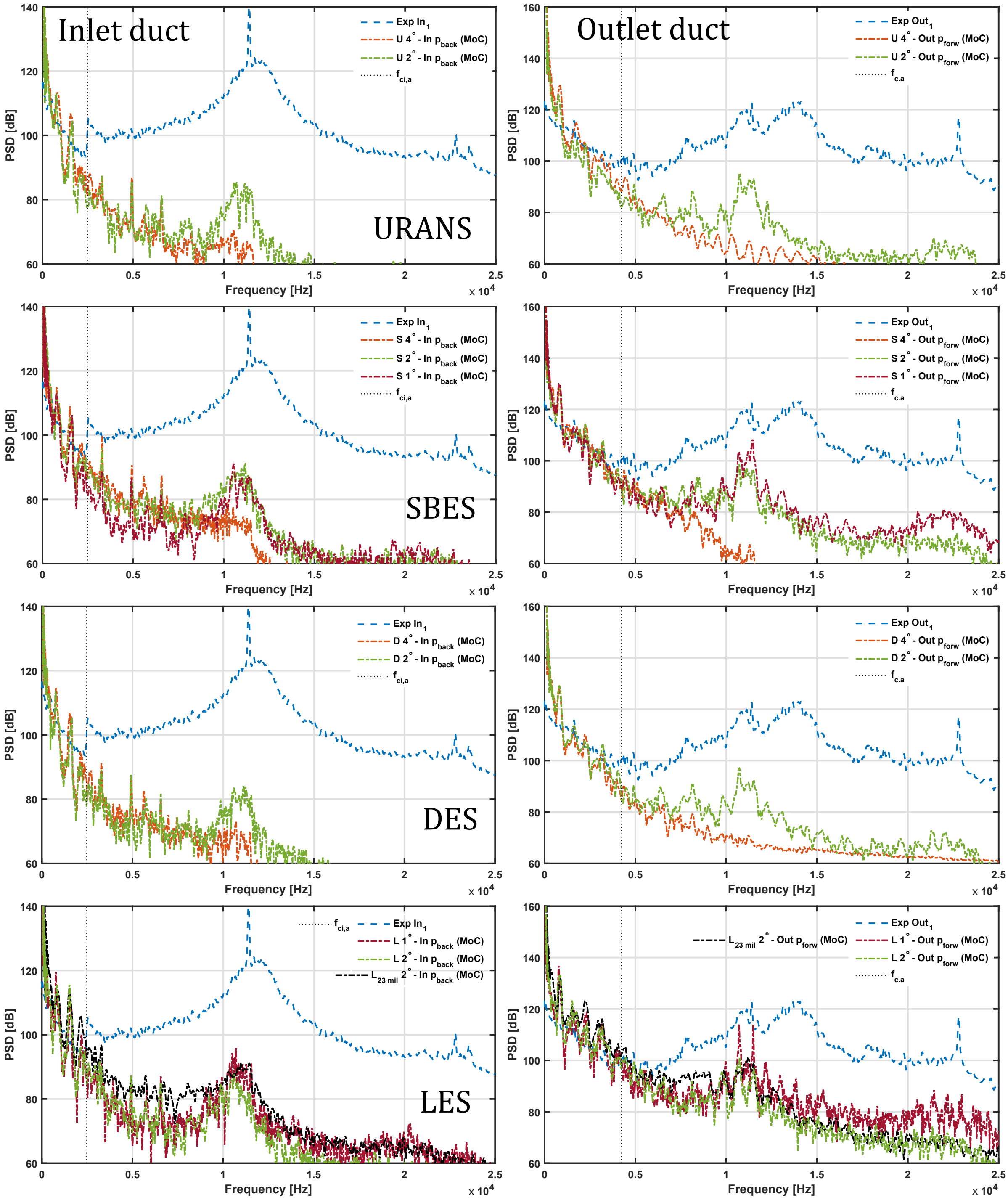

Fig. 3.16 High-frequency inlet (left) and outlet (right) duct spectra computed by various turbulence models using MoC are compared with the experimental spectra obtained from raw pressure signal for near surge operation.

The sensitivity of noise propagation to various numerical configurations is assessed from duct spectra presented in Figure 3.15 and Figure 3.16. Within the plane wave range (see Figure 3.15), the discrepancies seen between the predictions from different timestep sizes for a particular turbulence formulation are insignificant. The overall trends of the duct spectra obtained from beamforming and MoC spectra for various turbulence formulations are similar. The fluctuations are observed in the numerical spectra of inlet duct computed from both beamforming and MoC while the spectra of the outlet duct computed using MoC correlates relatively better than the one obtained using beamforming. Similar to the inducer/diffuser probe spectra, the duct spectra, computed specifically by the beamforming of LES and SBES data, are relatively better than corresponding DES and URANS results. As the human hearing is particularly sensitive in low-frequency range [143], the baseline model still stands out as a computationally optimal choice.

However, the analysis of duct spectra at higher frequencies (see Figure 3.16) indicates that above a specific frequency, the spectra abruptly decay and this frequency is inversely proportional to the size of the timestep. Therefore this cut-off frequency, up to which spectra can be appropriately predicted, increases with a decrease in the timestep. The spectra predicted by a timestep corresponding to 4° deviate from the respective 2° and 1° spectra at approximately 9 kHz leading to poor representation of the BPF tone in the spectra of any numerical configuration with 4° timestep. The deviations among the spectra corresponding to 2° and 1° models are observed beyond 20 kHz. It is worth pointing out that these findings on the size of timesteps

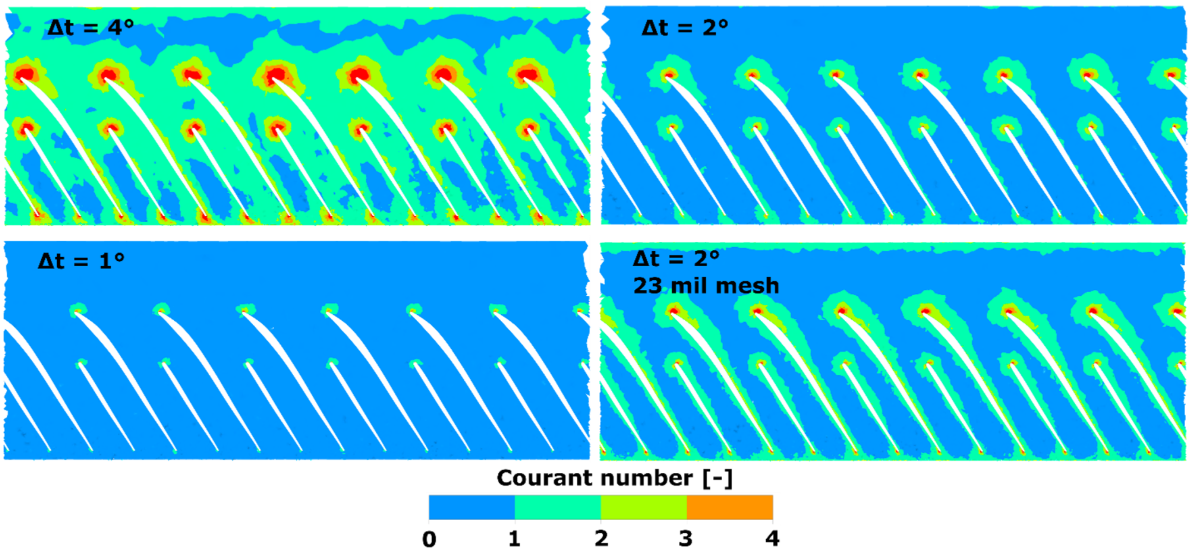

Fig. 3.17 Contours of average Courant number in the mid-span of the impeller for different sizes of the timestep. For the same timestep size (Δt = 2°), an increase in spatial resolution demonstrates an increase in Courant number.

are specific to the spatial resolution and may not be directly interpolated to other grids as the Courant number would change. The average Courant number in the majority of the rotor region for timesteps corresponding 1° and 2° is below unity (see Figure 3.17), whilst a higher value of approximately two is observed in the 4° timestep case. Interestingly, for the same timestep size corresponding to 2°, a relatively higher Courant number can be observed for the grid with the higher cell count due to the smaller element size.

Based on the results and discussion presented above, a timestep corresponding to 4° is optimal for investigating low-frequency content while a 2° timestep is optimal for exploring the acoustic characteristics at higher frequencies. The agreement at higher frequencies between numerical spectra computed from the pressure wave decomposed using MoC and experimental spectra computed from raw pressure signals is poor irrespective of the modelling parameters. This can be improved by either modelling the complete measurement rig or by using some means to decompose the experimental pressure signal as done in the case of the low-frequency plane wave range.

Table 3.8 Performance variables Π_{t-t} and η_s predicted by various numerical configurations for design point are compared with the experimental results.

Method	Δt [°]	Grid [mil]	Π_{t-t} [-]	η_s [%]	ε_π [%]	ε_η [%]
Experimental	-	-	2.35	76.8	-	-
URANS	4°	10	2.32	76	1.1	1.1
SBES	4°	10	2.32	76.1	1	0.9
	2°		2.33	76.1	1	0.9
LES	2°	10	2.37	78	0.8	1.5
LES	2°	23	2.38	77.9	1.2	1.5

3.6 Evaluation for design conditions

Similarly, the sensitivity of performance and acoustic predictions to the turbulence formulation and timestep size for design operation are quantified in upcoming subsections.

Impact on performance predictions

Compressor performance parameters and their relative deviation from experimental values for design operation are presented in Table 3.8. The performance predictions are within 1.5%

of the experimental values regardless of the turbulence formulation and timestep size. In addition to that, the velocity distributions in the impeller predicted by various models are also consistent as observed in Figure 6.4. Therefore, the baseline configuration (URANS – 4°) would be the computationally optimal choice for predicting the performance characteristics of the compressor operating at design conditions too.

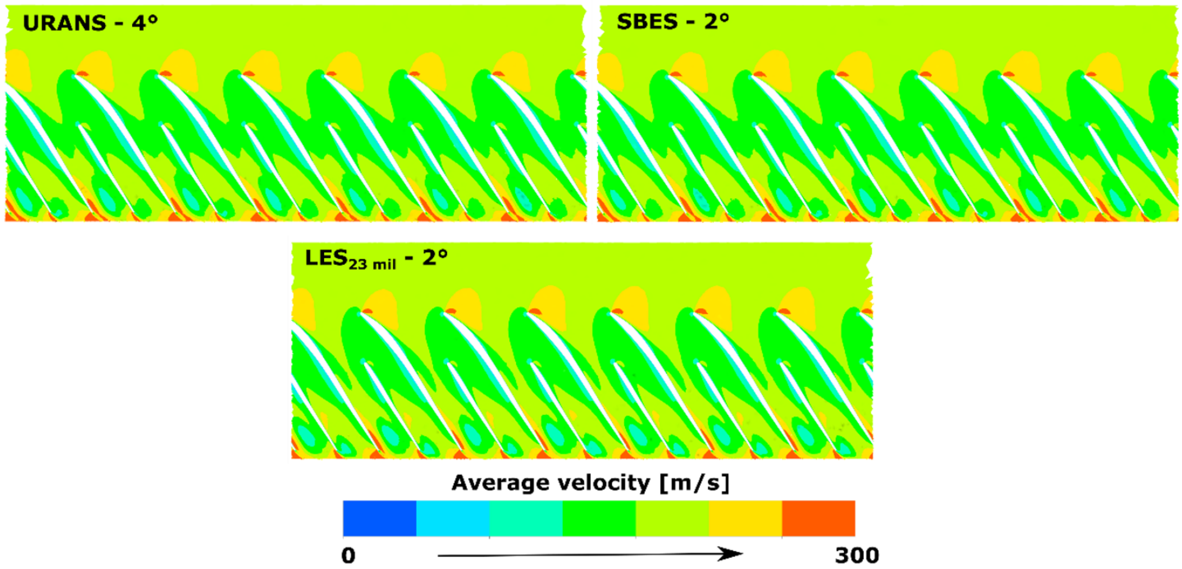

Fig. 3.18 Average velocity distribution for the design operation predicted by various numerical configurations at the mid impeller span.

3.6.1 Impact on acoustic predictions

Similar to the near surge case, the impact of timestep size on the spectra of inducer and diffuser probes (see Figure 3.19) is inconsequential irrespective of the turbulence formulation. Overall trends of both inducer and diffuser spectra are reasonably captured regardless of the turbulence formulation, although the broadband elevation observed in the region of 18.8 kHz for the diffuser spectrum is not replicated in any numerical configuration either. Tonal features are accentuated in the numerical spectra; specifically, the 'mid-tones' that are observed between adjacent RO tones are spuriously heightened as compared to experimental results. Overall levels are predicted significantly lower than corresponding experimental results for numerical models using the reference grid (10 million) while correlation is seen to be significantly improved in the LES model with higher spatial resolution (23 million). Even though the closest agreement with the measured spectra for inducer and diffuser positions is achieved by LES formulation with 23 million elements and 2° timestep, the baseline numerical configuration of the URANS

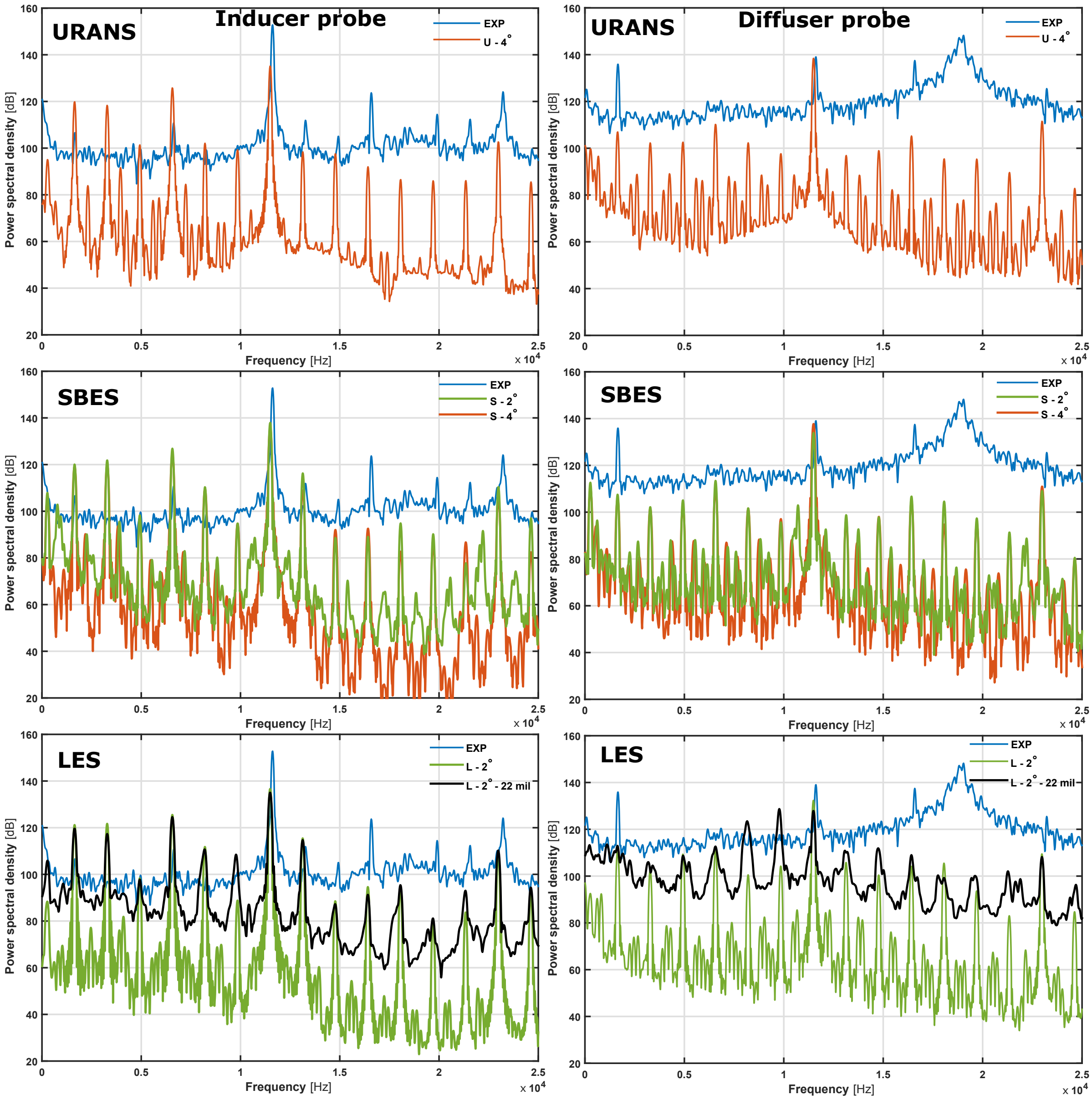

Fig. 3.19 Inducer (left) and diffuser (right) spectra computed from various turbulence models are compared with the experimentally measured values for design operation.

formulation with 10 million cells and 4° timestep reasonably captures the features of the spectra and stands out as a contender on the basis of computational trade-off for industrial analysis.

The low and high-frequency duct spectra are presented in Figure 3.20 and Figure 3.21 respectively. Unlike the low-frequency predictions for the near surge operation, the agreement with measured spectra for the design condition with the baseline grid (see Figure 3.20) is poor regardless of the turbulence formulation and timestep size. The predictions are improved by increasing the spatial resolution as seen for the grid with 23 million elements. Similarly, the

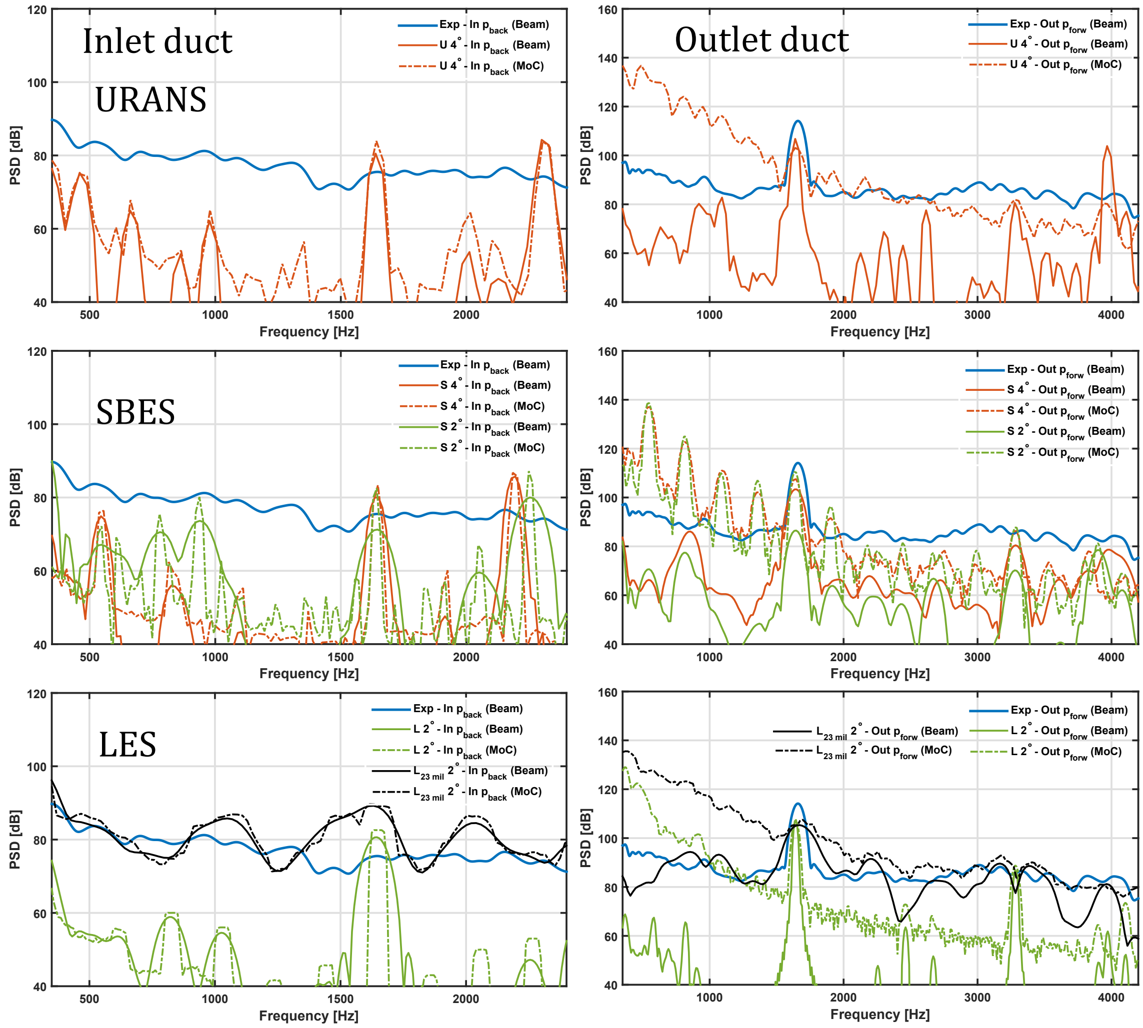

Fig. 3.20 Low-frequency inlet (left) and outlet (right) duct spectra computed by various turbulence models using beamforming (solid) and MoC (dashed) are compared with the beamformed experimental spectra for design operation.

numerical model with higher spatial resolution also yields relatively better agreement at higher frequencies (see Figure 3.21). Therefore, the LES formulation with a higher spatial resolution of 23 million cells and corresponding timestep size of 2° impeller rotation per timestep should be the used to explore duct spectra for the design condition. Counter-intuitively, the spectra for near surge operation, specifically the duct spectra, show better agreement with measured results for coarser numerical parameters than the corresponding configuration for design operation. The instability at near surge operation generates flow structures of relatively higher length scales as compared to the attached flow structures associated with design operation, therefore larger mesh cells can still reasonably capture the energetic flow structures observed near surge.

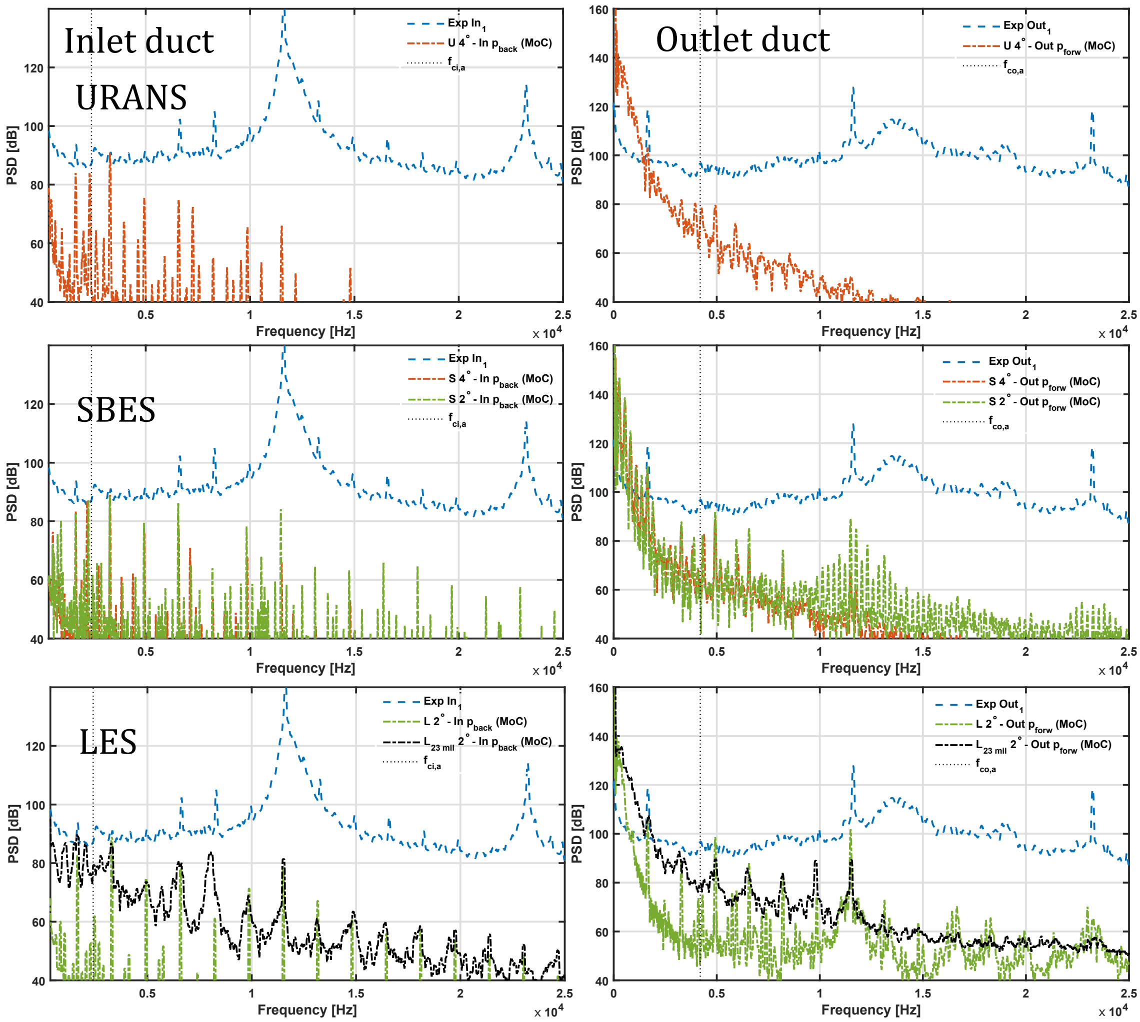

Fig. 3.21 High-frequency inlet (left) and outlet (right) duct spectra computed by various turbulence models using MoC are compared with the experimental spectra obtained from the raw pressure signal for design operation.

To summarise, agreement with the experimental spectra for both design and near surge operating conditions is best obtained by the LES formulation with 23 million cells and 2° timestep while the baseline configuration, i.e. URANS formulation with 4° timestep on the grid of 10 million cells is appropriate where lower computing times are a priority. The spectra predicted by SBES model show the expected improvement over the baseline configuration and therefore, a computational alternative to the LES model. Furthermore, for the explored grids, the timestep corresponding to 4° impeller rotation can be reasonably used to study low-mid frequency characteristics.

3.7 Conclusions

The development of the numerical configuration and justifications of various decisions regarding computational modelling used in this thesis have been presented in this chapter. Impeller rotation is established to be modelled using an unsteady rigid body motion method for computing flow-induced noise, while the pressure and mass flow rate are prescribed at the inlet and outlet boundary respectively. The impact of URANS, DES, SBES and LES turbulence formulations and corresponding spatial and temporal resolutions of 4°, 2° and 1° impeller rotation on performance and acoustic predictions are quantified. The results emphasise the importance of high spatial resolution for scale resolving turbulence formulations to yield better results. Furthermore, the information can be used to select appropriate numerical configuration considering time and accuracy trade-offs.

Although the baseline numerical configuration derived on the basis of literature is established to be an appropriate choice in terms of spatial resolution for both boundary layer and free stream flow, a grid with double the number of elements of baseline model is seen to improve the acoustic predictions for LES formulations. The performance predictions are observed to be within 1.5% of the measured values irrespective of turbulence and timestep parameters. Furthermore, the velocity distribution results in the impeller as predicted by different turbulence formulations are consistent. Therefore, the baseline model can be seen as the optimal choice for performance investigations.

Although the overall trend of the spectra for the noise generation quantified from inducer and diffuser probes are similar regardless of turbulence formulations and timestep sizes, tonal features are spuriously accentuated in the numerical spectra. The absolute values of the sound pressure levels and decay rates predicted by LES and SBES formulations are better than the similar predictions from DES and URANS formulations. Further improvements in the calculation of overall levels are observed by using high spatial resolution. The broadband elevations focused around approximately 19 kHz observed in the experimental spectra of inducer and diffuser probes for near surge and design operation respectively are not captured by any numerical configuration. Again, the baseline configuration is observed as the computationally optimal choice to predict the flow-induced noise near the inducer and diffuser.

The propagation of noise at lower frequencies (up to the plane wave range) towards the inlet and outlet ducts computed using beamforming and MoC are reasonably captured irrespective of numerical configuration for the near surge operation, while only the LES formulation with higher spatial resolution is seen to achieve similar correlation for the design condition. The agreement between measured and predicted spectra for the ducts at higher frequencies is poor. The impact of timestep size is clearly observed in the case of duct spectra as the decrease in the size of timestep increases the range of the frequency up to which spectra can be appropriately resolved. For the baseline grid of 10 million cells, a 4° timestep can resolve up to 9 kHz while 2° is observed to be appropriate up to 20 kHz.

In the light of the above discussion, the characteristics of the PS compressor are investigated using higher grid density (23 million) LES formulation while the modal decomposition presented in Chapter 4 is based on the results of SBES models with 10 million cells and 4° timestep for computational reasons. The investigation of the PS blocked configuration is also based on the aforementioned SBES model, as the significant differences in the lower frequencies observed during measurements are of primary interest.

Chapter 4

Flow field investigation for acoustic features*

Contents

*Content presented in this chapter has been partly published in the following papers:

- Acoustic characteristics of a ported shroud turbocompressor operating at design conditions [2]
- Acoustic and pressure characteristics of a ported shroud turbocompressor operating at near surge conditions [1]

4.1 Introduction

The primary objective of this thesis is to enhance the understanding of the acoustic features and establish the impact of the ported shroud (PS) on high-speed centrifugal compressors. In order to achieve that, acoustic characteristics of open and blocked compressor configurations are measured in Chapter 2. The measurements are then used to develop the optimal numerical configurations for modelling the aerodynamic and aeroacoustic characteristics of the compressor in Chapter 3. In this chapter, the relationship between the flow and the acoustic emission of the compressor for design and near surge operation is established by analysing the flow behaviour of the validated numerical configurations. Furthermore, the dominant flow structures possessing the highest energy content and their corresponding spectra are identified by decomposing the flow field.

The flow mechanisms corresponding to acoustic characteristics for design and near surge operation observed in literature are presented in Section 4.2. Flow behaviour for the design and near surge points under study are investigated in Section 4.3 while modal decomposition of the pressure field is presented in Section 4.4. Finally, the conclusions of this chapter are included in Section 4.5.

4.2 Literature review

The literature review for this chapter covers work on the flow features observed during the design and near surge operation of centrifugal compressor followed by the modal decomposition of the flow for investigating the link between flow and spectral features. Generally, the flow inside the compressor is observed to be steady and attached with low-intensity secondary flows for the design condition while near surge operation is marked by flow reversal, specifically near the inducer inlet along with the sporadic breakdown of the swirling flow in the volute. The acoustic spectra for the design operation are dominated by tonal features whereas, low-frequency broadband and narrowband features are the characteristics of near surge operation. It is worth pointing out that the literature on ‘whoosh’ noise is not covered as it was not observed in the experimental spectra of the cases under study.

Numerical investigations on the flow effects of PS slot geometry by Sivagnanasundaram et al. [144] showed the existence of two recirculation zones in the PS cavity. The flow mechanism and flow field of a ported shroud casing treatment are investigated in the works of Christou [122], Semlitsch et al. [38] and Sharma et al. [5]. Semlitsch et al. [38] identified high-speed jet-like structures exiting the PS cavity for near surge along with a reduction in flow disturbances in the blade passage as compared to the PS blocked configuration. The penalty in the efficiency at the off-design conditions is attributed to losses inside the cavity [58] along with the mixing losses associated with the interaction of the flow exiting the PS cavity with the incoming flow, as seen in the second law analysis [145] of the flow by Sharma et al. [5].

Acoustic characteristics for design operation of a large centrifugal compressor were experimentally determined by Raitor and Neise [27]. At lower operating speeds, the spectra were dominated by the so-called Tip Clearance Noise (TCN) while tonal features viz. Rotating Order (RO) and blade pass tones were observed at higher speeds. On the basis of the behaviour of axial counterparts, authors hypothesised TCN to be caused by the propagation of 'rotating instability' associated with the secondary tip leakage flow, while tonal features were postulated to be caused by sonic shock waves attached to leading edge of the impeller blades operating at higher speeds.

The numerical investigation of Guo et al. [112] and Chen et al. [146] proposed the volume of the volute as a determining factor for the surge frequency of the centrifugal compressor based on the standing wave observed in author's numerical results. Furthermore, the diffuser was observed to be the first component to stall followed by stage stall. Huang et al. [147] numerically identified five stalls cells propagating at 0.85 times the impeller speed for the near surge condition. The numerical work of Després et al. [108] analysing near surge operation of a turbocharger compressor revealed the propagation of the instability caused by inducer reverse flow up to one duct diameter upstream. The authors did not observe any rotating stall cells in their results.

Mendonça et al. [39] observed narrow band noise at 0.7RO in the spectra of compressor ducts expected to be caused by the inducer stall, as leading-edge separation and stalled blade passages were identified. A spiral mode propagating upstream from the compressor impeller was detected for the aforementioned narrowband noise. In the numerical work of Bousquet et al. [148], the spectral characteristics of a probe placed at the impeller inlet were dominated by BPF tone at higher mass flow or design point while a tone corresponding to 6RO was the main feature for the near surge operation. The authors revealed that this tone was caused by the 6 vortices that are shed per revolution. Jyothishkumar et al. [110] identified a tone at 0.5RO in the spectra at the diffuser probe for the near surge operation and implied rotating stall as the cause of this tone. Similarly, Sundström and Mihăescu [37] also observed narrowband noise at the frequency corresponding to 0.5RO in the spectra at the diffuser probe for the near surge operation. Fontanesi et al. [71] observed narrow band noise at 1.5RO and attributed it to the periodic flow detachment and re-attachment at the compressor by-pass valve.

The modal decomposition of the numerical flow data using Dynamic Mode Decomposition (DMD) and Proper Orthogonal Decomposition (POD) is heavily used by the researchers at KTH to investigate the flow mechanisms. Sundström et al. [35] analysed the flow instabilities associated with the compressor operating at lower mass flow rates by decomposing the velocity field. The authors [35] demonstrated the presence of the compression wave and tip leakage flow in the system and suggested these phenomena as the cause of deterioration in the incidence angle leading to a rotating stall. Similarly, Semlitsch and Mihăescu [36] decomposed the velocity field in the impeller downstream region and showed that the highest amplitudes of the dominant POD modes were located in the diffuser-volute transition region. The authors also observed that the leading two DMD modes illustrate the same flow phenomenon as the leading two POD modes. Further investigation presented by Sundström et al. [126] demonstrated the first POD mode as an oscillatory mode corresponding to the filling and emptying effect seen at surge. The second POD mode corresponds to the structures associated with the flow reversal from the ported shroud and is implied to be the mechanism of the tonal noise at 0.5RO.

4.3 Flow field analysis

In this section, firstly the mean flow behaviour of the design and near surge operating conditions is presented. The identified flow phenomena are then further explored to throw some light on the mechanism of flow-induced noise. The analysis in this section is based on the results of the numerical configuration that yielded the least deviation from the experimental results (see Chapter 3), i.e. the LES model with higher mesh density (23 million cells) using a timestep that corresponds to 2° impeller rotation per iteration.

4.3.1 Flow features

The mean flow field in the compressor with emphasis on the flow through the PS cavity is discussed here. The flow in the compressor at the design point is similar to the one without any casing treatment, with a small fraction of incoming flow going through the PS cavity (for further details, see Sharma et al. [5]). The typical 'inverted S-shaped' flow structures, similar to those observed by Sivagnanasundaram et al. [144] are also identified in the PS cavity which causes a smooth area reduction of approximately half a radius as shown in Figure 4.1 (top).

The flow can either be removed or added into the blade passages based on the position of the impeller blades as shown in Figure 4.2 (top). The fluid in the proximity of the suction surface of a blade is pulled into the PS slot while the pressure surface pushes the fluid from the slot into the PS cavity. The position at which fluid is being drawn in or pushed out is attached to the blades, and the annular location changes as the impeller rotates. Furthermore, the velocity of flow undergoing 'push and pull' behaviour depends on the angular position on the rotor. For example, the blade marked as '5' (see Figure 4.2) shows an increase in the

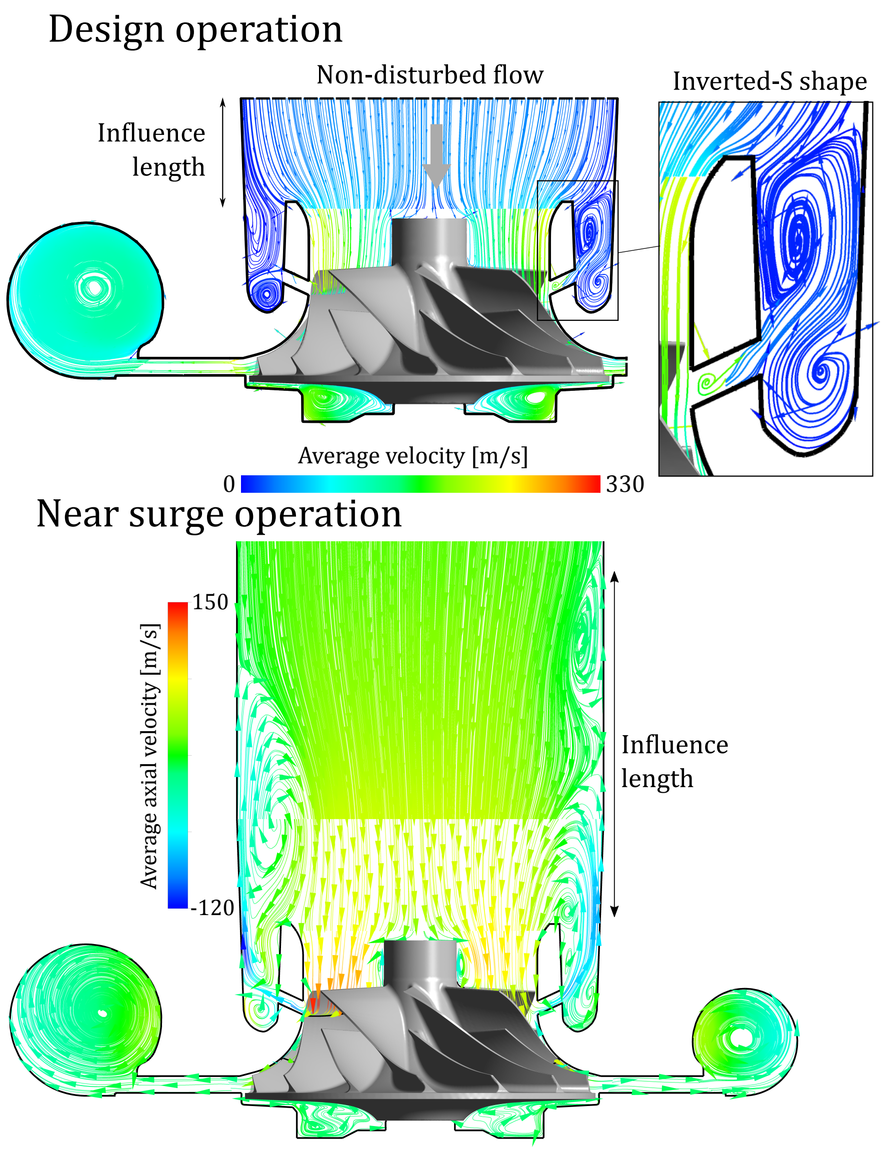

Fig. 4.1 Flow field characteristics for the design (top) and near surge (bottom) operation at the impeller axis plane. Surface streamlines coloured by average velocity magnitude for design condition demonstrate attached flow while the turbulent features formed by the interaction of the recirculating and the inlet flow are shown of near surge case.

velocity amplitude up till 32° and then decreases as observed in the 48° plot. Although the net flow is not significant, the back and forth motion of the fluid in the PS slot attached to the impeller could potentially act as an acoustic source amplifying the noise emission of the compressor.

Unlike the design operation, a significant fraction of incoming flow is observed to be recirculated through the PS cavity under near surge conditions. The flow with high circumferential velocity is removed from the impeller passages and recirculated to the inducer inlet via the PS

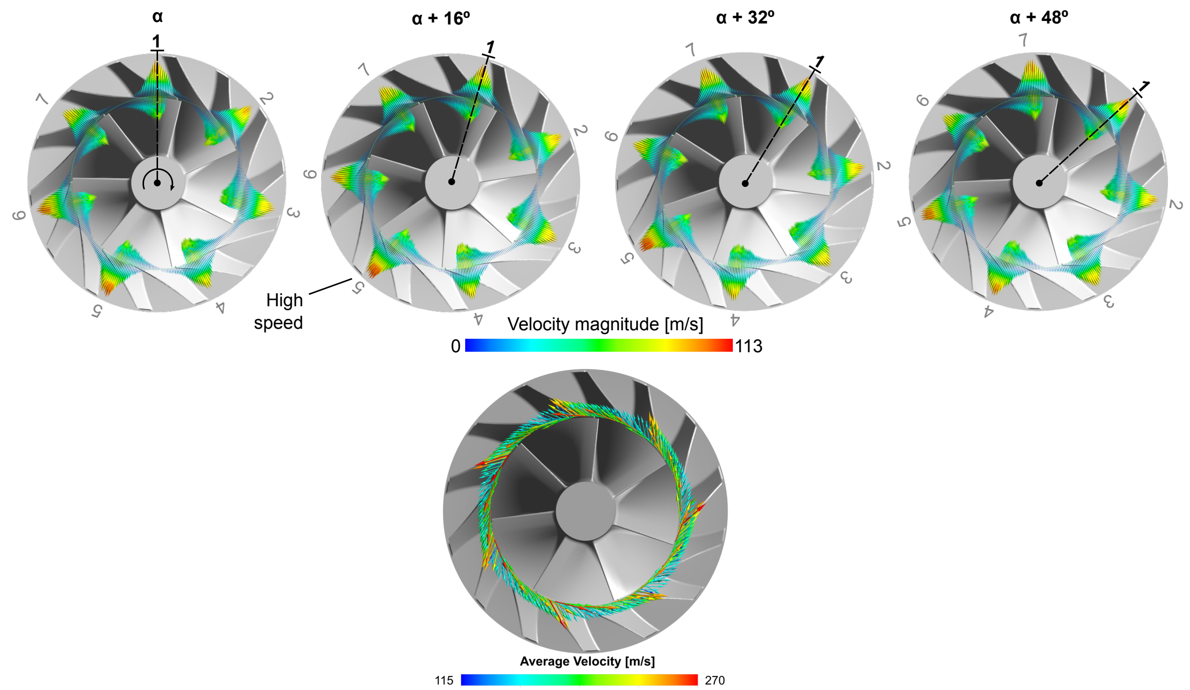

Fig. 4.2 Velocity vectors in the rotating frame at the PS slot location for design (top) and near surge (bottom) operation. The radially outward flow from blade passages into the PS cavity is observed for the near surge while four subsequent snapshots of velocity direction for design operation highlights how regions where the fluid is pushed out and pulled in rotate with the blades. A section of higher speeds is shown near the '5' mark, especially in the 16° and 32° plots.

cavity. The interaction of the recirculated flow with the inlet flow creates vortices as shown in Figure 4.1 (bottom). These flow structures cause a decrease in the effective area for the inlet flow, thereby increasing the bulk axial velocity of the inlet flow as observed in the velocity streamlines.

In addition to that, the increase in temperature of the inlet region is also a direct consequence of this interaction as the recirculated flow is hotter due to work imparted by the impeller. Furthermore, the swirl added into the compressor inlet flow by the recirculated flow significantly impacts the incidence at the leading edge of impeller blades. In opposed to the constant 'push and pull' behaviour of the fluid at the PS slot for design operation, Figure 4.2 (bottom) shows a unidirectional radially outward flow for the near surge operation. The flow exits the PS cavity in the form of high-speed jets corresponding to the structural struts.

In an effort to gain insights into the behaviour of the flow associated with the PS cavity that can act as a potential acoustic source, the flow exiting the PS cavity is further investigated for vortices and coherent structures. The predominant methods for vortex identification are either based on Velocity Gradient Tensor or on Vorticity [149]. The methods based on former include λ_2-criterion, Q-criterion, Δ-criterion, (Enhanced) Swirling-strength criterion and Triple

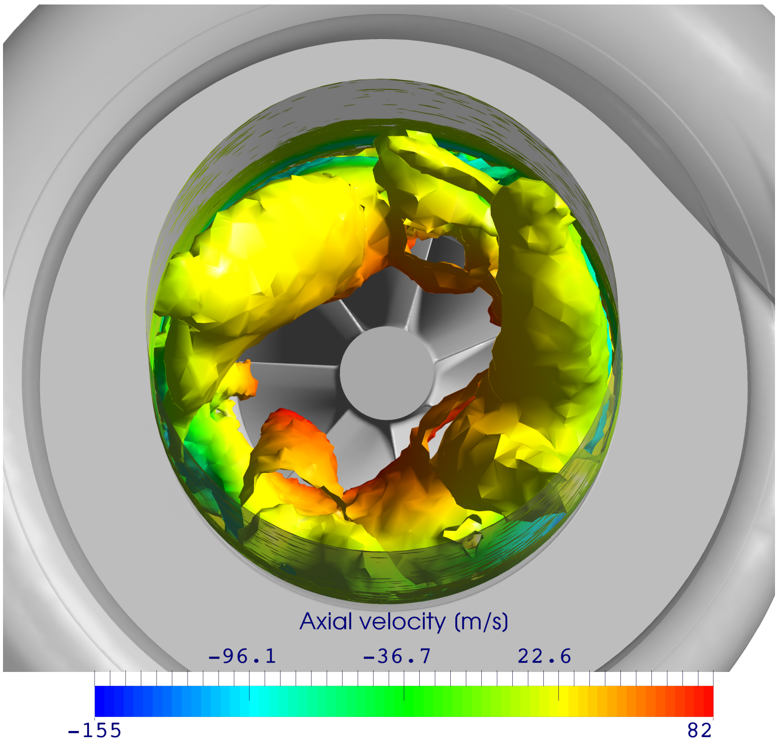

Fig. 4.3 High-speed jets corresponding to the struts are identified by λ_2 vortex criterion. The structures are coloured with average axial velocity.

decomposition) while the methods based on latter include Vorticity magnitude, Vorticity lines and Kinematic vorticity number. Further information on the methods of vortex identification including the ones specified above are well articulated in the work of Holmén [149]. The Galilean invariant property of λ_2 criterion makes it particularly suitable for identifying vortices in the flows where predominant flow direction is not clear and therefore, it is used in this work. This method uses the eigenvalues of a symmetric tensor computed from the velocity gradient to search for the pressure minima and establish vortex core [150].

Identification of the turbulent features in the inlet region using λ_2 criterion presented in Figure 4.3 clearly shows the interaction of jet-like recirculated flow with the inlet flow. These turbulent structures are hypothesised to be the mechanism of the losses identified in the 'Inlet-PS' mixing region [5].

The average velocity and pressure distribution in the mid-span impeller passages are presented in Figure 4.4. While the expected attached and smooth flow can be observed for the design condition, low-velocity stall cells corresponding to each main blade can be observed for the near surge condition. These stall cells are further investigated by studying the instantaneous meridional velocity distribution in the impeller passages for 50% blade span

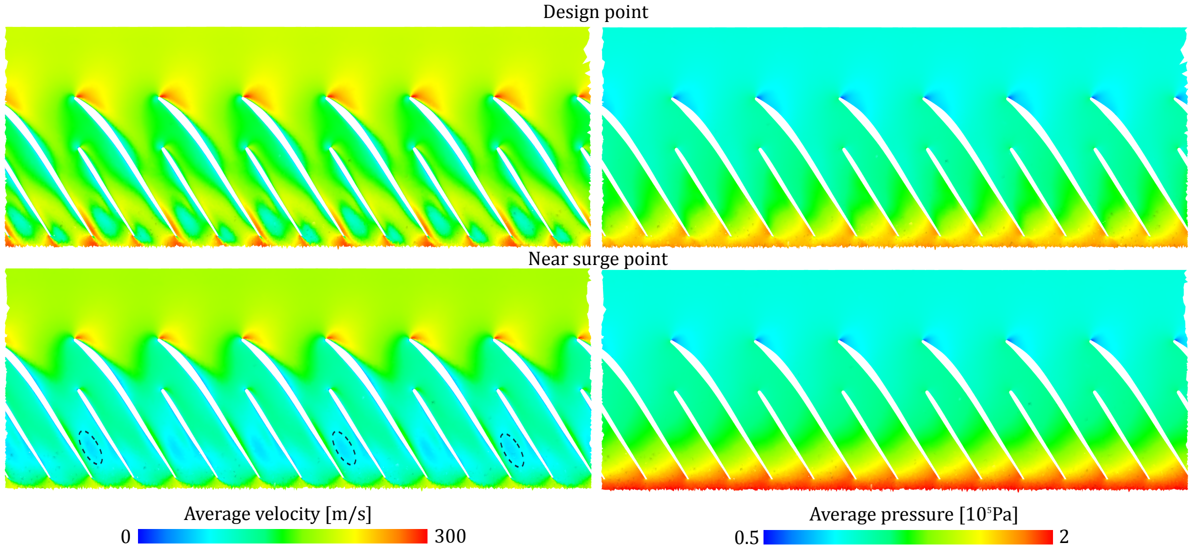

Fig. 4.4 Midspan blade-to-blade views of average velocity (left) and average pressure (right) for design (top) and near surge operation (bottom). The regularity of the impeller flow field is demonstrated for design operation while low-velocity stalls cells are observed for near surge condition.

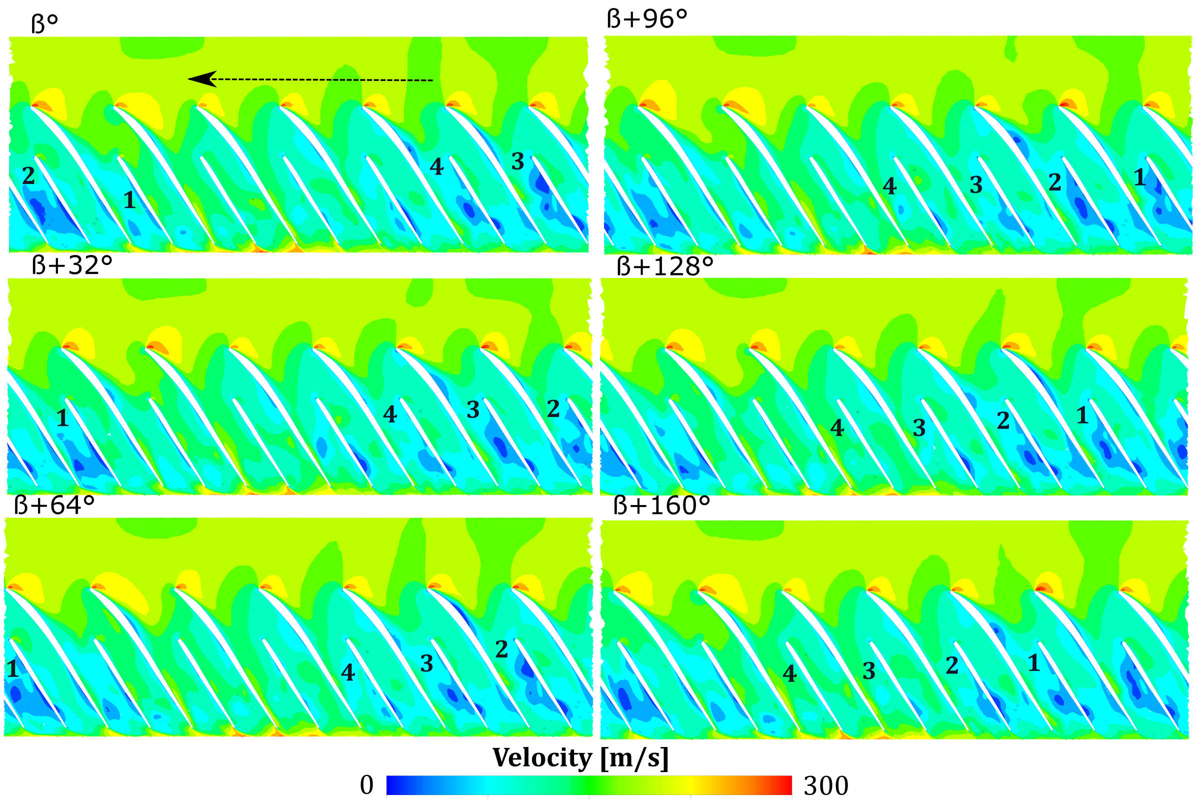

Fig. 4.5 Stall cell propagation demonstrated by colouring the 50% blade span surface with instantaneous meridional velocity for six subsequent impeller positions.

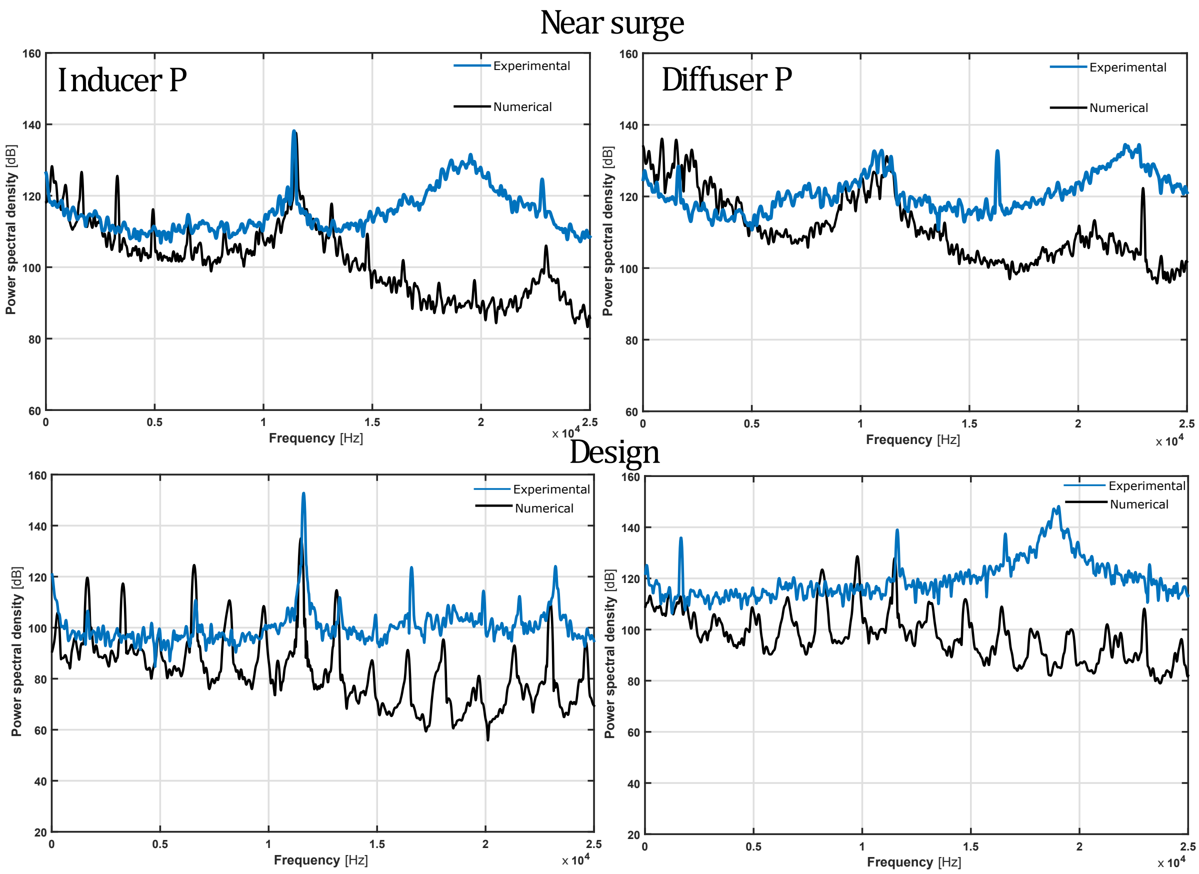

Fig. 4.6 Inducer (left) and diffuser (right) probe spectra for the design (bottom) and near surge (top) operation.

at six time instances, each corresponding to 32° impeller rotation as shown in the Figure 4.5. The propagation of multiple stall cells can be clearly seen in the plot by observing the flow behaviour in the specified blade passages 1, 2, 3 and 4. In the first time instance i.e. $\beta°$, stall initiation and fully developed stall can be observed in the passage 1 and passage 2 respectively while passage 3 and passage 4 are recovering from the stall. As the impeller blades rotates by 32° i.e. $\beta + 32°$, development of stall can be seen in the passage 1 while the strength of the stall is decreased in the passage 2, passage 3 and passage 4. Similarly, by sixth time instance i.e. $\beta + 160°$, the blade passage 4 and passage 3 are free of stall while passage 2 and passage 1 are recovering from the stall. These stall cells are seen to propagate circumferentially around the impeller with a speed of approximately (0.32-0.4)RO which corresponds to the peak seen in the diffuser spectra at 0.37RO.

4.3.2 Acoustic features

Inducer and diffuser spectra for the design and near surge operation of the studied speedline are presented Figure 4.6. The inducer spectrum for the design operation is dominated by the RO and blade pass tones while the primary characteristics for near surge point include blade pass and a broadband elevation centred around 19 kHz which is not captured by the numerical model. The diffuser spectrum for the design condition also predominantly consists of RO tones although the numerical spectrum accentuates these tonal features relative to measured values. Similar to the inducer spectrum for the near surge condition, broadband elevation observed in the measured diffuser spectrum for the design condition is not captured by the numerical model. On the other hand, the diffuser spectrum of the near surge operation show a broadband elevation in the region of 6 - 11.5 kHz along with the relatively stronger 0.4RO and 1RO tone. It is worth noting that the low-frequency tonal and broadband features associated with near surge operation are not observed for the current case. This can be attributed to the characteristics of PS casing treatment.

On the basis of literature available on axial compressors, the 'Buzz-saw' or RO tones are expected to be caused by the rotor-alone pressure field, dominated by shock waves attached

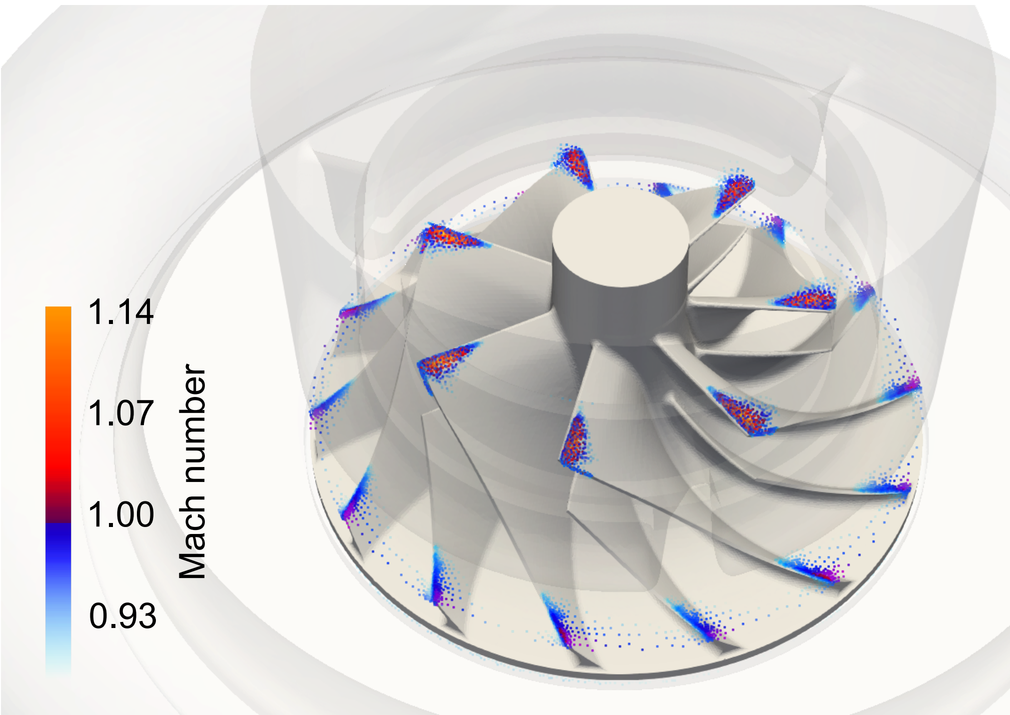

Fig. 4.7 Close-up view of the impeller, highlighting locations of the flow featuring transonic, sonic and supersonic speeds. Results show that main blade leading edges and both main and splitter blade trailing edges reach sonic conditions for design point.

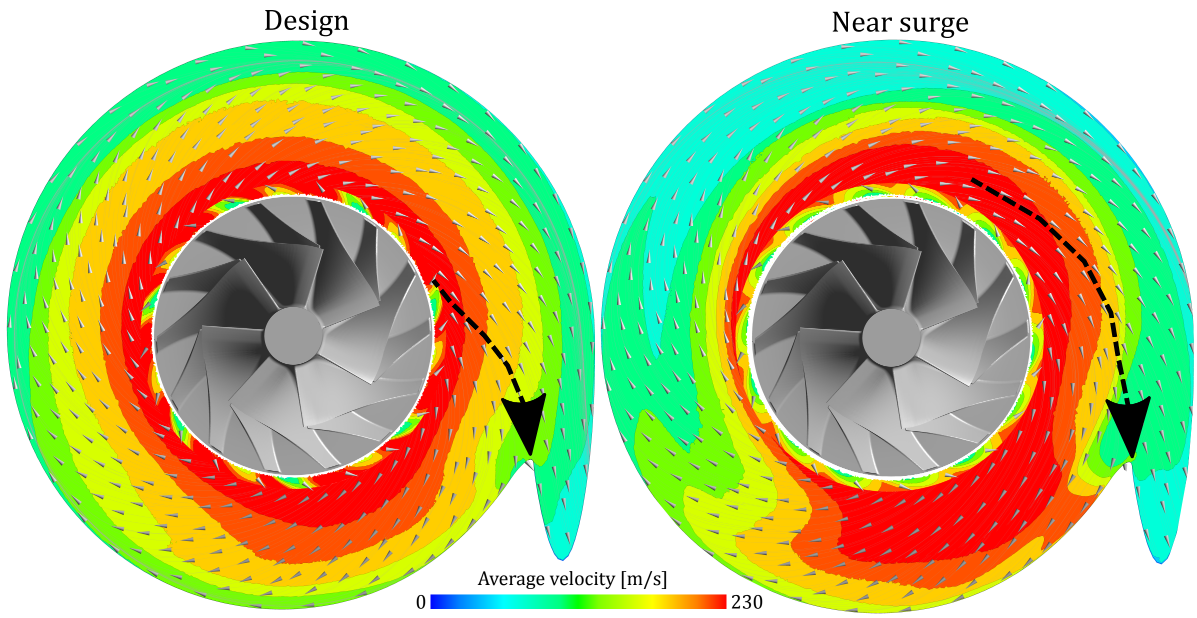

Fig. 4.8 Velocity vectors on the plane inside diffuser in vertical proximity with volute tongue for design (left) and near surge (right) operation. The flow coming out of impeller and interacting with the volute tongue is observed to travel relatively longer for the near surge point.

to the rotor blades at higher speeds [27]. In order to test the aforementioned hypothesis, regions with Mach number $0.9 < M < 1.14$ for the design operation are plotted in Figure 4.7 demonstrating the transonic conditions at the leading edges of the impeller main blades and at trailing edges of both main and splitter blades. It is expected that the velocity increase due to area reduction as observed in Figure 4.1 (top) plays a role in manifesting these sonic conditions. Nonetheless, the presence of sonic conditions is in line with the hypothesis of the aforementioned authors, and indeed, the mechanism of buzz-saw tone is fairly similar to that for the axial compressors.

As discussed in Chapter 2 (see Section 2.5), the expected mechanism of the broadband elevations around 19 kHz is the interaction of swirling flow with the structural components, viz. struts in the PS cavity for the case of the inducer spectrum of near surge condition and the volute tongue in the diffuser spectrum of design condition. It is interesting to observe similar broadband feature focused around 22 kHz in the diffuser spectrum of the near surge point. This raises an exciting question; are these two broadband effects (19 kHz and 22 kHz) caused by distinct flow mechanisms, or this is merely a shift in the frequency range due to a shift in the flow conditions from design to near surge? The flow in the impeller downstream region is investigated to throw some light on this issue. As seen in Figure 4.8, the distance travelled by the flow before interacting with the volute tongue is lower for design conditions relative to near surge conditions at similar speeds. This implies that the characteristic frequency at design point should be higher than the near surge case, but the opposite is observed. Therefore, the broadband around 22 kHz in the diffuser spectrum of near surge point seems to be a distinct feature and not a shift of the broadband observed in the corresponding spectrum of the design point. The broadband centred around 22 kHz could be a harmonic of TCN, and the related flow mechanism is explored with the help of modal decomposition presented in the next section.

4.4 Modal decomposition

Time-averaged aero-thermodynamic quantities such as mean pressure, velocity or turbulent kinetic energy profile can easily be computed by statistical post-processing of numerical or experimental data while phase averaging and Fourier transform can help in identifying the expected significant frequencies in the flow. Aforementioned conventional post-processing techniques might overlook structures that are coherent not only in time but also in space. Therefore, in order to identify the structures with well-defined properties of energy or time-dependency without any prior knowledge of the flow, modal decomposition methods are used. Moreover, as the advanced computational and experimental measurements techniques are generating large data sets of instantaneous flow variables, the reduction of flow field data to a low-dimensional form is ever more important in studying and understanding the dynamic behaviour of the flow.

Modal decomposition can be referred to as a mathematical procedure to extract the energetically and dynamically dominant features of the fluid flows. The outputs of this mathematical analysis are the spatial features of the flow called *modes* which are accompanied by characteristics value, defining either the energy levels or growth rates and frequencies. The modes can be computed by either modal decomposition of flow field data generated by experimental and numerical methods, or from the governing equations. The modal decomposition algorithms that use flow field data as input are referred to as *data-based* techniques in literature while the methods that use governing equations, specifically discrete operators from the Navier-Stokes equations, are referred to as *operator-based* techniques. The author recommends the work of Taira et al. [151] for a brief summary of the various modal decomposition techniques.

4.4.1 Theoretical background

The mathematical treatment of a key modal decomposition technique used to study a range of fluid flows is presented in this section. The discussion is limited to the data-based techniques which primarily comprises of Proper Orthogonal Decomposition (POD) and Dynamic Mode Decomposition (DMD), as numerical flow field data is used as an input for modal decomposition in this work. The decomposition methods presented here are based on the eigenvalue and singular value decompositions of matrices. Eigenvalue decomposition is limited to square matrices while singular value decomposition can be performed on rectangular matrices too. The principles of eigenvalue and singular value decomposition are not covered here but are readily available in the textbooks by Saad [152] and Horn and Johnson [153]. The optimal set of modes that can represent the given data on the basis of energy are determined by POD while the modes resolved by DMD are accompanied by a single frequency of oscillation. Although specific dynamic structures can be isolated with DMD, it is difficult to determine their physical relevance with certainty. Therefore, POD is an essential first step to identify the physically relevant flow structures whose frequency characteristics can then be later determined from the results of DMD. In this thesis, the macroscopic fluid structures which carry the most energy are the focus of the modal decomposition exercise. These large-scale structures are observed to be well resolved in SBES configuration (see Chapter 3), in addition to the lower computational and storage memory overhead benefits relative to LES afforded by SBES. Therefore, the pressure field computed from the SBES configuration with 10 million cells and timestep corresponding to $4°$ impeller rotation is used as an input for the modal flow decomposition.

Proper Orthogonal Decomposition (POD)

The Proper Orthogonal Decomposition (POD) computes the modes based on optimising the mean square of the studied flow variable and in essence, is an algorithm to decompose data into a minimal number of basis functions or modes to capture as much energy as possible. This technique was first applied in the context of probability theory to explore the relationship between variables in a dataset. However, it soon found application in many other fields, including fluid dynamics as demonstrated by Lumley [154] to extract the coherent structures from the turbulent flow field. The technique in itself is identified by several names which include POD [155], Karhunen–Loève expansion [156], principle component analysis (PCA) [157], Hotelling analysis, empirical eigenvalue decomposition and others depending on the field of application.

In applications of the POD to fluid flow, the unsteady component of vector or scalar flow field variable is assumed to be well represented in terms of a generalised Fourier series for some set of basis functions. The unsteady component $\mathbf{x}(\xi,t)$ of a flow field variable $\mathbf{q}(\xi,t)$ with a temporal mean $\bar{\mathbf{q}}(\xi)$ can be decomposed as

$$\mathbf{x}(\xi,t) = \mathbf{q}(\xi,t) - \bar{\mathbf{q}}(\xi) = \sum_j \mathbf{a}_j \phi_j(\xi,t) \tag{4.1}$$

where $\phi_j(\xi,t)$ and a_j represents the modes and expansion coefficients while ξ denotes the spatial vector. The optimal set of basis functions $\phi_j(\xi,t)$ for the available field data $\mathbf{q}(\xi,t)$ are sought in the method of the POD. The modes computed from Equation 4.1 are functions of space and time/frequency. Further splitting of space and time would lead to the need for computing only spatial modes. This can be achieved by separating the variables in the Equation 4.1, leading to the following expression

$$\mathbf{x}(\xi,t) = \mathbf{q}(\xi,t) - \bar{\mathbf{q}}(\xi) = \sum_j \mathbf{a}_j(t)\phi_j(\xi) \tag{4.2}$$

where modes $\phi_j(\xi)$ and expansion coefficients $\mathbf{a}_j(t)$ are functions of only space and time respectively. It is worth pointing out that the separation of variables employed to obtain the form presented in Equation 4.2 may not be appropriate for all problems i.e. a linear combination of modes and their respective temporal coefficients may not accurately represent the desired flow variable. Therefore, the selection of the form should be driven by the properties of the flow and the information to be extracted by the flow decomposition as shown in Holmes et al. [158].

The snapshots of the unsteady component of scalar field $\mathbf{q}(\xi,t)$ stacked into a matrix $\mathbf{X}$ for m discrete time instances are used as input for the POD. $\mathbf{X}$ is a $n \times m$ matrix with n as a number of grid points (spatial data) and m as the number of snapshots (temporal data).

$$\mathbf{X} = [\mathbf{x}(\xi,\mathbf{t_1})\,\mathbf{x}(\xi,\mathbf{t_2})\ldots\mathbf{x}(\xi,\mathbf{t_m})] \tag{4.3}$$

The optimal basis functions that can best represent the data described by $\mathbf{q}(\xi,t)$ in a minimal number of modes are $\phi_j(\xi)$ are then computed. This can either be done by computing eigenvectors ϕ_j and eigenvalues λ_j (Equation 4.4) from the covariance matrix $\mathbf{R}$ of $\mathbf{x}(\xi,t)$ which is a $n \times n$ matrix or by directly decomposing matrix $\mathbf{X}$ with Singular Value Decomposition (SVD) as represented in Equation 4.5.

$$\mathbf{R}\boldsymbol{\phi}_\mathbf{j} = \boldsymbol{\lambda}_\mathbf{j}\boldsymbol{\phi}_\mathbf{j} \tag{4.4}$$

where $\mathbf{R}$ is the *covariance matrix*

$$\mathbf{R} = \sum_{i=1}^{m} \mathbf{x}(t_i)\mathbf{x}^T(t_i) = \mathbf{X}\mathbf{X}^\mathbf{T} \tag{4.5}$$

$$\mathbf{X} = \Phi\Sigma\Psi^T \tag{4.6}$$

where orthonormal matrices Φ and Ψ are left and right singular vectors of $\mathbf{X}$ while diagonal matrix Σ contains singular values $(\boldsymbol{\sigma}_\mathbf{1}\,\boldsymbol{\sigma}_\mathbf{2}\ldots\boldsymbol{\sigma}_\mathbf{m})$.

The singular vectors Φ and Ψ are corresponding eigenvectors of $\mathbf{X}\mathbf{X}^\mathbf{T}$ and $\mathbf{X}^\mathbf{T}\mathbf{X}$ respectively while singular values can be related to eigenvalues by $\sigma_j^2 = \lambda_j$. The combination of $\Sigma\Psi^T$ represent the time evolution $a_j(t)$ term for corresponding ϕ_j. Therefore, SVD of $\mathbf{X}$ can directly yield POD modes Φ. Also, the robust nature of the SVD based method against round off errors [20] makes it a better candidate relative to the classical POD method and hence, SVD is used in this thesis to compute the POD modes. The output of POD would include the set of orthogonal modes $\phi_j(\xi)$ and their respective temporal coefficients $a_j(t)$ along with energy levels λ_j arranged by relative energy content. It is worth mentioning that the number of modes that should be considered (q) can be determined using the following principle

$$\sum_{j=1}^{q} \lambda_j \Big/ \sum_{j=1}^{n} \lambda_j \approx 1 \tag{4.7}$$

Since the matrix is of the order of grid points $(n \times m)$, a method similar to the method of snapshots [151] is used to make the SVD problem computationally tractable. The property of POD implying that decomposition using the data from a subset of the system instead of the entire system would yield the same dominant spatial modes is exploited and SVD is performed on a reduced or economy sized matrix which consists of a set of snapshots $\mathbf{x}(\xi_i, t)$ such that $i = 1, 2 \ldots r$ with $r \ll n$.

4.4.2 Methodology

The numerical results from the Hybrid RANS-LES (SBES) model described in Chapter 3 are used for modal decomposition. In the current work, the unsteady pressure scalar is the decomposed flow variable with the grid pressure values recorded for approximately 42 revolutions at a constant sampling time corresponding to 4° rotation of impeller. The pressure snapshots matrix $\mathbf{x}(\xi_i, t)$ is built using 10^6 (r) rows by randomly selecting from the available 10^7 (n) cells. The consistency in the pressure trace of the snapshot matrix is warranted by fixing the spatial vector ξ_i in the pressure scalar $\mathbf{x}(\xi_i, t)$ i.e. each column of matrix $\mathbf{X}$ should represent the same cell. This is achieved by selecting the reference 10^6 cells and then searching those reference cells across all snapshots. As the cells inside the rotating domain (impeller) change their position due to sliding mesh, they are not considered at this stage. The pressure snapshot matrix is then decomposed by economy SVD to yield modes and respective temporal coefficients.

4.4.3 Results

The results from the POD of the pressure variable for design and near surge point using the aforementioned methodology are described in the subsections below.

Design point

As stated above, the output of POD includes the set of orthogonal modes ϕ_j with their corresponding temporal coefficients $a_j(t)$ and energy levels λ_j. The energy levels for the first 14 modes (ϕ_2 to ϕ_{15}) computed from the pressure data of design operation is presented in the form of a Pareto chart in Figure 4.9 (left). First mode ϕ_1 describes the averaged steady pressure and subsequent, often alternated modes, account for the pressure oscillations. The first two modes in the chart i.e. ϕ_2 and ϕ_3 are seen to possesses significantly higher energy content relative to the rest of the modes. The dominant spectral features of these 14 POD modes obtained by computing and normalising the PSD of their respective temporal coefficients $a_j(t)$ are shown in Figure 4.10. It can be observed that the first two modes ϕ_2 and ϕ_3 that comprise the highest energy in the system are related to the expected blade pass tones. By assessing the spectral features presented in Figure 4.10, three modes ϕ_2, ϕ_4 and ϕ_8 corresponding to distinct frequency content are selected for further investigation with an intent to understand the dominant flow phenomenon for each mode.

The spectra of the modes ϕ_2, ϕ_4 and ϕ_8 shown in Figure 4.11 (left) further show the segregation of the dominant lower frequency (ϕ_4), medium frequency (ϕ_2, containing the BPF) and higher frequency (ϕ_8, containing a BPF harmonic) content. The spatial distribution for these three modes are shown in Figure 4.12 (left). The top plot of Figure 4.12 can be analysed to understand the spatial distribution of the pressure field associated with the frequency or acoustic features of mode ϕ_2. The positive and negative parts of the mode amplitude shown in the view of the whole domain indicates how the BPF and/or middle frequency content is propagating through the domain. A spiral structure is clearly observable in the outlet duct and the volute, whereas in the inlet side, the spiral structure is more complex, possibly due to the interactions of PS cavity pressure field and the struts with the incoming flow. Although this mode features the highest energy, it becomes attenuated not far from the compressor itself. Further insight into the sources of these oscillations can be obtained by plotting iso-volumes of only the highest energy areas of the mode, realized in the detailed compressor view of Figure 4.12 by only displaying the 5$^{\text{th}}$ and 95$^{\text{th}}$ percentiles of the mode amplitude ϕ_2. As $a_2(t)$ changes sign at approximately 11.5 kHz and is multiplied by these ϕ_2 amplitudes, the displayed regions will alternately hold the highest 5% of the mode energy. From the detailed view, it can

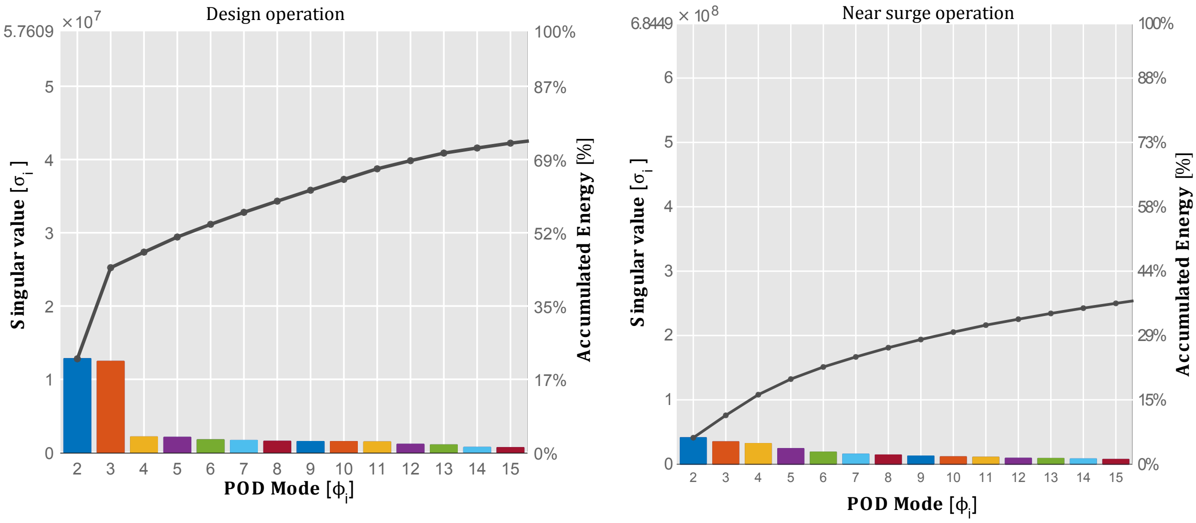

Fig. 4.9 Pareto chart of the energy levels λ_j arranged by relative energy content for the first 14 POD modes (ϕ_2 to ϕ_{15}) for design (left) and near surge (right) conditions.

be clearly observed that the sources of the BPF tonal noise are located both in the diffuser and PS cavity region due to their proximity to trailing and leading edges of the blades.

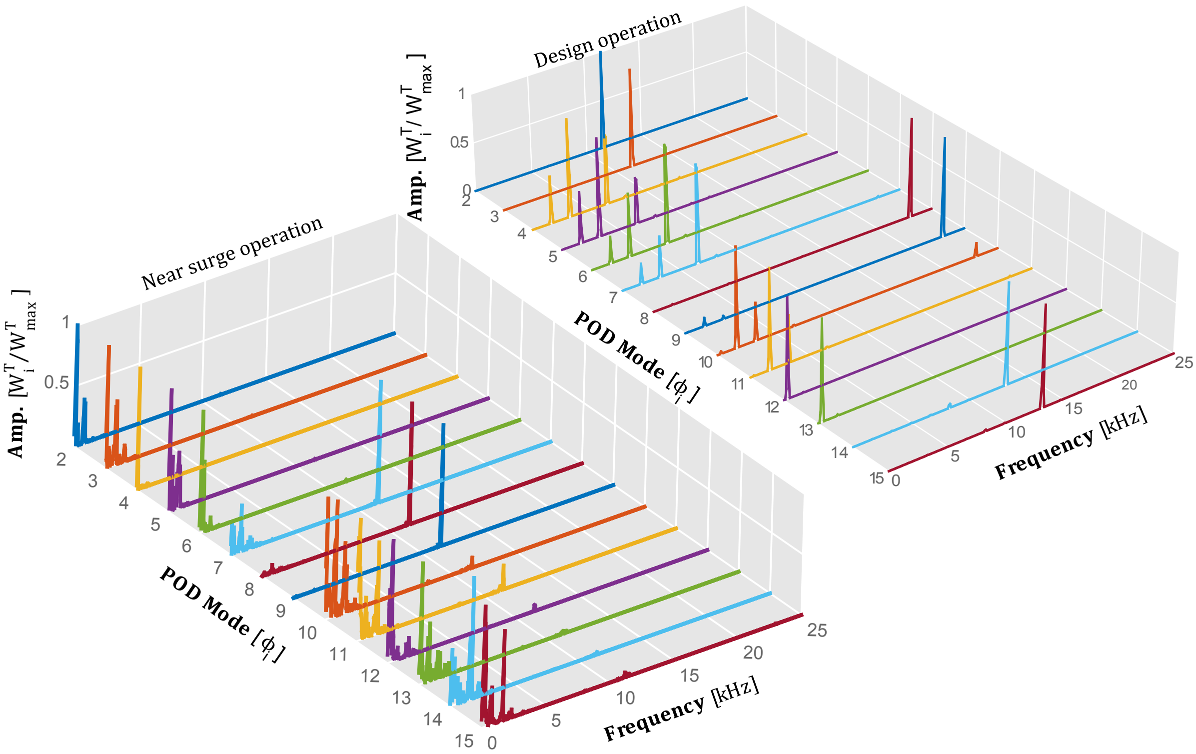

Fig. 4.10 The spectral content of the first 14 POD modes (ϕ_2 to ϕ_{15}) normalised by the maximum amplitude of each corresponding mode for design (right) and near surge (left) conditions.

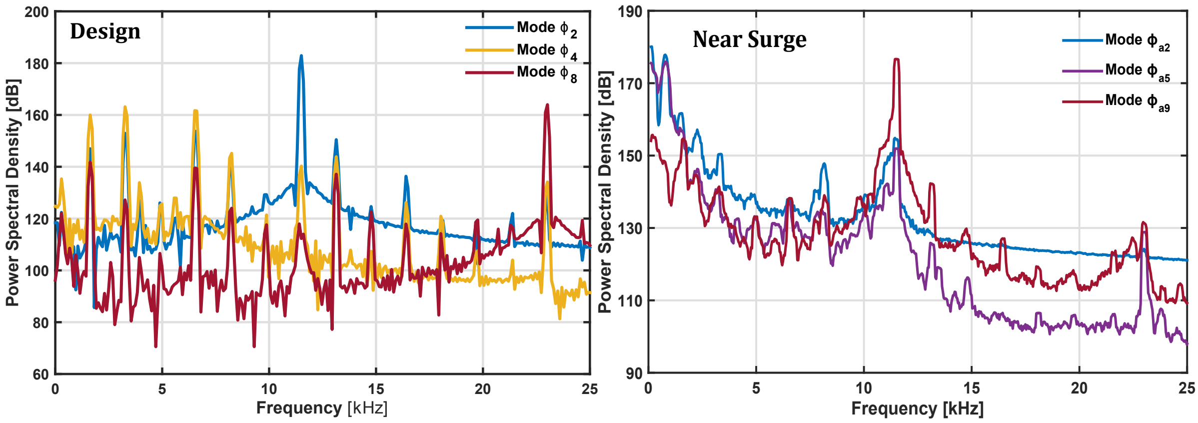

Fig. 4.11 The spectral content of the time evolution $a_j(t)$ of the selected POD modes for design (left) and near surge (right) conditions in order to analyse the distinct frequency content of the total flow field $\sum a_j \phi_j$

From the analysis of the spatial pressure distribution of the ϕ_4 mode corresponding to the lower frequency content, it is observed that for the outlet duct, the mode propagates in a plane wave fashion, whereas in the inlet duct, the spiral structure is still present. Regarding the top 5% energy, in this case, it is concentrated on the ported shroud. It appears that, even though the compressor with PS is behaving as a standard compressor in terms of performance, the interaction of impeller and PS cavity is creating pressure fluctuations that impacts the acoustic output of the compressor. Furthermore, the slot seems to provide an acoustic path that enhances the transmission of downstream (diffuser) produced oscillations to the inlet duct.

The higher frequency content illustrated by mode ϕ_8 appears to behave similarly to ϕ_2 when analysing the whole domain. The spatial distribution features spiral propagation in the inlet and alternating regions in the outlet, although in this case a relatively complex spiral shape can be seen in the first portion of the outlet before the area expansion, with an irregular transition to the rest of the duct. As for the higher energy sources of this mode shown in the detailed view at the bottom right of Figure 4.12, they show a clear pattern in the compressor diffuser, with only smaller structures along the ported shroud.

Surge point

Similar to the analysis presented for the design point, the energy levels for the first 14 modes (ϕ_2 to ϕ_{15}) computed from the pressure data of near surge operation are presented in the form of a Pareto chart in Figure 4.9 (right). The first mode ϕ_1 describes the time averaged pressure field and often displays alternating values in magnitude, implying the pressure oscillations. The energy is much more evenly distributed among the modes for near surge points as opposed to the design operation. The normalised spectral features of these POD modes are presented

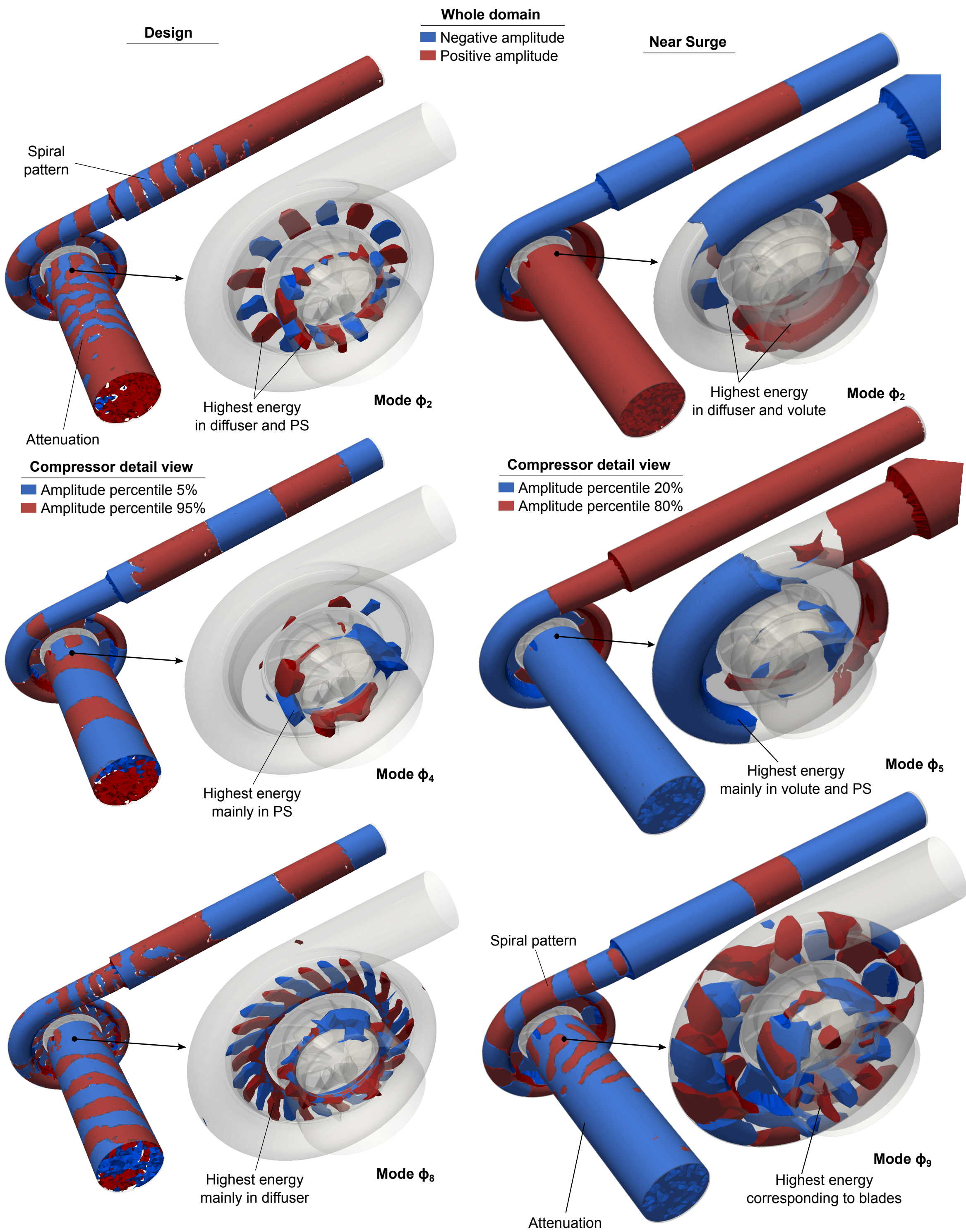

Fig. 4.12 Spatial distribution of the selected POD modes for design (left) and near surge (right) condition visualized by iso-surfaces of positive and negative values in the whole domain, and by iso-volumes of top 5% (design) and 20% (surge) energy in the compressor detail view.

in Figure 4.10. The presence of expected lower frequency content in the dominant modes is observed for near surge as opposed to the tonal noise for the design condition. Three modes ϕ_2, ϕ_5 and ϕ_9 are selected by assessing the normalised spectra shown in Figure 4.10 for further investigation.

The detailed spectra of these three modes ϕ_2, ϕ_5 and ϕ_9 presented in Figure 4.11 (right) shows a distinction in their respective content with ϕ_2 showing dominant content in the frequency range prior to first BPF while ϕ_9 presents the content in the range after the first BPF. Mode ϕ_5 shows the content present mildly all across the spectrum. Although BPF can be seen in the spectra of all three modes, the strength of the BPF varies; least for ϕ_2 and highest for ϕ_9. The spatial distributions for these three modes are shown in Figure 4.12. Mode ϕ_2 has the highest energy and corresponds to characteristics between the first and third rotating tone. The spatial distribution of the pressure field for ϕ_2 (top plot) is analysed to throw light on the source of the acoustic phenomenon and indicate how the low-mid frequency range broadband content propagates through the domain. The spatial distribution shows large fluctuating amplitudes in the impeller downstream region specifically the diffuser-volute region while the impeller upstream region presents a consistent pressure field. Further insight on the noise sources are gained by plotting iso-volumes of the highest energy areas of the mode in the detailed view of the Figure 4.12 wherein 20$^{\text{th}}$ and 80$^{\text{th}}$ percentiles of the mode amplitude are shown.

In the detailed view for ϕ_2, it can be clearly seen that the sources of low-mid frequency noises are located in the impeller downstream components, specifically the diffuser-volute region . The impeller upstream regions, including the ported shroud, do not show any high energy content for the ϕ_2 mode. It appears that even though the PS is recirculating the low momentum flow from blade passages to the impeller inlet, the behaviour of the recirculated flow does not have a significant impact on the generation or transmission of the mid-low frequency characteristics.

Mode ϕ_9 corresponds to the tonal characteristics of the compressor noise spectrum including BPF and ‘buzz-saw’ tones. Spatial distribution of the pressure field (bottom plot) indicates that the tonal noise propagates through the domain in the form of spiral structures that attenuate rapidly with distance from the impeller. A detailed view of the high energy structures indicates the rotating features associated with the leading and trailing edges of the blade in the PS and diffuser region respectively as the sources of tonal noise. The PS cavity is seen to propagate the rapidly attenuating rotor alone pressure field in the impeller upstream direction.

Mode ϕ_5 which corresponds to the amalgamation of the low and high frequency characteristics does shows some part of broadband noise as well as mild BPF tones. Spatial distribution of the pressure field (middle plot) is similar to that of ϕ_2, along with pressure features in the PS cavity region. The detailed view shows that the high-energy structures are concentrated mostly in the volute but some features can also be observed in the PS cavity region reinforcing that the broadband content is localised in the impeller downstream region while tonal content is propagated through both diffuser and PS cavity regions.

4.5 Conclusions

In this chapter, the dominant flow features of the compressor operating at the design and near surge conditions have been analysed to explore the mechanism responsible for the corresponding acoustic characteristics. Furthermore, the dominant flow structures and their frequency spectra are identified by decomposing the numerical pressure data using the POD. The analysis of flow features is based on the high grid density LES model while modal decomposition is performed on the data from SBES model.

For the design operation, although the flow inside the compressor appears to be steady and attached, a back and forth movement is observed at the PS slot with clear structures rotating with the blades, featuring differences in the speed at specific angular coordinates. On the contrary, a unidirectional radially outward flow was observed at the PS slot for the near surge operation. The flow then exits the PS cavity in the form of high-velocity jets that interact with the incoming flow leading to the propagation of unsteadiness upstream. Low-velocity stall cells were also identified and observed to propagate circumferentially along the blades at $0.3-0.4$ times the impeller speed.

The acoustic spectra for the design point are observed to be dominated by characteristic 'buzz-saw' or RO tonal noise. This tonal feature was attributed by previous researchers to sonic conditions being reached in the impeller, a phenomenon seen in axial compressors. The numerical results in this thesis confirm this hypothesis by identifying sonic regions attached to the leading edges of the main blades. Additionally, sonic conditions are also reached in the tips of the trailing edges for both main and splitter blades.

To investigate the acoustic influences, Proper Orthogonal Decomposition was applied to the pressure data computed via numerical simulations. The decomposition of the dynamic pressure field and therefore the spectral signature into its constituent modes allowed the separate analysis of lower, medium and higher frequency characteristics of the compressor pressure field. Inspection of the spatial distribution of the modal energy illustrated propagation patterns. For the design condition, the role of the diffuser and the ported PS cavity in housing the more energetic sources of the oscillations was demonstrated. In particular, while high-frequency content dominated by the BPF and its higher order harmonics shows a clear influence on the diffuser, at the lower and mid frequencies, it is the PS cavity that contains the largest amplitudes of the oscillations. For the near surge conditions, diffuser and volute were observed to be housing the more energetic sources of the broadband content. In contrast to the results of design conditions, the PS cavity was not seen to be associated with the significant source of noise content for near surge operation.

Chapter 5

Impact of the ported shroud on the acoustic features*

Contents

*Content presented in this chapter has been either published or under review for publication in the following papers:

- Impact of impeller casing treatment on the acoustics of a small high speed centrifugal compressor [3]
- Impact of impeller casing treatment on the acoustics characteristics of a compressor operating at design and near surge conditions [8]

5.1 Introduction

In the previous chapters, different numerical setups have been explored, and the results from selected configurations are used to analyse the acoustic characteristics of the ported shroud (PS) open configuration operating at the design and near surge condition of the designated speedline (99 krpm). In this chapter, the impact of casing treatment on the acoustic emission of the compressor is quantified by comparing the results of the open and blocked PS configurations for the design and near surge conditions of the investigated speed line.

The available literature is presented in Section 5.2 followed by the brief recapitulation of the numerical configuration in Section 5.3. The impact of casing treatment on design and near surge operating conditions are presented in Section 5.4 and Section 5.5 respectively.

5.2 Literature review

As pointed in the first chapter, the literature on the acoustic impact of casing treatment is scarce, and the general perception [57, 58] is that the casing treatment deteriorates the acoustic spectra of the compressor. Chen and Yin [57] and Chen and Lei [58] pointed out the 'noise issue', specifically BPF as the reason for the limited use of casing treatment in the compressors used in the turbochargers of passenger cars without providing any evidence for these claims.

During the time frame corresponding to the later part of this thesis research, a few [159, 109] studies on the acoustic impact of the casing treatment were published with somewhat contrary results.

Dehner et al. [159] experimentally investigated the impact of ported shroud casing treatment and observed a decrease in the overall noise levels at the inlet duct for design operation despite increased tonal content by using casing treatment. For near surge or low flow conditions, an increase in the overall noise levels was seen at the inlet. The spectrum measured at the outlet duct for the ported shroud compressor showed little differences at near surge condition while a decrease was again seen at the design conditions. It is worth pointing out that the casing treatment used in this work decreased the stable flow region of the compressor rather than increasing it.

Fardafshar and Koutsovasilis [109] explored the impact of the ported shroud by modelling the near-field spectra of the compressors with and without casing treatment at near surge and choke condition. The results showed higher noise levels for the compressor without casing treatment for near surge operation while lower noise levels for the same compressor were seen for choke operation.

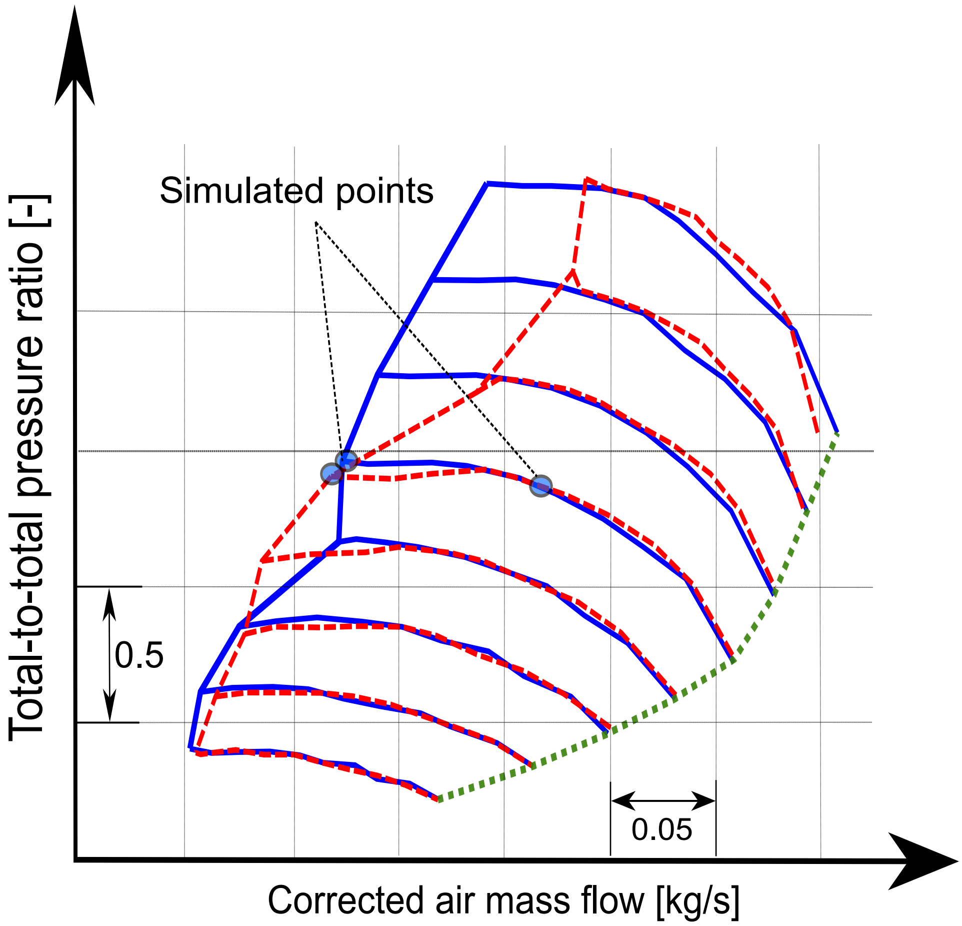

Fig. 5.1 Experimental compressor maps for the open and blocked configurations, highlighting the investigated operating points which include design and near surge conditions of 99 krpm speedline in both configurations.

5.3 Numerical configuration

The work in this chapter is focused on predicting the differences between two compressor configurations that were observed up until the blade pass frequency in the experimental measurements (see Chapter 2). In order to achieve this, the numerical configuration based on the SBES turbulence formulation with 10 million cells and timestep corresponding to 4° rotation of impeller per iteration is employed. The limitations of this numerical set-up which are specified in Chapter 3 include the inability to accurately capture the overall levels and decay rates. Since this chapter is concerned about the differences between the two configurations rather than the absolute values; the aforementioned numerical set-up is the computationally optimal choice.

The investigated design and near surge operating conditions for PS open and blocked configurations are highlighted in the compressor map presented in Figure 5.1. The PS blocked

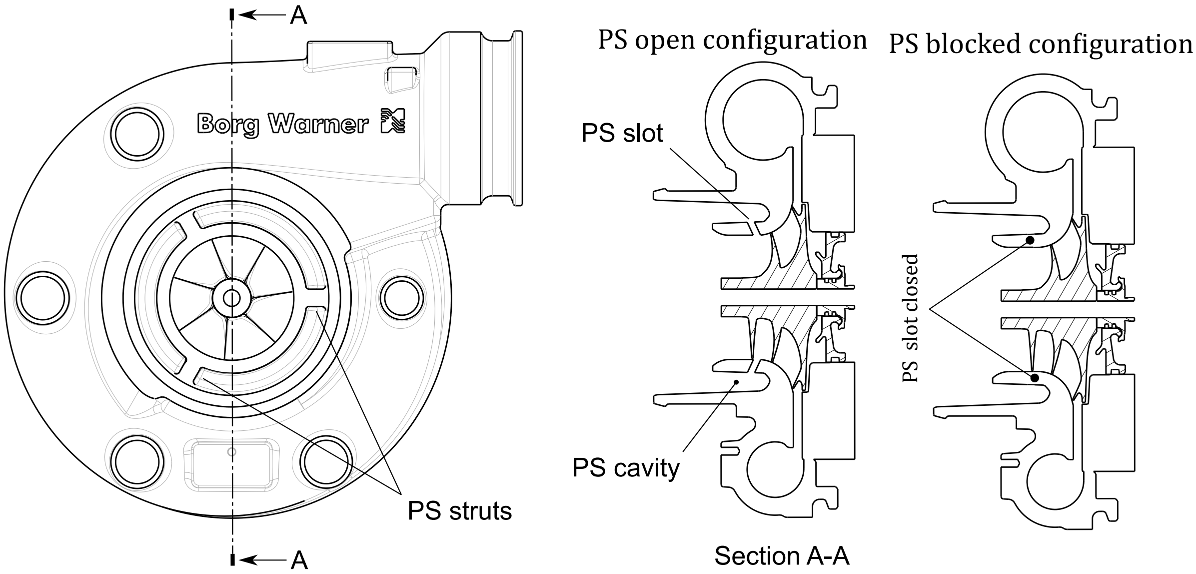

Fig. 5.2 Drawing of the compressor along with sectional views of the open and blocked compressor configurations achieved numerically by opening and closing the PS slot.

configuration is numerically modelled by removing the PS slot in the open configuration as shown in Figure 5.2.

The global performance parameters for the compressor (Equation 2.8) viz. Pressure ratio Π_{t-t} and isentropic efficiency η_s along with the relative deviation from experimental values (Equation 3.1) for the investigated configurations and operation are presented in Table 5.1. The deviation between the measured and predicted results of the blocked configuration, specifically for isentropic efficiency are relatively higher than the open configuration. This is expected to

Table 5.1 Comparison of the performance variables Π_{t-t} and η_s predicted by the numerical model with the experimental measurements for design and near surge conditions of two compressor configurations.

Results	Configuration	Case	Π_{t-t} [-]	η_s [%]	ε_π [%]	ε_η [%]
Experimental	PS open	Design	2.35	76.8	-	-
		Near surge	2.47	66.7	-	-
	PS blocked	Design	2.37	78.5	-	-
		Near surge	2.45	68.3	-	-
Numerical	PS open	Design	2.32	76.1	1	0.9
		Near surge	2.47	66.4	0.1	0.5
	PS blocked	Design	2.33	76.3	1.6	2.8
		Near surge	2.44	66	0.4	3.3

be caused by the use of two different temperature measurement systems with different accuracy levels for open and blocked configurations. Nevertheless, the performance parameters are predicted within reasonable limits. The acoustic results for two configurations are presented in the next sections.

5.4 Impact on design operation

The impact of PS casing treatment on the flow and acoustic features of design operation is discussed in this section.

5.4.1 Flow features

The mean flow field on the axial plane of the two compressor configurations operating at the design condition is shown in Figure 5.3 (top). The flow in the compressor for the two configurations is similar, with a smooth reduction of the area caused by the PS cavity is

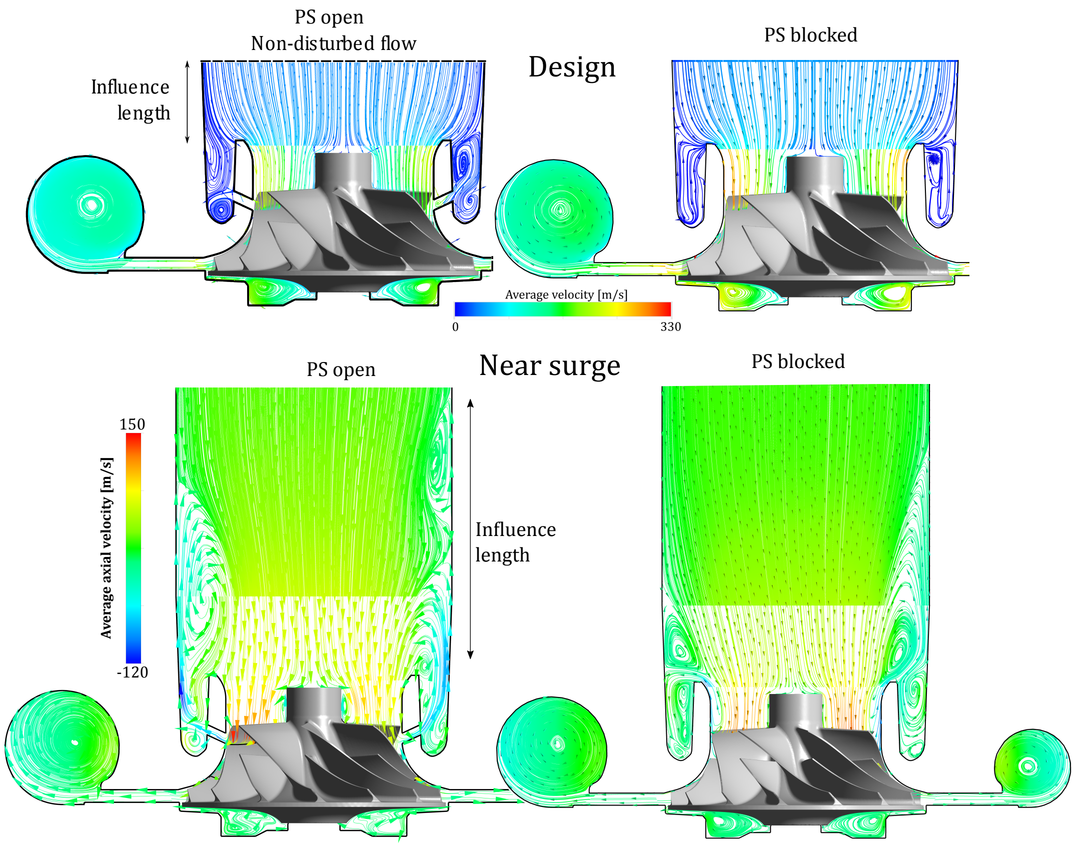

Fig. 5.3 Comparison of the flow field characteristics for the design (top) and near surge (bottom) operation for open (left) and blocked (right) configurations at the impeller axis plane.

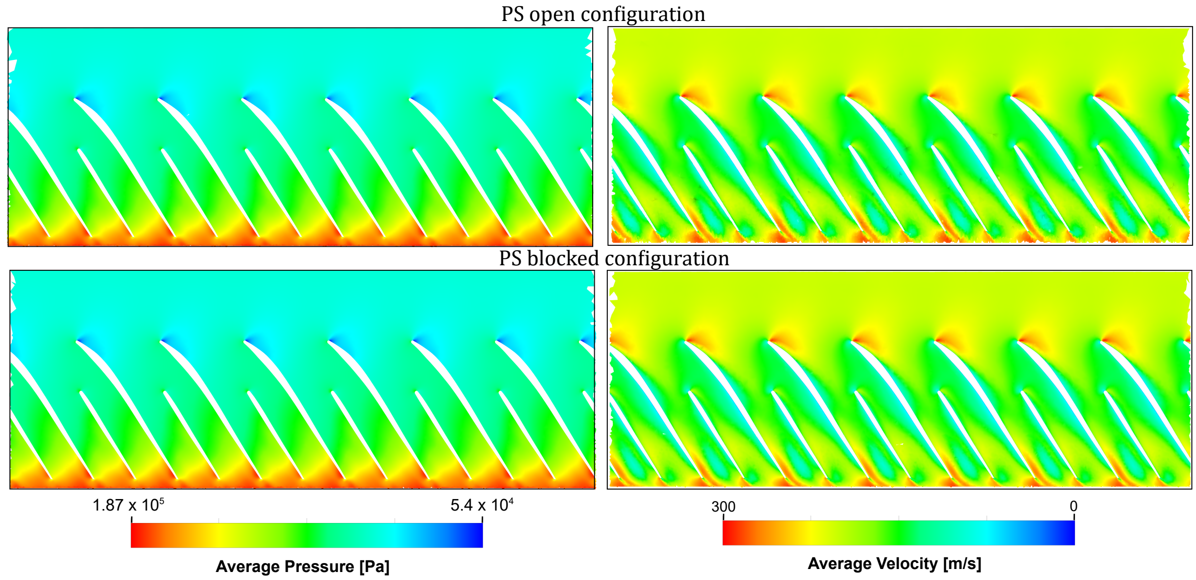

Fig. 5.4 Midspan blade-to-blade views of average velocity (right) and average pressure (left) for open (top) and blocked (bottom) compressor configurations operating at their respective design conditions.

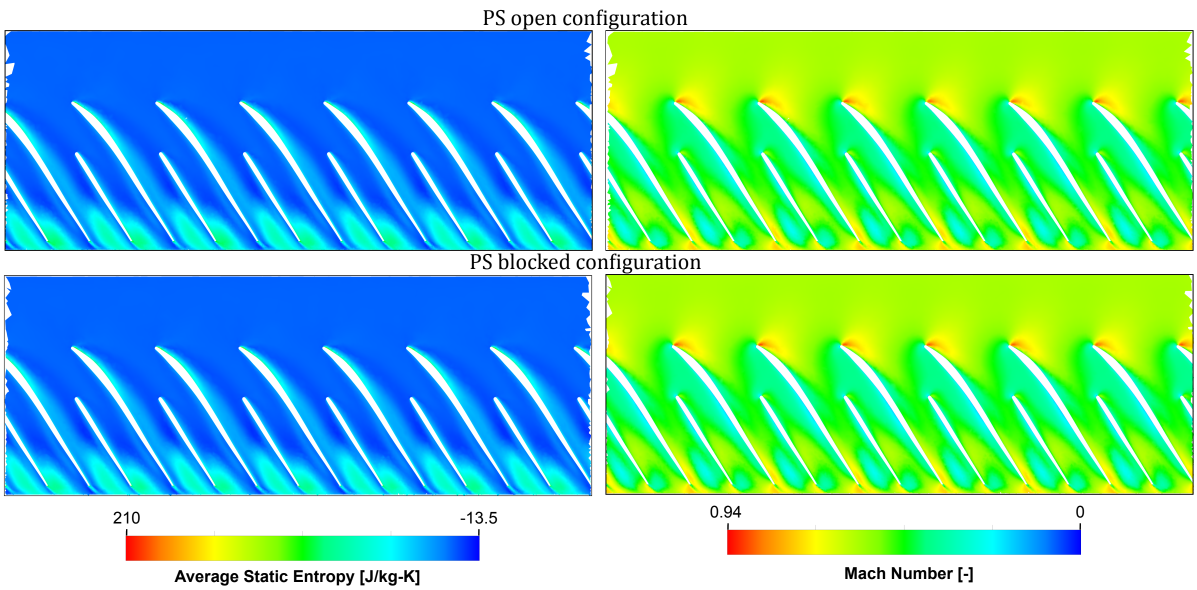

Fig. 5.5 Midspan blade-to-blade views of average Mach number (right) and average entropy generation (left) for open (top) and blocked (bottom) compressor configurations operating at their respective design conditions.

observed for both cases. The average velocity of the flow going in the impeller is relatively higher in the blocked configuration as 'push and pull' on the fluid at the PS slot as described previously is not existent.

Although insignificant differences in the average pressure and velocity distribution inside the impeller are observed for the two cases (see Figure 5.4), relatively higher entropy and thereby, losses are observed in Figure 5.5 (left) for the open configuration. This higher entropy corresponds to the lower isentropic efficiency for the open case as compared to the blocked case and is in line with the performance results presented in Table 5.1. Furthermore, the Mach number distribution for the two cases are also alike as observed in Figure 5.5 (right).

5.4.2 Acoustic characteristics

The generation and propagation of noise in two compressor configurations operating at design conditions are quantified with the help of inducer/diffuser probes and inlet/outlet duct probes respectively. The inducer and diffuser spectra for two configurations are presented in Figure 5.6

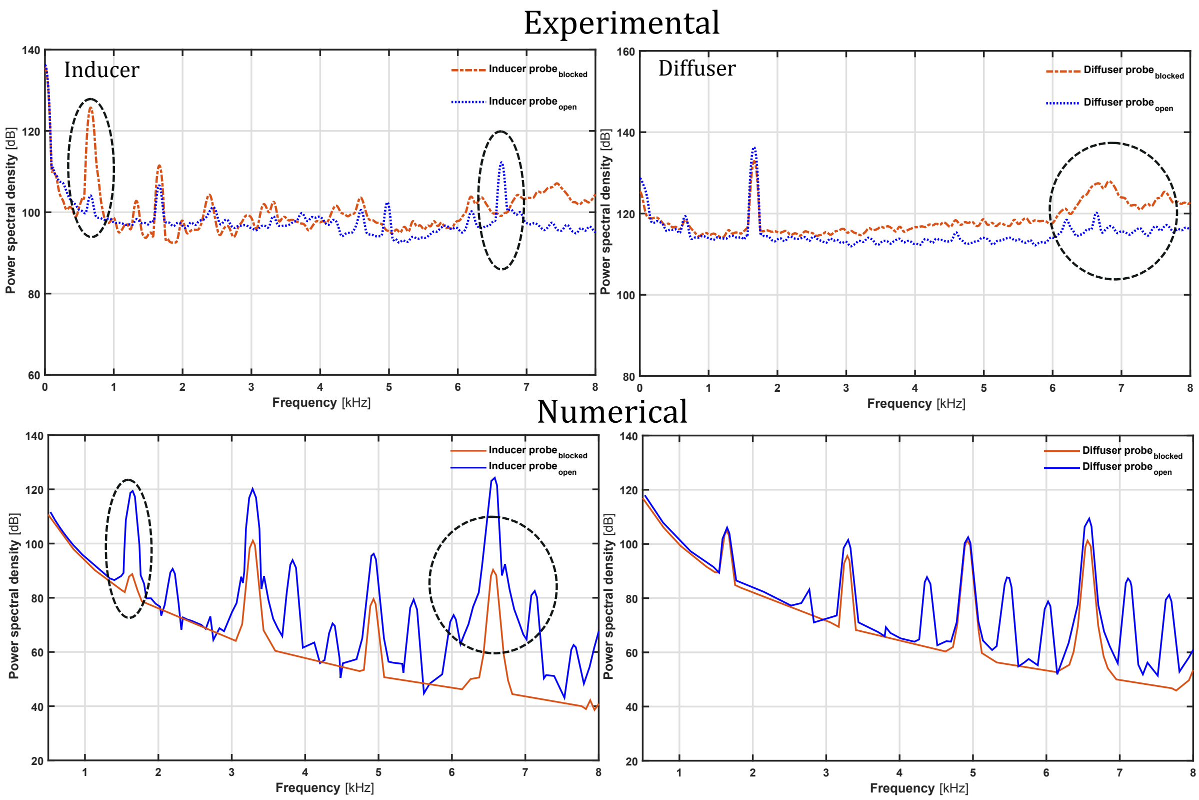

Fig. 5.6 Experimental (top) and numerical (bottom) spectra of inducer (left) and diffuser (right) probe for open (blue) and blocked (orange) compressor configurations operating at their respective design conditions are compared.

with the comparison of experimental results for PS open and blocked configuration are shown at the top half, and the results predicted by the numerical model are shown in the bottom half of the figure. In terms of the overall noise levels, the casing treatment does not have a significant impact on the generation of the noise at design operation. This observation from measured results is accurately captured by the numerical model. This being said, the measured inducer spectrum of the open configuration does show increased levels than the corresponding spectrum for blocked configuration at higher frequencies (see Section 2.5) which is not captured in the numerical results. The opposite trend is observed in the diffuser probes. Furthermore, as seen in Chapter 3, the predicted spectra does have accentuated tonal content relative to the measured values.

The propagation of noise at the inlet and the outlet duct for two configurations are compared in Figure 5.7. For the inlet duct, although overall levels are similar, higher tonal content is observed for the open configuration. The diffuser spectra for two configurations are not significantly different both in terms of overall levels and tonal content. Again, the numerical model faithfully capture these results. The higher tonal content in the inlet duct for design

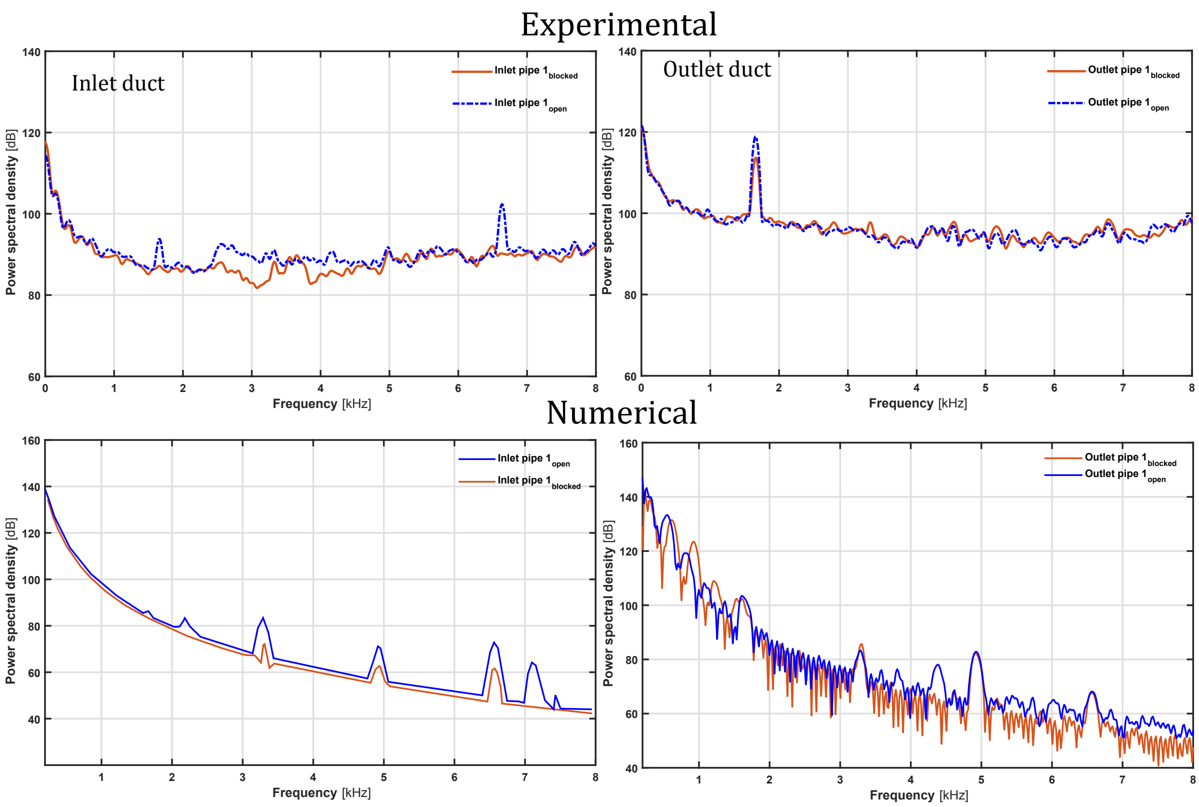

Fig. 5.7 Experimental (top) and numerical (bottom) spectra of inlet (left) and outlet (right) ducts for open (blue) and blocked (orange) compressor configurations operating at their respective design conditions are compared.

operation is expected due to the facilitation of the noise propagation via PS cavity. The results of the modal decomposition presented in the previous chapter (see Section 4.4) further reinforces these results.

5.5 Impact on near surge operation

The flow and acoustic features of the open and blocked compressor configurations operating near surge are discussed in this section.

5.5.1 Flow features

In Figure 5.3 (bottom), the mean flow fields at the compressor axial plane for two compressor configurations operating near surge are presented. Although the recirculation of the flow is observed for both cases, the propagation of instability in the upstream impeller direction is relatively higher for the open configuration. The reverse flow for the blocked configuration is observed to decrease the effective area for the incoming flow inside the impeller shroud along the decrease in the upstream area caused by the flow structures. This results in the higher axial velocity at the impeller inlet for the blocked configuration as compared to the open configuration.

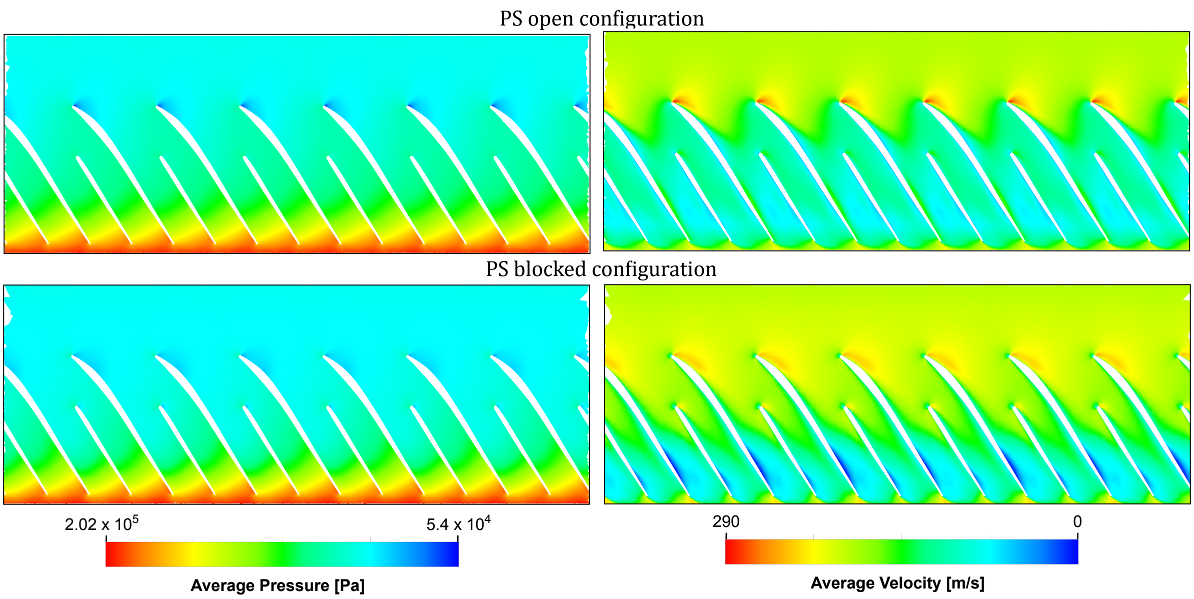

Fig. 5.8 Midspan blade-to-blade views of average velocity (right) and average pressure (left) for open (top) and blocked (bottom) compressor configurations operating at their respective near surge conditions.

In contrast to the design condition, significant differences in the average pressure and velocity distribution inside the impeller are observed for the open and blocked configuration operating near surge. The diffusion of velocity into pressure shown in Figure 5.8 (left) looks uniform for the open configuration with a constant increase in the pressure along the length of the blade. Contrary to this, the increase in pressure inside the impeller is abrupt in the blocked configuration and pressure rise is limited to the end of the impeller while the majority of the blade passage is observed to be at lower pressure. The comparison of velocity distribution among two configurations presented in Figure 5.8 (right) clearly shows high-intensity blade stalls for the blocked configuration. Both main and splitter blades are observed to be in a relatively intense stall for the blocked configuration while only main blades are observed to be stalled for the open configuration. The stalling of impeller blades in blocked configuration is

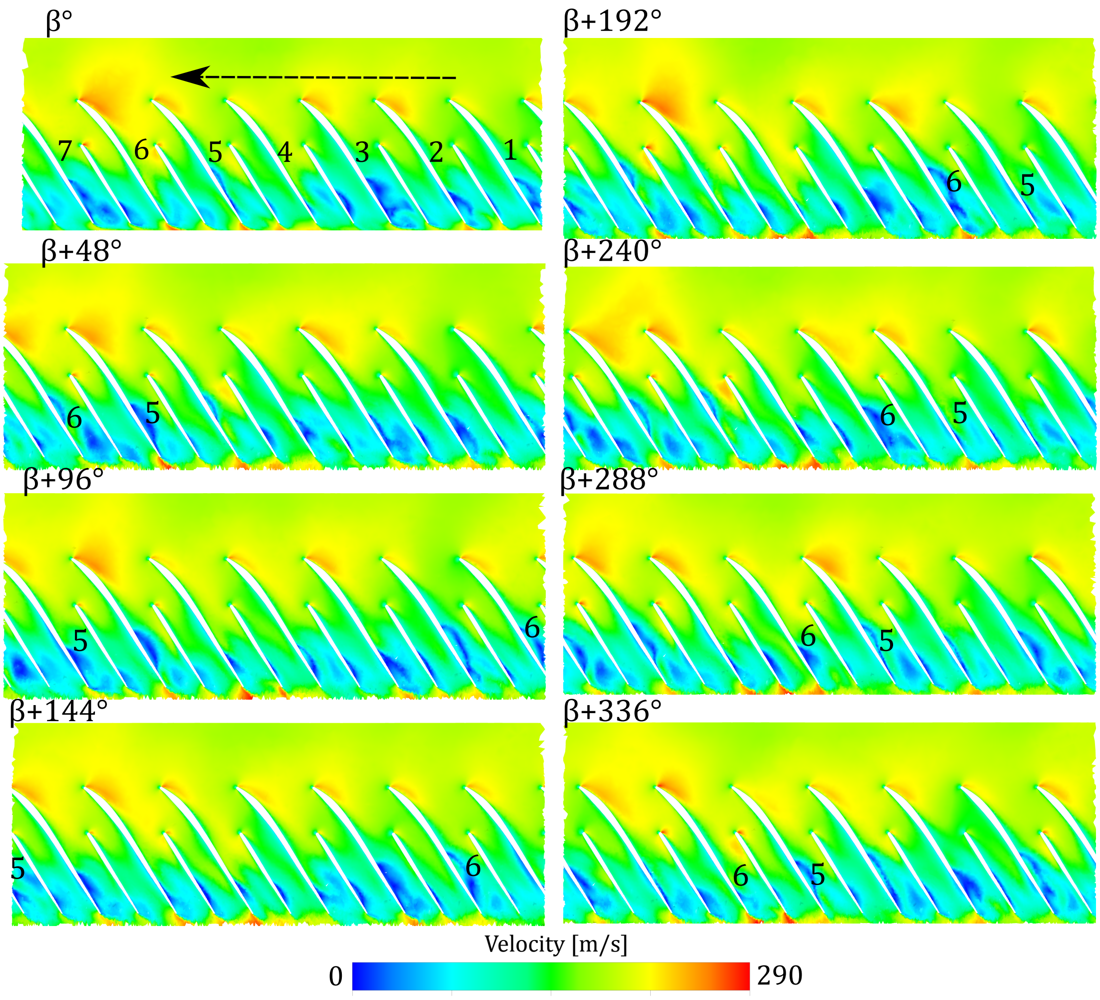

Fig. 5.9 Stall cell propagation demonstrated by analysing the instantaneous velocity distribution at impeller midspan for approximately one compressor revolution.

further investigated by analysing the instantaneous velocity distribution in the blade passages over approximately one revolution. The velocity distribution presented in Figure 5.9 clearly shows multiple (3 - 4) low-velocity stall cells propagating at different speeds around the impeller. For instance, blade passage 1, 2, 3 and 7 are observed to be stalled in the first time instance ($\beta°$). By following the stall in passage 5 and passage 6, it can be seen that the stall in passage 5 propagates circumferentially with the speed of 0.35 RO while stall in passage 6 propagates with 0.15 RO. The stalling and recovery of different blade passages can also be observed. This high intensity blade stall in blocked configuration is expected to increase the noise emission relative to the open configuration.

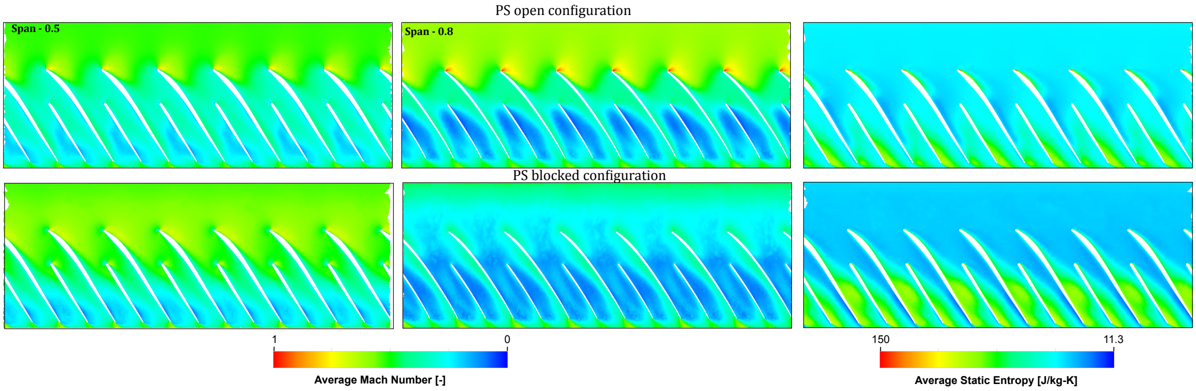

Fig. 5.10 Blade-to-blade views of average entropy generation (right) at 0.5 blade span along with the average Mach number distribution for 0.8 (middle) and 0.5 (left) blade span for open (top) and blocked (bottom) compressor configurations operating at their respective near surge conditions.

Furthermore, the distribution of Mach number inside the impeller for the two configurations at 0.5 and 0.8 blade spans are presented in Figure 5.10 (left) and Figure 5.10 (middle) respectively. The significantly lower Mach number for the blocked configuration further implies detached flow and blockage inside the blade passages. This trend is observed to further deteriorate at higher blade span.

The distribution of static entropy generation in the impeller mid-span region presented in Figure 5.10 (right) shows relatively higher generation of entropy for the blocked configuration implying greater losses compared to the open configuration. Despite lower losses in the impeller, the PS open configuration shows lower isentropic efficiency when compared to the blocked configuration. This can be explained by the results of second law analysis [5] performed by Sharma et al. [6] demonstrating that the ‘mixing’ region accounts for higher losses in the open configuration and therefore, the interaction of recirculating flow is the leading cause of the lower efficiency.

5.5.2 Acoustic characteristics

The comparison of the spectra of the inducer and diffuser probes for the two configurations operating near surge shows significant differences in terms of both overall levels and broadband features as shown in Figure 5.11. The blocked configuration is observed to generate higher noise levels at both inducer (Figure 5.11-left) and diffuser (Figure 5.11-right) locations. In the measured inducer spectrum, the blocked configuration is observed to yield similar or lower noise levels as compared to the open configuration below 2 kHz while a broadband elevation from 2 - 4.5 kHz can be observed. Similarly, the diffuser spectrum for the blocked configuration also yields relatively similar noise levels up till 0.5 kHz while a deviation in the spectra of two configurations is observed beyond 0.5 kHz. The numerical spectra reasonably replicate these differences between the two configurations.

The inlet and outlet duct spectra for the two configurations are compared in Figure 5.12. Similar to the results from the inducer probes, higher noise levels are seen beyond 2 kHz in the inlet duct of the blocked configuration while similar or lower noise levels as compared

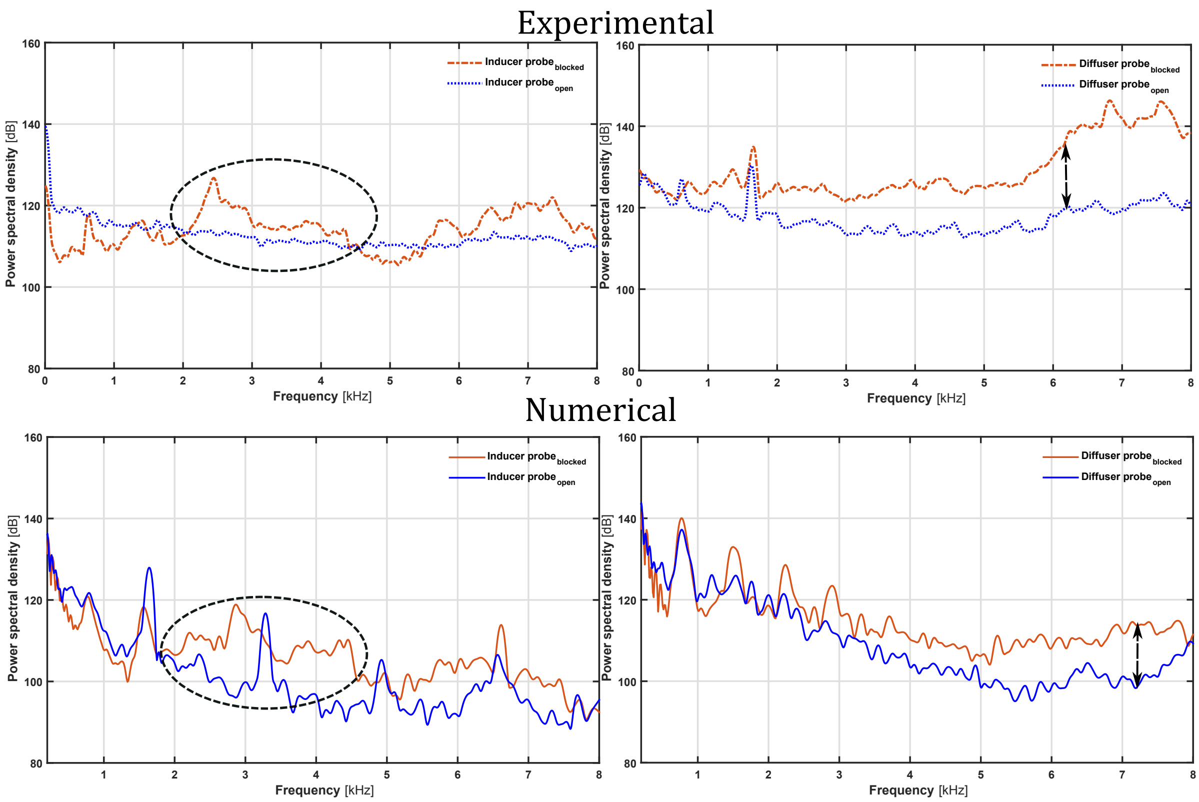

Fig. 5.11 Experimental (top) and numerical (bottom) spectra of inducer (left) and diffuser (right) probe for open (blue) and blocked (orange) compressor configurations operating at their respective near surge conditions are compared.

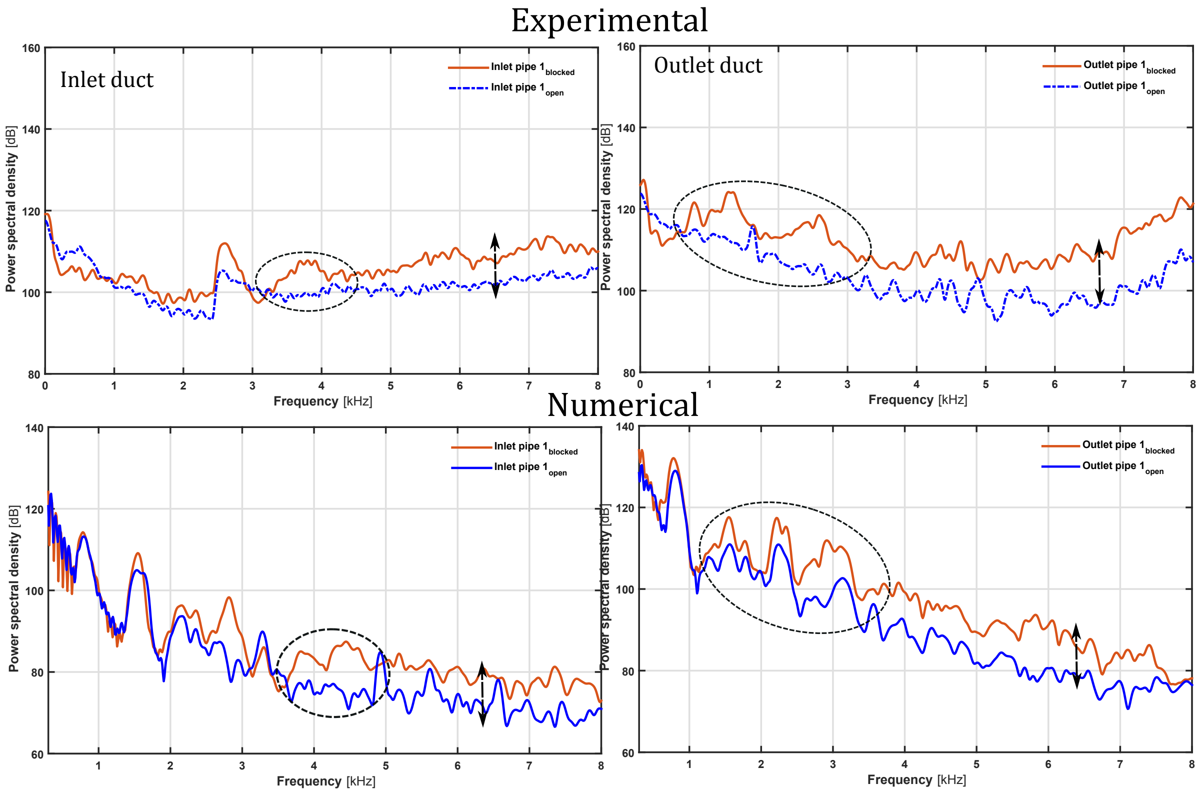

Fig. 5.12 Experimental (top) and numerical (bottom) spectra of inlet (left) and outlet (right) ducts for open (blue) and blocked (orange) compressor configurations operating at their respective near surge conditions are compared.

to open configuration are observed below 2 kHz. It is interesting to a see a small broadband effect in the region of 0.3 - 0.75 kHz for the inlet duct of the open configuration which is not observed in the blocked configuration and is expected to be caused directly or indirectly by the casing treatment. Furthermore, the broadband in the 2 - 4.5 kHz region, observed in the inducer spectrum of the blocked configuration is seen to be propagated to the inlet duct.

The spectra of the outlet duct are similar to the spectra of the diffuser probes with higher noise levels for the blocked configuration beyond 0.5 kHz while similar or lower levels are observed below 0.5 kHz. Broadband elevations in the region of 0.8 - 1.5 kHz and 2 - 3 kHz are observed in the outlet duct of the blocked configuration that are not seen in the diffuser spectrum. The first broadband, i.e. 0.8 - 1.5 kHz corresponds to the characteristic ‘whoosh’ noise frequency range. This broadband is captured by the numerical model, and overall, numerical spectra reasonably capture the impact of casing treatment as seen from the corresponding results.

Table 5.2 Differences in the measured overall sound pressure levels of PS open and blocked compressor configuration in the frequency range of 0.2-8.0 kHz

$\Delta_{f,l} = \mathrm{SPL}_{\mathrm{open}} - \mathrm{SPL}_{\mathrm{blocked}}$ [dB]					
Operating point	Frequency range [kHz]	Location			
		Δ Ind	Δ In	Δ Dif	Δ Out
99 krpm - BEP	0.2-8.0	-7.6	1.4	-2.2	-1.7
99 krpm - NS	0.2-8.0	-3.2	-4.8	-16.9	-6.6
130 krpm - BEP	0.2-8.0	3.5	3.3	2.1	-0.8
130 krpm - NS	0.2-8.0	16.7	-3.4	16.6	0.5

To quantify the impact of PS casing treatment, the differences in the overall amplitude of measured SPL spectra $\Delta_{f,l} = \mathrm{SPL}_{\mathrm{open}} - \mathrm{SPL}_{\mathrm{blocked}}$ for open and blocked compressor configurations within 0.2-8.0 kHz are presented in Table 5.2.

5.6 Conclusions

In this chapter, the impact of ported shroud casing treatment on the acoustic and flow features of the compressor operating at the design and near surge conditions have been quantified by modelling the open and blocked configuration of the compressors. The computationally optimal numerical configuration using the SBES formulation on a grid with 10 million cells and timestep corresponding to a 4° impeller rotation per iteration is used in this chapter. The numerical spectra are shown to capture the differences between the two configurations at the investigated operating points with reasonable accuracy. Although the casing treatment is generally seen to decrease the overall acoustic emission of the compressor up till 8 kHz for both operating conditions, particular instances with the increased propagation of tonal content in the direction upstream to the impeller are observed.

For the design operation, although the flow is similar between the two configurations, higher entropy generation in the impeller region is seen for the open configuration. The acoustic spectra of inducer and diffuser probes show slightly higher noise generation in the blocked configuration, but the propagation of noise at inlet and outlet ducts shows insignificant differences in the overall levels of two configurations with higher tonal content in the inlet duct spectrum of open configuration.

For the near surge operation, significant differences in the flow features and therefore, acoustic features are observed for the two configurations. The diffusion of velocity into pressure is seen to be abrupt in the impeller of the blocked configuration paired with the relatively high losses evident from the entropy generation. These losses are attributed to the intense stall observed in multiple blade passages of the blocked configuration. The blocked compressor is seen to generate higher flow-induced noise as compared to the open configuration. Both inducer and diffuser spectra show similar or lower noise levels for lower frequencies while significantly higher levels are observed beyond those cut-off frequencies for the blocked configuration. Broadband characteristics in the lower and medium frequency regions usually associated with near surge operation are observed in the spectra of the blocked configuration. Furthermore, broadband in the characteristic 'whoosh' noise frequency is also seen in the spectrum of the outlet duct for the blocked configuration.

Chapter 6

Changes in the acoustic features due to increase in the operational speed to 130 krpm *

Contents

*Content presented in this chapter has been submitted for publication in the following paper:

- Impact of operational speed on the acoustic characteristics of a high-speed centrifugal compressor with and without casing treatment [9]

6.1 Introduction

Up till this point in this thesis, several numerical configurations have been comprehensively explored to model the flow-induced noise in a turbocharger compressor. The validated numerical configurations have been then used to understand the flow phenomena responsible for various acoustic features observed in the spectra of the compressor. Furthermore, the impact of PS casing treatment on the acoustic emission of compressor operating at the design and near surge conditions of a selected (99 krpm) speedline is also quantified.

In this chapter, the impact of the operational speed on the acoustic and flow features is investigated by comparing the relevant characteristics at two different speedlines for both open and blocked configurations. The literature is presented in Section 6.2 while details on the numerical model and operating conditions are covered in Section 6.3. The impact of operating speed on the characteristics of design and near surge points is covered in Section 6.4 and Section 6.5 respectively. Finally, the conclusions are summarised are in Section 6.6.

6.2 Literature review

As mentioned in previous chapters, literature on the acoustic characteristics of compressors with casing treatment is scarce. To the best of the author's knowledge, the impact of operating speed on the acoustic emission of such compressors has not been explicitly investigated. This being said, the general trend observed in the experimental studies of Torregrosa et al. [31] and Dehner et al. [159] points towards an expected increase in the noise levels with the increase in operational speed of the compressor.

6.3 Numerical configuration

Similar to the previous chapter, the investigation of the impact of operating speed on the acoustic spectra of the compressor is limited to the relative differences observed in the lower-medium frequency ranges. Therefore, the numerical configuration based on the SBES turbulence formulation with 10 million cells and a timestep corresponding to $4°$ rotation of impeller per iteration is employed.

The characteristics of PS open and blocked compressor configurations operating at the 99 krpm speedline are compared with that of the 130 krpm speedline. The investigated operating conditions of both configurations are highlighted in the compressor maps presented in Figure 6.1. To quantify the impact of rotational speed, the operating points at two different speedlines must be aerodynamically and geometrically similar. The geometrical similarity is

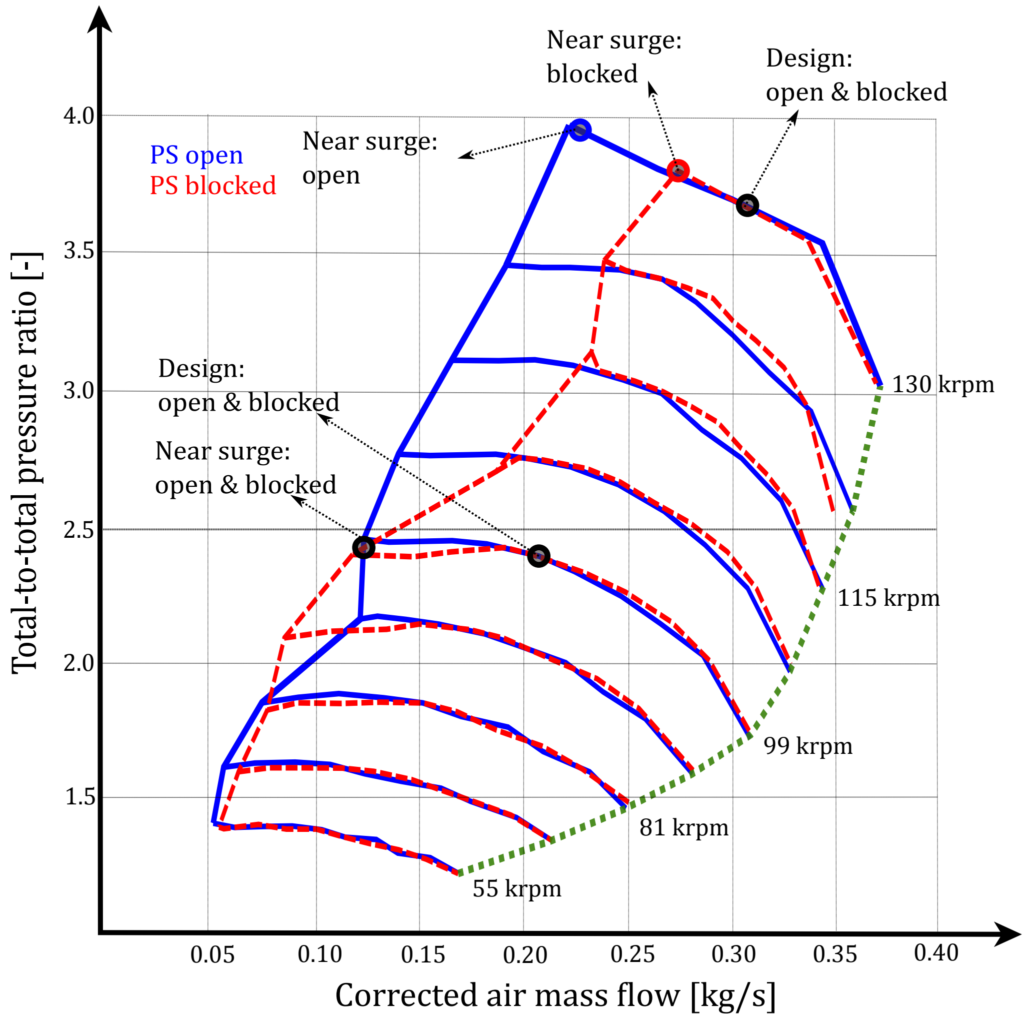

Fig. 6.1 Compressor maps for the open and blocked configurations, highlighting the investigated operating points on 99 krpm and 130 krpm speedline.

already established as the compared compressor configurations are same, while the aerodynamic similarity between different operating points is ascertained by assuring the similar values of flow coefficient (ψ) [2] for those points. The values of flow coefficient for the design and near surge points of two speedlines are presented in Table 6.1. The values of flow coefficient for the design conditions of the two speedlines are similar while the flow coefficient for near surge points is significantly different. Furthermore, the flow coefficient at the design points for open and blocked configurations are similar across the speedlines, while for the near surge point, the flow coefficients values between two configurations are only similar for the 99 krpm speedline. This implies that the impact of PS and operating speed on the acoustic emission of the compressor operating at design conditions can be established by directly comparing the

[2] $\Psi = {Q_{in}}/{U_{tip}A_{in}}$ where Q_{in} is volumetric mass flow, U_{tip} is impeller tip speed and A_{in} is the area of the inducer

Table 6.1 The values of flow coefficient (ψ) for the investigated design and near surge conditions of two speedlines.

Speedline	Configuration	Case	$\dot{m}$ [kg/s]	ψ [-]
99 krpm	PS open	Design	0.211	1.28
		Near surge	0.122	0.74
	PS blocked	Design	0.211	1.28
		Near surge	0.122	0.74
130 krpm	PS open	Design	0.295	1.3
		Near surge	0.227	1.04
	PS blocked	Design	0.295	1.3
		Near surge	0.245	1.12

acoustic spectra of respective configurations across the speedlines while the impact of PS on the acoustic emission of near surge point can only be established by comparing near surge spectra of two configurations operating at the 99 krpm speedline. The impact of operating speed on the spectra of near surge point cannot be accurately quantified by comparing the near surge spectra of the two speedlines as the flow coefficients and thereby, aerodynamic conditions would be very different. The differences in the acoustic spectra of the near surge points for the two speedlines would not be limited to the operating speed but an amalgamation of the alterations caused by differences in the aerodynamic phenomena due to different mass flow rates and corresponding thermodynamic variables. This being said, the near surge spectra of two speedlines are still their ‘near surge spectra’, and the comparison between two can provide information on the evolution of the near surge acoustics with speed, fully realising that the changes in the acoustic characteristics are not solely down to the changes in the operational speed.

Therefore, the characteristics of the design points for two speedlines viz. 99 krpm and 130 krpm are compared to understand the evolution of acoustic spectra with an increase in rotational speed for both open and blocked configurations. The near surge characteristics of the two speedlines are compared to understand the evolution of the acoustic features near surge acknowledging that the observed effects are not solely caused by changes in the operational speed.

The global performance parameters of the compressor (Equation 2.8) viz. Pressure ratio Π_{t-t} and isentropic efficiency η_s along with the relative deviation from experimental values (Equation 3.1) for the investigated configurations operating at 130 krpm speedline are presented

Table 6.2 Performance variables Π_{t-t} and η_s of two configurations operating at 130 krpm predicted by the numerical model are compared with the experimental measurements

Results	Configuration	Case	Π_{t-t} [-]	η_s [%]	ε_π [%]	ε_η [%]
Experimental	PS open	Design	3.86	72.2	-	-
		Near surge	4.16	68.3	-	-
	PS blocked	Design	3.94	72.8	-	-
		Near surge	3.98	69.2	-	-
Numerical	PS open	Design	3.74	71.4	3.1	1.1
		Near surge	4	67.8	3.8	0.7
	PS blocked	Design	3.84	72.1	2.5	1
		Near surge	3.85	68.3	3.3	1.3

in Table 6.2. The relative deviation between the predicted and measured performance variables are slightly higher than the corresponding values for the 99 krpm speedline. Nevertheless, the performance parameters are predicted within reasonable limits. The acoustic results for the two speedlines are presented in the next sections.

6.4 Evolution for design operation

The impact of the operational speed on the flow and acoustic features for the open and blocked configurations of the compressor operating at the design conditions are discussed here.

6.4.1 Flow features

The mean flow field on the axial plane of the two compressor configurations operating at the design conditions of the 99 krpm (top) and 130 krpm (bottom) speedlines are shown in Figure 6.2. With the increase in the operating speed, the expected increase in the velocity of the incoming flow has been observed for both configurations. Although the flow features observed in the inlet and rotor region for the design conditions of two speedlines are relatively similar, the formation of contra rotating vortices can be observed in the volute of the higher speedline. These contra rotating vortices are expected to be caused by the inability of the flow to follow the volute curvature due to higher swirl and velocity in the flow coming out of the impeller at higher speedline. Although the smooth reduction of the area caused by PS cavity is observed for both speedlines, the 'inverted-S' shape feature is not observed in the PS cavity for

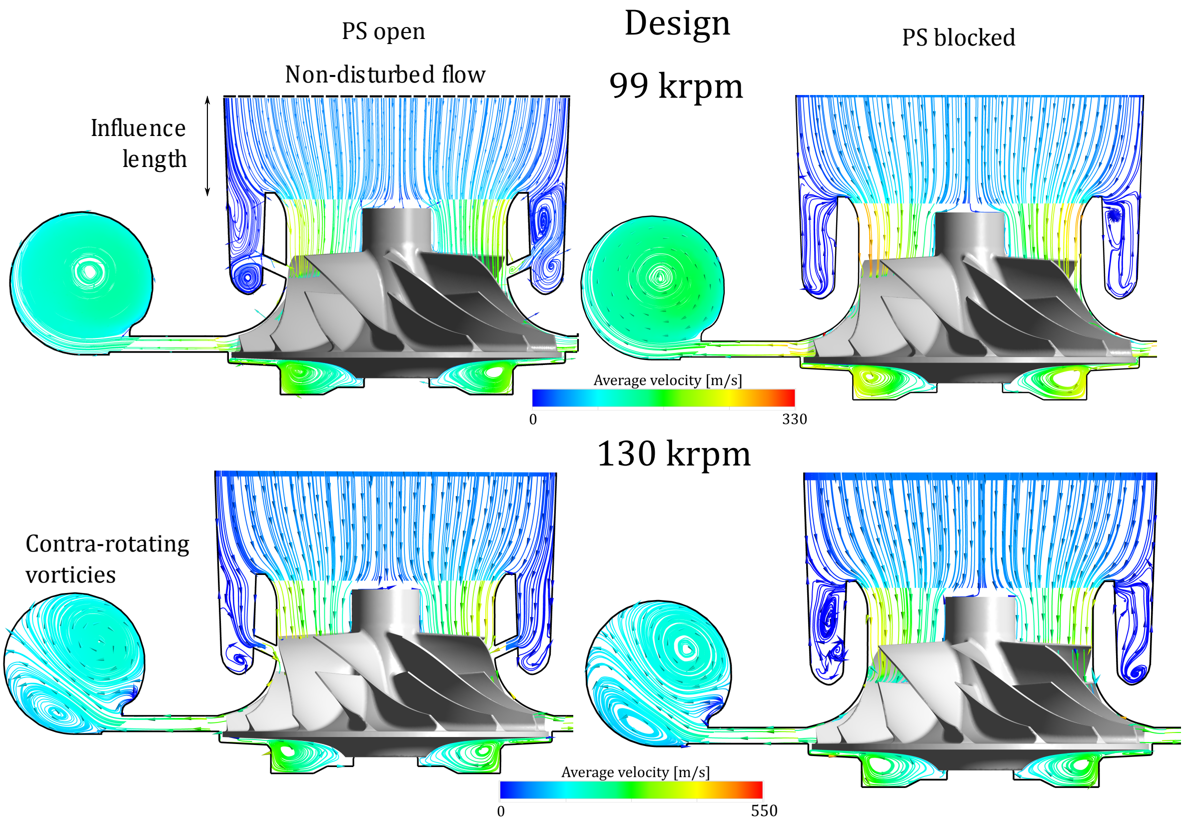

Fig. 6.2 Flow field characteristics observed at the design operation of 99 krpm (top) and 130 krpm (bottom) speedlines for open (left) and blocked (right) compressor configurations at the impeller axis plane.

the higher speedline. Furthermore, similar behaviour of the flow can also be observed in the blocked configurations for both speedlines.

The 'push and pull' of flow at the PS slot for open configuration shows an interesting dynamics (see Figure 6.3), wherein the flow distribution is primarily observed to be surge-like, i.e. pushed out of the impeller for the lower speedline whereas at the higher operational speed, the flow behaviour is choke-like, i.e. pulled into the impeller. Furthermore, the fluid undergoing 'push and pull' at the PS slot and recirculating in the PS cavity is seen to be relatively reduced for higher speedline.

The distribution of the velocity and pressure inside the impeller for two speedlines are presented in Figure 6.4 and Figure 6.5 respectively. The expected increase in the amplitude of the velocity and pressure with the increase in the operating speed is observed although the distribution is relatively identical. Similar observations are seen in the pressure and velocity distribution of the blocked configurations (Figure 6.4 and Figure 6.5 - bottom) too.

The distribution of the Mach number in the rotor midspan (see Figure 6.6) shows transonic-supersonic conditions for the higher speedline in contrast to subsonic-transonic conditions

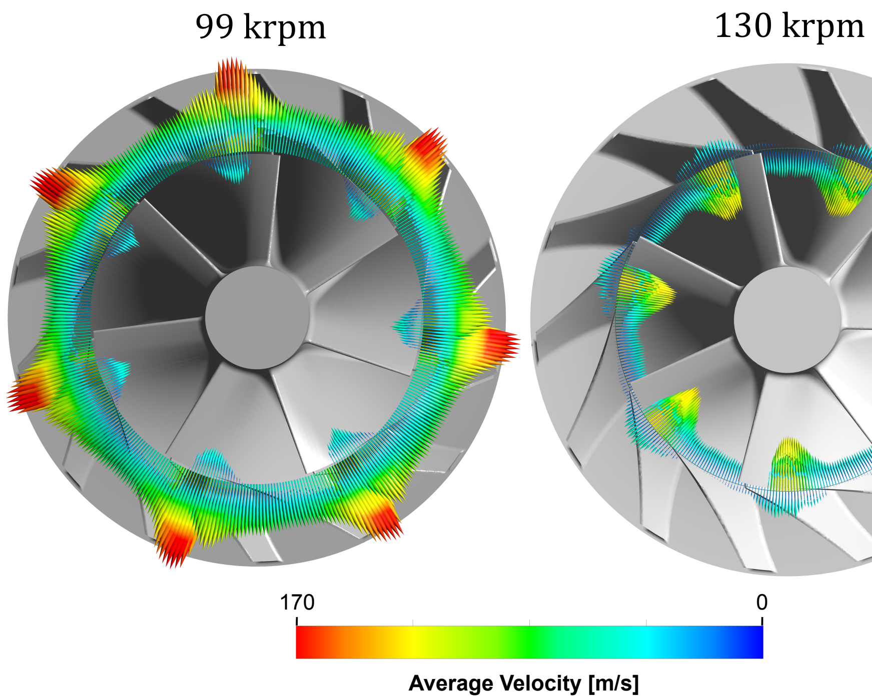

Fig. 6.3 Velocity vectors at the PS slot for the design point of 99 krpm (left) and 130 krpm (right) speedline.

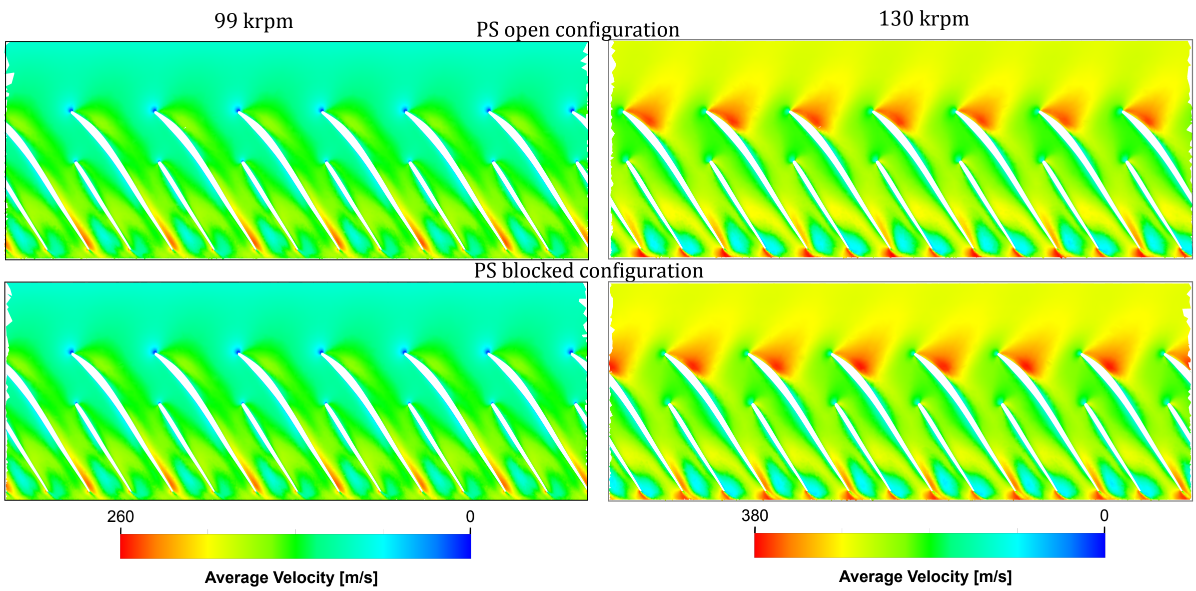

Fig. 6.4 Midspan blade-to-blade views of average velocity for the open (top) and blocked (bottom) configuration of compressors operating at the respective design conditions of 99 krpm (left) and 130krpm (right) speedline.

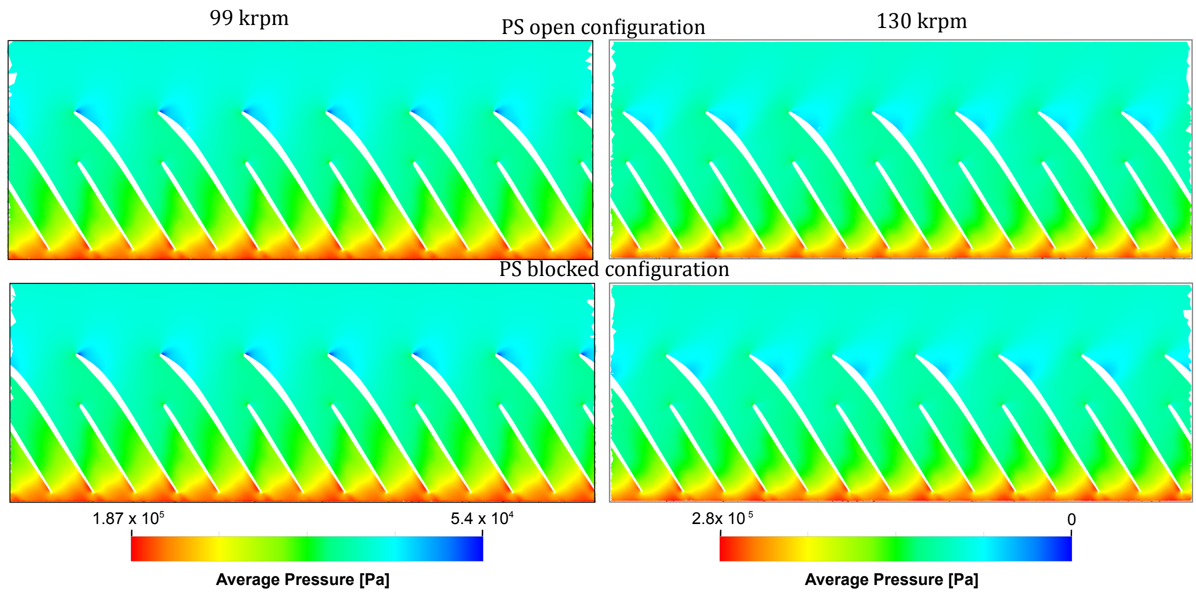

Fig. 6.5 Midspan blade-to-blade views of average pressure for the open (top) and blocked (bottom) configuration of compressors operating at the respective design conditions of 99 krpm (left) and 130krpm (right) speedline.

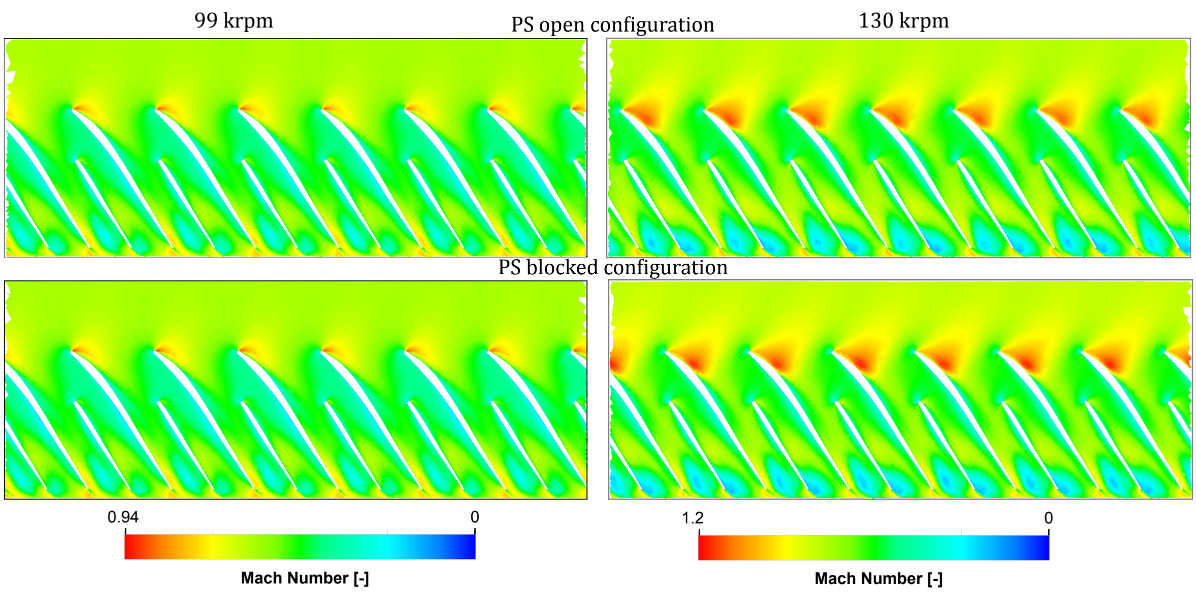

Fig. 6.6 Midspan blade-to-blade views of average Mach number for the open (top) and blocked (bottom) configuration of compressors operating at the respective design conditions of 99 krpm (left) and 130krpm (right) speedline.

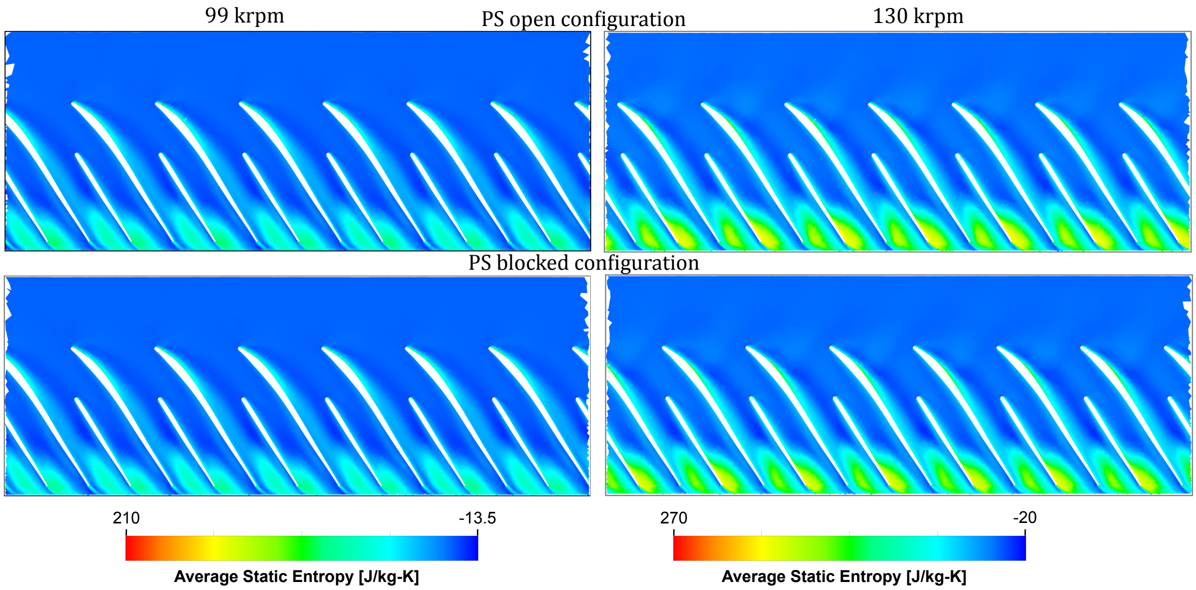

Fig. 6.7 Midspan blade-to-blade views of average entropy generation for the open (top) and blocked (bottom) configuration of compressors operating at the respective design conditions of 99 krpm (left) and 130krpm (right) speedline.

for the lower speedline. Similar distributions and the existence of high Mach numbers are also observed in the blocked configuration operating at the higher speedline. This implies the presence of stronger shock waves and thereby, intense RO tones are expected in the spectra of both open and blocked configurations operating at the 130 krpm speedline. The generation of entropy is observed to be significantly higher for both configurations operating at 130 krpm as seen in Figure 6.7. Therefore, operation at the higher speedline is expected to have relatively higher losses in the impeller relative to the operation at the lower speedline. Furthermore, the difference between the entropy generation in the open and blocked configurations is relatively lower for higher speedline.

6.4.2 Acoustic characteristics

The evolution of the generation and propagation of noise at the design conditions with an increase in the operating speed is quantified with the help of inducer/diffuser probes and inlet/outlet duct probes respectively. The inducer spectra of the two speedlines are shown in Figure 6.8 with the experimental results of the open and blocked configurations for both speedlines shown in the top half of the figure while the predicted spectra are presented in the bottom half of the figure. Significantly higher overall levels are observed in the inducer spectra of the higher speedline for both configurations, including intense RO tones corresponding to higher Mach numbers as shown in the flow characteristics. It is interesting to observe a peak

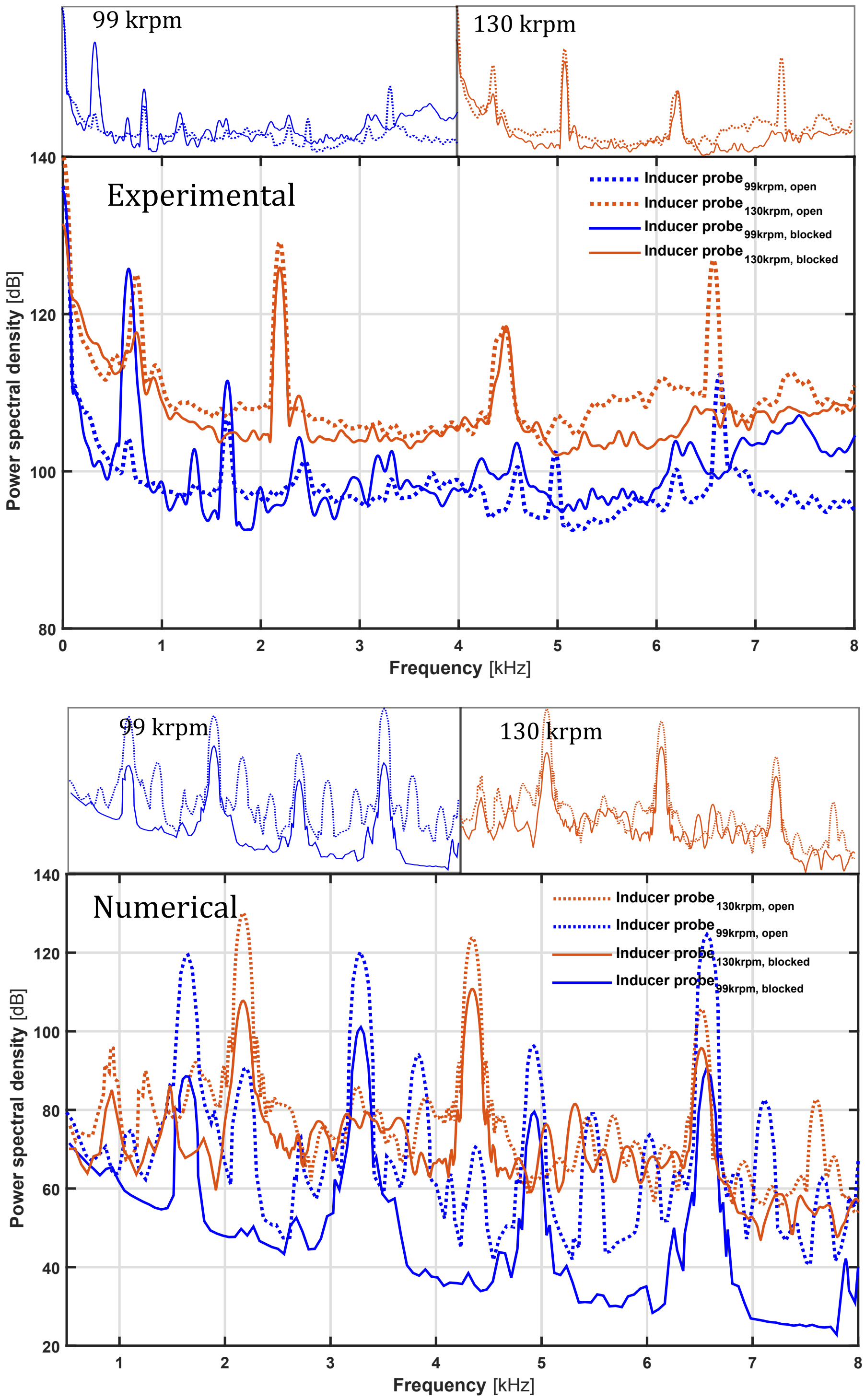

Fig. 6.8 Experimental (top) and numerical (bottom) spectra of inducer probe for open (dashed) and blocked (solid) compressor configurations operating at the respective design conditions of 99 krpm (blue) and 130 krpm (orange) speedline. The comparison of the open and blocked configurations for two speedlines are also presented in the zoomed section at the top of each plot to aid clarity.

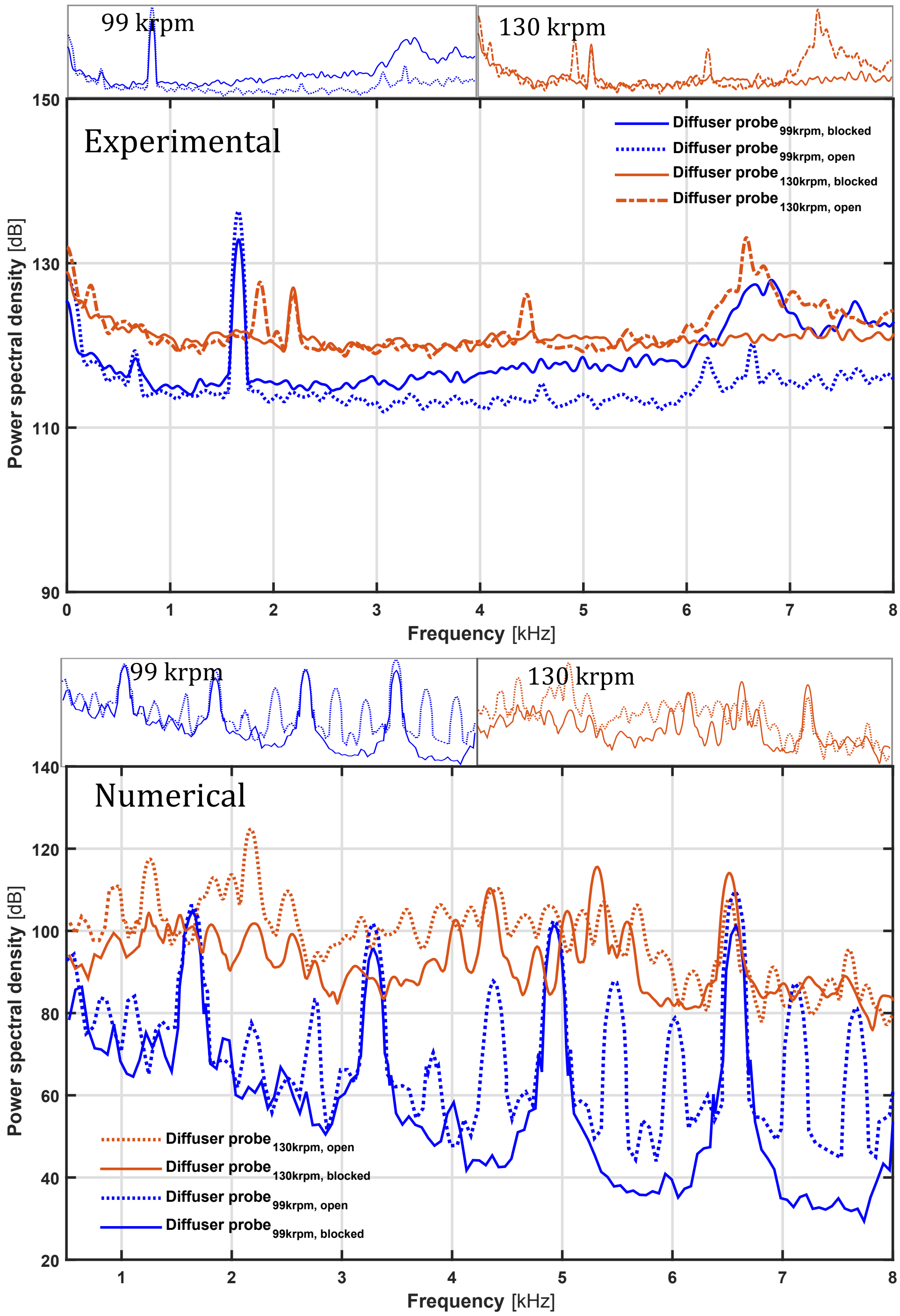

Fig. 6.9 Experimental (top) and numerical (bottom) spectra of diffuser probe for open (dashed) and blocked (solid) compressor configurations operating at the respective design conditions of 99 krpm (blue) and 130 krpm (orange) speedline. The comparison of the open and blocked configurations for two speedlines are also presented in the zoomed section at the top of each plot to aid clarity.

in the region of 0.65 - 0.75 kHz corresponding to 0.4RO and 0.3RO of the 99krpm and 130 krpm speedlines respectively. This tonal feature is dominant in the spectra of the blocked configuration for the 99 krpm speedline while the spectra of the open configuration show it more clearly for the 130 krpm speedline. As observed in the comparison between the open and blocked configurations for the two speedlines, the propagation of tonal content via the PS cavity makes the open configuration relatively noisier. The increased noise in the inducer spectra of the open configuration is relatively pronounced for the higher speedline. Although the already established limitations of the numerical model in terms of heightened tonal content and discrepancies in the overall levels and decay rates are observed, the predicted spectra reasonably capture the impact of operational speed.

The diffuser spectra for the two speedlines are presented in Figure 6.9 with the measured spectra being shown in the top half of the figure while predicted spectra are presented in the bottom half of the figure. Similar to the inducer spectra, the diffuser spectra for both configurations are observed to yield higher overall levels with an increase in rotational speed. Broadband elevation in the region of 6 - 7.5 kHz observed in the spectrum of blocked configuration operating at lower speedline is identified in the spectrum of the open configuration for the higher speedline. In the lower speedline, the diffuser spectrum of the blocked configuration is observed to yield significantly higher overall levels, whereas the spectra of the open and blocked configurations at higher speedline are relatively similar. The numerical model is unable to accurately predict the trends observed in the measured diffuser spectra at higher speedlines.

The propagation of noise at the inlet and the outlet ducts for two speedlines is compared in Figure 6.10 and Figure 6.11 respectively. Again, the overall levels for both inlet and outlet duct spectra are seen to increase with an increase in the operational speed. Similar to the inducer spectra, the noise at the inlet duct of the open configuration is observed to be relatively higher than the inlet duct of the blocked configuration, and this deviation between the spectra of two configurations is also relatively higher for the higher speedline. The outlet duct spectra for the open and blocked configurations are relatively similar for both speedlines. Furthermore, the numerical model reasonably captures these differences for both ducts.

6.5 Evolution for near surge operation

As mentioned before, the impact of operating speed on the spectra of the near surge point cannot be accurately quantified by directly comparing the near surge spectra of two speedlines as the flow coefficients are not similar. Therefore, the measured near surge spectra for two speedlines are briefly discussed in this section from the perspective of perceived noise levels

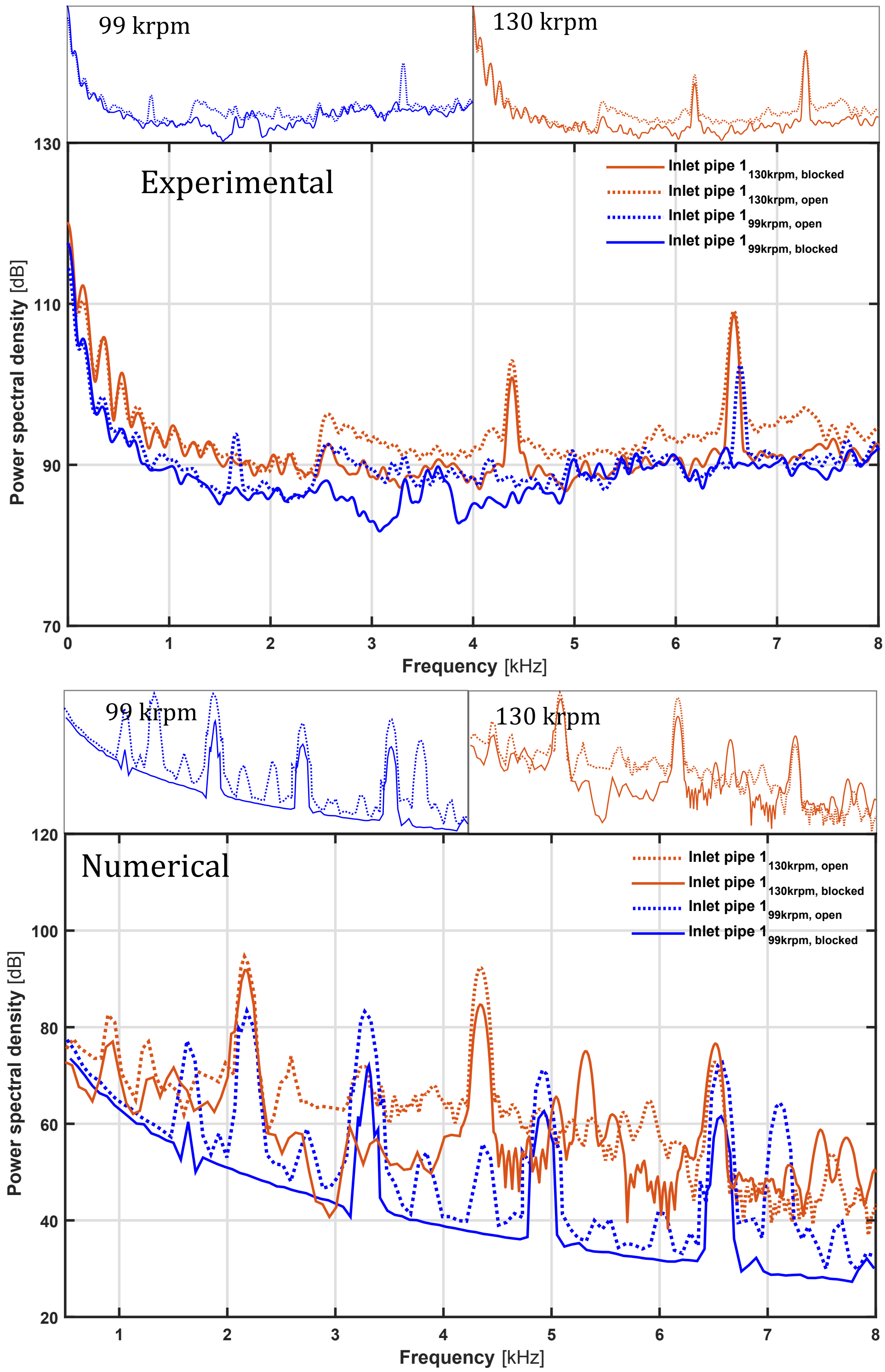

Fig. 6.10 Experimental (top) and numerical (bottom) spectra of the inlet duct for open (dashed) and blocked (solid) compressor configurations operating at the respective design conditions of 99 krpm (blue) and 130 krpm (orange) speedline. The comparison of the open and blocked configurations for two speedlines are also presented in the zoomed section at the top of each plot to aid clarity.

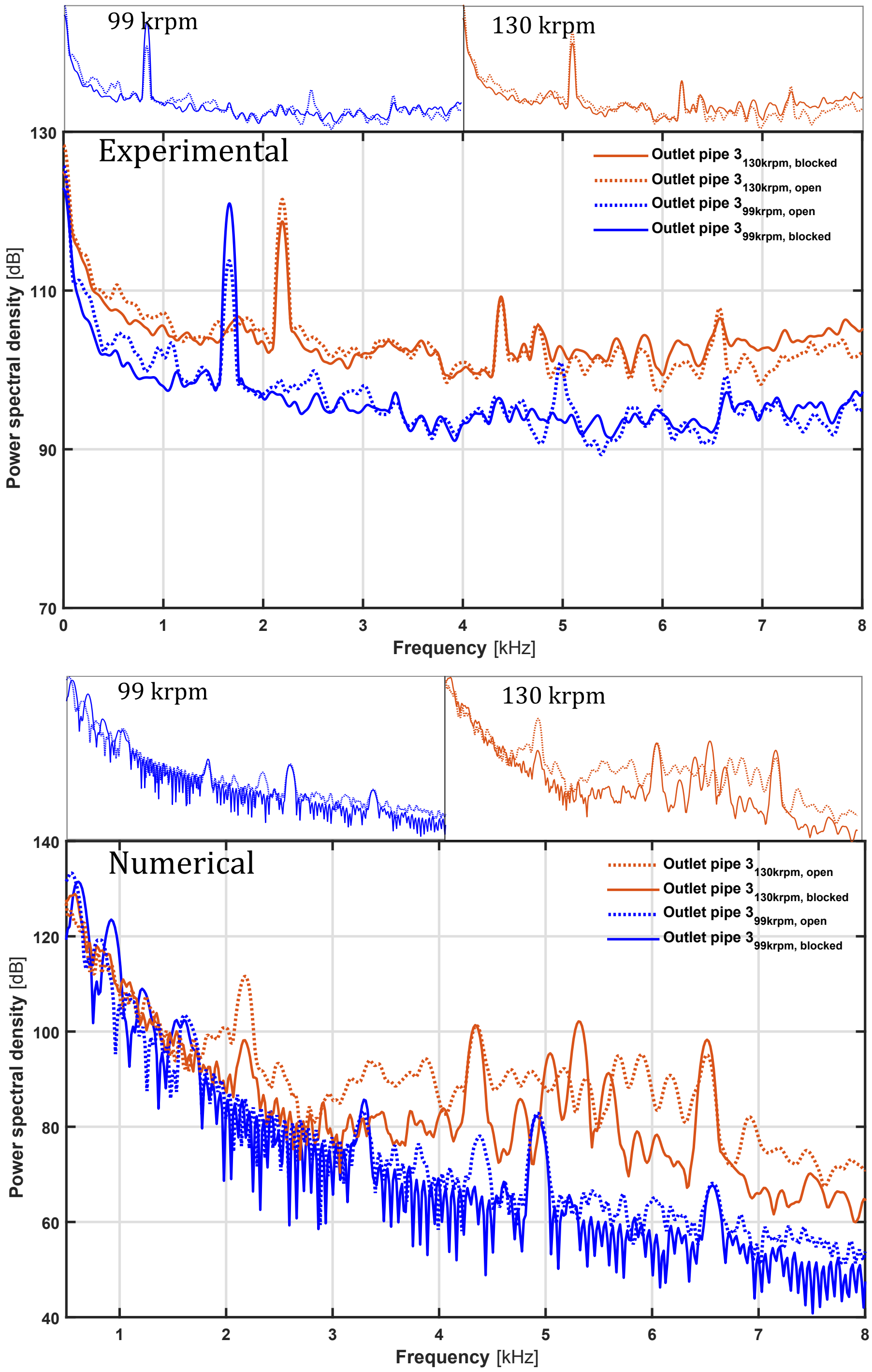

Fig. 6.11 Experimental (top) and numerical (bottom) spectra of the outlet duct for open (dashed) and blocked (solid) compressor configurations operating at the respective design conditions of 99 krpm (blue) and 130 krpm (orange) speedline. The comparison of the open and blocked configurations for two speedlines are also presented in the zoomed section at the top of each plot to aid clarity.

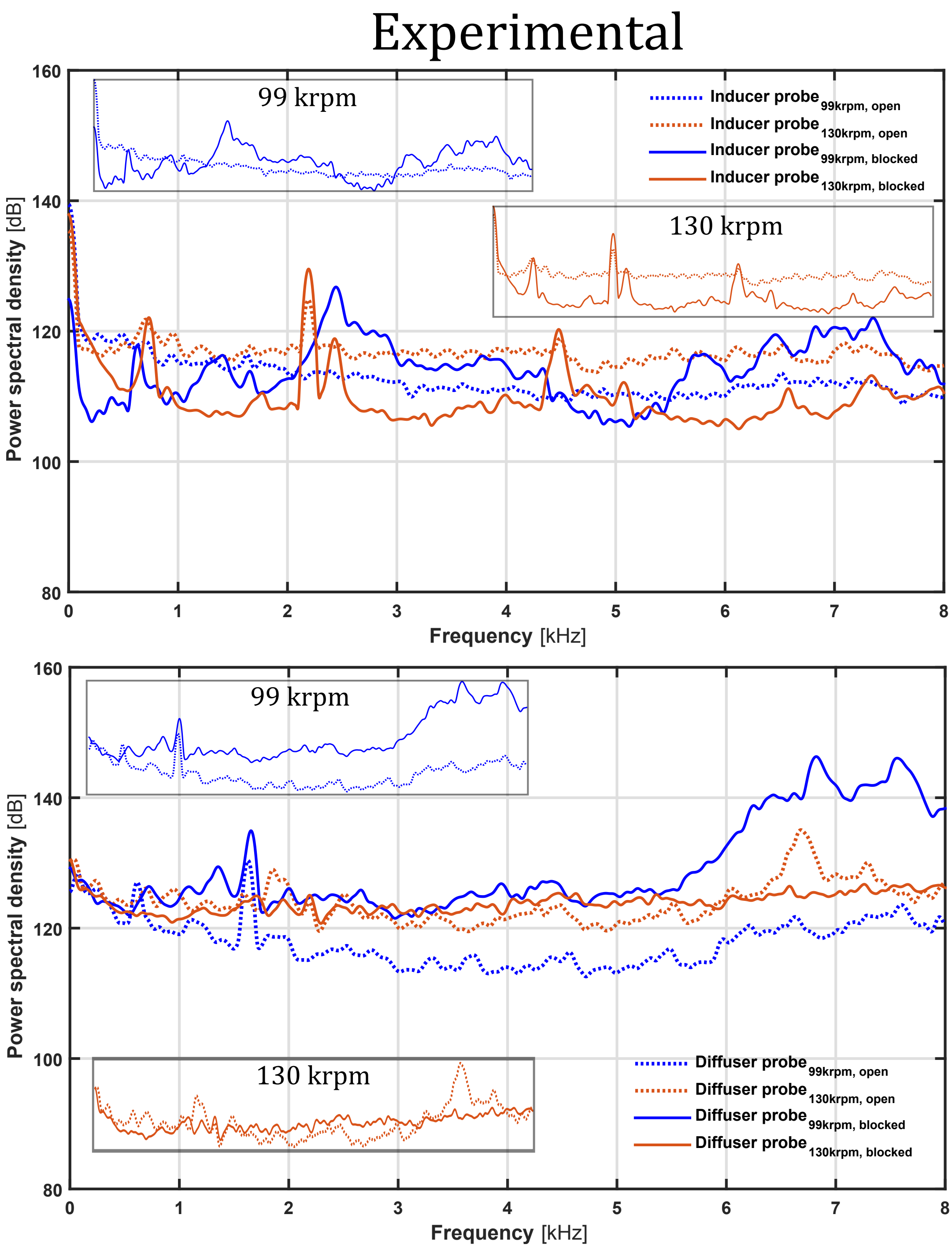

Fig. 6.12 Experimental spectra of inducer probe (top) and diffuser (bottom) probe for open (dashed) and blocked (solid) compressor configurations operating at the respective near surge conditions of 99 krpm (blue) and 130 krpm (orange) speedline. The comparison of the open and blocked configurations for two speedlines are also presented in the zoomed section at the top of each plot to aid clarity.

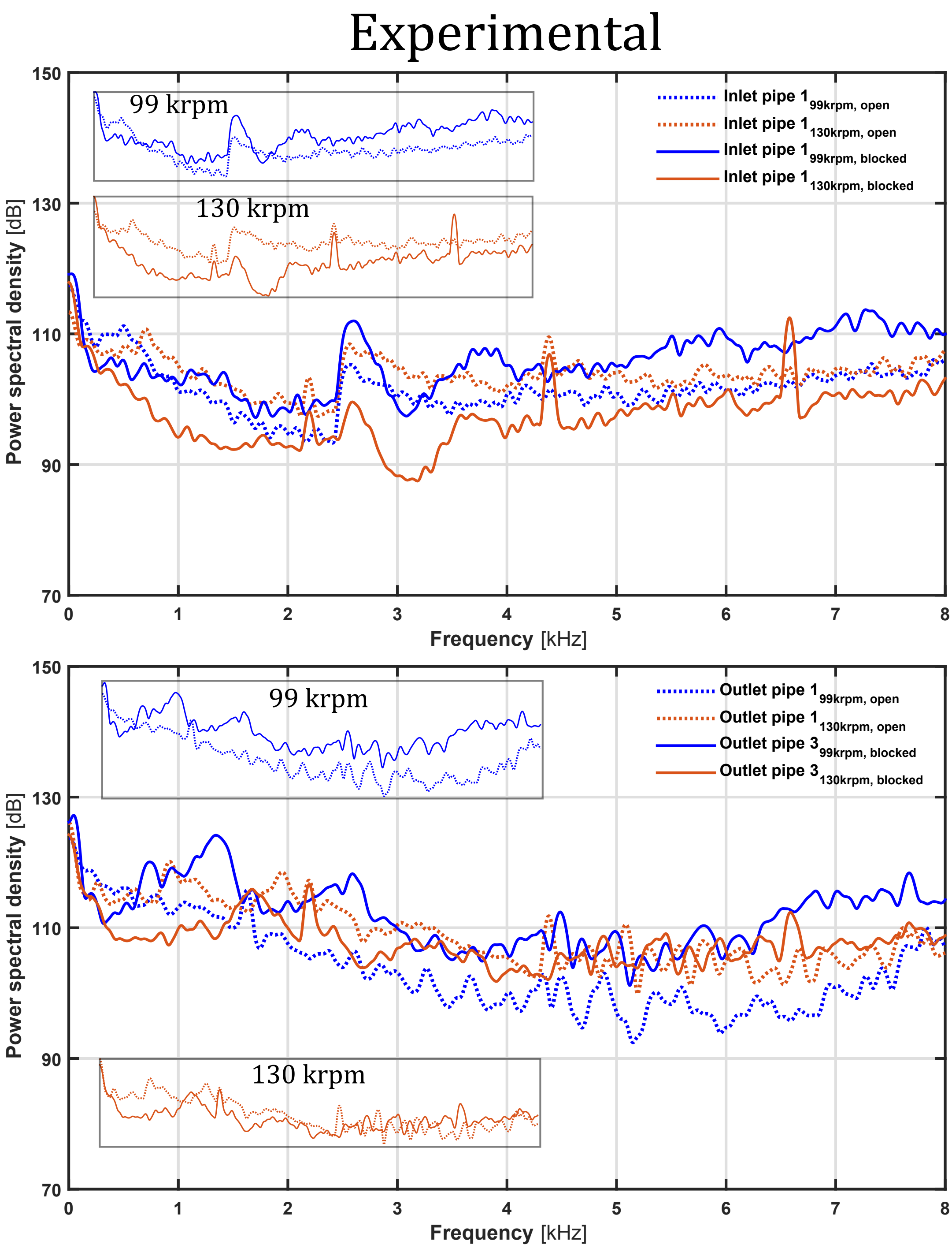

Fig. 6.13 Experimental spectra of the inlet (top) and outlet (bottom) duct for open (dashed) and blocked (solid) compressor configurations operating at the respective near surge conditions of 99 krpm (blue) and 130 krpm (orange) speedline. The comparison of the open and blocked configurations for two speedlines are also presented in the zoomed section at the top of each plot to aid clarity.

for different speedlines along with the acoustic changes brought by the use of casing treatment during near surge operation.

The generation of noise quantified from the spectra of inducer and diffuser probes for compressors operating at two speedlines are shown in Figure 6.12. For the open configuration, the near surge spectra of both inducer and diffuser probes are seen to yield higher levels with an increase in operational speed. It is interesting to note that while broadband features observed in the inducer spectrum of the blocked configuration for lower speedline increases the overall levels, the opposite is observed in the spectra of higher speedline. The inducer spectrum of the blocked configuration at higher speedline shows significantly lower overall levels relative to open configuration and therefore, could explain the comments of authors [57, 58] on PS casing treatment deteriorating the acoustic emission of the compressor. This is not exactly true as the higher noise levels for the compressor with casing treatment are expected to be caused by the lower mass flow rates at the surge limit. Although the purpose of the casing treatment is to push the surge limits at lower mass flow rates, for an aerodynamically similar near surge point (99 krpm speedline) the casing treatment is shown to alleviate the noise emission of the compressor.

The diffuser spectra of the blocked compressor at the lower speedline shows significantly higher overall levels relative to the open configuration while the diffuser spectra of the two configurations operating at the higher speedline show similar levels. This again shows the positive impact of casing treatment on the noise generation in the compressor as, in spite of lower mass flow rates, the spectra of open configurations are similar to a blocked configuration that is operating at a higher mass flow rate.

The propagation of this noise to the compressor ducts is shown in the inlet and outlet duct spectra presented in Figure 6.13. For the open configuration, the inlet and outlet duct spectra show higher levels at 130 krpm as seen in the inducer and diffuser spectra but with lower differences in the overall levels. Similar to the in-compressor probes, the blocked configurations show higher noise levels at the lower speedline while lower overall levels are observed for the higher speedline. These lower overall levels for the blocked configuration are again expected to be caused by the higher mass flow rate for the surge limit as compared to the open configuration.

6.6 Conclusions

In this chapter, the evolution of flow and acoustic features with an increase in the operational speed of the compressor are investigated by studying the spectra of the compressor at 99 krpm and 130 krpm speedlines. The computationally optimal numerical configuration using the SBES formulation on a grid with 10 million cells and a timestep corresponding to 4° impeller rotation per iteration is used in this chapter. The numerical spectra are shown to reasonably capture the differences between the two speedlines for the investigated configurations. Although the increase in operational speed is shown to generally increase the overall acoustic emission of the compressor for both configurations, particular care should be exercised to interpret the results of near surge operation as the points are not aerodynamically similar.

For the design operation, the expected increase in the velocity, pressure, Mach number and entropy are observed with the increase in the operational speed. The acoustic spectra of inducer and diffuser probes show higher noise generation at the higher speedline for both configurations. A similar trend of relatively higher noise levels at the higher speedline can also be observed in the inlet and outlet duct spectra. The differences between the inducer and inlet duct spectra of the open and blocked configuration are seen to increase at the higher speedline while the deviation in the diffuser and outlet duct spectra of two configurations decreases at the higher speedline.

For the near surge operation, the impact of operating speed cannot be established by directly comparing the spectra of two speedlines. The blocked configuration at higher speed is observed to yield lower overall levels relative to the open configuration as it is operating at higher mass flow rates. Furthermore, the comparison of near surge spectra of the two configurations operating at aerodynamically similar points, i.e. the near surge state of the 99 krpm speedline shows the positive impact of casing treatment on the acoustic emission by lowering the overall noise levels.

Chapter 7

Concluding remarks

Contents

7.1 Introduction

In this chapter, a critical review of this thesis is performed and concluding remarks on this work are presented. The key findings obtained during the course of this work and the significant contributions to the state-of-the-art in the numerical characterisation of the flow induced noise in centrifugal compressors are compiled in Section 7.2 and Section 7.3 respectively. The limitations of the numerical methodology and how it can impact the interpretation of the aforementioned findings are discussed in Section 7.4. Finally, Section 7.5 lays down potential paths that can be pursued in the continuation of this research and expansion of the knowledge of compressor aeroacoustics.

7.2 Summary of findings

As specified in Chapter 1, this research is aimed at enhancing the understanding of the impact of ported shroud casing treatment on the flow-induced acoustic characteristics of a small high-speed turbocharger compressor. After the careful review of the literature, the objectives specified in Section 1.3 were deduced. Each of these objectives has been thoroughly investigated in this thesis, and a brief summary of the various findings pertaining to each research question has been compiled.

7.2.1 Findings on objective 1

"Evaluation of the acoustic and aerodynamic performance characteristics of the compressor with ported shroud casing treatment operating at design and surge conditions"

The flow and acoustic characteristics of the compressor with casing treatment operating at the design and near surge conditions of the 99 krpm speedline are discussed in Chapter 4. The significant findings of this chapters are:

- For the design operation, although the flow inside the compressor appears to be steady and attached, a back and forth flow is observed through the PS slot, with clear structures rotating with the blades, featuring differences in speed at specific angular coordinates.
- A unidirectional radially outward flow was observed in the PS slot for the near surge operation. The flow then exits the PS cavity in the form of high-velocity jets that interact with the incoming flow leading to the propagation of unsteadiness upstream.

- Low-velocity stall cells were identified and observed to propagate circumferentially along the blades at 0.32-0.4 times the impeller speed for the near surge condition.

- The acoustic spectra for the design point were observed to be dominated by a characteristic 'buzz-saw' or RO tonal noise.

- The low-frequency broadband features associated with near surge operation of the centrifugal compressors are alleviated by the PS casing treatment and were not observed in the spectra of the near surge point. Furthermore, the characteristic 'whoosh' noise seen in literature was also not observed in the spectra of either design or near surge points.

7.2.2 Findings on objective 2

"Investigate the relationship between the flow field mechanisms and the acoustic emission of the compressor"

The relationship between the flow and acoustic features of the compressor with casing treatment operating at the 99 krpm speedline is examined in Chapter 4. The flow field of the compressor is evaluated using conventional post-processing [160] methods along with the novel application of the POD to decompose the computed pressure field for both design and near surge points of the 99 krpm speedline. The significant findings of these analyses are:

- The characteristic 'buzz-saw' or RO tones observed in the acoustic spectra at the design condition were hypothesised by previous researchers [27] to be caused by the sonic conditions being reached in the impeller, a phenomenon seen in axial compressors. This thesis confirmed the hypothesis by identifying sonic regions attached to the leading edges of the main blades. Additionally, sonic conditions are also reached in the tips of the trailing edges for both main and splitter blades.

- Propagation of rotating stall cells is found to be the underlying mechanism of the tonal noise observed at approximately 0.37RO in the spectrum of the diffuser probe for the near surge point.

- The decomposition of the dynamic pressure field generated the set of orthogonal modes $\phi_j(\xi)$ with their corresponding temporal coefficients $a_j(t)$ and energy levels λ_j . The results showed that the majority of the energy content for design point was accumulated in the first two modes (ϕ_2 - ϕ_3) and these two modes were observed to be related to the blade pass tones.

- For the near surge point, the energy was seen to be distributed much more evenly among the modes, and the dominant modes were observed to have a strong lower-mid frequency content.

- Spectral features computed from the temporal coefficients $a_j(t)$ of respective modes allowed the separate analysis of lower, medium and higher frequency characteristics of the compressor pressure field. Inspection of the spatial distribution of the modal energy illustrated propagation patterns. For the design condition, the diffuser and the PS cavity were found to house the more energetic sources of the oscillations. In particular, the high-frequency content, dominated by the BPF and its higher order harmonics, showed a clear influence of the diffuser. The PS cavity was seen to hold the largest amplitudes of the oscillations at the lower and mid frequencies.

- For the near surge conditions, the diffuser and volute were observed to be housing the more energetic sources of broadband content. In contrast to the results of design conditions, the PS cavity was not seen to be associated with the significant source of noise content for near surge operation.

7.2.3 Findings on objective 3

"Understand the differences in the acoustic features due to the implementation of the casing treatment"

The impact of PS casing treatment on the acoustic characteristics of the compressor was quantified by comparing the spectra of open and blocked compressor configurations operating at 99 krpm as the design and near surge points for both configurations are aerodynamically similar for this speedline. Chapter 5 is devoted to these comparisons and the significant findings of this chapter are:

- For the design operation, although the flow characteristics for the two configurations were similar, higher entropy generation in the impeller region was observed for the open configuration.

- The acoustic spectra of the inducer and diffuser probes for the design point showed slightly higher noise generation in the blocked configuration, but the propagation of noise at the inlet and outlet ducts showed insignificant differences in the overall levels of the two configurations, with higher tonal content in the inlet duct spectrum of the open configuration.

- For the near surge operation, the diffusion of velocity into pressure was observed to be abrupt in the impeller of the blocked configuration, paired with the relatively high losses. These losses were attributed to the intense stall observed on multiple blades of the blocked configuration.

- The inducer and diffuser spectra of the blocked configuration operating near surge showed similar and/or lower noise levels relative to the corresponding open configuration at lower frequencies, while significantly higher levels were observed beyond those cut-off frequencies for the blocked configuration.

- Characteristic broadband elevations in the lower and medium frequency regions associated with the near surge operation were observed in the spectra of the blocked configuration. Furthermore, broadband in the characteristic 'whoosh' noise frequency was also identified in the spectrum of the outlet duct for blocked configuration.

7.2.4 Findings on objective 4

"Analyse the changes in the flow behaviour and acoustic characteristics with an increase in the operating speed by investigating the operation of the compressor at a higher iso-speedline"

The impact of the operational speed on the acoustic and flow features was investigated by comparing the relevant characteristics of the 99 krpm and 130 krpm speedlines for both open and blocked configurations. The impact of operational speed was only established for the design conditions, while the changes in the near surge features of two speedlines were an amalgamation of operational speed and different aerodynamic conditions of the near surge states. This campaign is taken up in Chapter 6, and the significant findings of this chapter are:

- The increase in operational speed has been shown to generally increase the overall acoustic emission of the compressor for both configurations.

- The velocity, pressure, Mach number and entropy were observed to increase at the design condition with the increase in the operational speed.

- The acoustic spectra of the inducer and diffuser probes showed higher noise generation at the higher speedline for both configurations. A similar trend of relatively higher noise levels at the higher speedline was also observed in the inlet and outlet duct spectra.

- For the design operation, the differences in the overall levels observed for the inducer and inlet duct spectra of the two configurations were seen to increase at the higher speedline while the deviation in the overall levels for the diffuser and outlet duct spectra of the two configurations decreased at the higher speedline.

- For the near surge operation, the impact of operating speed could not be established by directly comparing the spectra of two speedlines. The blocked configuration at the higher speedline was observed to yield lower overall levels relative to the open configuration. This was not inherently due to PS design but was a secondary effect of decreasing the surge limit to a lower mass flow rate which led to a noisier open configuration.

7.2.5 Methodical findings

The critical parameters of the numerical set-up were evaluated in Chapter 3 from the standpoint of predicting flow-induced noise with reasonable computational efficiency. The significant findings of this chapter are:

- The performance predictions were observed to be within 1.5% of the measured values irrespective of the investigated turbulence and timestep parameters. Furthermore, the velocity distribution in the impeller predicted by different turbulence formulations was also consistent. Therefore, the baseline numerical configuration of this thesis could be used as an optimal choice for performance investigations.

- The overall trend of the noise generation spectra quantified from inducer and diffuser probes were similar regardless of turbulence formulations and timestep sizes. The absolute values of the sound pressure level and decay rates predicted by LES and SBES models showed better correlation with the measured results than the ones from DES and URANS models.

- The predominant dependence of noise propagation on the size of the timestep was clearly observed in the case of duct spectra as the decrease in the size of timestep increases the range of the frequency over which spectra could be appropriately resolved.

- The results emphasised the importance of high spatial resolution for scale resolving turbulence formulations to yield better results.

7.3 Summary of contributions

A doctoral project is required to make an original contribution that widens the horizon of knowledge in that area [161]. In this section, the main original contributions that are claimed by this thesis are outlined.

- Ported shroud casing treatment is observed to aid the propagation of the tonal noise in the direction upstream of the impeller. This effect can especially be seen for the design operation, and propagation of tonal noise increases at the higher operational speed of the compressor. This extends the work of Chen and Yin [57] and Chen and Lei [58] which claimed an increase in the noise (tonal) due to the use of casing treatment without providing any quantifiable evidence.

- The acoustic emission of the compressor operating near surge is alleviated (lower noise levels) by using PS casing treatment. This dismisses the claims made in studies [57, 58] on the deterioration of the acoustic emission by the use of casing treatment irrespective of the operating point of the compressor.

- The broadband features associated with the near surge operation, including ‘whoosh’ [28, 45, 47] noise are alleviated by the use of PS casing treatment. Although broadband noise at the near surge operation of the compressor has been investigated, the alleviation of this broadband noise by the casing treatment has not been presented in the literature.

- The application of POD to the pressure field of the compressor clearly shows the role of the PS cavity in housing tonal features while the impeller downstream region, specifically the diffuser, is observed to house the sources of broadband noise detected in lower and middle-frequency ranges. Although modal decomposition has been used to understand the precursors to surge [36, 37, 126] the relationship between flow field and acoustic features of the PS compressor are not established in the literature.

- The source of characteristic ‘buzz-saw’ or RO tones as the shock waves attached to the rotor is confirmed by identifying sonic regions attached to the leading edges of the main blades. This validates the hypothesis presented by Raitor and Neise [27] based on similar features seen in the spectra of axial compressors.

7.4 Limitations

The author believes that the objectives stated in Chapter 1 have been accomplished to a satisfactory level as evident from the summary presented in Section 7.2, but these conclusions are based on a numerical methodology that has some inherent limitations. Although the general agreement between experimental and numerical results validate the numerical methodology, limitations of the existing work are discussed to aid the interpretation of the work and to help pave the way for improving the current methodology.

The foremost limitation of this work is that only one centrifugal compressor has been studied and hence, the aforementioned conclusions are case dependent. The design of components like impeller, diffuser and volute are among many other potential factors that could alter the acoustic signature of the compressor. Furthermore, only two speedlines viz. 99 krpm and 130 krpm are investigated in this thesis. For significantly different operating speeds, the acoustic signature of the compressor could be different. Therefore, the conclusions summarised in Section 7.2 are limited to the compressor operational configurations investigated in this thesis and the extrapolation of these results should be treated with caution.

Secondly, the analysis of the numerical set-up is also performed for a single speedline (99 krpm), and the results such as the size of timestep and number of elements might not be the best for different operating speeds. Furthermore, only a single type of mesh element, i.e. polyhedral and a static value of tip clearance have been explored in this thesis.

The grid independence study in this thesis is performed only with URANS formulation in spite of the drastic improvements in the results of the scale resolving LES formulation observed on the grid with higher element count. Furthermore, the convective and transient terms are discretised using a blend of second order and first order schemes, which are known for relatively higher numerical diffusion. Ideally, entirely second or higher order schemes should be used to minimise the numerical diffusion.

The complete ducts of the measurement rig are not numerically modelled, and therefore reflections and/or standing waves are expected in the numerical domain as the NRBC are not used. Although the effect of reflections from the boundaries on the duct spectra has been diminished by using pressure wave decomposition, standing waves in the domain could still impact the spectra of the inducer and diffuser probes.

The broadband elevations centring on approximately 19 kHz observed in the experimental spectra of the inducer and diffuser probes for near surge and design operation respectively are not reproduced by the numerical model. These broadband elevations are hypothesised to be caused by the local interaction of swirling flows with the structural components. The tonal features in the numerical spectra are accentuated relative to the measured results. Furthermore, the agreement between measured and predicted spectra for the ducts is poor at higher frequencies in terms of overall levels and rate of decay. Unfortunately, due to lack of similar work, the author at this point in time cannot decide whether the model is not accurately representing the responsible flow phenomenon or these noise features are related to the experimental apparatus.

Finally, the modal decomposition of pressure field using POD assumes a linear combination of modes and their respective temporal coefficients which might not be an accurate representation of the flow, especially at off-design conditions. Furthermore, the impeller or rotating domain is not included in the model decomposition as the position of cells inside the rotor changes with each timestep.

7.5 Suggestions for future studies

In this section, potential directions for the future work are proposed that can contribute towards the hypotheses presented in this thesis and add further meaningful insights on the flow-induced noise in high-speed centrifugal compressors. The suggestions to improve the numerical model and overcome the aforementioned limitations are described in Section 7.5.1. Proposals for the continuation of the research along with the interesting dynamics observed during the course of this thesis that could not be explored due to constraints on time and resources are described in Section 7.5.2.

7.5.1 Improving thesis limitations

A mesh independence study similar to the one already done in this thesis could be performed for the LES model to understand the ideal mesh size, not for just noise generation, but for the propagation of noise to the compressor ducts too. Different kind of elements (hexahedra) and grids (structured) could be used, and spectra from these variants could be compared to the ones presented in this thesis to understand their corresponding impacts.

The boundary conditions could be changed to NRBC, specifically at the inlet in order to alleviate the reflected pressure wave content in the system. The use of NRBCs did present issues with numerical stability and convergence in this work. The improvements in the implementation of NRBCs in the direct method (CFD) are needed and hence, extension of the ducts with successive grid coarsening could be the starting point. Furthermore, higher order discretisation schemes could be used to decrease the numerical diffusion. Also, the turbulent intensity at the inlet section for the numerical and experimental test rig could be investigated as the literature [162] does show an impact of turbulence intensity on pressure spectra.

The virtual wall probes that match the position used in experimental measurements along with the virtual section probes could be used to monitor the pressures. The deviation between the numerical and experimental results, especially beyond plane wave region, can be reduced by employing section probes in the numerical model instead of the point probes used in this thesis as shown by Broatch et al. [34]. The section probes are expected to help in capturing the higher order effects introduced by swirl and related three-dimensional flow features seen in the compressor.

Although the changes in the static values of tip clearance are shown [33] to have insignificant effect on the noise spectra, dynamic changes in the tip clearance due to shaft motion could be a potential aeroacoustic source. Shaft motion and corresponding changes in the blade tip clearance should therefore be replicated in the numerical model. To achieve this, the method of RBM used in this thesis to model impeller motion would need replacing with a complete dynamic mesh approach, incurring a significant increase in computational overhead.

The modal decomposition of flow performed in this thesis using POD could be extended to include the rotor region. To achieve this, the current algorithm of modal decomposition should include an additional subroutine that can search for the reference spatial locations in the rotor region and, in case of the space being collapsed by the blades, it should increase the search radius and provide the pressure data of the nearest cell, thereby, building a coherent pressure trace of the cells.

7.5.2 Continuation of research

A range of small high-speed centrifugal compressors with diverse component designs could be studied at various speedlines to understand the global (expected features like BPF) and local features (dependent on geometry) of the aeroacoustic phenomena. The influence of geometry on the aeroacoustic mechanisms and spectra could also be quantified from such a campaign.

Broadband elevation corresponding to 'whoosh' noise was observed in the spectra of the PS blocked configuration operating near surge. The decomposition of the pressure field of this configuration could give an interesting insight into the flow mechanism responsible for 'whoosh' noise in the studied case.

Application of acoustic similarity laws to identify the aerodynamically and acoustically similar near surge states of open and blocked configurations can provide credible operating points to determine the impact of operating speed and casing treatment on the acoustic emission of the compressor.

The extension of the POD of the pressure field to DMD could provide insightful information to link the coherent flow structures to their corresponding frequency content. Such information could be crucial to better the acoustic design of future high-speed centrifugal machines.

Pressure wave decomposition methods such as beamforming used in this thesis are limited to the plane wave region. The extension of these methods to include higher frequencies could help with better predictions of duct spectra over a broader range.

Although the focus of this thesis was limited to internal flow, the significant extent of noise realised by the end user is generally through the vibration and radiated paths. Therefore, the extension of this work to include fluid-structure interaction and vibroaeroacoustics comes across as the obvious next step to realise the complete transfer path from noise generation to the user's ear.

References

[1] Sidharath Sharma, Alberto Broatch, Jorge García-Tíscar, AK Nickson, and JM Allport. Acoustic and pressure characteristics of a ported shroud turbocompressor operating at near surge conditions. *Applied Acoustics*, 148:434–447, 2019.

[2] Sidharath Sharma, Alberto Broatch, Jorge García-Tíscar, John M Allport, and Ambrose K Nickson. Acoustic characteristics of a ported shroud turbocompressor operating at design conditions. *International J of Engine Research*, 1:15, 2018.

[3] Sidharath Sharma, Jorge García-Tíscar, John M Allport, Martyn L Jupp, and Ambrose K Nickson. Impact of impeller casing treatment on the acoustics of a small high speed centrifugal compressor. In *ASME Turbo Expo 2018: Turbomachinery Technical Conference and Exposition*, pages V02BT43A010–V02BT43A010. American Society of Mechanical Engineers, 2018.

[4] Sidharath Sharma, Martyn Jupp, Simon Barrans, and Keith Nickson. The impact of housing features relative location on a turbocharger compressor flow. *International Journal of Mechanical Engineering and Robotics Research*, 6(6):451–457, 2017.

[5] Sidharath Sharma, Martyn L Jupp, Ambrose K Nickson, and John M Allport. Ported shroud flow processes and their effect on turbocharger compressor operation. In *ASME Turbo Expo 2017: Turbomachinery Technical Conference and Exposition*, pages V02CT44A017–V02CT44A017. American Society of Mechanical Engineers, 2017.

[6] Sidharath Sharma, Alberto Broatch, Jorge García-Tíscar, John M Allport, and Ambrose K Nickson. Impact of impeller casing treatment on the acoustic characteristics of a high speed centrifugal compressor: An experimental study. *Manuscript accepted by the journal of Aerospace Science and Technology*, 2019.

[7] Sidharath Sharma, Simon Barrans, Jorge García-Tíscar, John M Allport, and Ambrose K Nickson. Evaluation of modelling parameters for computing flow-induced noise in a small high-speed centrifugal compressor. *Manuscript submitted to the journal of Aerospace Science and Technology*, 2019.

[8] Sidharath Sharma, Simon Barrans, Jorge García-Tíscar, John M Allport, and Ambrose K Nickson. Effects of ported shroud casing treatment on the acoustic and flow behaviour of a centrifugal compressor. *Manuscript accepted by the International Journal of Engine Research*, 2019.

[9] Sidharath Sharma, Simon Barrans, Jorge García-Tíscar, John M Allport, and Ambrose K Nickson. Impact of operational speed on the acoustic characteristics of a high-speed

centrifugal compressor with and without casing treatment. *Manuscript to be submitted to the International Journal of Engine Research*, 2019.

[10] Ladislao Reti and Francesco di Giorgio Martini. Francesco di giorgio martini's treatise on engineering and its plagiarists. *Technology and Culture*, 4(3):287–298, 1963.

[11] Mats Abom. Turbomachinery aeroacoustics mats Åbom kth-the royal inst of technology. 04 2017.

[12] C. Soares. *Microturbines: Applications for Distributed Energy Systems*. Elsevier Science, 2011.

[13] Mattia Olivero. Evolution of a centrifugal compressor: From turbocharger to micro gas turbine applications. 2012.

[14] E. M. Greitzer. The stability of pumping systems—the 1980 freeman scholar lecture. *Journal of Fluids Engineering*, 103(2):193–242, 1981.

[15] C. Rodgers. Centrifugal compressor inlet guide vanes for increased surge margin. *Journal of Turbomachinery*, 113(4):696, 1991.

[16] A. Whitfield and A. H. Abdullah. The performance of a centrifugal compressor with high inlet prewhirl. *Journal of Turbomachinery*, 120(3):487–493, 1998.

[17] P. A. Eynon, A. Whitfield, M. R. Firth, A. J. Parkes, and R. Saxton. *A study of the flow characteristics in the inducer bleed slot of a centrifugal compressor*. ASME Technical Paper : GT. The American Society of Mechanical Engineers, New York, 1996.

[18] F. B. Fisher. Application of map width enhancement devices to turbocharger compressor stages. 1988.

[19] I MacDougal and R.L Elder. Improvement of operating range in a small, high speed, centrifugal compressor using casing treatments. In *I Mech E Conference Publications (Institution of Mechanical Engineers)*, pages 19–26.

[20] H. Stoffels and M. Schroeer. Nvh aspects of a downsized turbocharged gasoline powertrain with direct injection. *SAE Technical Papers*, 2003.

[21] J. Němec. Noise of axial fans and compressors: Study of its radiation and reduction. *Journal of Sound and Vibration*, 6(2):230–236, 1967.

[22] J. W. R. Griffiths. The spectrum of compressor noise of a jet engine. *Journal of Sound and Vibration*, 1(2):127–140, 1964.

[23] Jong-Soo Choi. Aerodynamic noise generation in centrifugal turbomachinery. *KSME Journal*, 8(2):161, 1994.

[24] Jong-Soo Choi, Dennis K. McLaughlin, and Donald E. Thompson. Experiments on the unsteady flow field and noise generation in a centrifugal pump impeller. *Journal of Sound and Vibration*, 263(3):493–514, 2003.

[25] L. Mongeau, D. E. Thompson, and D. K. McLaughlin. Sound generation by rotating stall in centrifugal turbomachines. *Journal of Sound and Vibration*, 163(1):1–30, 1993.

[26] L. Mongeau, D. E. Thompson, and D. K. McLaughlin. A method for characterizing aerodynamic sound sources in turbomachines. *Journal of Sound and Vibration*, 181(3):369–389, 1995.

[27] Till Raitor and Wolfgang Neise. Sound generation in centrifugal compressors. *Journal of sound and vibration*, 314(3):738–756, 2008.

[28] D. Evans and A. Ward. *Minimising Turbocharger Whoosh Noise for Diesel Powertrains*. SAE Paper : SAE Noise and Vibration Conference and Exhibition. Society of Automotive Engineers, Warrendale, Penn., 2005.

[29] Eric P Trochon. A new type of silencers for turbocharger noise control. Technical report, SAE Technical Paper, 2001.

[30] Hans Rämmal and Mats Åbom. Acoustics of turbochargers. Technical report, SAE Technical Paper, 2007.

[31] A. J. Torregrosa, A. Broatch, X. Margot, and J. García-Tíscar. Experimental methodology for turbocompressor in-duct noise evaluation based on beamforming wave decomposition. *Journal of Sound and Vibration*, 376:60–71, 2016.

[32] A. Broatch, J. Galindo, R. Navarro, and J. García-Tíscar. Numerical and experimental analysis of automotive turbocharger compressor aeroacoustics at different operating conditions. *International Journal of Heat and Fluid Flow*, 2016.

[33] J. Galindo, A. Tiseira, R. Navarro, and M. A. López. Influence of tip clearance on flow behavior and noise generation of centrifugal compressors in near-surge conditions. *International Journal of Heat and Fluid Flow*, 52(0):129–139, 2015.

[34] A. Broatch, J. Galindo, R. Navarro, and J. García-Tíscar. Methodology for experimental validation of a cfd model for predicting noise generation in centrifugal compressors. *The International journal of heat and fluid flow*, 50:134–144, 2014.

[35] Elias Sundström, Bernhard Semlitsch, and Mihai Mihăescu. Generation mechanisms of rotating stall and surge in centrifugal compressors. *Flow, Turbulence and Combustion*, 2017.

[36] Bernhard Semlitsch and Mihai Mihăescu. Flow phenomena leading to surge in a centrifugal compressor. *Energy*, 103:572–587, 2016.

[37] Elias Sundström, Bernhard Semlitsch, and Mihai Mihaescu. *Centrifugal Compressor: The Sound of Surge*. AIAA Aviation. American Institute of Aeronautics and Astronautics, 2015.

[38] B. Semlitsch, V. Jyothishkumar, M. Mihaescu, L. Fuchs, E. Gutmark, and M. Gancedo. Numerical flow analysis of a centrifugal compressor with ported and without ported shroud. *SAE Technical Papers*, 1, 2014.

[39] F. Mendonça, O. Baris, and G. Capon. Simulation of radial compressor aeroacoustics using CFD. In *Proceedings of the ASME Turbo Expo*, volume 8, pages 1823–1832, 2012.

[40] Ahsanul Karim, Keith Miazgowicz, Brian Lizotte, and Abdelkrim Zouani. Computational aero-acoustics simulation of compressor whoosh noise in automotive turbochargers. Technical report, SAE Technical Paper, 2013.

[41] A. Broatch, J. Galindo, R. Navarro, J. García-Tíscar, A. Daglish, and R. K. Sharma. Simulations and measurements of automotive turbocharger compressor whoosh noise. *Engineering Applications of Computational Fluid Mechanics*, pages 1–9, 2015.

[42] A. J. Torregrosa, A. Broatch, X. Margot, J. García-Tíscar, Y. Narvekar, and R. Cheung. Local flow measurements in a turbocharger compressor inlet. *Experimental Thermal and Fluid Science*, 88:542–553, 2017.

[43] J. Galindo, A. Tiseira, R. Navarro, D. Tarí, and C. M. Meano. Effect of the inlet geometry on performance, surge margin and noise emission of an automotive turbocharger compressor. *Applied Thermal Engineering*, 110:875–882, 2017.

[44] J.A. Calvo, V. Diaz, and J.L. San Roman. Controlling the turbocharger whistling noise in diesel engines. *International Journal of Vehicle Noise and Vibration*, 2(1):17–28, 2006.

[45] Caner Sevginer, M Ozgur Arslan, N Sonmez, and S Ilker Yilmaz. Investigation of turbocharger related whoosh and air blow nosie in a diesel powertrain. In *INTER-NOISE and NOISE-CON Congress and Conference Proceedings*, volume 2007, pages 3163–3172. Institute of Noise Control Engineering.

[46] Gladys Gaude, Thierry Lefevre, Romil Tanna, Kevin Jin, T. J. Bryan McKitterick, and Sylvie Armenio. Experimental and computational challenges in the quantification of turbocharger vibro-acoustic sources. *INTER-NOISE and NOISE-CON Congress and Conference Proceedings*, 2008(3):5754–5767, 2008.

[47] Charlie Teng and Steve Homco. Investigation of compressor whoosh noise in automotive turbochargers. 2009.

[48] H. Tiikoja, H. Rämmal, M. Abom, and H. Boden. Investigations of automotive turbocharger acoustics. *SAE International Journal of Engines*, 4(2):2531–2542, 2011.

[49] Neil Figurella, Rick Dehner, Ahmet Selamet, Kevin Tallio, Keith Miazgowicz, and Robert Wade. Noise at the mid to high flow range of a turbocharger compressor. *Noise Control Engineering Journal*, 62(5):306–312, 2014.

[50] Neil Figurella, Rick Dehmer, Ahmet Selamet, Kevin Tallio, Keith Miazgowicz, Robert Wade, Ahsanul Karim, Philip Keller, and John Shutty. Effect of inlet vanes on centrifugal compressor acoustics and performance. *Noise Control Engineering Journal*, 62(4):232–237, 2014.

[51] F. Kameier and W. Neise. Rotating blade flow instability as a source of noise in axial turbomachines. *Journal of Sound and Vibration*, 203(5):833–853, 1997.

[52] H. Rämmal and M. Åbom. Experimental determination of sound transmission in turbo-compressors. *SAE Technical Papers*, 2009.

[53] H. Rämmal, M. Åbom, H. Tiikoja, and H. Bodén. Experimental facility for the complete determination of sound transmission in turbochargers. *SAE Technical Papers*, 2010.

[54] Yong Woo Lee, Duck Joo Lee, Yumi So, and Doyoung Chung. Control of airflow noise from diesel engine turbocharger. Technical report, SAE Technical Paper, 2011.

[55] Jorge García Típscar. *Experiments on turbocharger compressor acoustics*. Thesis doctoral, 2017.

[56] Antonio J. Torregrosa, Alberto Broatch, Roberto Navarro, and Jorge García-Tíscar. Acoustic characterization of automotive turbocompressors. *International Journal of Engine Research*, 16(1):31–37, 2015.

[57] Hua Chen and JunFei Yin. *Turbocharger compressor development for diesel passenger car applications A2 - Group, Institution of Mechanical Engineers Combustion Engines & Fuels*, pages 15–27. Woodhead Publishing, 2006.

[58] Hua Chen and Vai-Man Lei. Casing treatment and inlet swirl of centrifugal compressors. *Journal of Turbomachinery*, 135(4):041010, 2013.

[59] E. Guillou, R. Dimicco, E. Gutmark, A. Mohamed, and M. Gancedo. Characterization of a ported shroud compressor using piv measurements. *SAE Technical Papers*, 2010.

[60] E. Guillou, M. Gancedo, E. Gutmark, and A. Mohamed. Piv investigation of the flow induced by a passive surge control method in a radial compressor. *Experiments in Fluids*, 53(3):619–635, 2012.

[61] F. Hellstrom, E. Guillou, M. Gancedo, R. Dimicco, A. Mohamed, E. Gutmark, and L. Fuchs. Stall development in a ported shroud compressor using piv measurements and large eddy simulation. *SAE Technical Papers*, 2010.

[62] Matthieu Gancedo, Erwann Guillou, Russell DiMicco, Ephraim Gutmark, and Ashraf Mohamed. *Dynamic Characterization of a Centrifugal Compressor with Ported Shroud*. Aerospace Sciences Meetings. American Institute of Aeronautics and Astronautics, 2011.

[63] Dimicco Russell, Gancedo Matthieu, Guillou Erwann, Gutmark Ephraim, and Mohamed Ashraf. *Ported Shroud Effects on the Unstable Dynamic Characteristics of a Radial Compressor*. Fluid Dynamics and Co-located Conferences. American Institute of Aeronautics and Astronautics, 2011.

[64] Gancedo Matthieu, Gutmark Ephraim, E. Guillou, and Mohamed Ashraf. *PIV Measurements of Flow in Recirculation Cavities at the Inlet of a Centrifugal Compressor*. Aerospace Sciences Meetings. American Institute of Aeronautics and Astronautics, 2012.

[65] M. Gancedo, E. Guillou, E. Gutmark, and A. Mohamed. Dynamic features and their propagation in a centrifugal compressor housing with ported shroud. *SAE Technical Papers*, 2012.

[66] Matthieu Gancedo, Ephraim Gutmark, and Erwann Guillou. Piv measurements of the flow at the inlet of a turbocharger centrifugal compressor with recirculation casing treatment near the inducer. *Experiments in Fluids*, 57(2):1–19, 2016.

[67] Guillou Erwann, M. Gancedo, Dimicco Russell, Gutmark Ephraim, and Mohamed Ashraf. *PIV Measurements of Surge Incipience in a Ported Shroud Compressor*. Fluid Dynamics and Co-located Conferences. American Institute of Aeronautics and Astronautics, 2010.

[68] Hyosung Sun and Soogab Lee. Numerical prediction of centrifugal compressor noise. *Journal of sound and vibration*, 269(1):421–430, 2004.

[69] Hyosung Sun, Hyungki Shin, and Soogab Lee. Analysis and optimization of aerodynamic noise in a centrifugal compressor. *Journal of Sound and Vibration*, 289(4–5):999–1018, 2006.

[70] D. L. Hawkings and J. E. Ffowcs Williams. *Sound Generation by Turbulence and Surfaces in Arbitrary Motion*, volume 264. 1969.

[71] Stefano Fontanesi, Stefano Paltrinieri, and Giuseppe Cantore. Cfd analysis of the acoustic behavior of a centrifugal compressor for high performance engine application. *Energy Procedia*, 45(0):759–768, 2014.

[72] A. J. Torregrosa, P. Fajardo, A. Gil, and R. Navarro. Development of non-reflecting boundary condition for application in 3d computational fluid dynamics codes. *Engineering Applications of Computational Fluid Mechanics*, 6(3):447–460, 2012.

[73] Wim De Roeck. Hybrid methodologies for the computational aeroacoustics analysis of confined subsonic flows, 2007.

[74] L Gamet and JL Estivalezes. Application of large-eddy simulations and kirchhoff method to jet noise prediction. *AIAA journal*, 36(12):2170–2178, 1998.

[75] M Wang, S Moreau, G Iaccarino, and M Roger. Les prediction of pressure fluctuations on a low speed airfoil. *Center for Turbulence Research Annual Research Briefs*, 2004.

[76] R Mankbadi, R Hixon, and L Povinelli. Very large eddy simulations of jet noise. In *6th Aeroacoustics Conference and Exhibit*, page 2008, 2000.

[77] Awatef Hamed, D Basu, and K Das. Detached eddy simulations of supersonic flow over cavity. In *41st Aerospace Sciences Meeting and Exhibit*, page 549, 2003.

[78] M. J. Lighthill. *On Sound Generated Aerodynamically. I. General Theory*, volume 211. 1952.

[79] M. J. Lighthill. On sound generated aerodynamically. ii. turbulence as a source of sound. *Proceedings of the Royal Society of London. Series A, Mathematical and Physical Sciences*, 222(1148):1–32, 1954.

[80] N. Curle. The influence of solid boundaries upon aerodynamic sound. *Proceedings of the Royal Society of London. Series A, Mathematical and Physical Sciences*, 231(1187):505–514, 1955.

[81] S. Khelladi, S. Kouidri, F. Bakir, and R. Rey. Predicting tonal noise from a high rotational speed centrifugal fan. *Journal of Sound and Vibration*, 313(1):113–133, 2008.

[82] I. Proudman. *The Generation of Noise by Isotropic Turbulence*, volume 214. 1952.

[83] ANSYS® Fluent Academic Research. *ANSYS Fluent-Solver Theory Guide*. Help System. ANSYS, Inc., USA, 2013.

[84] ANSYS® CFX Academic Research. *ANSYS CFX-Solver Theory Guide*. Help System. ANSYS, Inc., USA, 2013.

[85] Ajith V Pai, Stephen Walsh, Dan O'Boy, and Rui Chen. Turbocharger surge noise measurement and solution using experimental techniques. 2015.

[86] A. V. Pai, S. J. Walsh, D. J. O'Boy, and R. Chen. Air intake system noise in a turbocharged petrol engine during transient operation. In *42nd International Congress and Exposition on Noise Control Engineering 2013, INTER-NOISE 2013: Noise Control for Quality of Life*, volume 1, pages 288–295.

[87] Kyoung-Ku Ha, Tae-Bin Jeong, Shin-Hyoung Kang, Hyoung-Jin Kim, Kwang-Min Won, Chi-Yong Park, Woo-Youl Jung, and Kyung-Seok Cho. Experimental investigation on aero-acoustic characteristics of a centrifugal compressor for the fuel-cell vehicle. *Journal of Mechanical Science and Technology*, 27(11):3287–3297, 2013.

[88] Xinqian Zheng and Anxiong Liu. Phenomenon and mechanism of two-regime-surge in a centrifugal compressor. *Journal of Turbomachinery*, 137(8):081007–081007, 2015.

[89] Zheng Xinqian and Liu Anxiong. Experimental investigation of surge and stall in a high-speed centrifugal compressor. *Journal of Propulsion and Power*, 31(3):815–825, 2015.

[90] C. L. Morfey. Sound transmission and generation in ducts with flow. *Journal of Sound and Vibration*, 14(1):37–55, 1971.

[91] KR Holland and POAL Davies. The measurement of sound power flux in flow ducts. *Journal of Sound and Vibration*, 230(4):915–932, 2000.

[92] A. J. Torregrosa, A. Broatch, V. Bermúdez, and I. Andrés. Experimental assessment of emission models used for ic engine exhaust noise prediction. *Experimental Thermal and Fluid Science*, 30(2):97–107, 2005.

[93] Ann P Dowling and John E Ffowcs Williams. *Sound and sources of sound*. Horwood, 1983.

[94] L. J. Eriksson. Higher order mode effects in circular ducts and expansion chambers. *The Journal of the Acoustical Society of America*, 68(2):545–550, 1980.

[95] Mats Åbom and Hans Bodén. Error analysis of two-microphone measurements in ducts with flow. *The Journal of the Acoustical Society of America*, 83(6):2429–2438, 1988.

[96] F Payri, JM Desantes, and A Broatch. Modified impulse method for the measurement of the frequency response of acoustic filters to weakly nonlinear transient excitations. *The Journal of the Acoustical Society of America*, 107(2):731–738, 2000.

[97] BorgWarner Turbo Systems. Bradford, uk.

[98] J Weidemann. Analysis of the relations between acoustic and aerodynamic parameters for a series of dimensionally similar centrifugal fan rotors. *NASA Tech. Trans.*, 13:1, 1971.

[99] W. Neise. Application of similarity laws to the blade passage sound of centrifugal fans. *Journal of Sound and Vibration*, 43(1):61–75, 1975.

[100] W. Neise and B. Barsikow. Acoustic similarity laws for fans. *Journal of Engineering for Industry*, 104(2):162–168, 1982.

[101] Wan-Ho Jeon, Duck-Joo Lee, and Huinam Rhee. An application of the acoustic similarity law to the numerical analysis of centrifugal fan noise. *JSME international journal. Series C, Mechanical systems, machine elements and manufacturing*, 47(3):845–851, 2004.

[102] CMT-Motores Térmicos. Universitat politècnica de valència, 1979.

[103] J Galindo, JR Serrano, C Guardiola, and C Cervelló. Surge limit definition in a specific test bench for the characterization of automotive turbochargers. *Experimental Thermal and Fluid Science*, 30(5):449–462, 2006.

[104] JM Luján, V Bermúdez, JR Serrano, and C Cervelló. Test bench for turbocharger groups characterization. Technical report, SAE Technical Paper, 2002.

[105] YOKOGAWA. Dl850e/dl850ev scopecorder.

[106] Alberto Broatch, J Javier Lopez, Jorge García-Tíscar, and Josep Gomez-Soriano. Experimental analysis of cyclical dispersion in compression-ignited versus spark-ignited engines and its significance for combustion noise numerical modeling. *Journal of Engineering for Gas Turbines and Power*, 140(10):102808, 2018.

[107] P. Welch. The use of fast fourier transform for the estimation of power spectra: A method based on time averaging over short, modified periodograms. *IEEE Transactions on Audio and Electroacoustics*, 15(2):70–73, 1967.

[108] Guillaume Després, Ghislaine Ngo Boum, Francis Leboeuf, David Chalet, Pascal Chesse, and Alain Lefebvre. Simulation of near surge instabilities onset in a turbocharger compressor. *Proceedings of the Institution of Mechanical Engineers, Part A: Journal of Power and Energy*, 227(6):665–673, 2013.

[109] Nima Fardafshar and Panagiotis Koutsovasilis. *Ported Shroud Influence on the Aero-Acoustic Properties of Automotive Turbochargers: Quantification by Means of Simulation and Measurement*. 2018.

[110] V. Jyothishkumar, Mihaescu Mihai, Semlitsch Bernhard, and Fuchs Laszlo. *Numerical flow analysis in centrifugal compressor near surge condition*. Fluid Dynamics and Co-located Conferences. American Institute of Aeronautics and Astronautics, 2013.

[111] Isao Tomita, Seiichi Ibaraki, Masato Furukawa, and Kazutoyo Yamada. The effect of tip leakage vortex for operating range enhancement of centrifugal compressor. *Journal of Turbomachinery*, 135(5):051020–051020, 2013.

[112] Q. Guo, H. Chen, X. C. Zhu, Z. H. Du, and Y. Zhao. Numerical simulations of stall inside a centrifugal compressor. *Proceedings of the Institution of Mechanical Engineers, Part A: Journal of Power and Energy*, 221(5):683–693, 2007.

[113] Y. Egorov and F. Menter. Development and application of sst-sas turbulence model in the desider project. In Shia-Hui Peng and Werner Haase, editors, *Advances in Hybrid RANS-LES Modelling*, pages 261–270. Springer Berlin Heidelberg.

[114] Willi Mohring. *A well posed acoustic analogy based on a moving acoustic medium*. 2010.

[115] ANSYS® ICEM CFD Academic Research. *ANSYS ICEM CFD Help Manual*. Help System. ANSYS, Inc., USA, 2013.

[116] ANSYS® CFX Academic Research. *ANSYS CFX-Solver Modeling Guide*. Help System. ANSYS, Inc., USA, 2013.

[117] P. Chow, M. Cross, and K. Pericleous. A natural extension of the conventional finite volume method into polygonal unstructured meshes for cfd application. *Applied Mathematical Modelling*, 20(2):170–183, 1996.

[118] Michael Tritthart and Dieter Gutknecht. Three-dimensional simulation of free-surface flows using polyhedral finite volumes. *Engineering Applications of Computational Fluid Mechanics*, 1(1):1–14, 2007.

[119] F. R. Menter. Two-equation eddy-viscosity turbulence models for engineering applications. *AIAA Journal*, 32(8):1598–1605, 1994.

[120] Zhigang Sun, Chunqing Tan, and Dongyang Zhang. *Flow field structures of the impeller backside cavity and its influences on the centrifugal compressor*, volume 7, pages 1349–1360. 2009.

[121] G. Piñero, L. Vergara, J. M. Desantes, and A. Broatch. Estimation of velocity fluctuation in internal combustion engine exhaust systems through beamforming techniques. *Measurement Science and Technology*, 11(11):1585, 2000.

[122] George Alexander Christou. *Fluid mechanics of ported shroud centrifugal compressor for vehicular turbocharger applications*. Thesis, 2015.

[123] K. Hillewaert and R. A. Van den Braembussche. Numerical simulation of impeller–volute interaction in centrifugal compressors. *Journal of Turbomachinery*, 121(3):603–608, 1999.

[124] Zheji Liu and D Lee Hill. Issues surrounding multiple frames of reference models for turbo compressor applications. 2000.

[125] X Q Zheng, J Huenteler, M Y Yang, Y J Zhang, and T Bamba. Influence of the volute on the flow in a centrifugal compressor of a high-pressure ratio turbocharger. *Proceedings of the Institution of Mechanical Engineers, Part A: Journal of Power and Energy*, 224(8):1157–1169, 2010.

[126] E. Sundström, B. Semlitsch, and M. Mihaescu. Assessment of the 3d flow in a centrifugal compressor using steady-state and unsteady flow solvers. *SAE Technical Papers*, 2014-October, 2014.

[127] H.K. Versteeg and W. Malalasekera. *An Introduction to Computational Fluid Dynamics: The Finite Volume Method*. Pearson Education Limited, 2007.

[128] Jose Serrano, Pablo Olmeda, Francisco Arnau, Miguel Reyes-Belmonte, and Alain Lefebvre. Importance of heat transfer phenomena in small turbochargers for passenger car applications. *SAE International Journal of Engines*, 6(2):716–728, 2013.

[129] Stephen B. Pope. *Turbulent Flows*. Cambridge University Press, Cambridge, 2000.

[130] FR Menter and M Kuntz. Development and application of a zonal des turbulence model for cfx-5. *Ansys, CFX-Validation Report, Technical Report No. CFX-VAL17/0503*, 2003.

[131] F Menter. Stress-blended eddy simulation (sbes)—a new paradigm in hybrid rans-les modeling. In *Symposium on Hybrid RANS-LES Methods*, pages 27–37. Springer, 2016.

[132] David C Wilcox. *Turbulence modeling for CFD*, volume 2. DCW industries La Canada, CA, 1998.

[133] M. Lesieur, O. Métais, and P. Comte. *Large-Eddy Simulations of Turbulence*. Cambridge University Press, Cambridge, 2005.

[134] P. G. Tucker. Large-eddy simulation for acoustics. edited by c. wagner, t. hüttl & p. sagaut. cambridge university press, 2007. 441 pp. isbn 978 0521 871440. £65. *Journal of Fluid Mechanics*, 593:505–507, 2007.

[135] Fredrik Hellstrom, Ephraim Gutmark, and Laszlo Fuchs. Large eddy simulation of the unsteady flow in a radial compressor operating near surge. *Journal of Turbomachinery*, 134(5):051006–051006, 2012.

[136] B. Semlitsch, V. Jyothishkumar, M. Mihaescu, L. Fuchs, and E. J. Gutmark. Investigation of the surge phenomena in a centrifugal compressor using large eddy simulation. In *ASME International Mechanical Engineering Congress and Exposition, Proceedings (IMECE)*, volume 7 A.

[137] Elias Sundström, Bernhard Semlitsch, and Mihai Mihăescu. Acoustic signature of flow instabilities in radial compressors. *Journal of Sound and Vibration*, 434:221–236, 2018.

[138] F. Nicoud and F. Ducros. Subgrid-scale stress modelling based on the square of the velocity gradient tensor. *Flow, Turbulence and Combustion*, 62(3):183–200, 1999.

[139] M. Strelets. *Detached eddy simulation of massively separated flows*. Aerospace Sciences Meetings. American Institute of Aeronautics and Astronautics, 2001.

[140] F. R. Menter and M. Kuntz. *Adaptation of Eddy-Viscosity Turbulence Models to Unsteady Separated Flow Behind Vehicles*, pages 339–352. Springer Berlin Heidelberg, Berlin, Heidelberg, 2004.

[141] Philippe Spalart and Craig Streett. *Young-Person's Guide to Detached-Eddy Simulation Grids*. 2001.

[142] Fred Mendonca, Alex Read, Fabiano Imada, and Vinicius Girardi. Efficient cfd simulation process for aeroacoustic driven design. In *SAE Technical Paper 2010-36-0545, 2010.*

[143] Stanley A Gelfand. *Essentials of audiology*. New York: Thieme, 2007, 2007.

[144] Subenuka Sivagnanasundaram, Stephen Spence, Juliana Early, and B. Nikpour. *Experimental and numerical analysis of a classical bleed slot system for a turbocharger compressor*, pages 325–341. 2012.

[145] Heinz Herwig and Bastian Schmandt. How to determine losses in a flow field: A paradigm shift towards the second law analysis. *Entropy*, 16(6):2959, 2014.

[146] H. Chen, S. Guo, X. C. Zhu, Z. H. Du, and S. Zhao. Numerical simulations of onset of volute stall inside a centrifugal compressor. In *Proceedings of the ASME Turbo Expo*, volume 6, 2008.

[147] Weiguang Huang, Shaojuan Geng, Junqiang Zhu, and Hongwu Zhang. Numerical simulation of rotating stall in a centrifugal compressor with vaned diffuser. *Journal of Thermal Science*, 16(2):115–120, 2007.

[148] Yannick Bousquet, Xavier Carbonneau, Guillaume Dufour, Nicolas Binder, and Isabelle Trebinjac. *Analysis of the Unsteady Flow Field in a Centrifugal Compressor from Peak Efficiency to Near Stall with Full-Annulus Simulations*, volume 2014. 2014.

[149] Vivianne Holmén. Methods for vortex identification. *Master's Theses in Mathematical Sciences*, 2012.

[150] Jinhee Jeong and Fazle Hussain. On the identification of a vortex. *Journal of fluid mechanics*, 285:69–94, 1995.

[151] Kunihiko Taira, Steven L Brunton, Scott Dawson, Clarence W Rowley, Tim Colonius, Beverley J McKeon, Oliver T Schmidt, Stanislav Gordeyev, Vassilios Theofilis, and Lawrence S Ukeiley. Modal analysis of fluid flows: An overview. *arXiv preprint arXiv:1702.01453*, 2017.

[152] Y. Saad. *Numerical Methods for Large Eigenvalue Problems*. Classics in Applied Mathematics. Society for Industrial and Applied Mathematics, 2011.

[153] Roger A. Horn and Charles R. Johnson. *Topics in Matrix Analysis*. Cambridge University Press, Cambridge, 1991.

[154] J. L. Lumley. The structure of inhomogeneous turbulent flows. *Atmospheric Turbulence and Radio Wave Propagation*, 1967.

[155] Nadine Aubry. *On The Hidden Beauty of the Proper Orthogonal Decomposition*, volume 2. 1991.

[156] Y. C. Liang, H. P. Lee, S. P. Lim, W. Z. Lin, K. H. Lee, and C. G. Wu. Proper orthogonal decomposition and its applications—part i: Theory. *Journal of Sound and Vibration*, 252(3):527–544, 2002.

[157] Svante Wold, Kim Esbensen, and Paul Geladi. Principal component analysis. *Chemometrics and Intelligent Laboratory Systems*, 2(1):37–52, 1987.

[158] Philip Holmes, John L Lumley, Gahl Berkooz, and Clarence W Rowley. Turbulence, coherent structures, dynamical systems and symmetry. *Turbulence, Coherent Structures, Dynamical Systems and Symmetry, by Philip Holmes, John L. Lumley, Gahl Berkooz, Clarence W. Rowley, Cambridge, UK: Cambridge University Press, 2012*, 2012.

[159] Rick Dehner, A. Selamet, Michael Steiger, Keith Miazgowicz, and Ahsanul Karim. *The Effect of Ported Shroud Recirculating Casing Treatment on Turbocharger Centrifugal Compressor Acoustics*, volume 10. 2017.

[160] ANSYS® CFD-Post Academic Research. *ANSYS CFD-Post Help Manual*. Help System. ANSYS, Inc., USA, 2013.

[161] Penny Tinkler and Carolyn Jackson. Examining the doctorate: institutional policy and the phd examination process in britain. *Studies in higher education*, 25(2):167–180, 2000.

[162] Fang-Yuan Zhong. Studies on the aeroacoustics of turbomachinery. *Journal of Thermal Science*, 8(1):9–22, 1999.

Appendix A

Sources for Figure 1.1

Data

Aircraft fan:
Spittle, P. (2003). Gas turbine technology. Physics education, 38(6), 504.

Marine turbocharger:
Chesse P, Hetet J, Tauzia X, Roy P, Inozu B. Performance Simulation of Sequentially Turbocharged Marine Diesel Engines With Applications to Compressor Surge. ASME. J. Eng. Gas Turbines Power. 2000;122(4):562-569. doi:10.1115/1.1290587.

Car turbocharger:
Tíscar, J. G. (2017). Experiments on turbocharger compressor acoustics (Doctoral dissertation).

Dyson V2 compressor:
Wu, Y. A. (2014). Numerical investigation of the performance and flow behaviour of centrifugal compressors (Thesis). The University of Manchester.

μ gas turbine:
Olivero, M. (2012). Evolution of a centrifugal compressor: From turbocharger to micro gas turbine applications.

Ultra μ gas turbine:
Han, S., Seo, J., Park, J. Y., Choi, B. S., & Do, K. H. (2010). Design and simulation of 500W ultra-micro gas turbine generator. Proc. PowerMEMS, Leuven, 247-250.

Appendix B

LCMV beamforming procedure

A brief guiding procedure to compute the desired $\mathbf{P}^+$ and $\mathbf{P}^-$ decomposed spectra required in equation 2.2, using a LCMV (Linearly Restricted Minimum Covariance) strategy is reproduced in this appendix to section 2.3.1 from García-Tíscar [55].

For a more intuitive comprehension of the beamformer, one can consider its transmitting equivalent: a phased array emitter where the same signal $p(t)$, with its phase shifted by a quantity w_n^*, is fed to an n-element linear array of fixed transmitters, forming a plane wave emitted in the θ direction which can be steered at will adjusting each w_n^*. The beamforming method provides a way to mathematically tune the sensitivity of the overall system in order to isolate the downstream and upstream information of the acquired signal.

The approach in this case is the inverse: by tuning the weights w_n^* that multiply each recorded pressure signal $p_n(t)$ the pressure wave coming from the direction of arrival (DOA) θ that we are interested in may be resolved. The extension to a wideband beamformer is relatively straightforward. First the Fast Fourier Transform (FFT, denoted by $\mathscr{F}$) of the recorded pressure signals is computed:

$$\mathbf{P}_n(f_k) = \mathscr{F}\{p_n(t_k)\} \tag{B.1}$$

Subscript k indicates that the signal is acquired at discrete time steps. The described narrowband procedure is then followed for each discrete frequency to finally obtain the desired signal through the inverse transform:

$$p(t) = \mathscr{F}^{-1}\left\{\mathbf{w}^H(f_k)\,\mathbf{P}(f_k)\right\} \tag{B.2}$$

Here, $\mathbf{P}(f_k)$ is the $k \times n$ matrix of transformed signals and $\mathbf{w}^H(f_k)$ is the matrix of weights for each frequency. In order to compute the optimal weights for the desired DOAs ($\theta = -90^o$ for downstream and $\theta = 90^o$ for upstream waves, assuming a typical flow DOA of $\theta = 90^o$), several schemes can be used. For this study a LCMV beamformer was used, a well established procedure, which aims at minimizing the overall output power (variance) of the signal, while maintaining unitary gain in the precise desired direction.

The decomposed signals for each frequency f_k are obtained by weighting the transformed measurement matrix $\mathbf{P}(f_k) = [P_1 P_2 P_3] = \mathscr{F}\{[p_1 p_2 p_3]\}$ as follows:

$$\begin{aligned} \mathbf{P}^+(f_k) &= \mathbf{w}^{+H}\mathbf{P}(f_k) \\ \mathbf{P}^-(f_k) &= \mathbf{w}^{-H}\mathbf{P}(f_k) \end{aligned} \tag{B.3}$$

It can be shown that the corresponding weights for filtering the forward and backward signals are obtained for each frequency f_k by:

$$\begin{aligned} \mathbf{w}^+ &= \mathbf{g}^+ \left[\Sigma_p^{-1}\, \mathbf{A}^H(\Theta) \left[\mathbf{A}^H(\Theta)\, \Sigma_p^{-1}\, \mathbf{A}^H(\Theta)\right]^{-1}\right] \\ \mathbf{w}^- &= \mathbf{g}^- \left[\Sigma_p^{-1}\mathbf{A}^H(\Theta) \left[\mathbf{A}^H(\Theta)\, \Sigma_p^{-1}\, \mathbf{A}^H(\Theta)\right]^{-1}\right] \end{aligned} \tag{B.4}$$

Where $g^+ = [1\ 0]^T$ and $g^- = [0\ 1]^T$ are the desired response vectors (unitary gain in one direction and zero gain in the opposite). Σ_p denotes the covariance matrix. For certain discrete frequencies f_k it can be reduced to:

$$\Sigma_p(f_k) = [\mathbf{P}(f_k)\, \mathbf{P}^H(f_k)] \tag{B.5}$$

The constraints matrix $\mathbf{A}(\Theta) = [\mathbf{a}^+(\theta)\, \mathbf{a}^-(\theta)]^T$ contains the beamformer response array (signal lags) in both directions:

$$\begin{aligned} \mathbf{a}^+(\theta) &= \mathbf{a}(-90^\circ) = \left[1, \exp(j\beta^+ d_s), \exp(j\beta^+ 2d_s)\right]^T \\ \mathbf{a}^-(\theta) &= \mathbf{a}(90^\circ) = \left[1, \exp(-j\beta^- d_s), \exp(-j\beta^- 2d_s)\right]^T \end{aligned} \tag{B.6}$$

Here d_s is the distance between sensors and $\beta^\pm$ are complex wave numbers corrected for attenuation and mean flow:

$$\beta^+ = \frac{k + \alpha(1-j)}{1+M} \quad \text{and} \quad \beta^- = \frac{k + \alpha(1-j)}{1-M} \tag{B.7}$$

M represents the Mach number, $k = \omega/c$ the acoustic wave number and α the viscothermal attenuation coefficient, which can be computed as:

$$\alpha = \frac{1}{ra}\left(\frac{\nu\,\omega}{2}\right)^{1/2}\left[1 - (\gamma - 1)Pr^{-0.5}\right] \tag{B.8}$$

Duct radius is denoted here by r, a is the speed of sound, ν the cinematic viscosity, $\omega = 2\pi f_k$ the angular frequency and Pr is the Prandtl number.